

Additively Manufactured Implants: From design for form to design for morphing

Moosabeiki, Vahid

DOI

[10.4233/uuid:cfa4dd02-b32e-425b-8266-3ae8c153ce5e](https://doi.org/10.4233/uuid:cfa4dd02-b32e-425b-8266-3ae8c153ce5e)

Publication date

2025

Document Version

Final published version

Citation (APA)

Moosabeiki, V. (2025). *Additively Manufactured Implants: From design for form to design for morphing*. [Dissertation (TU Delft), Delft University of Technology]. <https://doi.org/10.4233/uuid:cfa4dd02-b32e-425b-8266-3ae8c153ce5e>

Important note

To cite this publication, please use the final published version (if applicable). Please check the document version above.

Copyright

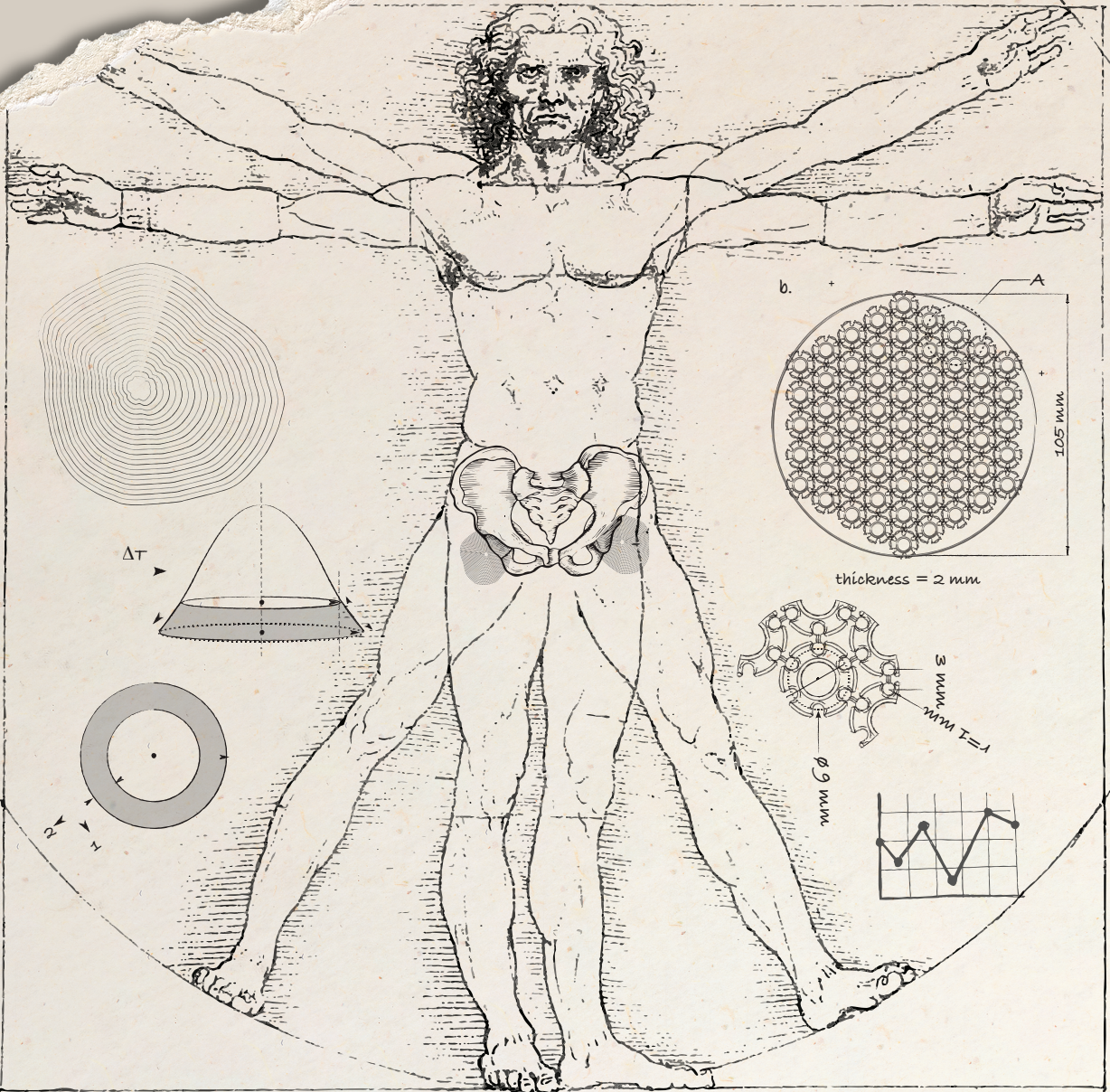
Other than for strictly personal use, it is not permitted to download, forward or distribute the text or part of it, without the consent of the author(s) and/or copyright holder(s), unless the work is under an open content license such as Creative Commons.

Takedown policy

Please contact us and provide details if you believe this document breaches copyrights. We will remove access to the work immediately and investigate your claim.

Additively manufactured implants: From design for form to design for morphing

Vahid Moosabeiki Dehabadi



Additively Manufactured Implants: **From design for form to design for morphing**

Additively Manufactured Implants: From design for form to design for morphing

Proefschrift

ter verkrijging van de graad van doctor
aan de Technische Universiteit Delft,
op gezag van de Rector Magnificus, Prof.dr.ir. T.H.J.J. van der Hagen,
voorzitter van het College voor Promoties,
in het openbaar te verdedigen op maandag 12 mei 2025 om 12:30 uur.

door

Vahid MOOSABEIKI DEHABADI

Werktuigkundig ingenieur,
K. N. Toosi University of Technology, Iran,
geboren te Yazd, Iran.

Dit proefschrift is goedgekeurd door de promotoren.

Samenstelling promotiecommissie bestaat uit:

Rector magnificus,	Voorzitter
Prof. dr. A.A. Zadpoor,	Technische Universiteit Delft, promotor
Dr. M.J. Mirzaali Mazandarani,	Technische Universiteit Delft, copromotor

Onafhankelijke leden:

Prof. dr. ir. P. Breedveld	Technische Universiteit Delft, Nederland
Prof. dr. F. Scarpa	University of Bristol, United Kingdom
Prof. dr. E. B. Wolvius	Erasmus MC, Nederland
Prof. dr. M.J. Santofimia Navarro	Technische Universiteit Delft, Nederland

Overig lid:

Dr. J. Zhou	Technische Universiteit Delft, Nederland
-------------	--

Reserve lid:

Dr. A. C. Akyildiz	Technische Universiteit Delft/Erasmus MC, Nederland
--------------------	--



The research leading to these results was part of the “Metallic Clay: Shape-Matching Orthopaedic Implants,” project number 16582, financed by the Dutch Research Council (NWO), The Netherlands.

Keywords: patient-specific; medical device; implant; shape morphing

Cover illustration: Hoorra Hosseini

Printed by: Gildeprint | www.gildeprint.nl

Copyright © 2025 by V. Moosabeiki Dehabadi

ISBN 978-94-6384-772-8

An electronic version of this dissertation is available at <http://repository.tudelft.nl/>

Summary

The growing need for personalized medical solutions has highlighted the importance of advancements in designing and producing patient-specific medical devices. Conventional manufacturing processes are effective in producing generic devices but often struggle to accommodate the unique anatomical variations of individual patients. This limitation may increase the risk of unfavorable surgical results and complications. Introducing 3D printing, or additive manufacturing (AM), has created new opportunities for the rapid and precise fabrication of customized implants, prosthetics, and orthotics tailored to fit patient anatomies. This technology not only enhances the functionality and durability of these devices but also contributes to faster recovery and improved patient outcomes.

However, several challenges remain: how to streamline the design process to deliver these tailored solutions swiftly and efficiently without compromising functionality, longevity, or durability. This thesis addresses these challenges by exploring strategies for integrating advanced computational models, design optimization techniques, and workflow automation into medical device design and production. These approaches aim to reduce the time from the initial concept to the final product, ensuring patients receive customized solutions promptly.

In addition to exploring the benefits of customization, this thesis investigates the use of generic but adaptable implants that can be quickly tailored to individual patient needs. This approach balances the need for rapid production with maintaining high standards of implant performance and patient outcomes, staying in the one-design-fits-all approach.

Chapter 2 provides an overview of the current state of 3D printing in medical applications, highlighting the challenges and advancements in the field. It also reviews recent developments in additive manufacturing technologies and materials science, setting the foundation for the subsequent chapters.

Chapter 3 reviews the critical design considerations for load-bearing implants, emphasizing the importance of balancing biomechanical properties with patient-specific anatomical needs. These considerations ensure that implants fit well and perform under the body's biomechanical demands.

Chapter 4 focuses on streamlining the design process for personalized implants, exploring the integration of workflow automation and optimization techniques to reduce the design-to-production timeline. By using experimentally validated computational models and automating critical stages of the design and manufacturing process, this

chapter demonstrates how time and effort can be significantly reduced, leading to more efficient and reliable production.

Chapter 5 continues the discussion on load-bearing implants by examining how computational modeling and design optimization can be applied further to improve the precision and efficiency of medical device production. The chapter outlines the methods used to achieve designs tailored to individual patients using various techniques.

Chapter 6 further optimizes patient-specific devices through advanced techniques, such as functionally graded materials (FGMs), to enhance their design. The chapter discusses how variations in material properties and the use of gradient technology improve device performance by adding functionality and more accurately replicating natural biological structures, resulting in superior outcomes in clinical applications.

Chapter 7 introduces the concept of adaptive design, where a flexible framework is developed to allow for rapid adjustments in implant design. This framework enables medical devices to be quickly and accurately customized for different patients, enhancing the overall design process and making it more adaptable to various clinical needs.

Chapter 8 explores the concept of shape matching through 4D printing, focusing on how 4D-printed structures can adapt to patients' specific curvatures and anatomical features. Integrating 4D printing into medical device design provides an innovative approach to creating adaptive, patient-specific solutions that can change shape over time or in response to environmental stimuli.

The results of this thesis indicate a substantial reduction in production time, improved fit and functionality of medical devices, and better patient outcomes as a result of implementing the proposed approaches. The contributions made in this thesis lay the groundwork for future advancements in personalized healthcare, providing a comprehensive framework for the efficient and effective design and fabrication of patient-specific medical devices.

Samenvatting

De groeiende behoefte aan gepersonaliseerde medische oplossingen heeft het belang benadrukt van vooruitgang in het ontwerpen en produceren van patiëntspecifieke medische hulpmiddelen. Traditionele productiemethoden zijn effectief in het vervaardigen van generieke apparaten, maar hebben vaak moeite om de unieke anatomische variaties van individuele patiënten te accommoderen. Deze beperking kan het risico op ongunstige chirurgische resultaten en complicaties vergroten. De introductie van 3D-printen, of additieve fabricage (AM), heeft nieuwe mogelijkheden gecreëerd voor de snelle en nauwkeurige fabricage van op maat gemaakte implantaten, prothesen en orthoses die zijn afgestemd op de anatomie van de patiënt. Deze technologie verbetert niet alleen de functionaliteit en duurzaamheid van deze hulpmiddelen, maar draagt ook bij aan een sneller herstel en betere patiëntresultaten.

Er blijven echter verschillende uitdagingen bestaan: hoe het ontwerpproces te stroomlijnen om deze op maat gemaakte oplossingen snel en efficiënt te leveren zonder concessies te doen aan functionaliteit, levensduur of duurzaamheid. Dit proefschrift behandelt deze uitdagingen door strategieën te onderzoeken voor de integratie van geavanceerde computationele modellen, ontwerptimalisatietechnieken en workflowautomatisering in het ontwerp en de productie van medische hulpmiddelen. Deze benaderingen zijn gericht op het verkorten van de tijd van het eerste concept tot het eindproduct, zodat patiënten snel gepersonaliseerde oplossingen kunnen ontvangen.

Naast het verkennen van de voordelen van maatwerk, onderzoekt dit proefschrift het gebruik van generieke maar aanpasbare implantaten die snel kunnen worden afgestemd op de behoeften van individuele patiënten. Deze benadering balanceert de noodzaak van snelle productie met het handhaven van hoge normen voor implantaatprestaties en patiëntresultaten, en blijft binnen de benadering van one-design-fits-all.

Hoofdstuk 2 biedt een overzicht van de huidige stand van zaken van 3D-printen in medische toepassingen, waarbij de uitdagingen en vooruitgangen in het veld worden belicht. Het bespreekt ook recente ontwikkelingen in additieve productietechnologieën en materiaalkunde, en legt zo de basis voor de daaropvolgende hoofdstukken.

Hoofdstuk 3 bespreekt de kritieke ontwerpoverwegingen voor dragende implantaten, waarbij de nadruk wordt gelegd op het belang van het balanceren van biomechanische eigenschappen met patiëntspecifieke anatomische behoeften. Deze overwegingen zorgen ervoor dat implantaten goed passen en presteren onder de biomechanische eisen van het lichaam.

Hoofdstuk 4 richt zich op het stroomlijnen van het ontwerpproces voor gepersonaliseerde implantaten, waarbij wordt onderzocht hoe workflowautomatisering en optimalisatietechnieken kunnen worden geïntegreerd om de tijd tussen ontwerp en productie te verkorten. Door gebruik te maken van experimenteel gevalideerde computationele modellen en kritieke stadia van het ontwerp- en productieproces te automatiseren, toont dit hoofdstuk aan hoe tijd en inspanning aanzienlijk kunnen worden verminderd, wat leidt tot efficiëntere en betrouwbaardere productie.

Hoofdstuk 5 vervolgt de discussie over dragende implantaten door te onderzoeken hoe computationele modellering en ontwerptimalisatie verder kunnen worden toegepast om de precisie en efficiëntie van de productie van medische hulpmiddelen te verbeteren. Het hoofdstuk schetst de methoden die zijn gebruikt om ontwerpen te realiseren die zijn afgestemd op individuele patiënten met behulp van verschillende technieken.

Hoofdstuk 6 optimaliseert patiëntspecifieke hulpmiddelen verder door middel van geavanceerde technieken, zoals functioneel gradiëntmateriaal (FGM), om hun ontwerp te verbeteren. Het hoofdstuk bespreekt hoe variaties in materiaaleigenschappen en het gebruik van gradiënttechnologie de prestaties van hulpmiddelen verbeteren door functionaliteit toe te voegen en natuurlijke biologische structuren nauwkeuriger te repliceren, wat resulteert in superieure resultaten in klinische toepassingen.

Hoofdstuk 7 introduceert het concept van adaptief ontwerp, waarbij een flexibel raamwerk wordt ontwikkeld dat snelle aanpassingen in implantaatontwerpen mogelijk maakt. Dit raamwerk stelt medische hulpmiddelen in staat om snel en nauwkeurig te worden gepersonaliseerd voor verschillende patiënten, wat het algehele ontwerpproces verbetert en het beter aanpasbaar maakt aan diverse klinische behoeften.

Hoofdstuk 8 verkent het concept van vormaanpassing door middel van 4D-printen, met de focus op hoe 4D-geprinte structuren zich kunnen aanpassen aan de specifieke krommingen en anatomische kenmerken van patiënten. Het integreren van 4D-printen in het ontwerp van medische hulpmiddelen biedt een innovatieve benadering om adaptieve, patiëntspecifieke oplossingen te creëren die van vorm kunnen veranderen in de loop van de tijd of als reactie op omgevingsstimuli.

De resultaten van dit proefschrift wijzen op een substantiële vermindering van de productietijd, een verbeterde pasvorm en functionaliteit van medische hulpmiddelen, en betere patiëntresultaten als gevolg van de implementatie van de voorgestelde benaderingen. De bijdragen van dit proefschrift leggen de basis voor toekomstige vooruitgangen in gepersonaliseerde gezondheidszorg, door een uitgebreid raamwerk te bieden voor het efficiënte en effectieve ontwerp en de fabricage van patiëntspecifieke medische hulpmiddelen.

Contents

Summary	vii
Samenvatting	ix
1 Introduction	17
1.1 Background	18
1.2 Significance of customization in medical devices.....	18
1.3 The evolution of medical device design	19
1.4 Problem statement and research objectives	21
1.5 Thesis aim and outline	21
Bibliography	23
2 Additive manufacturing of biomaterials— Design principles and their implementation	27
2.1 Introduction	28
2.2 Geometrical design of lattices	29
2.2.1 Library-based design	32
2.2.2 Topology optimization designs	36
2.2.3 Bio-inspired design	37
2.2.4 Meta-biomaterials	40
2.3 AM of biomedical metals and alloys.....	41
2.3.1 Biodegradable metals	42
2.3.2 Shape-memory alloys	45
2.3.3 In Situ alloying and composites	46
2.4 AM of biomedical polymers	47
2.4.1 Hydrogels.....	48
2.4.2 Natural polymers (hydrogel)	49
2.4.3 Synthetic polymers.....	52
2.4.4 Composites	63

2.5	AM of biomedical ceramics	64
2.5.1	Classification of ceramics	64
2.5.2	Properties of ceramics	65
2.5.3	Manufacturing methods for ceramics.....	66
2.5.4	Biomedical applications of ceramics.....	72
2.6	Conclusions and future research directions.....	73
	Bibliography	75
3	Design considerations for patient-specific bone fixation plates	101
3.1	Introduction.....	102
3.2	Methods.....	103
3.3	Results	103
3.3.1	Material	105
3.3.2	Geometry	105
3.3.3	Fixation	105
3.3.4	Manufacturing techniques.....	106
3.3.5	Clinical complications.....	107
3.4	Discussion	108
3.5	Conclusion	111
	Bibliography	133
4	Semi-automated digital workflow to design and evaluate patient-specific mandibular reconstruction implants	139
4.1	Introduction.....	140
4.2	Materials and methods	141
4.2.1	Bone model generation.....	141
4.2.2	Implant designing.....	142
4.2.3	FEA methods	144
4.2.4	Experimental methods	149
4.3	Results	152
4.3.1	FEA results	152

4.3.2	Experimental testing results.....	155
4.4	Discussion	158
4.4.1	Image processing, shape estimation, and implant designing .	159
4.4.2	FEA and experimental validation	160
4.5	Conclusion	164
4.6	Supplementary material.....	165
	Bibliography	167
5	3D printed patient-specific fixation plates for the treatment of slipped capital femoral epiphysis: topology optimization vs. conventional design	171
5.1	Introduction.....	172
5.2	Materials and methods	173
5.2.1	Image segmentation and virtual reconstruction.....	174
5.2.2	Synthetic bone	174
5.2.3	Computational modelling	175
5.2.4	Plate design	180
5.2.5	Experimental methods	182
5.3	Results	184
5.3.1	FEA results	184
5.3.2	Experimental test results.....	186
5.4	Discussion	187
5.5	Conclusions	191
5.6	Supplementary material.....	192
	Bibliography	195
6	Multi-material 3D printing of functionally graded soft-hard interfaces for enhancing mandibular kinematics of temporomandibular joint replacement prostheses	199
6.1	Introduction.....	200
6.2	Results and discussion	201
6.2.1	Prosthesis performance.....	203

6.2.2 Kinematics analysis	205
6.3 Methods	212
6.3.1 TMJ prosthesis design and manufacturing	212
6.3.2 Biomechanical testing	213
6.3.3 Computational modeling	214
6.3.4 Material property assignments	214
6.3.5 Loads and boundary conditions	215
6.3.6 Kinematic performance evaluation	216
6.4 Conclusions	217
Bibliography	219
7 Additively manufactured shape-morphing implants for the treatment of acetabular defects	223
7.1 Introduction	224
7.2 Materials and methods	226
7.2.1 Implant design and manufacturing	226
7.2.2 Synthetic hemipelvis models	226
7.2.3 Surgical implementation	227
7.2.4 CT scanning and analysis	228
7.2.5 Biomechanical testing	230
7.2.1 Statistical analysis	230
7.3 Results	231
7.3.1 Shape-matching performance	231
7.3.2 Biomechanical performance	231
7.4 Discussion	233
7.5 Conclusions	237
7.6 Supplementary material	238
Bibliography	239
8 Curvature tuning through defect-based 4D printing	243
8.1 Introduction	244

8.2	Results and discussion	247
8.3	Conclusion	259
8.4	Materials and methods	260
8.4.1	4D printing.....	260
8.4.2	Activation	261
8.4.3	Micro-computed tomography (μ CT).....	261
8.4.4	3D optical scanning.....	261
8.4.5	Dynamic mechanical analysis (DMA)	261
8.4.6	Measurement of expansion factors.....	262
8.4.7	Computational modeling	262
8.4.8	Curvature measurements	263
8.5	Supplementary material.....	264
	Bibliography	269
9	Concluding remarks.....	273
9.1	Main findings.....	274
9.2	General discussion	274
9.3	General discussion	276
9.4	Challenges and unresolved questions	279
	Bibliography	281
10	Acknowledgements.....	285
11	List of publications.....	289

1

Introduction

*“You never change things by
fighting the existing reality.
To change something,
build a new model that
makes the existing model obsolete.”
– Buckminster Fuller*

1.1 Background

In the fast-paced and ever-evolving field of medical device design, the ability to rapidly and efficiently produce high-quality, patient-specific medical devices has become increasingly essential [1-5]. While effective for producing standard medical devices, traditional manufacturing methods often fail to address individual patients' unique anatomical requirements. This gap can lead to unsatisfactory surgical outcomes, an elevated risk of complications, and the necessity for revision surgeries [6, 7].

Despite advancements in medical technology, standard implants often result in complications, such as implant loosening, infection, and poor osseointegration, leading to increased revision rates [8-12]. These complications affect patient outcomes and impose significant economic burdens on healthcare systems. Moreover, the unique characteristics of each defect pose a challenge for preformed implants, as securing them in place often requires the use of fillers or the removal of otherwise healthy tissue [13]. This highlights the limitations of standard implants in addressing the anatomical diversity of patients.

Recent advancements in digital manufacturing technologies, mainly 3D printing (additive manufacturing or AM), have opened up new opportunities for producing customized medical devices [14-20]. This transformative technology enables the rapid and precise fabrication of custom implants, prosthetics, and orthotics tailored to fit individual patient anatomies [4, 5, 21-23]. These devices can be refined by integrating advanced design strategies to ensure greater patient comfort and accelerate healing [21, 24].

1.2 Significance of customization in medical devices

Customization in medical devices plays a crucial role in enhancing patient recovery [21, 25-28]. A well-fitted implant ensures better anatomical conformity and improves biomechanical performance, reducing stress on surrounding tissues and promoting faster healing [29-31]. Additionally, incorporating advanced design features, such as lattice structures, into implants can support bone ingrowth and improve osseointegration, all while maintaining the mechanical strength necessary for long-term durability [22, 23, 32-34].

The ability to integrate complex structures within implants not only facilitates recovery but also ensures a better anatomical fit. This personalized approach enhances patient outcomes post-trauma or injury and improves the durability and functionality of medical devices, ensuring they last longer and perform more effectively over time [21-24, 35]. However, a critical gap remains in efficiently customizing implants for individual patients while maintaining high production throughput. Existing approaches either rely

on fully custom-made designs, which are time-consuming and costly, or generic implants that fail to account for patients' anatomical diversity.

1.3 The evolution of medical device design

Standard and generic medical devices have long been crucial in medical treatment. They are designed to serve a broad patient population by offering a one-size-fits-all solution. These devices are typically mass-produced using standardized dimensions and materials, which allows for cost-effective manufacturing and broad availability. The design process for standard devices generally involves creating a generic shape based on average anatomical data, aiming to accommodate most patients [36, 37]. This approach relies on extensive biomechanical testing and historical clinical data to ensure safety and effectiveness across various cases.

However, the limitations of standard implants become apparent when confronted with the anatomical variability found in individual patients. Because these devices are not tailored to specific anatomical features, they often fail to achieve an optimal fit, leading to several potential complications [13, 38]. For example, generic mandibular implants often struggle to conform precisely to the unique jaw structure of a patient, leading to issues such as misalignment, uneven load distribution, discomfort, reduced functionality, implant loosening, compromised aesthetics, and ultimately a higher risk of revision surgery [38-40]. Additionally, standard implants may require invasive procedures to modify the patient's anatomy to fit the implant, leading to longer recovery times and increased risk of infection [41, 42].

In contrast, patient-specific medical devices are designed to address the unique anatomical features of individual patients. This level of customization significantly enhances the fit, functionality, and comfort of medical devices. The design process for these devices begins with detailed imaging techniques, *e.g.*, CT or MRI scans, which capture the exact dimensions and contours of the anatomy. These images are then used to create a digital device model, ensuring it will conform precisely to the patient's needs. Advanced computational tools, including finite element analysis (FEA), are often employed to simulate the implant under various conditions, optimizing the design for both functionality and durability (Figure 1.1).

A key benefit of customized medical devices is their ability to provide a superior fit, which can enhance the biomechanical performance and the aesthetic outcome of the surgery [43, 44]. For instance, by precisely matching the patient's anatomy, customized implants reduce the need for additional modifications during surgery and minimize the risk of complications [44]. This approach is particularly valuable in complex cases, such as mandibular reconstructions [38-40] or joint replacements [37], where standard implants would be improved.

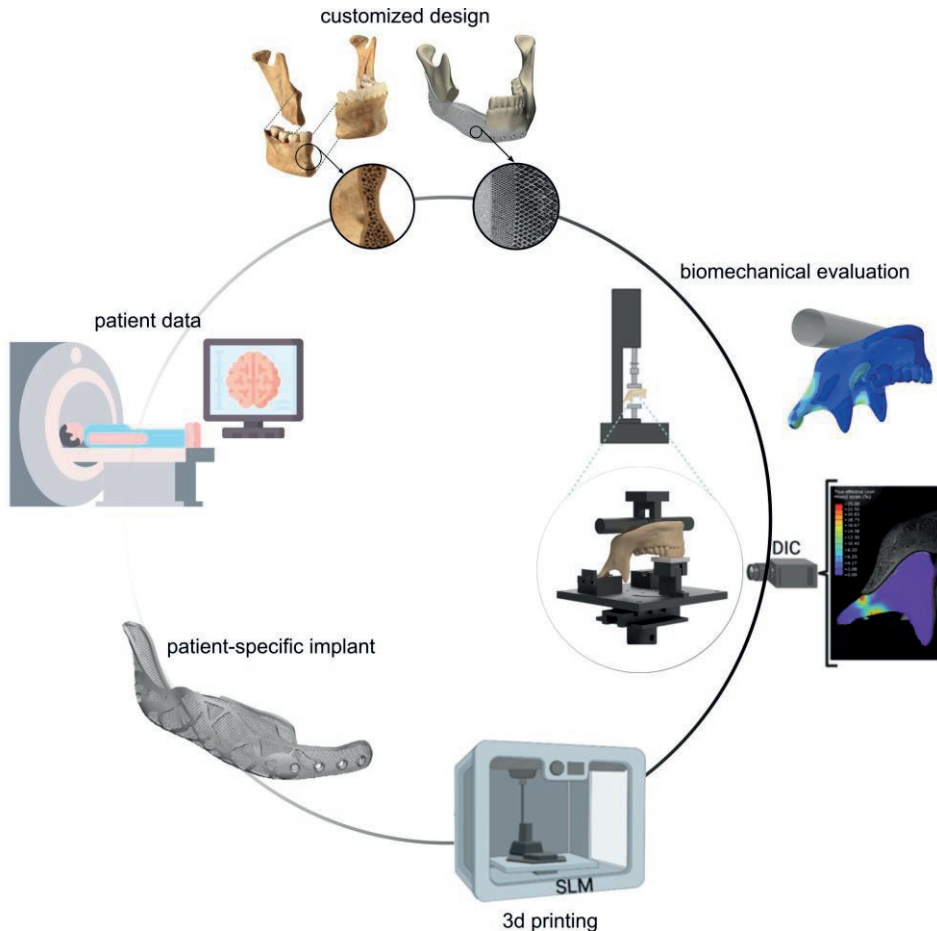


Figure 1.1. Workflow for designing and fabricating a patient-specific implant— The process begins with acquiring patient data through medical imaging, followed by the customized design of an implant with porous structures tailored to the patient’s anatomy (adapted from Mehta & Kuriakose (2021)). The designed implant undergoes biomechanical evaluation using physiologically relevant experiments and FEA to assess stress distribution. After validation, the implant is fabricated using 3D printing technique, resulting in a final patient-specific implant ready for clinical application.

Moreover, 3D printing has brought a revolutionary change to the production of customized implants. Unlike traditional manufacturing methods, which may involve extensive lead times and high costs for custom designs, 3D printing allows for the cost-effective and rapid production of customized medical devices. This technology allows for the creation of complex shapes and structures that would be impossible or expensive to produce with conventional methods. Furthermore, 3D printing can produce customized surgical tools, enhancing procedure precision. The ability to print complex designs and use biocompatible materials ensures that the resulting medical devices are both functional and durable, providing long-term benefits to patients [1, 21, 45].

1.4 Problem statement and research objectives

Despite 3D printing's potential to revolutionize medical device design, the primary challenge remains to streamline the design process to deliver tailored solutions as quickly and efficiently as possible without compromising functionality, longevity, or durability. The current state of medical device production still relies heavily on time-consuming and complex processes, which can delay the availability of patient-specific solutions and limit their widespread adoption.

This thesis focuses on two key objectives. First, it explores strategies to streamline the design process for medical devices by integrating advanced computational models and workflow automation to reduce the time from the initial concept to the final product. Second, it investigates using generic, adaptable implants that can be customized for individual patients without requiring fully custom-made designs. This dual approach aims to balance the need for rapid production with maintaining high standards of implant performance and patient outcomes.

1.5 Thesis aim and outline

This thesis aims to develop and evaluate methods for streamlining the development process for personalized medical devices using two distinct approaches. The first approach integrates advanced computational models, design optimization techniques, and workflow automation to reduce the time required from initial concept to final product. The goal is to enable the rapid deployment of customized medical devices that maintain high standards of functionality, durability, and longevity.

The second approach explored in this thesis is the feasibility of using generic, adaptable implants that can be quickly tailored to fit individual patient anatomies. These implants are designed to provide a customized fit without the need for a completely individualized design approach, thus providing a more efficient and affordable solution for managing complex medical conditions. By combining advanced manufacturing techniques with adaptive design principles, this research seeks to develop a framework for producing high-quality, patient-specific implants that can be delivered and implemented with unprecedented speed.

This thesis also addresses the potential of incorporating design features such as lattice structures into 3D-printed implants to enhance the healing process. By optimizing these structures, the research aims to create implants that fit better and actively support bone healing and integration, ultimately improving patient outcomes.

This thesis is structured into eight chapters, each addressing an essential aspect of the design and production process for patient-specific medical devices.

Chapter 2 provides a detailed review of additive manufacturing for biomaterials and emphasizes design strategies and advancements that enable the creation of customized medical devices tailored to individual patient needs.

Chapter 3 provides a detailed literature review on design considerations for patient-specific bone fixation plates. It examines critical design parameters, such as material properties, geometry, fixation mechanisms, and biomechanical factors that influence the effectiveness of these implants. The chapter emphasizes the importance of optimizing the biomechanical performance of bone plates to ensure their success in clinical applications.

Chapter 4 presents a semi-automated workflow to streamline the design of patient-specific implants. The workflow significantly reduces design time using advanced computational tools and additive manufacturing while maintaining high mechanical precision and patient-specific adaptation. This chapter emphasizes the transformative potential of digital workflows and additive manufacturing in improving implants' efficiency and biomechanical performance, especially in complex surgical applications.

Chapter 5 presents a comparative analysis of 3D-printed patient-specific fixation plates, focusing on topology optimization and comparing it with conventional design techniques. It evaluates the biomechanical performance of these plates, particularly in orthopedic applications, and highlights how the topology optimization technique can enhance stress distribution, anatomical conformity, and long-term implant durability.

Chapter 6 explores using functionally graded materials (FGMs) as an additional tool to enhance patient-specific device functionality. By utilizing gradients in material properties, the chapter demonstrates how FGMs improve the performance of implants, more effectively mimicking natural biological structures. This approach allows for better biomechanical integration, improving clinical outcomes and increasing implant longevity.

Chapter 7 introduces the concept of adaptive design through a flexible framework that allows for rapid adjustments in implant design. It focuses on a 3D-printed flexible mesh implant for acetabular defects and demonstrates how the mesh adapts to various anatomical geometries, providing a better fit and increased stability. This approach eliminates the need for fully customized designs while improving clinical outcomes for patients with complex defects.

Chapter 8 explores the concept of shape matching through 4D printing, emphasizing how 4D-printed structures can conform to specific curvatures and anatomical features of patients. The chapter investigates how shape-morphing structures can be created to react to external stimuli, offering dynamic, adaptive implants that evolve.

Chapter 9 summarizes the main findings presented in this thesis. Additionally, it outlines several suggestions for potential future research avenues.

Bibliography

1. M. Javaid, A. Haleem, Current status and applications of additive manufacturing in dentistry: A literature-based review, *Journal of Oral Biology and Craniofacial Research* 9(3) (2019) 179-185.
2. S.V. Murphy, A. Atala, 3D bioprinting of tissues and organs, *Nature Biotechnology* 32(8) (2014) 773-785.
3. B.C. Gross, J.L. Erkal, S.Y. Lockwood, C. Chen, D.M. Spence, Evaluation of 3D Printing and Its Potential Impact on Biotechnology and the Chemical Sciences, *Analytical Chemistry* 86(7) (2014) 3240-3253.
4. G.T. Klein, Y. Lu, M.Y. Wang, 3D Printing and Neurosurgery—Ready for Prime Time?, *World Neurosurgery* 80(3) (2013) 233-235.
5. J. Banks, Adding Value in Additive Manufacturing : Researchers in the United Kingdom and Europe Look to 3D Printing for Customization, *IEEE Pulse* 4(6) (2013) 22-26.
6. K.J. Bozic, S.M. Kurtz, E. Lau, K. Ong, V. Chiu, T.P. Vail, H.E. Rubash, D.J. Berry, The Epidemiology of Revision Total Knee Arthroplasty in the United States, *Clinical Orthopaedics and Related Research*® 468(1) (2010).
7. R. Pivec, A.J. Johnson, S.C. Mears, M.A. Mont, Hip arthroplasty, *The Lancet* 380(9855) (2012) 1768-1777.
8. K.J. Bozic, S.M. Kurtz, E. Lau, K. Ong, T.P. Vail, D.J. Berry, The epidemiology of revision total hip arthroplasty in the United States, *JBJS* 91(1) (2009) 128-133.
9. M. Junnila, I. Laaksonen, A. Eskelinen, P. Pulkkinen, L. Ivar Havelin, O. Furnes, A. Marie Fenstad, A.B. Pedersen, S. Overgaard, J. Kärrholm, G. Garellick, H. Malchau, K.T. Mäkelä, Implant survival of the most common cemented total hip devices from the Nordic Arthroplasty Register Association database, *Acta Orthopaedica* 87(6) (2016) 546-553.
10. N. Walter, T. Stich, D. Docheva, V. Alt, M. Rupp, Evolution of implants and advancements for osseointegration: A narrative review, *Injury* 53 (2022) S69-S73.
11. D. Apostu, O. Lucaciu, C. Berce, D. Lucaciu, D. Cosma, Current methods of preventing aseptic loosening and improving osseointegration of titanium implants in cementless total hip arthroplasty: a review, *Journal of International Medical Research* 46(6) (2018) 2104-2119.
12. W. Wang, Y. Ouyang, C.K. Poh, Orthopaedic implant technology: biomaterials from past to future, *Annals of the Academy of Medicine-Singapore* 40(5) (2011) 237.
13. N. Nagarajan, A. Dupret-Bories, E. Karabulut, P. Zorlutuna, N.E. Vrana, Enabling personalized implant and controllable biosystem development through 3D printing, *Biotechnology Advances* 36(2) (2018) 521-533.
14. R.J. Morrison, K.N. Kashlan, C.L. Flanagan, J.K. Wright, G.E. Green, S.J. Hollister, K.J. Weatherwax, Regulatory Considerations in the Design and Manufacturing of Implantable 3D-Printed Medical Devices, *Clinical and Translational Science* 8(5) (2015) 594-600.
15. A.K. Pal, A.K. Mohanty, M. Misra, Additive manufacturing technology of polymeric materials for customized products: recent developments and future prospective, *RSC advances* 11(58) (2021) 36398-36438.
16. I. Fidan, O. Huseynov, M.A. Ali, S. Alkunte, M. Rajeshirke, A. Gupta, S. Hasanov, K. Tantawi, E. Yasa, O. Yilmaz, Recent inventions in additive manufacturing: Holistic review, *Inventions* 8(4) (2023) 103.
17. L. Lin, P.S. Kollipara, Y. Zheng, Digital manufacturing of advanced materials: Challenges and perspective, *Materials Today* 28 (2019) 49-62.
18. S. Vanaei, N. Zirak, Diverse Application of 3D Printing Process, *Industrial Strategies and Solutions for 3D Printing: Applications and Optimization* (2024) 59-80.
19. M.H. Mobarak, M.A. Islam, N. Hossain, M.Z. Al Mahmud, M.T. Rayhan, N.J. Nishi, M.A. Chowdhury, Recent advances of additive manufacturing in implant fabrication—A review, *Applied Surface Science Advances* 18 (2023) 100462.
20. F. Garcia-Villen, F. López-Zárraga, C. Viseras, S. Ruiz-Alonso, F. Al-Hakim, I. Diez-Aldama, L. Saenz-del-Burgo, D. Scaini, J.L. Pedraz, Three-dimensional printing as a cutting-edge, versatile and personalizable vascular stent manufacturing procedure: Toward tailor-made medical devices,

Introduction

- International Journal of Bioprinting 9(2) (2023).
21. C. Li, D. Pisignano, Y. Zhao, J. Xue, *Advances in Medical Applications of Additive Manufacturing, Engineering* 6(11) (2020) 1222-1231.
 22. A.A. Zadpoor, J. Malda, *Additive Manufacturing of Biomaterials, Tissues, and Organs, Annals of Biomedical Engineering* 45(1) (2017) 1-11.
 23. A.A. Zadpoor, *Design for Additive Bio-Manufacturing: From Patient-Specific Medical Devices to Rationally Designed Meta-Biomaterials, International Journal of Molecular Sciences*, 2017.
 24. M.P. Francis, N. Kemper, Y. Maghdouri-White, N. Thayer, 9 - Additive manufacturing for biofabricated medical device applications, in: J. Zhang, Y.-G. Jung (Eds.), *Additive Manufacturing, Butterworth-Heinemann* 2018, pp. 311-344.
 25. C.M. Wixted, J.R. Peterson, R.J. Kadakia, S.B. Adams, *Three-dimensional Printing in Orthopaedic Surgery: Current Applications and Future Developments, JAAOS Global Research & Reviews* 5(4) (2021).
 26. W. Jamróz, J. Szafranec, M. Kurek, R. Jachowicz, *3D Printing in Pharmaceutical and Medical Applications – Recent Achievements and Challenges, Pharmaceutical Research* 35(9) (2018) 176.
 27. B.M. Holzapfel, J.C. Reichert, J.-T. Schantz, U. Gbureck, L. Rackwitz, U. Nöth, F. Jakob, M. Rudert, J. Groll, D.W. Hutmacher, *How smart do biomaterials need to be? A translational science and clinical point of view, Advanced Drug Delivery Reviews* 65(4) (2013) 581-603.
 28. K. Randhawa, J. West, K. Skellern, E. Josserand, *Evolving a Value Chain to an Open Innovation Ecosystem: Cognitive Engagement of Stakeholders in Customizing Medical Implants, California Management Review* 63(2) (2020) 101-134.
 29. D.L. Cohen, J.I. Lipton, L.J. Bonassar, H. Lipson, *Additive manufacturing for in situ repair of osteochondral defects, Biofabrication* 2(3) (2010) 035004.
 30. R.R. Patel, *Does patient-specific implant design reduce subsidence risk in lumbar interbody fusion? A bottom up analysis of methods to reduce vertebral endplate stress, University of Colorado at Denver*, 2018.
 31. H. Derar, *Applications of smart materials to orthopaedic total hip replacement: Design of stemless hip replacement prosthesis, The University of Maine* 2016.
 32. S.J. Hollister, *Porous scaffold design for tissue engineering, Nature Materials* 4(7) (2005) 518-524.
 33. S. Wu, X. Liu, K.W.K. Yeung, C. Liu, X. Yang, *Biomimetic porous scaffolds for bone tissue engineering, Materials Science and Engineering: R: Reports* 80 (2014) 1-36.
 34. A.A. Zadpoor, *Additively manufactured porous metallic biomaterials, Journal of Materials Chemistry B* 7(26) (2019) 4088-4117.
 35. A.A. Zadpoor, *Meta-biomaterials, Biomaterials Science* 8(1) (2020) 18-38.
 36. Y. Jun, K. Choi, *Design of patient-specific hip implants based on the 3D geometry of the human femur, Advances in Engineering Software* 41(4) (2010) 537-547.
 37. J.-A. Lee, Y.-G. Koh, K.-T. Kang, *Biomechanical and Clinical Effect of Patient-Specific or Customized Knee Implants: A Review, Journal of Clinical Medicine*, 2020.
 38. D. Radwan, F. Mobarak, *Plate-related complications after mandibular reconstruction: observational study osteotomy, Egyptian Journal of Oral and Maxillofacial Surgery* 9(1) (2018) 22-27.
 39. G.-J. Seol, E.-G. Jeon, J.-S. Lee, S.-Y. Choi, J.-W. Kim, T.-G. Kwon, J.-Y. Paeng, *Reconstruction plates used in the surgery for mandibular discontinuity defect, Jkaoms* 40(6) (2014) 266-271.
 40. B.P. Kumar, V. Venkatesh, K.A.J. Kumar, B.Y. Yadav, S.R. Mohan, *Mandibular Reconstruction: Overview, Journal of Maxillofacial and Oral Surgery* 15(4) (2016) 425-441.
 41. A.D. Pye, D.E.A. Lockhart, M.P. Dawson, C.A. Murray, A.J. Smith, *A review of dental implants and infection, Journal of Hospital Infection* 72(2) (2009) 104-110.
 42. D.G.K. Hong, J.-h. Oh, *Recent advances in dental implants, Maxillofacial Plastic and Reconstructive Surgery* 39(1) (2017) 33.
 43. L.R.R. da Silva, W.F. Sales, F.d.A.R. Campos, J.A.G. de Sousa, R. Davis, A. Singh, R.T. Coelho, B. Borgohain, *A comprehensive review on additive manufacturing of medical devices, Progress in Additive Manufacturing* 6(3) (2021) 517-553.

44. M. Meng, J. Wang, H. Huang, X. Liu, J. Zhang, Z. Li, 3D printing metal implants in orthopedic surgery: Methods, applications and future prospects, *Journal of Orthopaedic Translation* 42 (2023) 94-112.
45. M. Javaid, A. Haleem, R.P. Singh, R. Suman, 3D printing applications for healthcare research and development, *Global Health Journal* 6(4) (2022) 217-226.

2

Additive manufacturing of biomaterials— Design principles and their implementation

Additive manufacturing (AM, also known as 3D printing) is an advanced manufacturing technique that has enabled progress in the design and fabrication of customized or patient-specific (meta-)biomaterials and biomedical devices (e.g., implants, prosthetics, and orthotics) with complex internal microstructures and tunable properties. In the past few decades, several design guidelines have been proposed for creating porous lattice structures, particularly for biomedical applications. Meanwhile, the capabilities of AM to fabricate a wide range of biomaterials, including metals and their alloys, polymers, and ceramics, have been exploited, offering unprecedented benefits to medical professionals and patients alike. In this chapter, we provide an overview of the design principles that have been developed and used for the AM of biomaterials as well as those dealing with three major categories of biomaterials, *i.e.*, metals (and their alloys), polymers, and ceramics. The design strategies can be categorized as: library-based design, topology optimization, bio-inspired design, and meta-biomaterials. Recent developments related to the biomedical applications and fabrication methods of AM aimed at enhancing the quality of final 3D-printed biomaterials and improving their physical, mechanical, and biological characteristics are also highlighted. Finally, examples of 3D-printed biomaterials with tuned properties and functionalities are presented.

2.1 Introduction

Additive manufacturing (AM, also known as 3D printing) technologies are among the most feasible advanced manufacturing options to create complex structures for use in technology-driven industries, such as healthcare [1], automotive [2,3], and aerospace [4]. AM, being different from other manufacturing methods, such as subtractive and formative methods, results in less scrap and waste of materials and allows for lightweight complex structures, often hollow or porous, thus requiring less material input and energy input during their fabrication and service. Seven categories of AM, namely, binder jetting, directed energy deposition, material extrusion, material jetting, powder bed fusion, sheet lamination, and vat photopolymerization, have been recognized and defined in the ISO/ASTM 52900 standard [5].

Not all AM processes in the ASTM classification are equally developed and used for medical devices and biomaterial fabrication [6]. Here, we summarize the capabilities, limitations, and pros and cons of conventional processes and associated materials (*e.g.*, metals and their alloys, polymers, and ceramics) used in the fabrication of bio-materials (Table 2.1) in terms of printing speed, part sizes, degree of anisotropy, achievable resolution, the possibility of embedding cells in feedstock materials, the need for support, the need for post-processing, and costs. The success of each of these 3D printing processes relies, to a large extent, on the employment of optimized or suitable process parameters within the capabilities of the available AM machines that are associated with specific AM processes.

In addition to selecting the proper AM techniques and suitable printing parameters, the microarchitecture design of biomaterials is one of the critical aspects of their development. It is often necessary to design porous or lattice structures for biomedical applications. This implies that the morphologies and sizes of the pores of biomaterials must be fully open and interconnected to allow for the transport of nutrients and oxygen to cells [6–8].

The advent of AM technologies has provided unique opportunities for the accurate arrangement of the sizes and internal architectures of pores at a microscopic level and to produce organic geometries with complex internal architectures and passages [9–11]. This is one of the most important merits of AM over conventional fabrication technologies, such as casting and molding [12], in which the designer has virtually no control over the precise details of the internal geometries of porous materials. The main objective of this review article is to present a clear picture of how this technology can be applied for producing biomaterials with novel designs, what the challenges and limitations are, and where the technology is heading. We summarize the current design principles employed in the fabrication of AM biomaterials. We also review the applications of different AM processes in the fabrication of metallic, polymeric, and

ceramic biomaterials. It is intended to stimulate the further development and widespread application of the technology to turn design ideas into implants and other medical devices, as well as those of tissue engineering applications.

2.2 Geometrical design of lattices

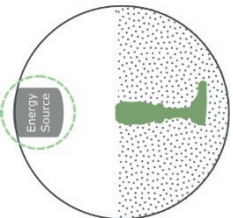
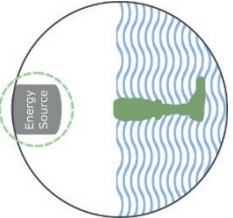
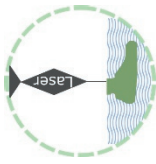
While AM offers almost unlimited possibilities to part designers, there are several constraints in the structural design of lattices that limit the theoretical ability of AM to fabricate porous structures with highly complex geometries. Several inherent limitations related to the processability of the designed part also exist in AM methods, which has led to the introduction of several guidelines to manage these constraints and limitations [13]. Some of these constraints are recognized as minimum feature size (*e.g.*, wall thickness, edges, and corners), the orientation of lattice structures on the build plate for self-overhanging, support materials, and support removal [14].

As an example, in powder bed fusion (PBF) techniques, overhanging structures, which are defined as parts of lattice structures that are not self-supported, can result in undesirable defects in lattice structures [15,16]. There are no underlying layers or solidified sections to support these overhanging parts during their fabrication, which is why the choice of orientation during building is critically important. The overhanging structure also depends on the critical fabrication angle [15]. Sacrificial support materials, therefore, need to be used for overhanging structures below a specific fabrication angle. These sacrificial support materials need to be removed (*e.g.*, in PBF techniques) or washed away (*e.g.*, in vat photopolymerization techniques) from the structures during post-processing, which may damage additively manufactured parts. To compensate for that and achieve optimum results with fewer support materials, the parts need to be designed with self-supported struts in lattice structures. Restricted build envelopes and the application of a single material in the manufacturing process of metallic materials can also be specified as other limitations, although achievable sizes have been considerably increased in recent years, and combinations of materials have become possible, *e.g.*, by means of a recoater. In some cases, the limitation of a combination of materials can be resolved by alloying elemental metallic powders [17]. This limitation can also be overcome by using multiple nozzles in extrusion-based AM techniques.

Table 2.1. Summary of the different AM techniques, useable materials, their pros and cons, and their biomedical applications.

Techniques and Materials	Pros	Cons	Biomedical Application
 <p><i>Material Extrusion (FDM)</i></p> <ul style="list-style-type: none"> • Hydrogels • Thermoplastics • Ceramics • Bio-inks 	<ul style="list-style-type: none"> + Low cost + Accessible + Composite materials + Open-source design 	<ul style="list-style-type: none"> - Slow - Anisotropy in printed part - Low resolution - Nozzles impart high shear forces on cells 	<ul style="list-style-type: none"> • Bioprinting of scaffolds for cell culture • Tissue and organ development • Production of rigid and soft anatomical models for surgical planning
 <p><i>Directed Energy Deposition (DED)</i></p> <ul style="list-style-type: none"> • Metal 	<ul style="list-style-type: none"> + Fast + Composite materials + Dense part 	<ul style="list-style-type: none"> - Expensive - Low resolution - Requires post-processing/machining 	<ul style="list-style-type: none"> • Limited use in biomedical application
 <p><i>Material Jetting (Polyjet)</i></p> <ul style="list-style-type: none"> • Photopolymer • Bio-inks 	<ul style="list-style-type: none"> + Good resolution + Good cell viability + Multiple cell/material deposition 	<ul style="list-style-type: none"> - Slow - Material waste - Limited material selection - Limited fabrication size 	<ul style="list-style-type: none"> • Bioprinting of scaffolds for cell culture tissue and organ development (soft tissue)

Table 2.1. (Continued)

<p>Powder-based</p> 		<p><i>PBF (SLS, SLM, DMLS, EBM)</i></p> <ul style="list-style-type: none"> • Thermoplastics • Metal powders • Ceramic powders 	<p>+ High strength and dense parts</p> <p>+ Fast</p> <p>+ No solvents required</p> <p>+ No support</p>	<p>- Most expensive</p> <p>- Post-processing required</p>	<ul style="list-style-type: none"> • Metallic implants • Dental craniofacial and orthopaedic • Temporary and degradable rigid implants 		
		<p><i>Binder Jetting</i></p> <ul style="list-style-type: none"> • Metal • Polymer • Ceramics 	<p>+ Low cost</p> <p>+ Fast</p> <p>+ Multi-color printing</p> <p>+ No support needed</p> <p>+ Large objects</p>	<p>- Low strength</p> <p>- Requires post-curing and post-processing</p> <p>- Powder poses a respiratory hazard</p>	<ul style="list-style-type: none"> • Degradable metallic implants • Generally used for hard, mineralised tissues 		
<p>Liquid-based</p> 		<p><i>SLA</i></p> <ul style="list-style-type: none"> • Photopolymer • Bio-resin • Ceramic resins 	<p>+ High resolution</p> <p>+ Fast</p> <p>+ Good cell viability</p> <p>+ Nozzle free</p>	<p>- Raw material toxicity</p> <p>- Limited material selection</p> <p>- Possible harm to DNA by UV</p>	<ul style="list-style-type: none"> • Bioprinting of scaffolds for cell culture • Tissue and organ development can be used for both soft and hard tissues 		
		<p><i>DLP</i></p> <ul style="list-style-type: none"> • Photopolymer • Bio-resin • Ceramic resins 					

Design principles

Creating the geometrical design of a lattice structure is the first step in designing AM lattices. Lattice structures can be broadly classified as open-cell or closed-cell cellular structures. Because it is not possible to remove the residual material (*e.g.*, entrapped powder particles in the case of PBF processes or supports in vat photopolymerization processes) in closed-cell lattices, open-cell lattices are mostly chosen for fabrication using AM techniques. There are various proposed design principles regarding the geometrical arrangement of lattice structures (an overview is provided in Table 2.2), which are discussed in detail in Section 2.2.1. In some cases, we may combine two or more of these design methods to obtain a more desirable lattice structure.

2.2.1 Library-based design

Computer-Aided Design (CAD), implicit surfaces, and image-based design can be categorized as traditional design strategies [18]. Open-source or commercial CAD tools/software have been used to develop CAD-based designs. These designs may then be transformed into the standard tessellation language (STL) format before going through the manufacturing process. In some cases, STL files can also be accessed through a software package installed on the 3D printing machine in order to control or modify the process parameters prior to or during printing. The final AM lattice structures can be generated by adjusting the process parameters of the input design file and setting the support material within the entire porous media.

Recently, other approaches (*e.g.*, the single point exposure scanning strategy [19] and vector-based approach [20] for selective laser melting (SLM) printing or voxel-based approach [21] for Polyjet printing) have been proposed, which can boost the fabrication speed of an object with even more geometrical complexities. This is because the STL files of designs with too many complexities and details are often very large. The designs resulting from these approaches usually have smaller file sizes, thus allowing for easier file manipulation. These approaches, therefore, enable the process engineer to load large files with detailed features in the 3D printing software.

A unit cell can be identified as the smallest feature size in lattice structures with periodic microstructures. Unit cells create an ordered design by tessellating in a 2.5D plane (*i.e.*, extruded in a 2D plane) or 3D space. Unit cells have already been identified in various forms, such as cubic or prismatic unit cells. They can be broadly categorized into two major groups, namely, beam-based and sheet-based unit cells. No specific repeating unit cells can be seen in lattices with irregular or random microstructures.

Beam-based unit cells

One of the most common geometries for producing metallic or non-metallic lattice structures is the beam- or strut-based design (Figure 2.1a), which includes beam-based unit cells that repeat spatially in 3D space. By reshaping the geometry, for example, by

changing the size and thickness of struts and reforming the topology or connectivity of recurrent unit cells, the overall physical characteristics of the lattices, such as the relative density, pore size, and pore geometry, can be adjusted accordingly [22,23]. Body-centred cubic (BCC), face-centered cubic (FCC), and their variations (analogous to crystalline structures [24,25], cubic, diamond, and octet-truss) are just some examples of well-known strut-based topologies [26].

From a micro-mechanical viewpoint, lattice structures can be classified into two categories, namely, bending-dominated and stretching-dominated unit cells. Stretching-dominated unit cells are typically stiffer and have higher mechanical strength than bending-dominated ones [27]. However, achieving a fully stretch-dominated unit cell is nearly impossible, as some areas of the struts in a unit cell can experience bending loads. Strut-based unit cells can be characterized by their Maxwell number [28].

Surface-based unit cells

Sheet-based unit cells (Figure 2.1b) belong to the category of implicit surface designs, in which mathematical equations define pore configurations. Triply periodic minimal surfaces (TPMS) are specific classes of sheet-based unit cells that provide high flexibility in the design of lattice structures [38]. The full integration of pores in TPMS makes them suitable for use in scaffold designs in tissue regeneration and tissue in-growth applications [38–40]. TPMS-based porous structures also have a zero-mean surface curvature that can be considered a unique property [8]. It must be emphasised that the fabrication of additively manufactured TPMS geometries with high quality is a challenging procedure. This limits the number of available TPMS designs with limited porosity. Some TPMS geometries, such as primitive, I-WP, gyroid, and diamond designs, can nevertheless be realized.

Disordered and random network designs

The arrangement of unit cells in lattice structures can be disordered, where the types or dimensions of the cells change within the object (Figure 2.1c). As an example of such disordered systems, functionally graded structures can be designed, where pore sizes vary within the lattices. AM of graded porous structures has recently become prevalent [41,42], particularly in biomedical engineering

Table 2.2. Summary of the different approaches for the geometrical design of lattices.

Design Strategy	Method	Geometry/ Mechanism Example	Unique Feature	Caution in 3D Printability
	Ordered unit cells	<ul style="list-style-type: none"> - Beam-based: FCC, BCC, octet-truss, and diamond - Sheet-based: TPMS, gyroid, diamond, and primitive 	<ul style="list-style-type: none"> - Use of (non-)commercial CAD tools - Simplicity in geometrical design - Originate from crystalline structures - Interconnectivity of pores - Control of the level of connectivity using either stretching- or bending-dominated unit cells (beam-based unit cells) - Control of the localized curvature using sheet-based designs (surface-based unit cell designs) 	<ul style="list-style-type: none"> - Design of self-overhanging structure and sacrificial support - Limitation in minimum feature sizes (<i>e.g.</i>, strut thickness) - Orientation with respect to the build plate
Library-based				
	Disordered unit cells	<ul style="list-style-type: none"> - Functionally graded - Control of the level of connectivity 	<ul style="list-style-type: none"> - Broader range of morphological and mechanical properties - Less sensitivity to local defects - Straightforward design and fewer complications with overall structural integrity - Smooth stress transition using localized geometrical adjustment - Independent tailoring of mechanical properties - Similarity to biological materials (<i>e.g.</i>, bone) 	<ul style="list-style-type: none"> - Design of self-supporting struts and their orientations with respect to the build plate - Limitation in minimum feature sizes (<i>e.g.</i>, strut thickness and orientations)
Topology optimization				
	Analytical mathematical models and computational approaches to design and obtain optimized microstructures	<ul style="list-style-type: none"> - ESO—evolutionary structural optimization - SIMP—solid isotropic material with penalization - BESO—bi-directional evolutionary structural optimization 	<ul style="list-style-type: none"> - Use of commercial tools and free codes - Local microstructural compatibility - Creating topology-optimized lattice structures with atypical properties considering multiple objective functions (<i>e.g.</i>, negative thermal expansion) - Design for multi-functional or mutually exclusive properties (<i>e.g.</i>, high elastic stiffness and permeability) - Used for tissue adaptation purposes and design of orthopaedic implants 	<ul style="list-style-type: none"> - Limitations in manufacturability due to the complexity of the final product - Optimization of the disposition of support materials during AM process to alleviate stress concentrations - Acceleration of support removal process

Table 2.2. (Continued)

Bio-inspired design	<ul style="list-style-type: none"> - Functional gradient and hierarchical structures - Vast design library of natural cellular materials - Multi-functionality and exceptional mechanical properties, such as graded stiffness, using co-continuous multi-material cellular structures - Limitation in minimum feature sizes - Smooth transitions of target parameters in three dimensions and minimized stress concentrations at interfaces - Use of multi-material 3D printing technology with extreme mechanical property mismatches
Image-based	<ul style="list-style-type: none"> - Mimicking the functionality and microstructural complexity of the native tissue - Creating patient-specific implants and medical devices
Designer material or mechanical metamaterial	<ul style="list-style-type: none"> - Original tissue obtained from non-destructive imaging (<i>e.g.</i>, MRI or CT) - Negative Poisson's ratio or auxetic behavior (<i>e.g.</i>, re-entrant, chiral, and rotating (semi-)rigid unit cells - Unprecedented multi-physics properties (<i>e.g.</i>, balance between mechanical properties and mass transport) - Tailor-made (mechanical) properties and functionality (<i>e.g.</i>, 2D to 3D shape morphing using origami-folding techniques) - Stronger interface between the designed part and the host tissue - Non-auxetic (<i>e.g.</i>, TPMS-based porous structures) - Outstanding quasi-static and fatigue performance
Kinematic or compliant mechanism-based designs	<ul style="list-style-type: none"> - Multi-stability - Self-folding - Kinematic mechanisms - Fabricating non-assembly mechanisms with compliant or rigid joints (<i>e.g.</i>, metallic clay) - Simple to very complex unit cell designs - Integration of different unit cells, particularly for the hybrid design of meta-biomaterials
Meta-biomaterials	

[43,44]. One crucial reason for this increasing interest is the feature that causes a smooth stress distribution in the product to avoid stress concentrations at abrupt geometrical alterations. However, their geometrical complexities cause the AM of graded arrangements to be challenging, particularly when they feature more stochastic or disordered graded designs. This can result in the manufacturing of struts that are incapable of self-support, resulting in a poor AM outcome.

In contrast to uniform lattice structures, disordered lattice structures have several advantages. First, they can be designed to exhibit a broader range of (*e.g.*, mechanical) properties rather than a particular targeted value. Therefore, the range of achievable properties can be expanded using random networks and may realize smooth variations in properties. An example is the rational design of microstructures to regulate elastic mechanical properties separately (*i.e.*, the duo of elastic stiffness and Poisson's ratio) [31,45]. The theoretical upper limits for the mechanical properties of lattices in 2D or 3D have been defined by Hashin and Shtrikman [46]. It has been observed that the application of lattices with anisotropic microstructures can enhance these theoretical upper bounds [47]. The second advantage is that random networks are less susceptible to local defects created during the AM process due to their stochastic nature. Third, their design process is much more straightforward than that for uniform and ordered networks. In ordered networks, the structural integrity and assembly of unit cells are fairly challenging tasks. In contrast, it is easier to combine several types of unit cells in random network lattices, such as combining stretch-dominated unit cells with bending-dominated unit cells.

2.2.2 Topology optimization designs

Topology optimization (TO) can be defined as the application of mathematical models to design optimized arrangements of microstructures of porous structures to obtain desired and optimum properties while satisfying certain conditions. TO algorithms combined with computational models help designers to determine topologically optimized constructs as well as local microstructural compatibility [32]. Several optimization approaches have rapidly evolved and been applied for this purpose in AM [48], among which “inverse homogenization” is an example [49,50]. TO using homogenization methods provides tools to realize targeted effective and unusual properties through the disposition of unit cells and material distribution in 3D space. Examples of these atypical properties are the negative thermal expansion coefficient [51] and the negative refraction index [52].

Various objective functions can be considered for the design of AM lattices. An example of an objective function can be defined based on maximizing the specific stiffness (*i.e.*, stiffness-to-mass ratio), which can lead to lattices with similar anisotropic spongy-bone microarchitectures [53]. There are some optimization models that have been developed by considering bone tissue adaptation processes [11,54,55] in order to create

the optimal designs of microstructures of lattice parts that are often used for the creation of bone scaffolds and orthopedic implants in biomedical engineering (Figure 2.1d) [56–59]. Strain energy can also be defined as another objective function for the TO of load-bearing lattice structures.

For multi-physics optimization problems, the TO of lattice structures can be defined such that multiple objective functions can be optimized [52]. This allows for the production of materials with multi-functional properties. Examples include the design of lattice geometries with two combined mutually exclusive properties, such as a maximized bulk modulus or elastic stiffness and permeability [60,61]. This can also be performed using the TO of functionally graded porous biomaterials [62].

Several optimization techniques have already been developed and applied in the design of optimized topologies for lattice structures with multi-functional properties. These include evolutionary structural optimization [63,64], solid isotropic materials with the penalization method [65–67], the bi-directional evolutionary structural optimization method [68,69], and level-set algorithms [70]. There are various commercial optimization tools (*e.g.*, TOSCA, Pareto works, and PLATO [71]) and free codes [71] available for the TO of AM lattices.

Current research integrates the design aspects of TO with AM fabrication features [72,73], such as the procedure that deals with optimizing the disposition of support materials during the AM process. This integration helps alleviate stress concentrations at struts and their junctions in lattice structures during or after 3D printing, when the support materials are being removed, thus saving material and shortening the lead time [16,74].

2.2.3 Bio-inspired design

Another approach in the design of lattice structures is bio-inspired design. Natural cellular materials, such as bone, cork, and wood, can enrich scaffold design libraries [75–77]. Various key design elements present in the structures of natural materials (*e.g.*, functional gradient and hierarchy) can be translated into bio-inspired porous materials, primarily for biomaterials employed in tissue engineering. An evident instance of natural cellular material is cancellous or trabecular bone—a porous biological material mainly composed of hydroxyapatite minerals and collagens shaped at several hierarchical levels. A connected network of trabeculae in the form of rods and plates forms the cellular structure of cancellous bone [78]. The distribution of trabecular microstructures is a functionally graded placement where the porosity close to the outer shell is lower than that of the inner shell of the bone.

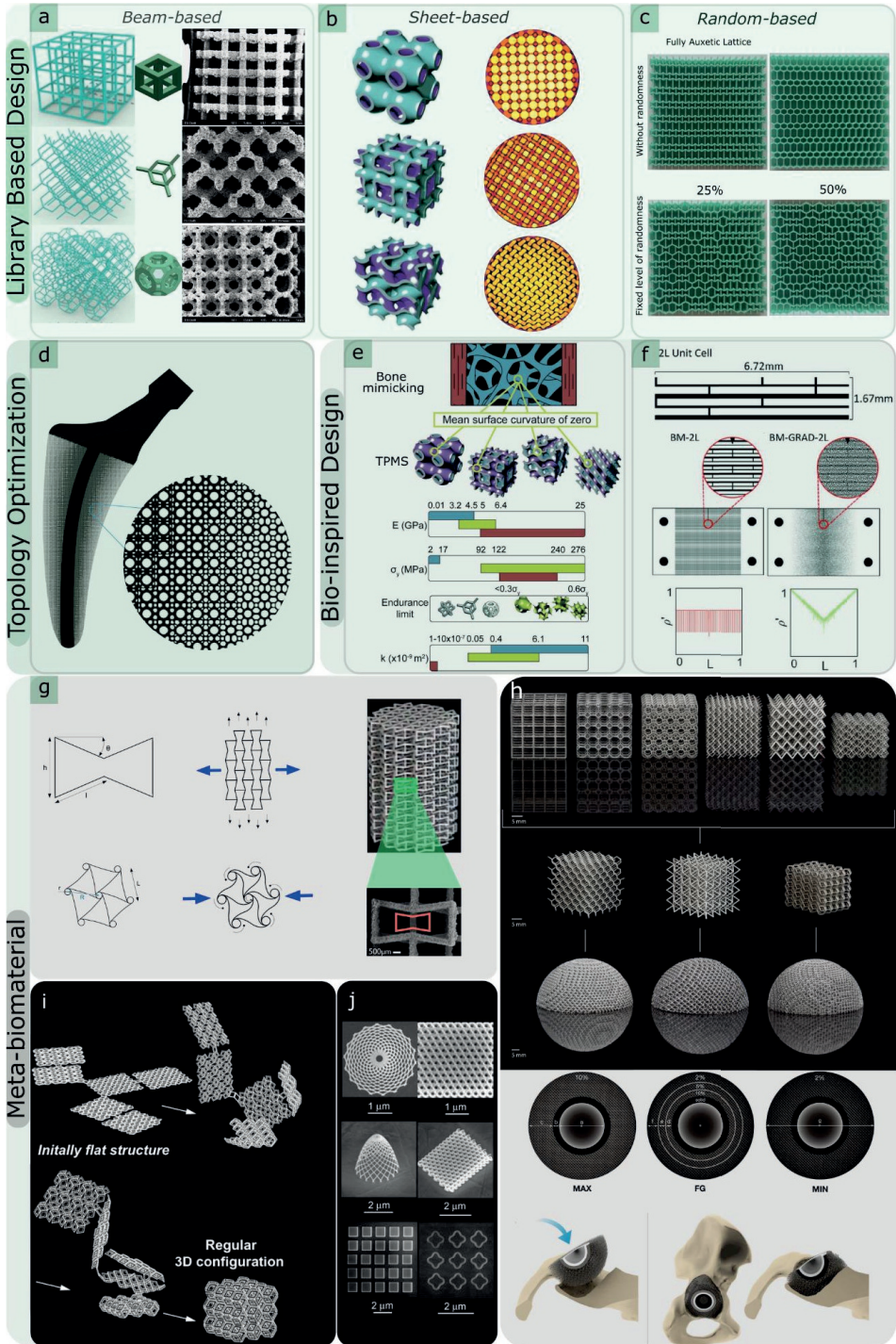


Figure 2.1. (a–c) Library-based designs: (a) beam-based unit cells, such as cubic, diamond, and truncated cuboctahedron (reprinted from Refs. [26,29] with permission, Copyright 2022 Elsevier), (b) surface-based unit cells, such as triply periodic minimal surfaces (TPMS) (reprinted from Ref. [30] with permission, Copyright 2022 Elsevier), and (c) disordered and random-based network structures (reprinted from [31] with permission, Copyright 2022 AIP Publishing); (d) topology optimization employed in an orthopaedic implant (reprinted from Ref. [32] with permission, Copyright 2022 Elsevier); (e,f) bio-inspired designs, such as functionally graded hierarchical soft–hard composites inspired by (e) bone (reprinted from Ref. [30] with permission, Copyright 2022 Elsevier) and (f) nacre-like design exhibiting brick-and-mortar hierarchical unit cell structures (reprinted from Ref. [33] with permission, Copyright 2022 John Wiley and Sons); (g–i) meta-biomaterial designs: (g) auxetic properties, including re-entrant unit cells and chiral structures [34,35] (reproduced from [34] with permission from the Royal Society of Chemistry), (h) non-auxetic unit cells, such as cube, truncated cube, truncated cuboctahedron, diamond, body-centred cubic, and rhombic dodecahedron; three non-auxetic unit cells (diamond, body-centred cubic, and rhombic dodecahedron) were chosen for further evaluation in deformable meta-implants after they were evaluated for their quasi-static mechanical properties [36], (i) self-folding of origami lattices [37]; (j) 2D and free-form 3D nano-patterns on the surface of flat origami sheets using electron beam-induced deposition (EBID) [37].

The design of bio-inspired lattice structures can benefit from mimicking these features (Figure 2.1e). Co-continuous multi-material cellular constructs with interpenetrated boundary phases exhibit multi-functionality and remarkable mechanical properties, such as gradient stiffness in one layout (Figure 2.1f) [79]. In this respect, AM technologies can create such components with smooth transitions of target parameters in three dimensions and minimize stress concentrations at interfaces [33,80–82].

The importance of this aspect becomes more visible for orthopedic implants used to treat large bone defects when the bone cannot go through the natural self-healing process. In such cases, external intervention is necessary to facilitate the healing process [9,83], but the repair can be challenging. The optimal biological choice is the use of either autograft (tissue taken from the patient) or allograft (tissue taken from another donor or person) [84]. However, these methods can lead to several secondary issues, such as problems with harvesting tissue from the patient or the risk of transmitting diseases between patients in the case of allograft tissue. The alternative solution is to design and implant biomimetic materials and constructs to repair skeletal defects.

One method of establishing the geometry of biomimetic lattice constructs is to derive the original configuration by using non-destructive imaging methods, such as computed tomography (CT) or magnetic resonance imaging (MRI). Image-based design methods have been extensively used to design implants and bio-prostheses in tissue reconstruction applications [85]. These non-destructive imaging modalities have also been used to determine the shape variations of long bones at different anatomical locations [86]. Another significant advantage of using the imaging method is the possibility of developing patient-specific implants, where the geometry of the implant is based on the configuration of the target bone of the individual [87–89].

2.2.4 Meta-biomaterials

“Batch-size-indifference” and “complexity-for-free” are two additional characteristics of design for AM [11,90]. These features have flourished in the creation of patient-specific meta-biomaterial implants with tailored properties using “designer material”. Designer materials, also known as mechanical metamaterials, are defined as advanced engineering materials that exhibit remarkable properties based on their microarchitectural designs rather than their chemical compositions [91,92]. One of these atypical characteristics is the negative Poisson’s ratio or auxetic property [93], which is defined as a lateral expansion upon longitudinal extension. Penta-mode metamaterials [94], shape matching [95–97], rate dependency [98,99], crumpling [100], and action-at-a-distance [101] are other examples of these unusual properties that can be achieved by the rational design of engineered mechanical metamaterials. Three major types of unit cells with auxetic properties can be identified, namely, re-entrant, chiral, and rotating (semi-)rigid (Figure 2.1g) [34]. These designs have been implemented and additively manufactured in 2D or 3D. Among the abovementioned designs, the re-entrant unit cell is one of the most straightforward designs that enables the control of the values of Poisson’s ratio by merely changing the angle of struts. It is also the more researched type of unit cells with auxetic properties as compared to the other designs.

There are reports on auxetic behavior in skeletal tissues, such as tendons [102] and trabecular bone. It has been observed that scaffolds with auxetic properties promote neural differentiation. This can be attributed to them providing mechanical cues to pluripotent stem cells [103]. There is not much evidence on the advantages of auxetic behavior in improving bone tissue regeneration thus far. Nevertheless, it has been reported that the hybrid design of meta-biomaterials (*i.e.*, the rational combination of unit cells with positive and negative values of Poisson’s ratio) enhances the longevity of orthopedic implants [104]. As evidence, it has been observed that the hybrid design of meta-biomaterials for the hip stem prevents the development of a weak interface between the implant and bone and, consequently, prevents the loosening of the implant. This is particularly important because wear particles released by implant loosening can cause inflammatory responses in the body [105–107]. Additionally, auxetic meta-biomaterials exhibit superior quasi-static [108] and fatigue performance [35], enabling them to be good candidates for load-bearing (*e.g.*, hip stems) applications. The surface and under-structure of meta-biomaterials can also be engineered using post-processing techniques, such as abrasive polishing, electropolishing [109], and hot isostatic pressing [110], which can improve their surface finish and mechanical properties.

Other geometrical designs with non-auxetic properties (cube, diamond, rhombic dodecahedron, etc. [111]) have also been explored for use in biomedical devices, such as space-filling scaffolds (Figure 2.1h) [36].

Owing to the unique features of TPMS-based porous structures, these geometries are immensely popular as designs for meta-biomaterials [30,112–115]. First, their mean surface curvature is fairly similar to that of trabecular bone [116–118]. Second, the importance of surface curvature as a mechanical cue in tissue regeneration has been reported [8,119–121] and extensively discussed in several studies [29]. Therefore, it can be assumed that TPMS-based porous meta-biomaterials may enhance tissue regeneration performance. It has also been reported that TPMS-based geometries can provide a perfect balance between mechanical properties (*i.e.*, elastic modulus and yield stress) and mass transport characteristics (*i.e.*, permeability) [30,122] and achieve a balance similar to that of bone. The multi-physics properties of TPMS-based geometries can also be decoupled by combining multi-material 3D printing and parametric designs using mathematical approaches (*e.g.*, hyperbolic tiling) [123].

Different forms of 2D and 3D shape-shifting mechanism-based designs (*e.g.*, multi-stability [124] or self-folding techniques using the origami or kirigami approach [125,126]) have also been employed to create advanced meta-bioimplants with enhanced properties and functionalities (Figure 2.1i). Examples are deployable meta-bioimplants [127,128] and 3D foldable curved-sheet (*i.e.*, TPMS) lattices made with origami-folding techniques [129]. One of the benefits of the transition between (2D) flat constructs to 3D meta-biomaterials is that, in such cases, the surfaces can be decorated with additional functionalities. Examples of such induced features are nano-patterns (Figure 2.1j) [37].

Kinematic or compliant mechanisms can also be employed in the design of meta-biomaterials. This allows for fabricating non-assembly mechanisms with compliant or rigid joints [130]. Non-assembly designs have shown great potential in the fabrication of orthopedic implants using shape-morphing metallic clays [131].

2.3 AM of biomedical metals and alloys

There are many areas in which metals and their alloys can be used in biomedical applications. Upon their contact with the biological environment, most metals undergo corrosion and ion release, which may be harmful to the body. Therefore, they must show an excellent biocompatibility response *in vivo* [132]. Titanium (Ti) and most of its alloys, stainless steel, cobalt (Co)-based alloys (such as CoCrMo), zirconium (Zr), niobium (Nb), and tantalum (Ta) are some examples of biocompatible metals and alloys. They exhibit magnificent corrosion resistance and good mechanical properties and are excellent biocompatible materials [133].

Among various biocompatible metals and alloys, Ti and its alloys (*e.g.*, Ti6Al4V) are probably the most extensively studied materials [25]. Ti6Al4V is relatively inexpensive and has lower ductility than pure Ti. However, pure Ti with lower mechanical strength but higher ductility is considered a highly biocompatible metal. Stainless steel, while being cheaper than others, is relatively biocompatible. Laser powder bed fusion (L-

Design principles

PBF) processes can easily manufacture stainless steel, and its elastic modulus is higher than that of Ti6Al4V [25]. Ti6Al4V exhibits appropriate fatigue behavior in terms of fatigue strength, but its fatigue strength is lower in comparison to some other metallic materials, such as CoCr [134].

Biomedical metals and alloys are good candidates for use as porous implants in orthopaedic applications (Figure 2.2a,b). However, their elastic moduli are significantly larger than those of the replacing bones. To prevent stress shielding from occurring at the bone–implant interface, the elastic modulus and yield strength of metallic implants must be tuned accordingly. Several methods can enhance the mechanical properties of bone and metal interfaces, such as creating graded metallic porous implants. Another feasible approach is to introduce certain elements to the structure of the alloys, which reduces the elastic moduli of porous structures; for example, adding β -phase-stabilising elements (*e.g.*, Ta, Nb, Zr, and Mo) to Ti can create β -type Ti alloys with lower elastic moduli as compared to Ti6Al4V. Examples of such β -type Ti alloys that improve the mechanical compatibility of implants are Ti13Nb13Zr (with an elastic modulus of 79 GPa) [135] and Ti29Nb13Ta4.6Zr (with an elastic modulus of 55–65 GPa) [136].

Surface treatments and coatings can improve the performance of metallic implants in regenerating bone tissue (Figure 2.2c–e) [137–144]. It has been reported that surface modification processes, such as introducing bioactive glass and mesoporous bioactive glass to the surfaces of Ti6Al4V scaffolds [140], can enhance the bone tissue regeneration performance. Furthermore, surface biofunctionalization processes using plasma electrolytic oxidation (PEO) [141] with or without silver, zinc, or copper nanoparticles can have potential immunomodulatory effects and can minimise implant-associated infections (Figure 2.2d) [138,142,143]. Furthermore, the bactericidal and osteogenic performance of metallic implants can be controlled by decorating their surfaces with nanostructures. An example is using inductively coupled plasma reactive ion etching to fabricate Ti nanostructures [144]. Layer-by-layer coating biofunctionalization is another approach to impart multiple functionalities simultaneously (*e.g.*, improved tissue growth factors as well as antibacterial behavior) to metallic (*e.g.*, pure titanium [139]) implants (Figure 2.2e).

2.3.1 Biodegradable metals

Biodegradable materials used for biomedical implants are defined as materials that can gradually degrade in the human body over time. They can be either polymer-based or metal-based [146] biomaterials. The primary function of biodegradable metals is to be temporarily present in the body to assist in the healing process and vanish following its completion. The parts and products of biodegradable metals may be fabricated utilizing AM techniques. Some examples include pure iron [147] and magnesium alloy (WE43) [148] porous structures. Many medical devices and implants may benefit from

biodegradable metals, such as Mg alloys that have already been used as biodegradable materials for cardiovascular stents [149] and bone screws [150]. Fe-Mn-Si alloys, such as the alloy with about 30% mass Mn and 6% mass Si [151], were found to exhibit the shape-memory effect, which looks quite promising for medical and other industrial applications. Martensitic transformation also enhances the mechanical properties of alloys, such as hardness, strength, and fatigue resistance [152].

The rate of biodegradation or bio-absorbability of biodegradable metallic implants in the body is a crucial parameter. For example, the degradation rate of Zn-based alloys, which are known as one of the most suitable biodegradable metals, is around 20–300 $\mu\text{m}/\text{y}$ in vitro [153,154], while for Fe- and Mg-based alloys, this rate is lower than 50 $\mu\text{m}/\text{y}$ and higher than 300 $\mu\text{m}/\text{y}$, respectively, in in vitro conditions [155,156]. The degradation rate of pure Mg is the highest when it comes in contact with the chloride-containing physiological environment. Hydrogen gas is produced at a high rate by the corrosion of Mg, which cannot be managed inside the host body. However, the degradation rate of Fe-based biodegradable metals is much slower. Alloying has been recognized as an effective way to tune the biodegradation rate. Mg-based alloys with elements such as Y, Sr, Zn, Zr, and Ca have exhibited significantly lower biodegradation rates as compared to pure Mg. These alloys also exhibit good strength properties, making them suitable for manufacturing load-bearing implants or implant components [157].

Apart from alloying, the biodegradation rate can also be regulated by increasing the surface area. Therefore, two practical tools that can be used to manipulate the degradation rates of such materials are the geometry and level of porosity. In addition to the effect of environmental conditions, other physical conditions, such as cyclic mechanical loading, can increase the biodegradation rate of Mg alloy (WE43) [158], porous iron [159], or zinc [160] scaffolds.

The AM fabrication process for porous biomaterials using biodegradable metals is considerably challenging, particularly in the case of Mg and its alloys, which have high flammability, strong chemical activity, low melting points, and low evaporation temperatures. For some Mg alloys, there is the potential of developing crystallization cracks because of fusible eutectics, great deformation, and stresses due to a high linear thermal expansion coefficient and a broad range of crystallization temperatures [161]. Their fabrication thus requires special safety precautions and process modifications.

Another approach to creating biodegradable porous metals is to use extrusion-based AM techniques (Figure 2.2f). For such techniques, it is necessary to create an ink formulation that matches the 3D printing process as well as the debinding and sintering steps [145,162]. In vitro corrosion results showed an improvement in 3D-printed iron scaffolds compared to bulk materials [145]. This can even be more controlled by creating functionally graded biodegradable porous metals (*e.g.*, iron [163] and zinc [164]).

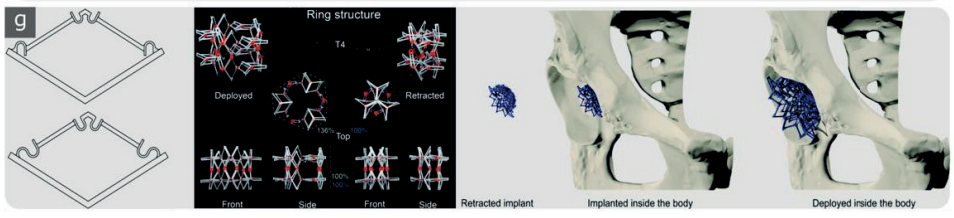
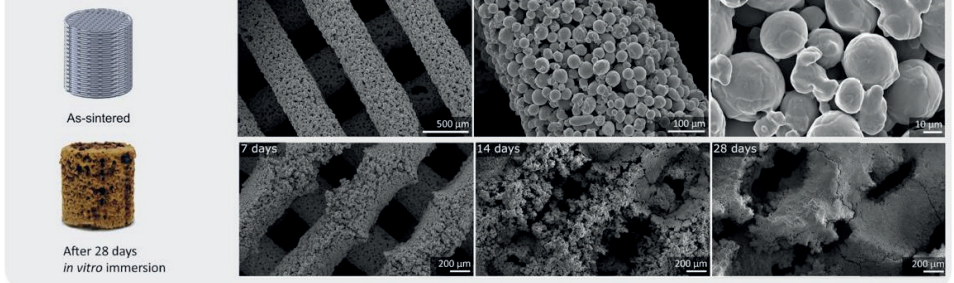
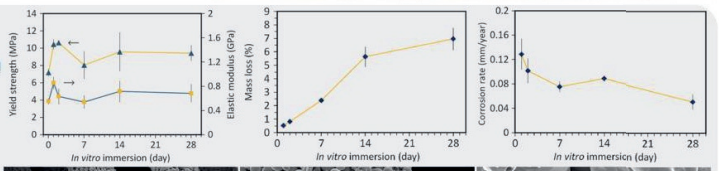
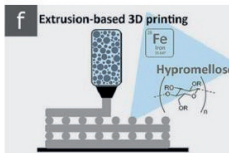
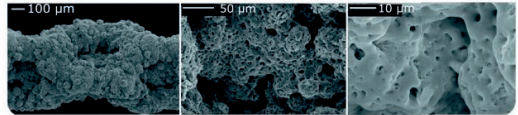
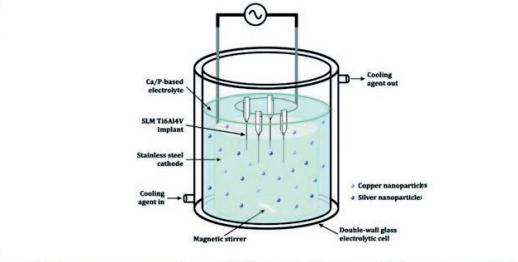
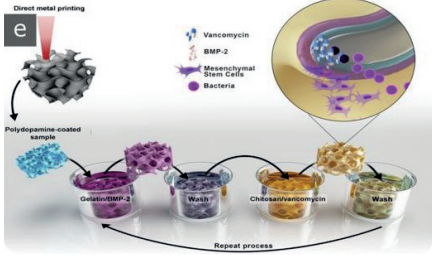
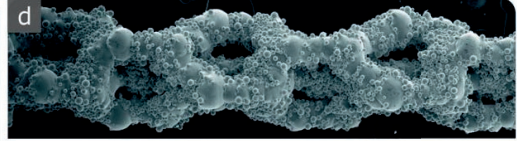
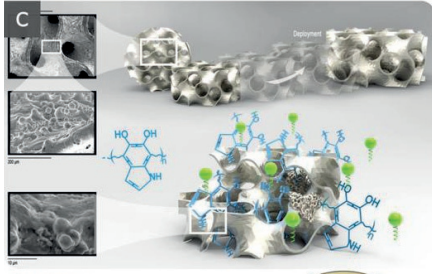
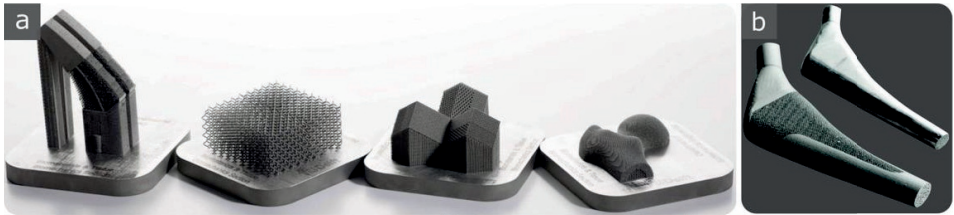


Figure 2.2. (a) Examples of porous metallic structures and bio-implants with various functionalities (reprinted from Ref. [92] with permission, Copyright 2022 Elsevier); (b) a hybrid implant that combines solid and porous parts in a single device (reproduced from Ref. [25] with permission from the Royal Society of Chemistry); (c–e) biofunctionalization of AM products; (c) surface biofunctionalization of a porous Nitinol structure using polydopamine-immobilised rhBMP-2 (reprinted with permission from [137], Copyright 2022 American Chemical society); (d) self-defending additively manufactured implants bearing silver and copper nanoparticles; (top) scanning electron microscope (SEM) imaging was used to image the surface morphology of a selective laser melted Ti–6Al–4V implant, (middle) a schematic drawing of the electrolytic employed for plasma electrolytic oxidation (PEO) biofunctionalization process, and (bottom) SEM images showing the surface morphology after PEO biofunctionalization at different magnifications (reproduced from Ref. [138] with permission from the Royal Society of Chemistry); (e) the layer-by-layer coating process for the biofunctionalization of additively manufactured meta-biomaterials [139]; (f) a schematic of extrusion-based 3D printing process for the fabrication of porous scaffolds; SEM images showing as-sintered and as-degraded iron scaffolds as well as in vitro corrosion products after 7, 14, and 28 days of immersion and the yield strengths, elastic moduli, mass loss percentages, and corrosion rates of the scaffolds before and after in vitro immersion for up to 28 days [145]; (g) the principle of deployable implants demonstrated schematically by arranging bi-stable implants (reproduced from Ref. [128] with permission from the Royal Society of Chemistry).

It is also notable that employing non-biodegradable materials for implants may terminate natural bone ingrowth, which may require subsequent surgery to facilitate further bone growth. Therefore, biodegradable materials are a better option for many implant applications. However, a critical concern regarding biodegradable materials is the cytotoxicity phenomenon that arises from the biodegradation process within the body of the patient [25].

2.3.2 Shape-memory alloys

Shape-memory materials have the ability to return from a deformed state (temporary shape) to their original (permanent) shape when provoked by external stimuli [165]. This effect arises from the temperature-driven phase transformation of shape-memory alloys (SMAs). SMAs have recently gained increasing popularity for their use in orthopaedic implants as well as cardiovascular devices. A typical SMA is Nitinol (NiTi), which comprises equal atomic percentages of Ni and Ti. The shape-memory effect of NiTi emerges from the change from austenite to martensite at high and low temperatures, respectively [166,167].

Bulk NiTi with an elastic modulus of approximately 48 GPa, which is significantly lower than those of Ti alloys, can recover relatively large strains of up to 8%. It is pseudoelastic, which implies that NiTi is capable of recovering large strains upon unloading at a constant temperature [168,169]. These properties make NiTi a suitable candidate for the manufacturing of many medical devices, including surgical guides, stents, orthodontic wires, plates, and staples for bone fracture healing purposes.

The lattice structures of an approximately equiatomic Ni-Ti alloy are recognized as favorable bioimplants and biological micro-electro-mechanical systems (bio-MEMS). This can be attributed to their unique combination of thermal and mechanical shape

memories, which is based on the reversible martensitic phase as well as high corrosion resistance, superelasticity, and biocompatibility properties [167,170]. Because Ni is highly allergenic, its presence in NiTi may raise concerns regarding the biomedical applications of Nitinol [171,172]. Some surface modification techniques or element replacement may be required to alleviate this effect while maintaining bio-compatibility (Figure 2.2c) [137,173]. For example, TiNb and other developed alloys (*i.e.*, TiNbX, where X = Zr, Ta, or Hf) exhibit elastic strains of up to 4.2% [174].

The potential applications of SMAs include deployable orthopaedic implants [127,128] and 4D-printed implants (*i.e.*, implants with 3D-printed structures whose properties change over time) (Figure 2.2g) [96,175–177].

According to the findings of Tsaturyants et al. [178], a combination of thermal cycling and heat treatment can decrease the temperature range of martensitic transformation and also greatly enhance the mechanical properties of the Nitinol alloy processed by L-PBF. They concluded that a combination of heating–cooling cycles of 350 and 400 °C over the temperature range of martensitic transformation can result in a 10 to 15 °C decrease in the martensitic transformation temperature and can also add another step to the transformation sequence of the structure. They also observed a ~7% increase in the maximum stress and dislocation yield stress, as well as a ~10% increase in the difference between the dislocation and transformation yield stresses of the developed structure, by applying 10-cycle heating–cooling.

2.3.3 In Situ alloying and composites

The capability of dispensing materials within 3D lattice structures and placing several materials in desired positions within the entire structure is granted with AM technologies. Such a capability increases the design complexity, particularly when there is already a need for the intricate geometry design of lattice structures.

In situ alloying is defined as the process of combining several feedstock materials with different compositions and simultaneously feeding them into the melt pool. Such a compositional mixture can attain customized properties and functionalities [179]. SLM-processed in situ Ti-26Nb alloy for biomedical applications is an example of a compositional mixture [180].

Generally, adding reinforcing particles (mostly ceramics) and in situ alloying to metal matrices can greatly enhance the mechanical characteristics, such as hardness, stiffness, and strength. Combining them with metal also affects the intrinsic properties, including toughness and/or electrical/thermal conductivity. Reinforcing particles can be introduced through ex situ mixing methods, such as ball milling, or formed in situ during AM processes by combining metal matrix and alloying elements or ceramic reinforcing particles. Laser power and other process parameters of the L-PBF process may be tuned to ensure complete melting of the metal matrix and alloying elements for full interaction

with the surrounding ex situ particles as well as a maximum response between the matrix and alloying elements [181]. Under dedicated L-PBF process conditions, a Ti-TiB porous composite was created through an in situ reaction between the Ti matrix and TiB₂ reinforcing particles [182]. However, owing to several factors, such as weak interfacial bonding, incomplete reactions, interfacial cracks, and inhomogeneous dispersion of the added particles, it is difficult to create a perfect composite lattice structure. Metallic porous composites are not limited to ex situ or in situ composites. It is also possible to fabricate porous metallic glass composites by using L-PBF methods, in which the reinforcing agents are generally crystalline phases distributed in the porous amorphous matrix [183].

The capability of L-PBF processes to produce various metal matrix composites has already been demonstrated. Distinct advantages can provide benefits for the production of desired parts [162,184]. These include the ability to build cellular structures that are reinforced by composite components at desired locations. Such advantages have provided researchers with opportunities to introduce lattice or non-lattice structures built on functionally graded materials (FGM) for biomedical applications, which can be considered for further investigation and exploration [162,184].

2.4 AM of biomedical polymers

Polymers were the first materials used in AM. Their lower melting points, compared to ceramics and metals, as well as their modifiable chemical structures, make them suitable for manufacture using AM technologies, such as material extrusion, powder bed fusion (PBF), and vat photopolymerization [185,186].

In addition to possessing properties suited to manufacturing, polymers for biomedical applications should be compatible with the host tissue and degrade after tissue regeneration. As a result, polymers require other properties, such as biocompatibility and biodegradability, to be suitable for implants and other biomedical applications related to natural tissue regeneration, where the polymer is intended to be replaced by the tissue [187]. Polymers with such characteristics can be broadly classified as natural and synthetic polymers.

Synthetic polymers are more hydrophobic and mechanically more stable than natural polymers due to their slower degradation rates. On the contrary, faster degradation, which may result in lower mechanical strength over time, is ideal for tissue re-generation, as the persistence of biomaterials implanted in the host tissue may trigger physical impairment [187]. Furthermore, the fatigue behavior of 3D-printed polymeric materials is also of great importance for medical devices [188,189]. Therefore, the choice of materials and their combinations to obtain properties suitable for targeted medical devices is challenging.

2.4.1 Hydrogels

When considering the biomedical applications of polymers, it is necessary to include hydrogel, a new and promising polymeric material with a substantial role in various aspects of healthcare and biomedical engineering. Hydrogels are described as three-dimensional crosslinked polymer networks that are able to absorb and retain a large quantity of water [190–193]. Owing to several important properties, such as hydrophilicity, biocompatibility, and nontoxicity [194–196], hydrogels have been instrumental in tissue engineering and pharmaceutical applications, including drug delivery, wound healing dressings, and in vitro cell culturing [191,197]. Hydrogels are suitable for extrusion-based bioprinting because of their non-Newtonian shear thinning behavior, but there are some limitations in terms of the printing characteristics [198]. Following extrusion-based 3D printing and before crosslink formation, hydrogels have poor shape fidelity, limiting their capacity to form larger structures [198–200]. In recent years, new techniques for cell-seeded biofabrication and novel bio-inks have been developed to overcome this shortcoming [201].

Hydrogels show viscoelastic behavior, and therefore, their rheological properties are of great importance, as they can determine the success of the 3D printability of these materials [202–204]. The rheological properties of hydrogels originate from their microstructures and can provide information on the rate and nature of deformation under imposed strain or stress. There are several procedures to control molecular structures and, consequently, the rheological properties of hydrogels. Examples of these procedures are chemical (*e.g.*, water and/or other solvents) and physical (*e.g.*, UV irradiation) crosslinking, which can be used to tune the elastic properties of hydrogels [205,206].

The main advantages of hydrogels include their biocompatibility, better encapsulation, growth, and protection of cells and fragile drugs due to their high water content, modifiable mechanical characteristics as a result of crosslinking, better transfer of nutrients to cells and waste products from cells, controllable drug release, and the simplicity of patterning using 3D printing [190,197]. Their limitations include difficulties in physically manipulating structures, restricted use in load-bearing applications due to their poor mechanical properties, time-consuming printing optimization, and difficult sterilization [190,197].

Three types of hydrogels can be realized and classified based on the origin of their polymers, namely, natural, synthetic, and synthetic–natural or hybrid hydrogels [207].

Anionic polymers, such as hyaluronic acid (HA), alginate, carrageenan, pectin, chondroitin sulphate, dextran sulphate [190], cationic polymers (such as chitosan and polylysine [191]), natural polymers (such as agarose), and amphiphilic polymers (such as collagen, fibrin and carboxymethyl chitin [197,208]), are just a few examples of a wide range of natural biodegradable polymers and their derivatives that produce hydrogels.

Moreover, synthetic polymers can also be used to create hydrogels. Examples are polyacrylamide (PAAM), polyethylene glycol (PEG), and polyvinyl alcohol (PVA). Recently, synthetic polymers have gained popularity over natural polymers owing to their higher water absorption capacity, better mechanical strength, slower degradation, and durability [209,210].

Hydrogels can also be classified according to their polymeric composition and preparation method. The first examples are homopolymeric hydrogels, which are composed of a single structural unit derived from a sole type or monomer [211]. Second, copolymeric hydrogels are formed from two or more species and at least one hydrophilic constituent ordered in an irregular or interchanging configuration within the chain of the polymer network [212]. Third, multipolymer interpenetrating polymeric network (IPN) hydrogels are composed of two independent crosslinked natural and/or synthetic components, forming a network [213,214].

2.4.2 Natural polymers (hydrogel)

Many natural biopolymer hydrogels, such as alginate, cellulose, agarose, fibrin, chitosan, gelatine, hyaluronic acid, and gellan gum, have already been employed in bio-printing applications [215]. Natural polymer hydrogels, such as gelatine, chitosan, alginate, and collagen, have been used to repair biological tissues, including bone, nerve, cartilage, and skin [216]. They usually have good biocompatibility and cause minimal inflammatory and immunological responses in the host tissue. Furthermore, they have been evaluated for use as scaffolds in tissue engineering because they are naturally biodegradable, in addition to being biocompatible and possessing vital biological functions; however, most natural polymers do not meet clinical requirements owing to concerns about potential immunogenic reactions as well as relatively low strength and toughness [217,218]. Chemical and physical modifications or other processes, such as compositing and introducing micro- or nano-structures, can be utilized to impart specific functionalities and improve these deficiencies [207].

Natural polymers are classified into four categories: proteins, polysaccharides, protein-polysaccharide hybrid polymers, and polynucleotides [219]. The first category (*i.e.*, proteins) includes collagen, fibrin, gelatine, silk, lysozyme, and genetically engineered proteins (such as calmodulin, elastin-like polypeptides, and leucine zipper) [216–218]. HA, chitosan, dextran, and agarose belong to the second category (*i.e.*, polysaccharides) [220,221]. Collagen-HA, gelatine-chitosan, laminin-cellulose, and fibrin-alginate are examples of the third category, which is a hybrid of proteins and polysaccharides [222]. Finally, polynucleotides include DNA and RNA [223]. In this review, we focus on the three most commonly used classes of hydrogels, namely, collagen, gelatine, and alginate. More information on different classes of natural hydrogels can be found extensively in previous studies [207,224–226].

Collagen

Collagen, a vital component of the extracellular matrix (ECM) that regulates cell functions and mimics tissue characteristics [227], is a popular biopolymer in AM [186,228]. Material extrusion is the more common method of manufacturing 3D collagen structures in comparison to powder bed techniques because collagen denatures at high temperatures, and good flowability of the powder bed cannot be achieved [229,230].

Owing to its outstanding biological features, such as good biodegradability, cell adaptability, and antigenicity, many applications can be identified for collagen in tissue engineering and drug delivery systems [231]. However, the degradation rate and mechanical properties of natural collagen are not adequate for tissue engineering purposes. For instance, the elastic modulus of atelopeptide collagen hydrogel (Type I Collagen) is approximately 65.5 KPa [232], which is much lower than that of the actual articular cartilage. Some modifications, such as crosslinking or mixing with other materials, can be applied to improve these properties and make them suitable for specific applications in tissue regeneration [226,233].

Several factors, such as the collagen concentration and the variety of crosslink, can define the resulting microstructure and mechanical properties of collagen-based scaffolds [234]. For example, if the genipin percentage is approximately 0.1%, there is no significant change in porosity. A higher concentration, however, causes a decrease in the porosity of the scaffold [234].

In many tissue engineering applications and wound healing, the combination of collagen with other materials has led to the enhancement of its properties [235]. For example, the combination of synthetic polymers with collagen improves its mechanical strength, and its combination with growth factors modifies its regeneration behavior in tissue engineering applications [236].

Gelatine

Gelatine is another natural biopolymer derived from animal by-products, such as bones, connective tissues, and skin. Gelatine is popular because it is inexpensive and has desirable biological properties (*e.g.*, biocompatibility, biodegradability, and non-immunogenicity [237,238]). Gelatine can provide an appropriate structure and necessary nutrients for the growth and distribution of cells. The most common gelatine application is the formation of hydrogels and vessels for controlled drug release [237,239].

A novel method for organ and tissue printing on a gelatine matrix is based on the presence of hepatocytes [240]. Hepatocytes are the primary epithelial cells of the liver, which maintain their morphology in culture dishes coated with ECM components [240]. The printing of gelatine constructs can be performed using the extrusion method with

hepatocytes at a lateral resolution of 10 μm , allowing hepatocytes to remain viable for approximately two months [241].

Gelatine in its unmodified form experiences sol–gel transition, but the gelation speed is slow, which cannot ensure the exactness of the construct formation. Gelatine methacrylate (GelMA) may be used to speed up the process and overcome this shortcoming [242]. This relatively inexpensive solution results in good biocompatibility and biodegradability [243,244]. The combination of GelMA and methacrylate polyvinyl alcohol can be used in the presence of a visible light photo-initiator to generate a bio-resin for digital light processing lithography [215]. Freeform fabrication without the generation of lattices is possible with a small resolution of 20–50 μm by applying this method [215].

Alginate

Alginate is an important hydrogel that can be obtained from brown algae and has wide applications in tissue engineering, drug delivery, wound healing, and bioprinting [191,208,245,246]. It is formed from blocks of (1, 4)-linked β -D-mannuronate (M) and α -L-guluronate (G) residues [191]. The three factors that affect the physical properties of alginate are its composition (*i.e.*, M/G ratio), G-block length, and molecular weight [247]. Increases in the length of the G-block and molecular weight enhance the mechanical properties of alginate [191]. The gelation temperature, which influences the gelation rate, is essential for these properties. A gel can be formed as a result of the interaction between the carboxylic acid of alginate and bivalent counter ions, such as calcium ions (Ca^{2+}) [248]. At lower temperatures, the reactivity of ionic crosslinkers (*i.e.*, calcium ions) decreases, resulting in slower crosslinking and a more ordered network structure [249].

The popularity of alginate as a biomaterial for biomedical applications stems from its easy and fast gelation, low cost, and lack of immunogenicity [250]. Printability is another advantage of alginate-based hydrogels. This indicates that printing capabilities can be easily modified by providing different polymer densities or adding calcium chloride to change the crosslink [251–253]. Their mechanical properties are also tuneable, implying that they can be adjusted to improve printability and accuracy [192].

Utilizing various crosslinkers and combining other polymers, such as gelatine, can rectify the mechanical properties as well as the cell affinity of alginate because alginate does not provide sufficient cell attachment and proliferation [254]. Thus, the biocompatibility and support of cellular function and differentiation in alginate and the good cell attachment characteristics of gelatine can be achieved [216]. Therefore, alginate–gelatine with excellent rheological properties has been introduced in various biomedical applications [216]. This alteration in rheological properties also changes the viscosity [251] of the hydrogel and makes it suitable for extrusion-based 3D printing.

2.4.3 Synthetic polymers

Synthetic polymers, such as synthetic hydrogels and thermoplastics, have been used in 3D printing processes for considerable time. Synthetic polymers have higher mechanical strength, a better controlled degradation rate, and improved processability compared to natural polymers. Their low thermal expansion coefficient, glass transition temperature, and melting point compared to natural polymers make them suitable for desired applications.

However, robust secondary bonding is still required for the best resulting strength, as a 3D printing procedure involves the layer-by-layer addition of materials. Although PMMA (*i.e.*, polymethyl methacrylate) has many favorable characteristics for use in medical applications, such as medicine, denture bases, filling of bone and skull defects, bone implant fixation screws, and vertebrae stabilization, it is not widely employed in 3D printing due to the poor bonding between 3D-printed PMMA and the build plate as well as metals [255]. It requires a higher temperature, is susceptible to warp and distortion, needs glue to adhere to the bed, and requires a bed temperature of at least 60 °C [256]. In a study on 3D-printed PMMA, infiltration with epoxy was applied to increase the tensile strength and elastic modulus of the printed part from 2.91MPa and 223 MPa to 26.6 MPa and 1190 MPa, respectively [257]. In addition, infiltration with wax was shown to improve the surface quality of the part [257].

In AM for biofabrication, direct printing of a cell-seeded material or “bio-ink” can be clearly distinguished from the printing of a cell-free scaffold with a “biomaterial ink” that can be directly implanted or seeded with the cells afterwards [217]. Bio-inks are generally produced from hydrogels, which are very well established as suitable materials for 3D cell cultures. They also have excellent biocompatibility and highly adaptive physical, mechanical, and biological properties [194,258,259].

Biomaterial inks composed of thermoplastics, ceramics, composites, and metals are often used to provide a rigid scaffold for the permanent or slow-degrading stabilization of a construct, while bio-inks can provide a much softer scaffold, and the deposition of a new ECM can be replaced more quickly by the embedded cell population [198,217,260].

Synthetic hydrogels

Synthetic hydrogels can be easily synthesized and manipulated together on a large scale at a molecular level by polymerization, crosslinking, and functionalization [261]. However, the majority of them only function as passive scaffolds for cells. They do not promote any active cellular interactions by themselves. Natural polymers, including proteins, have different structures and are involved in the regulation of active cellular responses, biological recognition, and cell-triggered remodeling. Consequently, combining the properties of synthetic and natural polymers to create hybrid hydrogels has

developed into a direct method of developing bioactive hydrogel scaffolds for tissue engineering [219].

Three primary classes of synthetic polymers are recognized for creating synthetic hydrogels, namely, non-biodegradable, biodegradable, and bioactive polymers [219]. Tissue engineering applications of non-biodegradable hydrogels primarily involve bone and cartilage [262], with relatively limited applications in vascular constructs or other soft tissues. For these applications, maintaining physical and mechanical integrity is essential for the hydrogel. A vital consideration in the scaffold design is the mechanical stability of the gel, which can be enhanced by introducing crosslinking components and comonomers and by modifying the level of crosslinking [263–265]. A much higher degree of crosslinking can also result in brittleness and decreased elasticity, and therefore, the optimal degree of crosslinking must be identified.

In order to provide the desired flexibility of the crosslinked chains and facilitate the movement or diffusion of the incorporated bioactive agent, an adequate elasticity of the gel is required. Therefore, there is a need to compromise between mechanical strength and flexibility by selecting the best components and percentages in the construction of non-biodegradable hydrogels as tissue-engineering scaffolds [219].

Copolymerization of different vinylated monomers or macromers, such as 2-hydroxyethyl methacrylate (HEMA) and 2-hydroxypropyl methacrylate (HPMA), can produce non-biodegradable synthetic hydrogels [262,266–268]. Another method to generate non-biodegradable hydrogels is to use non-biodegradable polymers, such as modified polyvinyl alcohol (PVA) and PEG [269–271].

PEG has several unique properties, such as solubility in water and organic solvents, nontoxicity, moderate protein adherence, and no immunogenicity. These properties make PEG the most widely investigated polymer for creating hydrogels [262,268]. Another synthetic hydrophilic polymer that can be mixed with other water-soluble polymers to create hydrogels in tissue-engineering applications is PVA [270,271].

An essential consideration in the construction of scaffolds for tissue engineering is biodegradability. The desirable rate ensures that biodegradation corresponds to new tissue regeneration at the corresponding site [272–274].

The most widely used biodegradable polymers for scaffold fabrication are polyesters, including polylactic acid (PLA), polyglycolic acid (PGA), polycaprolactone (PCL), and their copolymers [273,275]. They can be employed to improve hydrophilic polymers, such as PEG, to develop acrylate macromers or amphiphilic polymers, and to produce biodegradable hydrogels via chemical or physical crosslinking [276–287]. A lack of cell-specific bioactivities, such as cell adhesion, migration, and cell-mediated biodegradation, is the major limitation in their use as tissue-engineering scaffolds. These limitations can be alleviated by introducing bioactive molecules into the synthetic

Design principles

hydrogels [272,288–290]. Bioactive elements can be attached to the hydrogel network, such as peptides, during or after hydrogel formation [217,258]. Different ECM component-derived peptides or bioactive molecules, such as cell-adhesive [259,260] and enzyme-sensitive [291,292], have been used to modify synthetic polymers for fabricating bioactive hydrogels.

Physical properties (*e.g.*, network parameters and diffusive profile), mechanical strength, and biological properties (*e.g.*, cell adhesion, migration, and scaffold biodegradation) can be engineered using molecular design [219]. Unlike natural hydrogels, bioactive synthetic hydrogels offer much broader control to improve the matrix architecture and chemical composition and provide a biomimetic environment for tissue regeneration and cell growth.

Poly(lactic Acid) (PLA)

PLA can be produced from renewable resources [293]. Its biocompatibility, biodegradability, and bioresorbability have made it a suitable candidate for a broad range of biomedical applications, including neural and vascular regeneration [294], stents [295–297], surgical sutures [298], plates and screws for craniomaxillofacial bone fixation [299], interference screws in the ankle, knee, and hand, tacks and pins for ligament attachment, anchors [300], spinal cages [295,301], soft-tissue implants, tissue-engineering scaffolds, tissue cultures, drug delivery devices [302], and craniofacial augmentations in plastic surgery [303].

PLA can be produced using various polymerization methods from lactic acid, including polycondensation, ring-opening polymerization, and direct processes, such as azeotropic dehydration and enzymatic polymerization [304]. Compared to other biopolymers, there are numerous advantages associated with the production of PLA: (i) Eco-friendly: it can be obtained from renewable resources in nature (*e.g.*, corn, wheat, or rice). PLA is biodegradable, recyclable, and compostable [305,306], and its production consumes carbon dioxide [307]. (ii) Biocompatibility: biocompatibility is undoubtedly the most important aspect of PLA, particularly with respect to biomedical applications. (iii) Processability: thermal processing of PLA is easier compared to that of other biopolymers, such as poly(hydroxy alcanoate) (PHA), PEG, and PCL.

Some of the shortcomings of PLA can be listed as: (i) Insufficient toughness: PLA is a brittle material with less than 10% elongation at the breaking point. (ii) Low degradation rate: the degradation rate of PLA depends on many factors, such as its crystallinity, molecular weight, distribution, morphology, water diffusion rate into the polymer, and stereoisomeric content. This feature leads to a prolonged *in vivo* lifetime, which in some cases can be up to 3 to 5 years [308]. (iii) Hydrophobicity: PLA is considered to be relatively hydrophobic. Its static water contact angle is assumed to be approximately 80 °C. This feature causes low cell affinity, and in some cases,

inflammatory responses from the living host in direct contact with biological fluids have been observed [309]. (iv) Lack of reactive side-chain groups: PLA is chemically inert with no reactive side-chain groups, which results in an exciting approach towards surface and bulk improvements [310]. Considering the facts mentioned above, PLA bioactivity must be modified for its application in tissue engineering.

Several fabrication methods, such as particle/salt leaching [311–313], solvent casting [314,315], phase separation [316], gas foaming [317], freeze-drying [318], and electrospinning [319], have been employed to fabricate 3D scaffolds using PLA as the base material. Despite the successful manufacturing of scaffolds using these processes, these conventional methods have some drawbacks, namely, poor reproducibility, the use of toxic solvents, and limited control over the geometry of the scaffold and pores [320].

PLA-based scaffolds can also be formed through the SLA technique by copolymerization of other materials, such as poly (D, L-lactide) and PEG, to achieve relatively good structures [321]. However, some limitations hinder the application of this technique for manufacturing PLA-based scaffolds, such as restrictions on the layer thickness and laser radiation to avoid over-curing or cytotoxic effects while using encapsulated cells [322]. Another disadvantage of this method is its high cost; furthermore, it is a more time-consuming process than other AM techniques.

PLA, unlike other biodegradable polymers (*e.g.*, PCL), has limited use in SLS 3D scaffold manufacturing [323]. Because commercial PLA is typically available as millimeter-sized pellets, a process for developing particles with a smaller size prior to the SLS process is required to ensure the high resolution of 3D objects. Aside from the limitations on particle dimensions, the poor mechanical properties of sintered PLA scaffolds have also been reported [324,325].

The most common and cost-efficient technology for the 3D printing of PLA is Fused Deposition Modelling (FDM). PLA has appropriate thermal characteristics for FDM processing, which requires extrusion at temperatures ranging from 200 °C to 230 °C [326].

Process conditions and technical variables affect biocompatibility or accelerate polymer degradation, and they should be optimized such that the material does not experience excessively high shear stress during extrusion [322]. In addition, they affect the mechanical properties of additively manufactured PLA under static [327–333] and cyclic [334–336] loading. These process conditions can be identified as the thickness of layers (layer height), infill density, filling pattern, diameter and temperature of the nozzle, feed rate, printing speed, and build plate temperature; additionally, they exert a significant influence on the mechanical properties [337,338]. Increasing the layer height, for example, generates many voids in the microstructure of the printed part and reduces its tensile strength [339–341]. The tensile strengths and elastic moduli of 3D-printed parts

Design principles

are also affected by the extrusion temperature [342]. If the processing temperatures are too high, it can reduce the molecular weight of the polymer [343].

In addition to suitable mechanical properties, PLA-based scaffolds manufactured by the FDM method should also possess the desired biological properties to promote cell ingrowth. In this regard, the biocompatibility of PLA can be realized following the FDM process, ensuring that there is no cytotoxicity toward osteoblast-like cells [343]. It must also be determined whether the macro-patterns generated by the FDM equipment can induce cell differentiation and osteogenic processes [344].

Another consideration is that the hydrophobicity of PLA may limit its application in regenerative medicine, as it hinders cell adhesion and proliferation and the release of acidic by-products during the degradation process [345]. A promising approach is applying a bioactive coating on the surface of a 3D-printed PLA-based scaffold to improve its biofunctionality [346]. An alternative modification to enhance the biological properties of PLA is combining the base material with natural or ceramic additives [347]. A number of bioactive compounds for this purpose have been identified, such as chitosan [348], alginate [349], collagen [350], and calcium phosphates [351].

As an example, enhancement of stem cell adhesion, proliferation, and differentiation can result from coating the 3D-printed scaffold surface with polydopamine (PDA) [346,352,353] and acetylated collagen [354]. Ceramic additives can also be incorporated into the PLA matrix. This addition improves the hydrophilicity, osteoconductivity, mineralization upon implantation, and mechanical properties of 3D structures [355,356]. An alternative approach is to mix the PLA matrix with natural polymers or their derivatives [357], such as o-carboxymethyl chitosan (CMC), which can substantially improve the hydrophilicity of the surface of the scaffold. The tensile modulus can also be increased with the controlled portion of CMC [357].

Applying a surface treatment to 3D objects to modify their topography or surface chemistry is another approach. The surface treatment can positively affect the attachment of cells and biological compounds to the structure [358,359]. Plasma treatment is one of the most investigated methods developed to enhance the surface chemistry of PLA-based parts without affecting their overall properties. It can also improve the roughness of 3D-printed parts [360–362]. However, some surface modifications, such as alkali treatment, which is one of the most common surface treatment options, can result in undesirable morphological changes and have an adverse effect on the bulk mechanical properties of PLA constructs [363].

PLA materials have applications other than 3D-printed porous scaffolds, and they show shape-memory effects, which implies that they can switch between a permanent shape and a temporary shape when activated by an external thermal stimulus. When heated above their glass transition temperature, extruded PLA filaments (*i.e.*, 3D-printed)

shorten in the printing direction and thicken simultaneously. By rationally placing printed filaments into a multi-layer construct, a complex 3D structure can be obtained after the flat construct is thermally activated [176]. These unique features have been used in the design of 4D-printed objects, including the shape-shifting of flat constructs to pre-programmed 3D shapes [96,97], and reconfigurable [364] and deployable [127,128] mechanical metamaterials, which employ design strategies such as instability-driven pop-up (Figure 2.3a), self-folding origami (Figure 2.3b), and sequential shape-shifting (Figure 2.3c). PLA materials can also be used to form moulds that can later be used to create soft mechanical metamaterials with shape-matching properties [95] (Figure 2.3d). Furthermore, PLA materials can be used for the design and fabrication of low-cost prosthetics, such as hand prosthesis and artificial fingers (Figure 2.3e) [365], and non-assembly mechanisms for medical devices [366,367].

Polycaprolactone (PCL)

PCL, a semi-crystalline poly (α -hydroxyester), is a low-cost polyester characterized by its remarkable viscoelastic and rheological properties upon heating. These features make it an excellent candidate for melt-based extrusion printing. It is also a proper thermoplastic material for FDM, owing to its low melting point and high decomposition temperature (350 °C) [370,371]. PCL is also biodegradable, as it resorbs slowly by hydrolysis owing to its high crystallinity and hydrophobic properties [372,373]. Its degradation period is more extended than that of polylactide, making it suitable for applications requiring long degradation times. During the more extended degradation period, the structural stability of the scaffolds can be substantially enhanced, and the rapid degradation of natural polymers can be counterbalanced [374].

The degradation mechanism of PCL is controlled by microorganisms or hydrolysis of ester linkages in a physiological environment [375]. Its nontoxic nature and excellent tissue compatibility make it a popular material for implantable devices. It has been widely utilized in resorbable sutures, biodegradable scaffolds in regenerative medicine, and drug delivery mechanisms [372]. Other PCL applications include scaffolds for tissue engineering of bone and cartilage [376].

However, due to a lack of a bioactive surface and cell adhesion properties, as well as its hydrophobicity, the cell adhesion and proliferation of PCL require improvement [373]. For example, the surface of electrospun PCL nanofibers can be improved by applying various methods, such as plasma treatment, physical adsorption or surface coating of drugs, proteins, and genes, and surface graft polymerization [377].

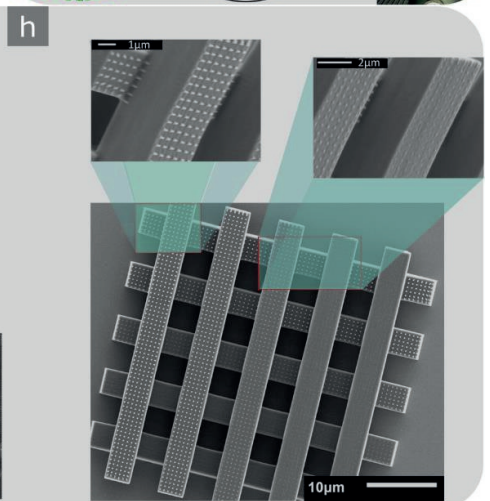
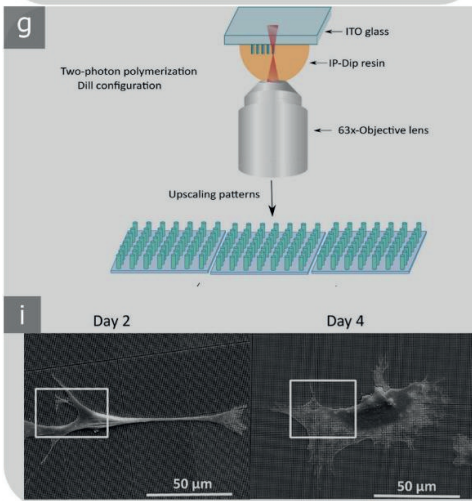
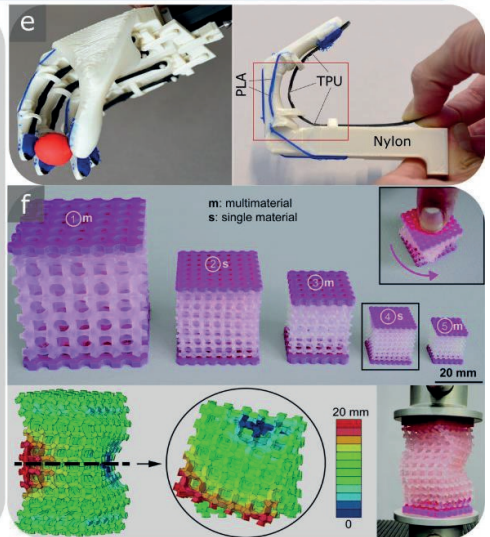
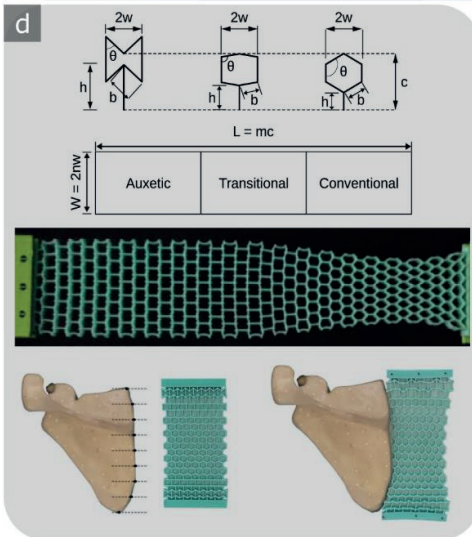
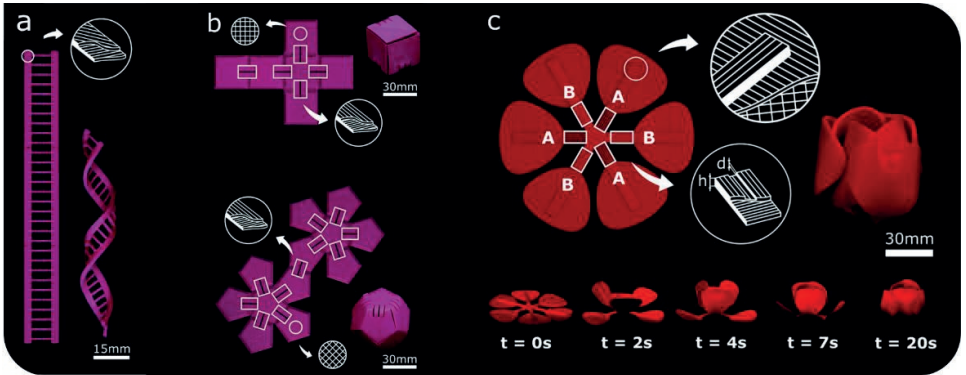


Figure 2.3. (a–c) Shape-shifting of the shape-memory polymers, *i.e.*, (a) self-twisting: after activation, two flat self-twisting strands form a DNA-inspired shape, (b) self-bending: on activation, a flat printed construct is folded into a cubic box, and (c) sequential shape-shifting: folding the initially flat petals into a tulip in two steps by controlling the printing directions at specific locations (*i.e.*, A, and B); the time lapses show the folding sequence for both designs (reproduced from Ref. [176] with permission from the Royal Society of Chemistry); (d) shape matching of the scapula with a specimen fabricated by three zones of auxetic, transition, and conventional unit cells [95]; (e) 3D-printed hand prosthesis [365]; (f) buckling-driven soft mechanical metamaterials for external prosthetics and wearable soft robotics, such as exoskeletons and exosuits (reproduced from Ref. [98] with permission from the Royal Society of Chemistry); (g–i) cell culture using submicron patterns: (g) a schematic view of the two-photon polymerisation method [368]; (h) SEM image showing submicron-scale topographies incorporated into a porous micro-scaffold [368] with (i) cells cultured on patterned surfaces after 2 and 4 days of cell culture [369].

Moreover, the introduction of other materials, such as natural polymers in scaffolds, can provide some beneficial properties, including better ductility, biocompatibility, biodegradability, and so forth. When alginate and PCL are mixed via FDM, the composite scaffolds show significantly improved wetting behavior and water absorption characteristics compared to those of pure PCL scaffolds [378]. Biological properties, such as cell-seeding efficiency, calcium deposition, osteoblast cell viability, and alkaline phosphatase activity, have also been improved due to the alginate constituent [379]. A combination of electrospinning, 3D printing, and a physical punching process is also employed to manufacture PCL/alginate fibrous scaffolds to further enhance the cellular adhesion properties of PCL. The scaffold alginate content vastly improves the hydrophilic properties and water absorption characteristics compared to those of PCL scaffolds, which is beneficial with respect to cell viability, proliferation, and osteogenic differentiation [380].

PCL can also be co-deposited (printed along) with calcium phosphate (CaP), followed by sintering to manufacture a scaffold, or coated on the surface of printed and sintered CaP scaffolds to improve the mechanical strength and elastic modulus of CaP-based materials [381,382] (Figure 2.4a). CaP has been developed as scaffolds for bone growth and approved as bone fillers by the U.S. Food and Drug Administration (FDA). However, when used alone, it is not capable of providing adequate mechanical properties for hard tissue repair or replacement. In order to establish stable scaffold amalgamation within the host body and ensure that successive regeneration of the host tissue develops continuously, adequate mechanical strength is required. This implies that the compressive strength, elastic strength, tensile strength, and fatigue strength of the polymer/ceramic scaffold must all be sufficient at load-bearing sites and maintained at a sufficient level after implantation until new tissue is ready to restore function [382,383].

Interpenetrating hydrogels with various densities of pectin-g-PCL and gelatine methacrylate resulted in the development of strong hydrogels with enhanced mechanical properties (*i.e.*, compressive and tensile moduli) following double crosslinking by UV light and Ca²⁺ ions, whereas crosslinking only by UV light alone led to a reduction in

mechanical properties [372]. These hydrogels were observed to promote the in-growth of pre-osteoblasts cells in vitro and hence were found to have excellent potential for bone tissue engineering [386].

Poly(lactic-co-glycolic) Acid (PLGA)

PLGA is a biomaterial that has been widely used in the production of drug-releasing devices due to its excellent biocompatibility and controllable biodegradability properties [387–389]. PLGA is simple to process, and AM techniques can be applied for scaffold fabrication and bone reconstruction in tissue engineering [390].

There are various methods for controlling the degradation rate, such as altering the molecular weight of the polymer and changing the ratio of its ester linkages of glycolic acid to lactic acid (LA) [391]. A higher percentage of LA results in less hydrophilic PGLA, and hence, the degradation rate is lower because less water can be absorbed by the polymer [392].

Sole PGLA has weak mechanical properties and cell affinity, and it is commonly preferred to be compounded together with a ceramic constituent to form a polymer/ceramic composite scaffold for tissue engineering applications. Consequently, composites with polymer matrices, including biologically active nanoparticles, have gained particular attention in the biomedical field [393,394].

Solvent casting [395], fiber spinning [396], electrospinning [397], and dip coating [398] are some of the methods that can be used to produce medical devices composed of PLGA materials. In addition, 3D printing can also be used to manufacture PLGA devices for drug delivery purposes because of its adaptability in producing optional configurations and the ability to fine-tune the placement of drug-loaded substances [208,399,400]. By using 3D printing fabrication technologies, additional parameters, such as geometry, porosity, and polymer composition, can also be tailored [401–406].

PLGA parts can be printed using either low-temperature solvent-based or high-temperature solvent-free processes [399,400]. High-temperature processes are not suitable for heat-sensitive drugs because they require temperatures greater than 95 °C, while the glass transition temperature of PLGA is 35 °C to 60 °C [399,407].

However, harsh solvents are generally used in low-temperature fabrication methods, potentially denaturing the incorporated drugs [408,409]. As the presence of organic solvents in PLGA parts can be harmful to the body during the bioprinting of PLGA, special care must be taken to remove the solvent in the low-temperature fabrication method in the context of drug delivery applications [410].

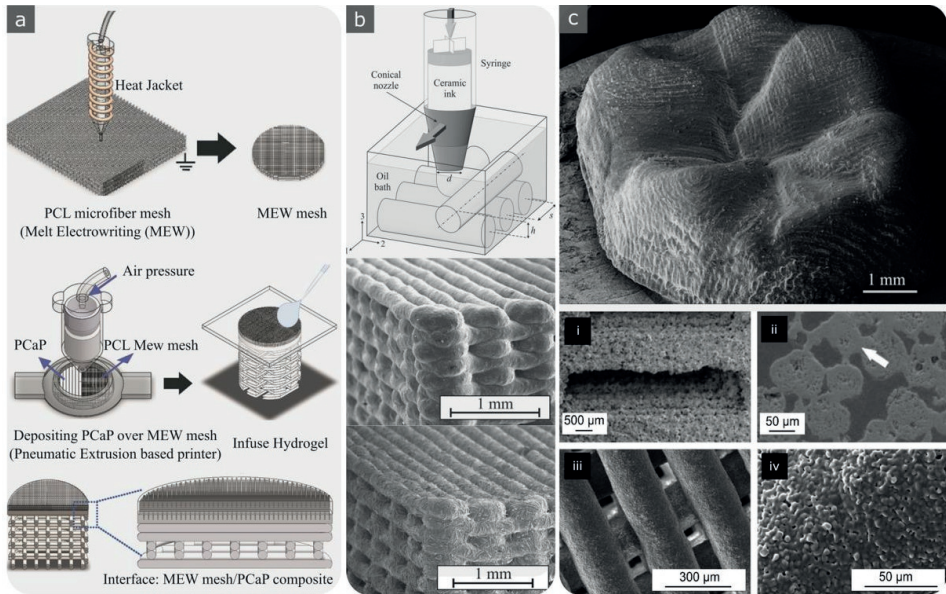


Figure 2.4. (a) An example of a hybrid 3D printing technique used for the fabrication of ceramic-hydrogel connections representing osteochondral interfaces [382]; (b) the robocasting fabrication process and SEM images of the scaffolds created by robocasting; the ceramic ink is moved through conical deposition nozzles, which are plunged in an oil bath to create a self-supporting 3D ceramic rod network (reprinted from Ref. [384] with permission, Copyright 2022 John Wiley and Sons); (c) SEM micrograph showing the occlusal surface of a zirconia molar crown using the direct inkjet printing technique and SEM images showing hydroxyapatite scaffolds produced by: powder-based 3D printing in (i) and (ii); direct ink writing in (iii) and (iv) (reprinted from Ref. [385] with permission, Copyright 2022 John Wiley and Sons).

Different solvents can be used for the 3D printing of PLGA parts. Dimethylacetamide is used as the ink for printing PLGA parts for loading drugs. However, because it has a high boiling temperature, only 2D structures can be created using this solvent [411]. Extrusion-based systems can use solvents, such as chloroform [412], tetraglycol [400], and acetone [413], in order to overcome the rheological limitations of inkjet systems.

Essentially, applying these solvents also results in poor printability or undesirable leaching of the solvent from the scaffolds after printing. The leaching of the solvent is not appropriate for an “ideal” drug delivery process, and it can cause toxicity during in vivo drug release or in the course of in vitro studies [414]. Therefore, mild solvents must be introduced for 3D printing of PLGA to manufacture drug-releasing biodegradable products.

Methyl ethyl ketone (MEK) has been used as a mild organic solvent in a recently developed novel low-temperature 3D printing technique for developing PLGA constructs [414]. MEK has been found to be a promising solvent in the 3D printing of PLGA devices that are parts of drug release systems. MEK application results in printed constructs with

Design principles

high shape fidelity, from which MEK can be removed following the printing procedure [414].

Proprietary polymers

Proprietary polymers refer to commercial (photo-resist resin) polymers that have been widely used in various (high-precision) 3D printing processes. The chemical compositions of these classes of polymers are often unknown and cannot be altered. Vero™ and Agilus™ are examples of UV-photo-cured polymers used in Stratasys™ Polyjet 3D printing machines. A combination of these polymers with different shore harnesses already exists, which allows for a wide range of elastic stiffness properties in multi-material 3D printing. These materials have been widely used to mimic the bio-inspired design features of biological materials [33,80–82]. They have also been used in the design of multi-material mechanical metamaterials [184,415] with programmable properties, such as strain-rate dependency [99] and controlled buckling-driven functionalities (Figure 2.3f) [98]. Such materials have several applications in soft robotics and exoskeletal devices.

Other examples of such commercial resins are IP-QTM, IP-STM, and IP-LTM, which are used for 3D micro-fabrication with high resolution using a Nanoscribe™ machine that works on the basis of direct laser melting using two-photon polymerisation (Figure 2.3g). This fabrication method is used for the surface modification and decoration of biomaterials through the addition of nano-patterns (Figure 2.3h). The printing process can be adjusted in a way to easily fabricate large areas of nano-topographical features. Nano-topographical features can be printed at the submicron level in the form of nano-pillars. Nano-pillars can act as a mechanical killing mechanism to kill bacteria while keeping cells alive. This has been reportedly achieved by adjusting geometrical parameters, such as interspacing, height, and shape, using computational modelling [416,417]. Different geometrical designs can be fabricated using AM processes at very high resolutions. Furthermore, the physical properties (*e.g.*, wettability) of such surfaces, the mechanical properties [418], and their interactions with human cells can be analysed (Figure 2.3i) [369]. Topographical features can also be incorporated into micro-fluidic systems [368]. Electron beam-induced deposition (EBID) is another 3D printing technique that has been used for fabricating objects with features at the nanoscale. It works on the basis of dissociating precursor molecules (*i.e.*, trimethyl-platinum (IV)) using a focussed electron beam. The killing efficiencies of different types of bacteria (*e.g.*, *Escherichia coli* and *Staphylococcus aureus*) in relation to various types of nano-pattern distributions have been analysed [419–421]. The mechano-bactericidal effects of such nano-pillars have also been investigated using atomic force microscopy [422].

2.4.4 Composites

Polymer composites or polymer matrix composites are obtained by incorporating reinforcements of particles, fibres, or nanomaterials into polymers. This results in better mechanical properties and functionality. Such composites are extensively used in a wide range of medical applications, including dental treatments, regenerative medicine, and tissue engineering. The materials that are used for these applications must be biocompatible and have the required mechanical and physical properties. A bio-composite is also classified as a composite that contains natural reinforcing fibres [423]. AM of composite structures has attracted a lot of attention recently due to its flexibility and the ability to produce high-performance products while being able to control the geometry of composite structures and constituents and minimising waste [424].

Particle-reinforced polymer composites

Particles can be easily and economically incorporated into the polymer matrix either in powder form or liquid form, depending on the method of 3D printing. They can greatly enhance the physical and mechanical properties of the product; for example, adding iron or copper [425] particles or glass beads can improve the tensile modulus of the polymer matrix [426].

Fibre-reinforced polymer composites

Glass fibres [427] and carbon fibres [428,429] are the most preferred reinforcements used for polymer matrix composites to enhance their mechanical properties. In addition to the type of reinforcement, the orientation and void fraction of the fibres determine the properties of the final printed product [430]. During the 3D printing process, some voids may be formed, which can affect the mechanical properties of the final 3D-printed structure [431]. The porosity of 3D-printed parts due to voids can be significantly reduced by adding expandable microspheres to the polymer [432]. To date, it has been nearly impossible to print continuous fibres, and only short fibres could be 3D printed. Recently, there have been major developments in establishing the relationship between process parameters and printed composite specimens [433,434].

Another major development concerns shape-memory polymer composites that can expand 3D printing to 4D printing technology by incorporating the time factor. These composites are of great interest due to their ability to recover deformation [435]. In addition to temperature-responsive shape-memory composites, water-responsive shape-memory composites have also been developed by applying AM methods [436]. In the cited study, a composite composed of cellulose fibrils and acrylamide changed its shape when immersed in water.

Nanocomposites

Nanomaterials have also been incorporated into matrix materials to enhance their mechanical properties. Shofner et al. [437] demonstrated that the addition of 10 wt% carbon nanofiber could increase the tensile strength of 3D-printed parts by up to 39%, although the elongation decreased, and brittleness increased. In another study, the addition of just 0.2% graphene oxide to an SLA-fabricated photopolymer composite caused increases of 62% in tensile strength and 12.8% in elongation [438], which is quite remarkable. The introduction of nanomaterials, such as carbon nanotubes, can also significantly improve the electrical properties in addition to the mechanical properties of the composite [439].

Functionally graded polymer nanocomposites have been realised by 3D printing. This can be performed by introducing different volume fractions of nanomaterials to specific locations of the structure of the part [440].

2.5 AM of biomedical ceramics

According to the definition of Richerson [441], “most solid materials that aren’t metal, plastic, or derived from plants or animals are ceramics”. Kingery [442] defined ceramics as non-metallic and inorganic solids, and they can be found in the form of oxides, nitrides, and carbides, which is thus far the most widely accepted definition. Inorganic semiconductors, diamond and graphite, for example, all belong to the category of ceramics. Here, we refer to ceramics as non-metallic and inorganic solids that can have metallic components, and for their formation, they can be subjected to the heating process for hardening purposes.

Ceramics may contain a variety of covalent, ionic, and metallic bonds, distinguishing them from many solid molecular iodine crystals, such as individual I₂ molecules and paraffin wax composed of long-chain alkane molecules. Ceramics are generally considered to be hard, corrosion-resistant, and brittle materials [442]. Recent advances in ceramics have introduced many new possibilities for practical applications. Advanced ceramics have been favoured as one of the most important materials for various industrial and medical applications in recent years. Investigating, producing, and employing solids with ceramics as the main constituent is a field that is distinguished as ceramic science or industry. This can also include research concerning the refinement of raw materials, the development of new products from chemical mixtures, and the individual characteristics of their components [443].

2.5.1 Classification of ceramics

Ceramic products have a wide range of applications, ranging from simple building tiles to advanced magnetic components and electronic modules. They can be classified as

traditional and advanced ceramic materials. The major developments of advanced ceramics occurred in the 20th century [443].

Ceramics can also be categorised as monolithic ceramics and composite ceramics based on the number of chemical constituents. Monolithic ceramics can be further classified into two categories: crystalline solids and amorphous materials. Crystalline solids can be single-crystal or polycrystal, while amorphous materials can be glass or other amorphous non-crystals, such as amorphous silicon. An example of composite ceramic is concrete [444].

2.5.2 Properties of ceramics

The electrical and thermal properties of metals are controlled by loose electrons. In ceramics, however, the valence electrons are bound, not loose, resulting in poor thermal and electrical conduction. Exceptions are unavoidable; for instance, diamond, which is also classified as a ceramic, has the highest known thermal conductivity [445].

Ceramics exhibit atypical compressive and tensile properties, which differ from those of metals and polymers, and this is a vital design consideration when using ceramics in load-bearing applications [445]. Moreover, the toughness of ceramics is often relatively low. To compensate for the low toughness, they can be mixed with other materials, such as metals or polymers, to form composites [446].

The most important and common mechanical characteristics of ceramics are linear elastic deformation and brittle fracture under tension [447]. Most ceramics (*e.g.*, polycrystalline alumina) are reasonably elastic at room temperature, and some other ceramics, such as MgO single crystals, show slight residual deformation when the stress is relieved [448]; however, this minor non-linearity is often neglected.

Stochastic strength behavior is another characteristic of ceramics. This can be seen when testing identical ceramics. This behavior is related to flaws in the micro-structure and the effectiveness degree of the flaws. Such behavior has to be taken into consideration when ceramic materials are used in the design of any product [449].

Ceramics exhibit time-dependent material properties. Creep, which is defined as time-dependent deformation under constant applied stress, is an example [443]. Permanent deformation behavior can be easily observed in the viscous behavior of a liquid. At elevated temperatures, some ceramics, such as glass, also act as extremely viscous fluids, and under these conditions, the consideration of liquid-like behavior is appropriate. There have been many studies so far to determine changes in viscosity as a function of temperature [450].

Another type of permanent deformation is plastic deformation, which occurs mostly in metals but can also be observed in ceramics at high temperatures [451]. The parameter χ , called the “brittleness measure”, has been introduced to study and define the

deformational characteristics and inelasticity of ceramics. In some ceramics, such as aluminium oxide reinforced by zirconium dioxide and zirconium dioxide stabilised by yttrium oxide, χ is equal to 1, which indicates that they obey Hooke's law. In another category of ceramics, χ is <1 , which implies that they hold on to residual stresses. Some examples of the second category are cordierite, silicon nitride with boron nitride, corundum refractory material with zirconium dioxide, and zirconium dioxide stabilised by magnesium oxide [452].

2.5.3 Manufacturing methods for ceramics

Ceramics can normally withstand harsh operating environments, which can be beneficial to many industries. Owing to a wide range of favourable mechanical properties and characteristics, chemical inertness, and excellent features at high temperatures, ceramics are desirable materials in biomedical applications. However, advanced manufacturing techniques are required to achieve superior properties as well as efficient production [390].

Ceramic parts can be produced by using a variety of existing methods, and they can be classified into the following five categories [453]:

1. Casting/solidification methods: in this category, the liquid and solid states of the starting material change, and this is accompanied by some volumetric changes in most cases.
2. Deformation methods: in this category, ceramic structures are formed through a plastic deformation process.
3. Machining and material removal methods: an abrasive process is applied to remove the material from a ceramic block.
4. Joining methods: in this category of methods, different ceramic bits and pieces are combined using various joining techniques.
5. Solid free-form fabrication methods: this category of methods includes various AM methods for the fabrication of ceramics.

The first four categories are considered to be among the conventional methods of fabricating ceramic parts. In the last category, several AM techniques are suitable, and nearly all of them, except for material jetting, have been used to produce ceramic structures. To achieve complex bulk or porous materials, AM technologies, such as SLS, lithography-based ceramic manufacturing (LCM), SLM, and FDM, have been adopted.

Geometry design is a significant factor in ceramic AM, and it has received considerable attention in recent studies [454]. The operating conditions of AM ceramic products dictate some other required characteristics, *e.g.*, certain electrical and mechanical characteristics. The use of ceramics, in combination with other groups of materials that have different properties and are realised by applying suitable co-

manufacturing procedures, is becoming more extensive than ever before and, in some cases, even essential for the development of novel biomaterials and medical devices [385].

To meet the requirements for certain applications, direct AM has been proposed and widely used to produce ceramic parts and ceramic-reinforced metal matrix composites. A high-power-density laser beam is used to generate heat in the AM process. In several ways, the laser deposition-additive manufacturing (LD-AM) technique outperforms other direct AM methods with respect to production performance, the ability to remanufacture components, and the production of functionally graded composite materials; however, issues such as poor bonding, cracking, and lowered toughness persist in LD-AM-built products [455]. However, in practice, a binder, usually a polymer with a low melting point, is used in indirect AM to help consolidate the layers during AM. The binder is, in most cases, removed through a process called debinding, followed by sintering.

Although AM has been more successful in metals and polymers than in ceramics, there is a growing interest in using AM technologies to produce high-quality dense ceramic products. The appropriate technique is determined by the sizes, shapes, binder concentrations, and surface conditions of the proposed product, as well as the type of ceramic used [456].

Powder-based 3D printing (P-3DP)

In regard to ceramic materials, binder jetting and SLS are the two common and globally accepted powder-based 3D printing (P-3DP) processes [457].

Binder Jetting— There are two main categories of material-binder arrangements that can be employed for producing scaffolds: (i) the ceramic powder is mixed with an organic binder that can be dissolved in water or a solvent and sprayed on the printing bed [455], or the ceramic powder can be combined with a polymer that can act as a binder [456,458]; (ii) a reactive liquid binder that allows low-temperature activation and promotes the densification of ceramic powder at relatively low temperatures is applied. Many studies have been conducted on calcium phosphate, in which the binder is phosphoric acid [459].

For some biomedical applications, polymer-derived ceramics have been developed by means of P-3DP of a preceramic polymer powder containing no inert or active fillers. Without the use of external binders, the sprayed solvent can melt the preceramic polymer powder and combine the particles while filling the gaps between them [460]. Following heat treatment, the resultant product can retain some residual porosity, as the product does not experience sintering. To resolve this issue, the preceramic polymer is combined with a glass powder and reactive fillers to produce a bio-ceramic scaffold based on wollastonite–apatite [461]. Reviews on the developed strategies for the material and design of ceramic scaffolds used with the P-3DP method can be found in a number of studies [462,463].

Design principles

Most of the research in the area of 3D printing of porous ceramic structures based on powders is focussed on producing scaffolds for tissue engineering applications. The pores in the scaffolds must be in a range of 50 to 1000 μm , and the scaffolds must contain a porosity greater than 60%, which is required for productive bone ingrowth and proper vascularisation of implants. Another important dimension is the residual micro-porosity in the resultant product, which is preferably kept under 10 μm to increase the surface area, which in turn results in better protein absorption and ion transfer. It is important to note that pores smaller than 500 μm cannot be directly printed owing to the limitation on the resolution and difficulty in removing excess powder particles [385].

P-3DP is a suitable method for building porous ceramic structures. An important restriction in using P-3DP is the low density that can be achieved, partly due to the low powder-packing density in the powder bed, thereby limiting the design variation and automatic part production. Commonly, the ceramic powder particle size exceeds 20 μm , which does not provide sufficiently high sintering activity for the production of dense ceramics. One of the solutions is to use ceramic slurry instead of the dry powder. In some cases, heat treatment following the manufacturing of the part enhances the density [385].

Selective Laser Sintering (SLS)— In the SLS method, the density of the material at each location can be specified by either direct sintering of ceramic powder or by combining it with a binder, such as a polymer or an inorganic material that is melted by using a laser beam. Most ceramics are rather stable when exposed to high temperatures, and therefore, direct sintering is not a straightforward method for their fabrication. Moreover, the limited duration of the laser action on the powder results in inappropriate sintering [464–467] owing to a lack of extensive atomic diffusion and thus insufficient neck formation and growth.

Incorporating thermally activated binders into ceramic powders has resulted in acceptable porous ceramic structures [468,469]. Another application in this regard is selected laser curing, developed by Friedel et al. [470], in which preceramic powder is used to fabricate a polymer-derived ceramic part.

Kolan et al. [471] manufactured bioactive glass scaffolds with a porosity of 50% and pore sizes between 300 and 800 μm by applying a polymer binder, SLS, and subsequent debinding and sintering at 675–695°. SLS is also used to fabricate hydroxyapatite–silica scaffolds for bone replacement with pore sizes of 750 to 1050 μm and porosities of 25% to 32%. For this purpose, a slurry composed of hydroxyapatite powder and silica sol as a binder is used in SLS, and the subsequent sintering is performed at 1200 °C [472].

Another possibility in the development of scaffolds for tissue engineering purposes is applying biocompatible polymers as binder, for example, a scaffold developed from poly (L-lactide-co-glycolide)–hydroxyapatite (HAP) and β -tricalcium phosphate (β -TCP)

or from polyetheretherketone–hydroxyapatite as bone substitutes [473,474]. The manufactured scaffolds are actually biopolymer–ceramic composites, and no further post-processing is needed [385].

SLM is another option being explored, as the presence of a liquid phase ensures rapid densification [475]. Mixtures of alumina and zirconia powders with sizes of 20 and 70 μm are used as feedstock materials to achieve a high packing density of particles in the powder bed. To minimise the risk of thermally induced stresses in the workpiece, the powder bed is preheated up to 1600 $^{\circ}\text{C}$ prior to printing. The formation of the alumina–zirconia eutectic can decrease the melting points of the individual ceramics (especially ZrO_2 : 2710 $^{\circ}\text{C}$) to 1860 $^{\circ}\text{C}$. The above considerations allow the creation of dense ceramic products that can potentially display exceptional mechanical properties. However, there is always the possibility of crack development in ceramic parts, and unrestrained fluid infiltration at the laser point may cause the formation of an undesirable surface on the outside of the workpiece [385].

Stereolithography (SLA)

This approach is based on the photopolymerization of a liquid resin containing ceramic powder, which is performed in consecutive layers in the same way as other indirect AM techniques. The slurry is composed of a photo-initiator, a monomer solution, and other additives that help in the dispersion of the ceramic powder. The desired volume fraction of the ceramic powder is normally between 40 and 60% [476,477]. The manufacture of dense ceramic products is possible by applying the SLA technique, followed by sintering as a post-processing method [476].

Many investigators have used the SLA method to create high-quality porous ceramic products for a variety of industries. Kirihara [478], for example, used this technique to fabricate ceramic dendrite structures with geometrically ordered lattices and demonstrated that with an acrylic resin, hydroxyapatite scaffolds for tissue engineering purposes could be manufactured with a porosity of 75% and lattice density of about 98% after post-SLA dewaxing at 600 $^{\circ}\text{C}$ for 2 h and sintering at 1250 $^{\circ}\text{C}$ for 2 h were applied. Chu et al. [479] created porous hydroxyapatite structures with a target porosity of 40% and controllable pore geometry of either radial or orthogonal channels from HAP suspension in acrylates.

Bian et al. [480] manufactured a biphasic biomimetic osteochondral scaffold with a bone phase, a cartilage phase, and a transitional structure between bone and cartilage. The scaffold was initially produced by creating a porous β -TCP scaffold using SLA of ceramic suspensions, followed by drying and sintering, and finally, gel casting and freeze-drying of a collagen solution were performed to introduce the cartilage phase. The pore sizes of the bone phase were measured to be 700 to 900 μm , with a porosity of 50 to 60 %, while those of the cartilage phase were 200 to 500 μm .

Extrusion-based 3D printing: Robocasting, Direct Ink Writing, and FDM

One of the most popular AM methods for the fabrication of porous ceramic structures is the direct deposition of slurry. In this process, viscous ceramic paste is extruded through a nozzle in the shape of a filament, and then it undergoes a transformation from pseudoplastic to dilatant by extruding and drying in air. Air drying restricts the minimal calibre of the nozzle to 500 μm in order to avoid clogging. A solution to this issue is the development of special inks with reversible gel conversion, which is known as robocasting (Figure 2.4b) [481]. The ink initially acts like a viscous gel in the printing head, but the shear stress of the extrusion disrupts the internal structure of the gel and significantly reduces the viscosity. The viscosity expands again following extrusion. The rheological characteristics of the filament must be properly arranged to prevent its distortion and bowing, particularly in cases where there are spanning features in the configuration of the part [385].

Many studies have been conducted to explore the use of the robocasting process for the fabrication of porous bio-ceramic scaffolds. Genet et al. [482] investigated the mechanical behavior of robocasts and sintered porous hydroxyapatite scaffolds based on the Weibull theory. From the experimental data, they demonstrated that the expansion of porosity resulted in a reduction in compressive strength. By using a special ink with a thermally reversible gel, Franco et al. were able to create scaffolds out of HAP, tricalcium phosphate (TCP), and biphasic calcium phosphate [483]. They also realised that by increasing the gel content, the micro-porosity of struts could be substantially increased from 5 to 40%, resulting in a reduction in bending strength from 25 to 2 MPa [483].

Miranda et al. [484] succeeded in creating HAP scaffolds with an overall porosity of 39% and a strut microporosity of 5% and investigated their failure modes under uniaxial loading conditions. They demonstrated a value of approximately 50 MPa for the compressive strength of the fabricated scaffolds and found that the strength could be increased up to twofold by placing them in a simulated body fluid [384]. Fu et al. [485] created relatively strong bioglass scaffolds with dense rods of 100 μm in diameter and an overall porosity of 60% with unidirectional pores. The mechanical strength in the direction parallel to the pore channels reached 136 MPa, while the strength in the direction normal to the pore channels was 55 MPa.

Porogens can be added to ceramic paste to obtain porosity at different levels [486]. Dellinger et al. affixed poly(methyl methacrylate) (PMMA) particles to the ink and built scaffolds with three ranges of porosity. Macro-pores in a range of 100 to 600 μm were created by arranging and locating them among rods of HAP; micro-pores with sizes of 1 to 30 μm were generated within the rods by introducing PMMA particles; and sub-micro-pores with sizes under 1 μm were obtained as the output of imperfect sintering [486].

FDM of ceramics has been introduced as one of the methods that involve the extrusion of ceramic paste and is similar to the methods used in the manufacturing of polymer parts. In this method, a mixture of ceramic and polymer powder that liquefies during extrusion is extruded and returns to the solid phase as it cools down. Following 3D printing, the polymeric part is removed, and the remaining ceramic part is sintered. Grida et al. [487] used a combination of 55 vol% zirconia with wax and extruded the feedstock by applying nozzles with calibres from 76 to 510 μm . Park et al. [488] used a paste containing 40 wt% HAP mixed with molten PCL at a temperature of 120 $^{\circ}\text{C}$ and extruded the feedstock with a nozzle size of 400 μm and a scaffold strand distance of 600 μm . Kalita et al. [489] also used FDM to fabricate polypropylene–TCP composite scaffolds with a compression strength of 12.7 MPa, an overall porosity of 36%, and an average pore size of 160 μm .

In general, scaffolds constructed with DIW techniques are mechanically stronger than those built with powder-based methods [385]. However, in the case of powder-based indirect AM techniques, there are fewer geometry restrictions, and therefore, constructing cylindrical shapes with either radial or orthogonal pores is preferred because the resulting structure is more similar to natural bone than that obtained with DIW methods [385].

The scaffolds produced by P-3DP methods have sintering necks between the original powder particles, resulting in a high residual porosity [490], while the ones produced by DIW can be subjected to sintering to become more dense (Figure 2.4c). However, absolutely dense scaffolds cannot be constructed by this method owing to the unavoidable presence of approximately 15% micro-porosity in the scaffold [484]. The remaining micro-porosity is useful for tissue engineering, but it may have an adverse effect on the mechanical properties of the struts [385].

Negative AM techniques

By applying negative replica methods, some restrictions concerning the shape and functioning of the products can be overcome. In these techniques, AM is used to create a polymer mould, which can then be filled with ceramic slurry. Subsequently, the polymer must be dissolved, followed by ceramic sintering to produce the finished product [491].

The initial polymeric mould can be created using any of the AM methods. Detsch et al. printed a wax mould and filled it with HAP slurry in their study. They also duplicated the exact shape using the robocasting method and obtained 44% porosity, whereas negative AM produced 37% porosity. The scaffolds created using both methods had the same pore and strut thickness dimensions [492]. The SLA method can also be employed to create resin moulds for HAP scaffolds with 50% porosity [493]. In the study conducted by Woesz et al., a gel-casting method was applied to enhance the mechanical properties of the ceramic green body [493].

Design principles

Freeze foaming is another method for producing porous ceramic structures. The most common foaming processes are generally those originating from the exhaustion of environmentally harmful unstable organic pore-formers or whole polymer scaffolds [494].

When the freeze foam materials are composed of HAP or zirconia (ZrO₂) or their composite mixtures, biocompatible or bio-inert products can be manufactured based on the properties of the individual materials [495,496].

By combining the LCM and novel freeze-foaming methods, biocompatible structures can be obtained, which may be the next generation of bio-composites. They can result in a combination of dense and porous structures in an isolated product. Although AM technology has the advantage of allowing for customised features, freeze foaming creates porous structures with adaptive pores and porosities, allowing for the growth and differentiation of mesenchymal stem cells [494].

2.5.4 Biomedical applications of ceramics

With the advancement of ceramic technology, state-of-the-art ceramics have been developed for biomedical purposes [497]. The first scientifically managed medical uses of ceramics were in dentistry, where porcelain is used to make crowns, and in orthopaedics, where plaster of Paris gypsum (calcium sulphate dehydrate) is used to treat fractures [498].

Today, most research and development on dental prosthetic restorations are focussed on ceramics rather than metals, as ceramics have an advantage because of the white to ivory colour of their oxides [401]. In fact, in addition to mechanical properties, aesthetic considerations, such as colour and translucency, are prioritised in dental applications. In tooth repairs without the application of metals, the colour of the soft tissue maintains a higher resemblance to that of the native tissue compared to porcelain combined with metallic elements. Furthermore, ceramics are not susceptible to corrosion or galvanic effects that are inevitable in the case of metals [401].

Yttrium-stabilised tetragonal zirconia has recently been recognised as another appropriate choice for many dental applications, but observations of in vitro stability demonstrate that aging can be an issue [499]. There are not many studies available regarding its prolonged in vivo durability in oral environments [499].

Bio-ceramics can be classified into two groups, namely, bio-inert and bioactive [499]. Unlike bio-inert ceramics, bioactive ceramics must provide adequate surface conditions for cell adhesion and bone growth [500]. The most common bioactive ceramics contain calcium phosphate components, such as HAP and TCP, which are similar to the mineral constituents of bone to a great extent [500].

Bioactive ceramics have been mainly utilised as coatings on metallic orthopaedic implants. This is especially important in areas where a robust interface with the bone is needed, such as femoral stems and metal-backed acetabular cups in hip prostheses or tibial and femoral stems in total knee replacement systems [499].

Owing to the osteoconductive properties of calcium phosphates, they have been widely used as artificial bone grafts and substitutes for autografts and allografts since the mid-1980s [500]. Unlike natural grafts, artificial bone replacements do not require invasive surgery and can be supplied in large quantities [501]. Another advantage, in comparison to allografts, is a lower risk of rejection and disease transmission. The most common bone replacements are porous structures constructed from biphasic calcium phosphates, such as HAP-TCP composites [501].

The rate of absorption of TCP is higher than that of HAP, allowing for the management of the gross degradation rate of the HAP-TCP composite and customisation of the composite material for the patient, for example, faster resorption for patients with more rapid bone reconstruction [501].

However, recent bone replacements based on calcium phosphate have not been completely effective because porosities at the micro- and nano-scales can cause a variety of physical and chemical features that can affect biological characteristics [501].

Another shortcoming of ceramics is their brittleness and low crack resistance [502]. As inherent brittleness is a critical weakness of ceramics, there are a large number of review articles on the failure of ceramics [503].

2.6 Conclusions and future research directions

Major biomedical applications of biomaterials can be summarised as scaffolds for bone repair, tissue regeneration, reconstructive and orthopaedic implants, cardiovascular devices and prostheses, dental restorations, ophthalmic devices, and drug delivery systems. These products are manufactured from a wide range of biocompatible materials, including metals, polymers, and ceramics, or a combination of these materials.

AM technologies have provided excellent opportunities for the ease of manufacturing and cost-effective production of many new and advanced products from various materials for the abovementioned biomedical applications.

All of the AM techniques in the ASTM classification, especially material extrusion (*e.g.*, FDM), directed energy deposition (DED), material jetting (*e.g.*, Polyjet), PBF (*e.g.*, SLS, SLM, DMLS, and EBM), and binder jetting, are not equally developed and used for medical devices and biomaterial fabrication. The capabilities, limitations, pros, and cons of each technique and associated materials (*e.g.*, metals and their alloys, polymers, and ceramics) as well as considerations for the AM fabrication of biomaterials such as printing speed, part sizes, degree of anisotropy, achievable resolution, the possibility of

Design principles

embedding cells in feedstock materials, the need for support, the need for post-processing, and printing costs, all are important factors that need to be taken into account. The success of each of these 3D printing processes relies, to a large extent, on the employment of optimised or suitable process parameters within the capabilities of the available AM machines.

Aside from selecting the proper AM techniques and suitable printing parameters, the microarchitecture design of biomaterials is one of the critical aspects of their development. It is often necessary to design porous or lattice structures for biomedical applications. This implies that pores with certain morphologies and sizes inside the biomaterials must be fully open and interconnected to allow for the transport of nutrients and oxygen to cells.

In addition to new horizons in producing biomedical devices and products, the versatility of AM methods in enhancing the properties of materials opens up the possibilities of new breakthroughs in the biomedical engineering industry. The possibility of the customisation of design as well as properties is a major consideration in the research and development of AM.

Considering the wide range of requirements in tissue engineering and artificial organs, the current developments of biomaterials seem to be far from satisfactory and require more research in the future. The prolonged existence of biomaterials in the body without immune rejection is still an issue in most cases, which needs more research. Better materials are expected to satisfy the requirements of artificial joints with respect to wear reduction and durability. In addition to biocompatibility, cellular responses to the biomaterial are expected to acclimate with the host tissue in most tissue engineering cases. This necessitates the addition of some bioactive factors to stimulate the desired responses or to prevent a specific reaction, which can be a future path for the development of biomaterials in the AM industry. Another future direction of research in regard to AM is related to micro- and nano-printing of multi-materials, especially bimaterials, and the joining methods of various metals, as well as multi-material 3D printing. It is expected that by using AM techniques, in many cases, the issues of conventional joining methods, such as welding and soldering, can be overcome.

Bibliography

1. Zadpoor, A.A.; Malda, J. Additive manufacturing of biomaterials, tissues, and organs. *Ann. Biomed. Eng.* 2017, 45, 1–11. <https://doi.org/10.1007/s10439-016-1719-y>.
2. Böckin, D.; Tillman, A.-M. Environmental assessment of additive manufacturing in the automotive industry. *J. Clean. Prod.* 2019, 226, 977–987. <https://doi.org/10.1016/j.jclepro.2019.04.086>.
3. Dämmer, G.; Bauer, H.; Neumann, R.; Major, Z. Design, additive manufacturing and component testing of pneumatic rotary vane actuators for lightweight robots. *Rapid Prototyp. J.* 2022, 28, 20–32. <https://doi.org/10.1108/rpj-03-2021-0052>.
4. Lyons, B. *Additive Manufacturing in Aerospace: Examples and Research Outlook; The Bridge: Commerce, CA, USA, 2014; Volume 44.*
5. ISO, I.A.A.F. *Additive Manufacturing—General Principles—Terminology*; ISO: Geneva, Switzerland, 2015.
6. Bobbert, F.; Zadpoor, A. Effects of bone substitute architecture and surface properties on cell response, angiogenesis, and structure of new bone. *J. Mater. Chem. B* 2017, 5, 6175–6192.
7. Karageorgiou, V.; Kaplan, D. Porosity of 3D biomaterial scaffolds and osteogenesis. *Biomaterials* 2005, 26, 5474–5491. <https://doi.org/10.1016/j.biomaterials.2005.02.002>.
8. Wauthle, R.; van der Stok, J.; Amin Yavari, S.; Van Humbeeck, J.; Kruth, J.P.; Zadpoor, A.A.; Weinans, H.; Mulier, M.; Schrooten, J. Additively manufactured porous tantalum implants. *Acta Biomater.* 2015, 14, 217–225. <https://doi.org/10.1016/j.actbio.2014.12.003>.
9. Bose, S.; Vahabzadeh, S.; Bandyopadhyay, A. Bone tissue engineering using 3D printing. *Mater. Today* 2013, 16, 496–504. <https://doi.org/10.1016/j.mattod.2013.11.017>.
10. Murr, L.E.; Gaytan, S.; Medina, F.; Lopez, H.; Martinez, E.; Machado, B.; Hernandez, D.; Martinez, L.; Lopez, M.; Wicker, R. Next-generation biomedical implants using additive manufacturing of complex, cellular and functional mesh arrays. *Philos. Trans. R. Soc. A Math. Phys. Eng. Sci.* 2010, 368, 1999–2032.
11. Zadpoor, A.A. Design for additive bio-manufacturing: From patient-specific medical devices to rationally designed meta-biomaterials. *Int. J. Mol. Sci.* 2017, 18, 1607.
12. Gokuldoss, P.K.; Kolla, S.; Eckert, J. Additive manufacturing processes: Selective laser melting, electron beam melting and binder jetting—Selection guidelines. *Materials* 2017, 10, 672.
13. Kranz, J.; Herzog, D.; Emmelmann, C. Design guidelines for laser additive manufacturing of lightweight structures in TiAl6V4. *J. Laser Appl.* 2015, 27, S14001.
14. Wang, X.; Xu, S.; Zhou, S.; Xu, W.; Leary, M.; Choong, P.; Qian, M.; Brandt, M.; Xie, Y.M. Topological design and additive manufacturing of porous metals for bone scaffolds and orthopaedic implants: A review. *Biomaterials* 2016, 83, 127–141.
15. Su, X.-b.; YANG, Y.-q.; Peng, Y.; Sun, J.-f. Development of porous medical implant scaffolds via laser additive manufacturing. *Trans. Nonferrous Met. Soc. China* 2012, 22, s181–s187.
16. Calignano, F. Design optimization of supports for overhanging structures in aluminum and titanium alloys by selective laser melting. *Mater. Des.* 2014, 64, 203–213.
17. Dutta, B.; Froes, F.H.S. *The additive manufacturing (AM) of titanium alloys*. In *Titanium Powder Metallurgy*; Elsevier: Amsterdam, The Netherlands, 2015; pp. 447–468.
18. Giannitelli, S.M.; Accoto, D.; Trombetta, M.; Rainer, A. Current trends in the design of scaffolds for computer-aided tissue engineering. *Acta Biomater.* 2014, 10, 580–594.
19. Onal, E.; Medvedev, A.; Leeftang, M.; Molotnikov, A.; Zadpoor, A. Novel microstructural features of selective laser melted lattice struts fabricated with single point exposure scanning. *Addit. Manuf.* 2019, 29, 100785.
20. Ahmadi, S.; Hedayati, R.; Jain, R.A.K.; Li, Y.; Leeftang, S.; Zadpoor, A. Effects of laser processing parameters on the mechanical properties, topology, and microstructure of additively manufactured porous metallic biomaterials: A vector-based approach. *Mater. Des.* 2017, 134, 234–243.
21. Doubrovski, E.L.; Tsai, E.Y.; Dikovskiy, D.; Geraedts, J.M.; Herr, H.; Oxman, N. Voxel-based fabrication through material property mapping: A design method for bitmap printing. *Comput.-Aided Des.* 2015, 60, 3–13.

Design principles

22. Maconachie, T.; Leary, M.; Lozanovski, B.; Zhang, X.; Qian, M.; Faruque, O.; Brandt, M. SLM lattice structures: Properties, performance, applications and challenges. *Mater. Des.* 2019, 183, 108137.
23. Kumar, M.; Mohol, S.S.; Sharma, V. A computational approach from design to degradation of additively manufactured scaffold for bone tissue engineering application. *Rapid Prototyp. J.* 2022. <https://doi.org/10.1108/rpj-12-2021-0336>.
24. Maskery, I.; Aboulkhair, N.T.; Aremu, A.; Tuck, C.; Ashcroft, I. Compressive failure modes and energy absorption in additively manufactured double gyroid lattices. *Addit. Manuf.* 2017, 16, 24–29.
25. Zadpoor, A.A. Additively manufactured porous metallic biomaterials. *J. Mater. Chem. B* 2019, 7, 4088–4117.
26. Yavari, S.A.; Ahmadi, S.; Wauthle, R.; Pouran, B.; Schrooten, J.; Weinans, H.; Zadpoor, A. Relationship between unit cell type and porosity and the fatigue behavior of selective laser melted meta-biomaterials. *J. Mech. Behav. Biomed. Mater.* 2015, 43, 91–100.
27. Deshpande, V.; Ashby, M.; Fleck, N. Foam topology: Bending versus stretching dominated architectures. *Acta Mater.* 2001, 49, 1035–1040.
28. Deshpande, V.S.; Fleck, N.A.; Ashby, M.F. Effective properties of the octet-truss lattice material. *J. Mech. Phys. Solids* 2001, 49, 1747–1769.
29. Callens, S.J.; Uyttendaele, R.J.; Fratila-Apachitei, L.E.; Zadpoor, A.A. Substrate curvature as a cue to guide spatiotemporal cell and tissue organization. *Biomaterials* 2020, 232, 119739.
30. Bobbert, F.; Lietaert, K.; Eftekhari, A.A.; Pouran, B.; Ahmadi, S.; Weinans, H.; Zadpoor, A. Additively manufactured metallic porous biomaterials based on minimal surfaces: A unique combination of topological, mechanical, and mass transport properties. *Acta Biomater.* 2017, 53, 572–584.
31. Mirzaali, M.; Hedayati, R.; Vena, P.; Vergani, L.; Strano, M.; Zadpoor, A. Rational design of soft mechanical metamaterials: Independent tailoring of elastic properties with randomness. *Appl. Phys. Lett.* 2017, 111, 051903.
32. Garner, E.; Kolken, H.M.; Wang, C.C.; Zadpoor, A.A.; Wu, J. Compatibility in microstructural optimization for additive manufacturing. *Addit. Manuf.* 2019, 26, 65–75.
33. Mirzaali, M.J.; Cruz Saldívar, M.; Herranz de la Nava, A.; Gunashekar, D.; Nouri-Goushki, M.; Doubrovski, E.L.; Zadpoor, A.A. Multi-material 3D printing of functionally graded hierarchical soft-hard composites. *Adv. Eng. Mater.* 2020, 29, 1901142.
34. Kolken, H.M.; Zadpoor, A. Auxetic mechanical metamaterials. *RSC Adv.* 2017, 7, 5111–5129.
35. Kolken, H.; Garcia, A.F.; Du Plessis, A.; Rans, C.; Mirzaali, M.; Zadpoor, A. Fatigue performance of auxetic meta-biomaterials. *Acta Biomater.* 2021, 126, 511–523.
36. Kolken, H.; de Jonge, C.; van der Sloten, T.; Garcia, A.F.; Pouran, B.; Willemsen, K.; Weinans, H.; Zadpoor, A. Additively manufactured space-filling meta-implants. *Acta Biomater.* 2021, 125, 345–357.
37. Janbaz, S.; Noordzij, N.; Widyaratih, D.S.; Hagen, C.W.; Fratila-Apachitei, L.E.; Zadpoor, A.A. Origami lattices with free-form surface ornaments. *Sci. Adv.* 2017, 3, eaao1595.
38. Kapfer, S.C.; Hyde, S.T.; Mecke, K.; Arns, C.H.; Schröder-Turk, G.E. Minimal surface scaffold designs for tissue engineering. *Biomaterials* 2011, 32, 6875–6882.
39. Yoo, D.-J. Computer-aided porous scaffold design for tissue engineering using triply periodic minimal surfaces. *Int. J. Precis. Eng. Manuf.* 2011, 12, 61–71.
40. Yoo, D.J. Porous scaffold design using the distance field and triply periodic minimal surface models. *Biomaterials* 2011, 32, 7741–7754.
41. Choy, S.Y.; Sun, C.-N.; Leong, K.F.; Wei, J. Compressive properties of functionally graded lattice structures manufactured by selective laser melting. *Mater. Des.* 2017, 131, 112–120.
42. Loh, G.H.; Pei, E.; Harrison, D.; Monzon, M.D. An overview of functionally graded additive manufacturing. *Addit. Manuf.* 2018, 23, 34–44.
43. Han, C.; Li, Y.; Wang, Q.; Wen, S.; Wei, Q.; Yan, C.; Hao, L.; Liu, J.; Shi, Y. Continuous functionally graded porous titanium scaffolds manufactured by selective laser melting for bone implants. *J. Mech. Behav. Biomed. Mater.* 2018, 80, 119–127.
44. Monzón, M.; Liu, C.; Ajami, S.; Oliveira, M.; Donate, R.; Ribeiro, V.; Reis, R.L. Functionally graded

- additive manufacturing to achieve functionality specifications of osteochondral scaffolds. *Bio-Des. Manuf.* 2018, 1, 69–75.
45. Mirzaali, M.; Pahlavani, H.; Zadpoor, A. Auxeticity and stiffness of random networks: Lessons for the rational design of 3D printed mechanical metamaterials. *Appl. Phys. Lett.* 2019, 115, 021901.
 46. Hashin, Z.; Shtrikman, S. A variational approach to the theory of the elastic behaviour of multiphase materials. *J. Mech. Phys. Solids* 1963, 11, 127–140.
 47. Berger, J.; Wadley, H.; McMeeking, R. Mechanical metamaterials at the theoretical limit of isotropic elastic stiffness. *Nature* 2017, 543, 533–537.
 48. Bendsoe, M.P.; Sigmund, O. *Topology Optimization: Theory, Methods, and Applications*; Springer Science & Business Media: Berlin, Germany, 2013.
 49. Sánchez-Palencia, E. Non-homogeneous media and vibration theory. *Lect. Notes Phys.* 1980, 127. <https://doi.org/10.1007/3-540-10000-8>.
 50. Bensoussan, A.; Lions, J.-L.; Papanicolaou, G. *Asymptotic Analysis for Periodic Structures*; American Mathematical Society.: Providence, RI, USA, 2011; Volume 374.
 51. Sigmund, O.; Torquato, S. Design of materials with extreme thermal expansion using a three-phase topology optimization method. *J. Mech. Phys. Solids* 1997, 45, 1037–1067.
 52. Zhou, J.; Dong, J.; Wang, B.; Koschny, T.; Kafesaki, M.; Soukoulis, C.M. Negative refractive index due to chirality. *Phys. Rev. B* 2009, 79, 121104.
 53. Wu, J.; Aage, N.; Westermann, R.; Sigmund, O. Infill optimization for additive manufacturing—approaching bone-like porous structures. *IEEE Trans. Vis. Comput. Graph.* 2017, 24, 1127–1140.
 54. Zadpoor, A.A.; Campoli, G.; Weinans, H. Neural network prediction of load from the morphology of trabecular bone. *Appl. Math. Model.* 2013, 37, 5260–5276.
 55. Zadpoor, A.A. Open forward and inverse problems in theoretical modeling of bone tissue adaptation. *J. Mech. Behav. Biomed. Mater.* 2013, 27, 249–261.
 56. Fraldi, M.; Esposito, L.; Perrella, G.; Cutolo, A.; Cowin, S. Topological optimization in hip prosthesis design. *Biomech. Modeling Mechanobiol.* 2010, 9, 389–402.
 57. Chuah, H.G.; Rahim, I.A.; Yusof, M.I. Topology optimisation of spinal interbody cage for reducing stress shielding effect. *Comput. Methods Biomech. Biomed. Eng.* 2010, 13, 319–326.
 58. Hollister, S.J.; Maddox, R.; Taboas, J.M. Optimal design and fabrication of scaffolds to mimic tissue properties and satisfy biological constraints. *Biomaterials* 2002, 23, 4095–4103.
 59. van Kootwijk, A.; Moosabeiki, V.; Saldívar, M.C.; Pahlavani, H.; Leeftang, M.A.; Niar, S.K.; Pellikaan, P.; Jonker, B.P.; Ahmadi, S.M.; Wolvius, E.B.; et al. Semi-automated digital workflow to design and evaluate patient-specific mandibular reconstruction implants. *J. Mech. Behav. Biomed. Mater.* 2022, 132, 105291.
 60. Guest, J.K.; Prévost, J.H. Optimizing multifunctional materials: Design of microstructures for maximized stiffness and fluid permeability. *Int. J. Solids Struct.* 2006, 43, 7028–7047.
 61. Ryan, G.; Pandit, A.; Apatsidis, D.P. Fabrication methods of porous metals for use in orthopaedic applications. *Biomaterials* 2006, 27, 2651–2670.
 62. Zhang, X.-Y.; Fang, G.; Leeftang, S.; Zadpoor, A.A.; Zhou, J. Topological design, permeability and mechanical behavior of additively manufactured functionally graded porous metallic biomaterials. *Acta Biomater.* 2019, 84, 437–452.
 63. Xie, Y.M.; Steven, G.P. A simple evolutionary procedure for structural optimization. *Comput. Struct.* 1993, 49, 885–896.
 64. Xie, Y.M.; Steven, G.P. Basic evolutionary structural optimization. In *Evolutionary Structural Optimization*; Springer: Berlin/Heidelberg, Germany, 1997; pp. 12–29.
 65. Zhou, M.; Rozvany, G. The COC algorithm, Part II: Topological, geometrical and generalized shape optimization. *Comput. Methods Appl. Mech. Eng.* 1991, 89, 309–336.
 66. Bendsoe, M.P. Optimal shape design as a material distribution problem. *Struct. Optim.* 1989, 1, 193–202.
 67. Wang, R.; Chen, Y.; Peng, X.; Cong, N.; Fang, D.; Liang, X.; Shang, J. Topological design of the hybrid structure with high damping and strength efficiency for additive manufacturing. *Rapid Prototyp. J.* 2022. <https://doi.org/10.1108/rpj-10-2021-0285>.

Design principles

68. Huang, X.; Xie, Y.M. Bi-directional evolutionary topology optimization of continuum structures with one or multiple materials. *Comput. Mech.* 2009, 43, 393.
69. Huang, X.; Xie, Y. Bidirectional evolutionary topology optimization for structures with geometrical and material nonlinearities. *AIAA J.* 2007, 45, 308–313.
70. Wang, M.Y.; Wang, X.; Guo, D. A level set method for structural topology optimization. *Comput. Methods Appl. Mech. Eng.* 2003, 192, 227–246.
71. Blacker, T.D.; Robbins, J.; Owen, S.J.; Aguilovalentin, M.A.; Clark, B.W.; Voth, T.E. PLATO Platinum Topology Optimization; Sandia National Lab.(SNL-NM): Albuquerque, NM, USA, 2015.
72. Challis, V.J.; Roberts, A.P.; Grotowski, J.F.; Zhang, L.C.; Sercombe, T.B. Prototypes for bone implant scaffolds designed via topology optimization and manufactured by solid freeform fabrication. *Adv. Eng. Mater.* 2010, 12, 1106–1110.
73. Xiao, D.; Yang, Y.; Su, X.; Wang, D.; Sun, J. An integrated approach of topology optimized design and selective laser melting process for titanium implants materials. *Bio-Med. Mater. Eng.* 2013, 23, 433–445.
74. Hussein, A.; Hao, L.; Yan, C.; Everson, R.; Young, P. Advanced lattice support structures for metal additive manufacturing. *J. Mater. Processing Technol.* 2013, 213, 1019–1026.
75. Nam, J.; Starly, B.; Darling, A.; Sun, W. Computer aided tissue engineering for modeling and design of novel tissue scaffolds. *Comput.-Aided Des. Appl.* 2004, 1, 633–640.
76. Bucklen, B.; Wettergreen, W.; Yuksel, E.; Liebschner, M. Bone-derived CAD library for assembly of scaffolds in computer-aided tissue engineering. *Virtual Phys. Prototyp.* 2008, 3, 13–23.
77. EYu, K.; Balasubramanian, S.; Pahlavani, H.; Mirzaali, M.J.; Zadpoor, A.A.; Aubin-Tam, M.E. Spiral Honeycomb Microstructured Bacterial Cellulose for Increased Strength and Toughness. *ACS Appl. Mater. Interfaces* 2020, 12, 50748–50755. <https://doi.org/10.1021/acsami.0c15886>.
78. Ding, M.; Lin, X.; Liu, W. Three-dimensional morphometric properties of rod-and plate-like trabeculae in adolescent cancellous bone. *J. Orthop. Transl.* 2018, 12, 26–35.
79. Mansouri, M.; Montazerian, H.; Schmauder, S.; Kadkhodapour, J. 3D-printed multimaterial composites tailored for compliancy and strain recovery. *Compos. Struct.* 2018, 184, 11–17.
80. Mirzaali, M.J.; Edens, M.E.; de la Nava, A.H.; Janbaz, S.; Vena, P.; Doubrovski, E.L.; Zadpoor, A.A. Length-scale dependency of biomimetic hard-soft composites. *Sci. Rep.* 2018, 8, 12052. <https://doi.org/10.1038/s41598-018-30012-9>.
81. Mirzaali, M.J.; Herranz de la Nava, A.; Gunashekar, D.; Nouri-Goushki, M.; Doubrovski, E.; Zadpoor, A.A. Fracture behavior of bio-inspired functionally graded soft–hard composites made by multi-material 3D printing: The case of colinear cracks. *Materials* 2019, 12, 2735.
82. Mirzaali, M.J.; Herranz de la Nava, A.; Gunashekar, D.; Nouri-Goushki, M.; Veeger, R.P.E.; Grossman, Q.; Angeloni, L.; Ghatkesar, M.K.; Fratila-Apachitei, L.E.; Ruffoni, D.; et al. Mechanics of bioinspired functionally graded soft-hard composites made by multi-material 3D printing. *Compos. Struct.* 2020, 237, 111867. <https://doi.org/10.1016/j.compstruct.2020.111867>.
83. Koolen, M.; Amin Yavari, S.; Lietaert, K.; Wauthle, R.; Zadpoor, A.A.; Weinans, H. Bone regeneration in critical-sized bone defects treated with additively manufactured porous metallic biomaterials: The effects of inelastic mechanical properties. *Materials* 2020, 13, 1992.
84. Parthasarathy, J. 3D modeling, custom implants and its future perspectives in craniofacial surgery. *Ann. Maxillofac. Surg.* 2014, 4, 9.
85. Hollister, S.J.; Levy, R.A.; Chu, T.M.; Halloran, J.W.; Feinberg, S.E. An image-based approach for designing and manufacturing craniofacial scaffolds. *Int. J. Oral Maxillofac. Surg.* 2000, 29, 67–71.
86. Tümer, N.; Arbabi, V.; Gielis, W.P.; de Jong, P.A.; Weinans, H.; Tuijthof, G.J.; Zadpoor, A.A. Three-dimensional analysis of shape variations and symmetry of the fibula, tibia, calcaneus and talus. *J. Anat.* 2019, 234, 132–144.
87. Dérand III, P.; Rännar, L.-E.; Hirsch, J.-M. Imaging, virtual planning, design, and production of patient-specific implants and clinical validation in craniomaxillofacial surgery. *Craniomaxillofac. Trauma Reconstr.* 2012, 5, 137–143.
88. Jardini, A.L.; Larosa, M.A.; Maciel Filho, R.; de Carvalho Zavaglia, C.A.; Bernardes, L.F.; Lambert, C.S.; Calderoni, D.R.; Kharmandayan, P. Cranial reconstruction: 3D biomodel and custom-built implant created using additive manufacturing. *J. Cranio-Maxillofac. Surg.* 2014, 42, 1877–1884.

89. Mohammed, M.; Fitzpatrick, A.; Malyala, S.; Gibson, I. Customised design and development of patient specific 3D printed whole mandible implant. In Proceedings of Proceedings of the 27th Annual International Solid Freeform Fabrication Symposium, Austin, TX, USA, 8–10 August 2016; pp. 1708–1717.
90. Zadpoor, A.A. Frontiers of additively manufactured metallic materials. *Materials* 2018, 11, 1566. <https://doi.org/10.3390/ma11091566>.
91. Zadpoor, A.A. Mechanical meta-materials. *Mater. Horiz.* 2016, 3, 371–381.
92. Zadpoor, A.A. Mechanical performance of additively manufactured meta-biomaterials. *Acta Biomater.* 2019, 85, 41–59. <https://doi.org/10.1016/j.actbio.2018.12.038>.
93. Evans, K.E.; Alderson, A. Auxetic materials: Functional materials and structures from lateral thinking! *Adv. Mater.* 2000, 12, 617–628.
94. Hedayati, R.; Leeftang, A.; Zadpoor, A. Additively manufactured metallic pentamode meta-materials. *Appl. Phys. Lett.* 2017, 110, 091905.
95. Mirzaali, M.; Janbaz, S.; Strano, M.; Vergani, L.; Zadpoor, A.A. Shape-matching soft mechanical metamaterials. *Sci. Rep.* 2018, 8, 965.
96. van Manen, T.; Janbaz, S.; Zadpoor, A.A. Programming the shape-shifting of flat soft matter. *Mater. Today* 2018, 21, 144–163. <https://doi.org/10.1016/j.mattod.2017.08.026>.
97. Janbaz, S.; Hedayati, R.; Zadpoor, A. Programming the shape-shifting of flat soft matter: From self-rolling/self-twisting materials to self-folding origami. *Mater. Horiz.* 2016, 3, 536–547.
98. Janbaz, S.; Bobbert, F.; Mirzaali, M.; Zadpoor, A. Ultra-programmable buckling-driven soft cellular mechanisms. *Mater. Horiz.* 2019, 6, 1138–1147.
99. Janbaz, S.; Narooei, K.; van Manen, T.; Zadpoor, A. Strain rate-dependent mechanical metamaterials. *Sci. Adv.* 2020, 6, eaba0616.
100. Mirzaali, M.; Habibi, M.; Janbaz, S.; Vergani, L.; Zadpoor, A. Crumpling-based soft metamaterials: The effects of sheet pore size and porosity. *Sci. Rep.* 2017, 7, 13028.
101. Hedayati, R.; Mirzaali, M.; Vergani, L.; Zadpoor, A. Action-at-a-distance metamaterials: Distributed local actuation through far-field global forces. *APL Mater.* 2018, 6, 036101.
102. Gatt, R.; Wood, M.V.; Gatt, A.; Zarb, F.; Formosa, C.; Azzopardi, K.M.; Casha, A.; Agius, T.P.; Schembri-Wismayer, P.; Attard, L. Negative Poisson's ratios in tendons: An unexpected mechanical response. *Acta Biomater.* 2015, 24, 201–208.
103. Yan, Y.; Li, Y.; Song, L.; Zeng, C. Pluripotent stem cell expansion and neural differentiation in 3-D scaffolds of tunable Poisson's ratio. *Acta Biomater.* 2017, 49, 192–203.
104. Kolken, H.M.; Janbaz, S.; Leeftang, S.M.; Lietaert, K.; Weinans, H.H.; Zadpoor, A.A. Rationally designed meta-implants: A combination of auxetic and conventional meta-biomaterials. *Mater. Horiz.* 2018, 5, 28–35.
105. Goodman, S.B. Wear particles, periprosthetic osteolysis and the immune system. *Biomaterials* 2007, 28, 5044–5048.
106. Revell, P.A. The combined role of wear particles, macrophages and lymphocytes in the loosening of total joint prostheses. *J. R. Soc. Interface* 2008, 5, 1263–1278.
107. Sundfeldt, M.; V Carlsson, L.; B Johansson, C.; Thomsen, P.; Gretzer, C. Aseptic loosening, not only a question of wear: A review of different theories. *Acta Orthop.* 2006, 77, 177–197.
108. Kolken, H.; Lietaert, K.; van der Sloten, T.; Pouran, B.; Meynen, A.; Van Loock, G.; Weinans, H.; Scheyns, L.; Zadpoor, A.A. Mechanical performance of auxetic meta-biomaterials. *J. Mech. Behav. Biomed. Mater.* 2020, 104, 103658.
109. Teo, A.Q.A.; Yan, L.; Chaudhari, A.; O'Neill, G.K. Post-Processing and Surface Characterization of Additively Manufactured Stainless Steel 316L Lattice: Implications for BioMedical Use. *Materials* 2021, 14, 1376.
110. Ahmadi, S.; Kumar, R.; Borisov, E.; Petrov, R.; Leeftang, S.; Li, Y.; Tümer, N.; Huizenga, R.; Ayas, C.; Zadpoor, A. From microstructural design to surface engineering: A tailored approach for improving fatigue life of additively manufactured meta-biomaterials. *Acta Biomater.* 2019, 83, 153–166.
111. de Jonge, C.P.; Kolken, H.; Zadpoor, A.A. Non-auxetic mechanical metamaterials. *Materials* 2019,

Design principles

- 12, 635.
112. Al-Ketan, O.; Rowshan, R.; Al-Rub, R.K.A. Topology-mechanical property relationship of 3D printed strut, skeletal, and sheet based periodic metallic cellular materials. *Addit. Manuf.* 2018, 19, 167–183.
 113. Ataee, A.; Li, Y.; Fraser, D.; Song, G.; Wen, C. Anisotropic Ti-6Al-4V gyroid scaffolds manufactured by electron beam melting (EBM) for bone implant applications. *Mater. Des.* 2018, 137, 345–354.
 114. Mohammed, M.I.; Gibson, I. Design of three-dimensional, triply periodic unit cell scaffold structures for additive manufacturing. *J. Mech. Des.* 2018, 140, 071701.
 115. Yáñez, A.; Cuadrado, A.; Martel, O.; Afonso, H.; Monopoli, D. Gyroid porous titanium structures: A versatile solution to be used as scaffolds in bone defect reconstruction. *Mater. Des.* 2018, 140, 21–29.
 116. Bidan, C.M.; Wang, F.M.; Dunlop, J.W. A three-dimensional model for tissue deposition on complex surfaces. *Comput. Methods Biomech. Biomed. Eng.* 2013, 16, 1056–1070.
 117. Jinnai, H.; Nishikawa, Y.; Ito, M.; Smith, S.D.; Agard, D.A.; Spontak, R.J. Topological similarity of sponge-like bicontinuous morphologies differing in length scale. *Adv. Mater.* 2002, 14, 1615–1618.
 118. Jinnai, H.; Watashiba, H.; Kajihara, T.; Nishikawa, Y.; Takahashi, M.; Ito, M. Surface curvatures of trabecular bone microarchitecture. *Bone* 2002, 30, 191–194.
 119. Bidan, C.M.; Kommareddy, K.P.; Rumpler, M.; Kollmannsberger, P.; Brechet, Y.J.; Fratzl, P.; Dunlop, J.W. How linear tension converts to curvature: Geometric control of bone tissue growth. *PLoS ONE* 2012, 7, e36336.
 120. Bidan, C.M.; Kommareddy, K.P.; Rumpler, M.; Kollmannsberger, P.; Fratzl, P.; Dunlop, J.W. Geometry as a factor for tissue growth: Towards shape optimization of tissue engineering scaffolds. *Adv. Healthc. Mater.* 2013, 2, 186–194.
 121. Rumpler, M.; Woesz, A.; Dunlop, J.W.; Van Dongen, J.T.; Fratzl, P. The effect of geometry on three-dimensional tissue growth. *J. R. Soc. Interface* 2008, 5, 1173–1180.
 122. Yan, C.; Hao, L.; Hussein, A.; Wei, Q.; Shi, Y. Microstructural and surface modifications and hydroxyapatite coating of Ti-6Al-4V triply periodic minimal surface lattices fabricated by selective laser melting. *Mater. Sci. Eng. C* 2017, 75, 1515–1524.
 123. Callens, S.J.; Arns, C.H.; Kuliesh, A.; Zadpoor, A.A. Decoupling minimal surface metamaterial properties through multi-material hyperbolic tilings. *Adv. Funct. Mater.* 2021, 31, 2101373.
 124. Shan, S.; Kang, S.H.; Raney, J.R.; Wang, P.; Fang, L.; Candido, F.; Lewis, J.A.; Bertoldi, K. Multistable architected materials for trapping elastic strain energy. *Adv. Mater.* 2015, 27, 4296–4301.
 125. Callens, S.J.; Zadpoor, A.A. From flat sheets to curved geometries: Origami and kirigami approaches. *Mater. Today* 2018, 21, 241–264.
 126. van Manen, T.; Janbaz, S.; Ganjian, M.; Zadpoor, A.A. Kirigami-enabled self-folding origami. *Mater. Today* 2020, 32, 59–67. <https://doi.org/10.1016/j.mattod.2019.08.001>.
 127. Bobbert, F.; Janbaz, S.; van Manen, T.; Li, Y.; Zadpoor, A. Russian doll deployable meta-implants: Fusion of kirigami, origami, and multi-stability. *Mater. Des.* 2020, 191, 108624.
 128. Bobbert, F.; Janbaz, S.; Zadpoor, A. Towards deployable meta-implants. *J. Mater. Chem. B* 2018, 6, 3449–3455.
 129. Callens, S.J.; Tümer, N.; Zadpoor, A.A. Hyperbolic origami-inspired folding of triply periodic minimal surface structures. *Appl. Mater. Today* 2019, 15, 453–461.
 130. Cuellar, J.S.; Smit, G.; Plettenburg, D.; Zadpoor, A. Additive manufacturing of non-assembly mechanisms. *Addit. Manuf.* 2018, 21, 150–158.
 131. Leeftang, S.; Janbaz, S.; Zadpoor, A.A. Metallic clay. *Addit. Manuf.* 2019, 28, 528–534.
 132. Gepreel, M.A.-H.; Niinomi, M. Biocompatibility of Ti-alloys for long-term implantation. *J. Mech. Behav. Biomed. Mater.* 2013, 20, 407–415.
 133. Long, M.; Rack, H. Titanium alloys in total joint replacement—A materials science perspective. *Biomaterials* 1998, 19, 1621–1639.
 134. Ahmadi, S.; Hedayati, R.; Li, Y.; Lietaert, K.; Tümer, N.; Fatemi, A.; Rans, C.; Pouran, B.; Weinans, H.; Zadpoor, A. Fatigue performance of additively manufactured meta-biomaterials: The effects of topology and material type. *Acta Biomater.* 2018, 65, 292–304.

135. Davidson, J.; Mishra, A.; Kovacs, P.; Poggie, R. New surface-hardened, low-modulus, corrosion-resistant Ti-13Nb-13Zr alloy for total hip arthroplasty. *Bio-Med. Mater. Eng.* 1994, 4, 231–243.
136. Kuroda, D.; Ninomi, M.; Morinaga, M.; Kato, Y.; Yashiro, T. Design and mechanical properties of new β type titanium alloys for implant materials. *Mater. Sci. Eng. A* 1998, 243, 244–249.
137. Gorgin Karaji, Z.; Speirs, M.; Dadbakhsh, S.; Kruth, J.-P.; Weinans, H.; Zadpoor, A.; Amin Yavari, S. Additively manufactured and surface biofunctionalized porous nitinol. *ACS Appl. Mater. Interfaces* 2017, 9, 1293–1304.
138. van Hengel, I.; Tierolf, M.; Valerio, V.; Minneboo, M.; Fluit, A.; Fratila-Apachitei, L.; Apachitei, I.; Zadpoor, A. Self-defending additively manufactured bone implants bearing silver and copper nanoparticles. *J. Mater. Chem. B* 2020, 8, 1589–1602.
139. Yavari, S.A.; Croes, M.; Akhavan, B.; Jahanmard, F.; Eigenhuis, C.; Dadbakhsh, S.; Vogely, H.; Bilek, M.; Fluit, A.; Boel, C. Layer by layer coating for bio-functionalization of additively manufactured meta-biomaterials. *Addit. Manuf.* 2020, 32, 100991.
140. Zhang, G.; Zhao, P.; Lin, L.; Qin, L.; Huan, Z.; Leeftang, S.; Zadpoor, A.A.; Zhou, J.; Wu, L. Surface-treated 3D printed Ti-6Al-4V scaffolds with enhanced bone regeneration performance: An in vivo study. *Ann. Transl. Med.* 2021, 9, 39.
141. Fazel, M.; Salimijazi, H.; Shamanian, M.; Apachitei, I.; Zadpoor, A. Influence of hydrothermal treatment on the surface characteristics and electrochemical behavior of Ti-6Al-4V bio-functionalized through plasma electrolytic oxidation. *Surf. Coat. Technol.* 2019, 374, 222–231.
142. Razzi, F.; Fratila-Apachitei, L.; Fahy, N.; Bastiaansen-Jenniskens, Y.M.; Apachitei, I.; Farrell, E.; Zadpoor, A.A. Immunomodulation of surface biofunctionalized 3D printed porous titanium implants. *Biomed. Mater.* 2020, 15, 035017.
143. Van Hengel, I.; Putra, N.; Tierolf, M.; Minneboo, M.; Fluit, A.; Fratila-Apachitei, L.; Apachitei, I.; Zadpoor, A. Biofunctionalization of selective laser melted porous titanium using silver and zinc nanoparticles to prevent infections by antibiotic-resistant bacteria. *Acta Biomater.* 2020, 107, 325–337.
144. Ganjian, M.; Modaresifar, K.; Zhang, H.; Hagedoorn, P.-L.; Fratila-Apachitei, L.E.; Zadpoor, A.A. Reactive ion etching for fabrication of biofunctional titanium nanostructures. *Sci. Rep.* 2019, 9, 18815.
145. Putra, N.; Leeftang, M.; Minneboo, M.; Taheri, P.; Fratila-Apachitei, L.; Mol, J.; Zhou, J.; Zadpoor, A. Extrusion-based 3D printed biodegradable porous iron. *Acta Biomater.* 2021, 121, 741–756.
146. Hermawan, H. Biodegradable metals: State of the art. In *Biodegradable Metals*; Springer: Berlin/Heidelberg, Germany, 2012; pp. 13–22.
147. Li, Y.; Jahr, H.; Lietaert, K.; Pavanram, P.; Yilmaz, A.; Fockaert, L.; Leeftang, M.; Pourn, B.; Gonzalez-Garcia, Y.; Weinans, H. Additively manufactured biodegradable porous iron. *Acta Biomater.* 2018, 77, 380–393.
148. Li, Y.; Zhou, J.; Pavanram, P.; Leeftang, M.; Fockaert, L.; Pourn, B.; Tümer, N.; Schröder, K.-U.; Mol, J.; Weinans, H. Additively manufactured biodegradable porous magnesium. *Acta Biomater.* 2018, 67, 378–392.
149. Erbel, R.; Di Mario, C.; Bartunek, J.; Bonnier, J.; de Bruyne, B.; Eberli, F.R.; Erne, P.; Haude, M.; Heublein, B.; Horrigan, M. Temporary scaffolding of coronary arteries with bioabsorbable magnesium stents: A prospective, non-randomised multicentre trial. *Lancet* 2007, 369, 1869–1875.
150. Windhagen, H.; Radtke, K.; Weizbauer, A.; Diekmann, J.; Noll, Y.; Kreimeyer, U.; Schavan, R.; Stukenborg-Colsman, C.; Waizy, H. Biodegradable magnesium-based screw clinically equivalent to titanium screw in hallux valgus surgery: Short term results of the first prospective, randomized, controlled clinical pilot study. *Biomed. Eng. Online* 2013, 12, 62.
151. Sato, A.; Kubo, H.; Tadakatsu, M. Mechanical properties of Fe–Mn–Si based SMA and the application. *Mater. Trans.* 2006, 47, 571–579.
152. Sawaguchi, T.; Maruyama, T.; Otsuka, H.; Kushibe, A.; Inoue, Y.; Tsuzaki, K. Design concept and applications of Fe-Mn-Si-based alloys—from shape-memory to seismic response control. *Mater. Trans.* 2016, 57, 283–293. <https://doi.org/10.2320/matertrans.MB201510>.
153. Wen, P.; Jauer, L.; Voshage, M.; Chen, Y.; Poprawe, R.; Schleifenbaum, J.H. Densification behavior of pure Zn metal parts produced by selective laser melting for manufacturing biodegradable implants.

Design principles

- J. Mater. Processing Technol. 2018, 258, 128–137.
154. Hou, Y.; Jia, G.; Yue, R.; Chen, C.; Pei, J.; Zhang, H.; Huang, H.; Xiong, M.; Yuan, G. Synthesis of biodegradable Zn-based scaffolds using NaCl templates: Relationship between porosity, compressive properties and degradation behavior. *Mater. Charact.* 2018, 137, 162–169.
 155. Li, H.; Zheng, Y.; Qin, L. Progress of biodegradable metals. *Prog. Nat. Sci. Mater. Int.* 2014, 24, 414–422.
 156. Zheng, Y.; Gu, X.; Witte, F. Biodegradable metals. *Mater. Sci. Eng. R Rep.* 2014, 77, 1–34.
 157. Yuan, L.; Ding, S.; Wen, C. Additive manufacturing technology for porous metal implant applications and triple minimal surface structures: A review. *Bioact. Mater.* 2019, 4, 56–70.
 158. Li, Y.; Jahr, H.; Zhang, X.; Leeftang, M.; Li, W.; Pouran, B.; Tichelaar, F.; Weinans, H.; Zhou, J.; Zadpoor, A. Biodegradation-affected fatigue behavior of additively manufactured porous magnesium. *Addit. Manuf.* 2019, 28, 299–311.
 159. Li, Y.; Lietaert, K.; Li, W.; Zhang, X.; Leeftang, M.; Zhou, J.; Zadpoor, A. Corrosion fatigue behavior of additively manufactured biodegradable porous iron. *Corros. Sci.* 2019, 156, 106–116.
 160. Li, Y.; Li, W.; Bobbert, F.; Lietaert, K.; Dong, J.; Leeftang, M.; Zhou, J.; Zadpoor, A. Corrosion fatigue behavior of additively manufactured biodegradable porous zinc. *Acta Biomater.* 2020, 106, 439–449.
 161. Shalomeev, V.; Tabunshchyk, G.; Greshta, V.; Korniejenko, K.; Duarte Guigou, M.; Parzych, S. Casting welding from magnesium alloy using filler materials that contain scandium. *Materials* 2022, 15, 4213. <https://doi.org/10.3390/ma15124213>.
 162. Putra, N.; Mirzaali, M.; Apachitei, I.; Zhou, J.; Zadpoor, A. Multi-material additive manufacturing technologies for Ti-, Mg-, and Fe-based biomaterials for bone substitution. *Acta Biomater.* 2020, 109, 1–20.
 163. Li, Y.; Jahr, H.; Pavanram, P.; Bobbert, F.; Puggi, U.; Zhang, X.-Y.; Pouran, B.; Leeftang, M.; Weinans, H.; Zhou, J. Additively manufactured functionally graded biodegradable porous iron. *Acta Biomater.* 2019, 96, 646–661.
 164. Li, Y.; Pavanram, P.; Zhou, J.; Lietaert, K.; Bobbert, F.; Kubo, Y.; Leeftang, M.; Jahr, H.; Zadpoor, A. Additively manufactured functionally graded biodegradable porous zinc. *Biomater. Sci.* 2020, 8, 2404–2419.
 165. Andani, M.T.; Moghaddam, N.S.; Haberland, C.; Dean, D.; Miller, M.J.; Elahinia, M. Metals for bone implants. Part 1. Powder metallurgy and implant rendering. *Acta Biomater.* 2014, 10, 4058–4070.
 166. Buehler, W.J.; Gilfrich, J.; Wiley, R. Effect of low-temperature phase changes on the mechanical properties of alloys near composition TiNi. *J. Appl. Phys.* 1963, 34, 1475–1477.
 167. Elahinia, M.H.; Hashemi, M.; Tabesh, M.; Bhaduri, S.B. Manufacturing and processing of NiTi implants: A review. *Prog. Mater. Sci.* 2012, 57, 911–946.
 168. Haberland, C.; Elahinia, M.; Walker, J.M.; Meier, H.; Frenzel, J. On the development of high quality NiTi shape memory and pseudoelastic parts by additive manufacturing. *Smart Mater. Struct.* 2014, 23, 104002.
 169. Morgan, N. Medical shape memory alloy applications—The market and its products. *Mater. Sci. Eng. A* 2004, 378, 16–23.
 170. Mitchell, A.; Lafont, U.; Hołyńska, M.; Semprimoschnig, C. Additive manufacturing—A review of 4D printing and future applications. *Addit. Manuf.* 2018, 24, 606–626.
 171. Biesiekierski, A.; Wang, J.; Gepreel, M.A.-H.; Wen, C. A new look at biomedical Ti-based shape memory alloys. *Acta Biomater.* 2012, 8, 1661–1669.
 172. Köster, R.; Vieluf, D.; Kiehn, M.; Sommerauer, M.; Kähler, J.; Baldus, S.; Meinertz, T.; Hamm, C.W. Nickel and molybdenum contact allergies in patients with coronary in-stent restenosis. *Lancet* 2000, 356, 1895–1897.
 173. Obbard, E.; Hao, Y.; Akahori, T.; Talling, R.; Niinomi, M.; Dye, D.; Yang, R. Mechanics of superelasticity in Ti–30Nb–(8–10) Ta–5Zr alloy. *Acta Mater.* 2010, 58, 3557–3567.
 174. Miyazaki, S.; Kim, H.Y.; Hosoda, H. Development and characterization of Ni-free Ti-base shape memory and superelastic alloys. *Mater. Sci. Eng. A* 2006, 438, 18–24.
 175. Gladman, A.S.; Matsumoto, E.A.; Nuzzo, R.G.; Mahadevan, L.; Lewis, J.A. Biomimetic 4D printing.

- Nat. Mater. 2016, 15, 413–418.
176. van Manen, T.; Janbaz, S.; Zadpoor, A.A. Programming 2D/3D shape-shifting with hobbyist 3D printers. *Mater. Horiz.* 2017, 4, 1064–1069.
 177. van Manen, T.; Dehabadi, V.M.; Saldívar, M.C.; Mirzaali, M.J.; Zadpoor, A.A. Theoretical stiffness limits of 4D printed self-folding metamaterials. *Commun. Mater.* 2022, 3, 43. <https://doi.org/10.1038/s43246-022-00265-z>.
 178. Tsaturyants, M.; Sheremetyev, V.; Dubinskiy, S.; Komarov, V.; Polyakova, K.; Korotitskiy, A.; Prokoshkin, S.; Borisov, E.; Starikov, K.; Kaledina, D.; et al. Structure and properties of Ti-50.2Ni alloy processed by laser powder bed fusion and subjected to a combination of thermal cycling and heat treatments. *Shape Mem. Superelasticity* 2022, 8, 16–32. <https://doi.org/10.1007/s40830-022-00363-4>.
 179. Bourell, D.; Kruth, J.P.; Leu, M.; Levy, G.; Rosen, D.; Beese, A.M.; Clare, A. Materials for additive manufacturing. *CIRP Ann.* 2017, 66, 659–681.
 180. Fischer, M.; Joguet, D.; Robin, G.; Peltier, L.; Laheurte, P. In situ elaboration of a binary Ti–26Nb alloy by selective laser melting of elemental titanium and niobium mixed powders. *Mater. Sci. Eng. C* 2016, 62, 852–859.
 181. Khorasani, M.; Ghasemi, A.; Leary, M.; Sharabian, E.; Cordova, L.; Gibson, I.; Downing, D.; Bateman, S.; Brandt, M.; Rolfe, B. The effect of absorption ratio on meltpool features in laser-based powder bed fusion of IN718. *Opt. Laser Technol.* 2022, 153, 108263. <https://doi.org/10.1016/j.optlastec.2022.108263>.
 182. Attar, H.; Löber, L.; Funk, A.; Calin, M.; Zhang, L.; Prashanth, K.; Scudino, S.; Zhang, Y.; Eckert, J. Mechanical behavior of porous commercially pure Ti and Ti–TiB composite materials manufactured by selective laser melting. *Mater. Sci. Eng. A* 2015, 625, 350–356.
 183. Liang, S.-X.; Wang, X.; Zhang, W.; Liu, Y.-J.; Wang, W.; Zhang, L.-C. Selective laser melting manufactured porous Fe-based metallic glass matrix composite with remarkable catalytic activity and reusability. *Appl. Mater. Today* 2020, 19, 100543.
 184. Mirzaali, M.; Caracciolo, A.; Pahlavani, H.; Janbaz, S.; Vergani, L.; Zadpoor, A. Multi-material 3D printed mechanical metamaterials: Rational design of elastic properties through spatial distribution of hard and soft phases. *Appl. Phys. Lett.* 2018, 113, 241903.
 185. Singh, S.; Prakash, C.; Singh, R. *3D Printing in Biomedical Engineering*; Singh, S., Prakash, C., Singh, R., Eds.; Springer: Berlin/Heidelberg, Germany, 2020.
 186. Bose, S.; Ke, D.; Sahasrabudhe, H.; Bandyopadhyay, A. Additive manufacturing of biomaterials. *Prog. Mater. Sci.* 2018, 93, 45–111. <https://doi.org/10.1016/j.pmatsci.2017.08.003>.
 187. Tabata, Y. Biomaterial technology for tissue engineering applications. *J. R. Soc. Interface* 2009, 6 (Suppl. 3), S311–S324. <https://doi.org/10.1098/rsif.2008.0448.focus>.
 188. Dizon, J.R.C.; Espera Jr, A.H.; Chen, Q.; Advincula, R.C. Mechanical characterization of 3D-printed polymers. *Addit. Manuf.* 2018, 20, 44–67.
 189. Safai, L.; Cuellar, J.S.; Smit, G.; Zadpoor, A.A. A review of the fatigue behavior of 3D printed polymers. *Addit. Manuf.* 2019, 28, 87–97.
 190. Turnbull, G.; Clarke, J.; Picard, F.; Riches, P.; Jia, L.; Han, F.; Li, B.; Shu, W. 3D bioactive composite scaffolds for bone tissue engineering. *Bioact. Mater.* 2018, 3, 278–314. <https://doi.org/10.1016/j.bioactmat.2017.10.001>.
 191. Lee, K.Y.; Mooney, D.J. Alginate: Properties and biomedical applications. *Prog. Polym. Sci.* 2012, 37, 106–126. <https://doi.org/10.1016/j.progpolymsci.2011.06.003>.
 192. Di Giuseppe, M.; Law, N.; Webb, B.; Macrae, R.A.; Liew, L.J.; Sercombe, T.B.; Dilley, R.J.; Doyle, B.J. Mechanical behaviour of alginate-gelatin hydrogels for 3D bioprinting. *J. Mech. Behav. Biomed. Mater.* 2018, 79, 150–157. <https://doi.org/10.1016/j.jmbbm.2017.12.018>.
 193. Kopeček, J. Hydrogel biomaterials: A smart future? *Biomaterials* 2007, 28, 5185–5192. <https://doi.org/10.1016/j.biomaterials.2007.07.044>.
 194. Drury, J.L.; Mooney, D.J. Hydrogels for tissue engineering: Scaffold design variables and applications. *Biomaterials* 2003, 24, 4337–4351. [https://doi.org/10.1016/s0142-9612\(03\)00340-5](https://doi.org/10.1016/s0142-9612(03)00340-5).
 195. Lee, J.H.; Kim, H.W. Emerging properties of hydrogels in tissue engineering. *J. Tissue Eng.* 2018, 9, 2041731418768285. <https://doi.org/10.1177/2041731418768285>.

Design principles

196. Green, J.J.; Elisseeff, J.H. Mimicking biological functionality with polymers for biomedical applications. *Nature* 2016, 540, 386–394. <https://doi.org/10.1038/nature21005>.
197. Hoffman, A.S. Hydrogels for biomedical applications. *Adv. Drug Deliv. Rev.* 2012, 64, 18–23. <https://doi.org/10.1016/j.addr.2012.09.010>.
198. Malda, J.; Visser, J.; Melchels, F.P.; Jungst, T.; Hennink, W.E.; Dhert, W.J.; Groll, J.; Huttmacher, D.W. 25th anniversary article: Engineering hydrogels for biofabrication. *Adv. Mater.* 2013, 25, 5011–5028. <https://doi.org/10.1002/adma.201302042>.
199. Ribeiro, A.; Blokzijl, M.M.; Levato, R.; Visser, C.W.; Castilho, M.; Hennink, W.E.; Vermonden, T.; Malda, J. Assessing bioink shape fidelity to aid material development in 3D bioprinting. *Biofabrication* 2017, 10, 014102. <https://doi.org/10.1088/1758-5090/aa90e2>.
200. Jungst, T.; Smolan, W.; Schacht, K.; Scheibel, T.; Groll, J. Strategies and Molecular Design Criteria for 3D Printable Hydrogels. *Chem. Rev.* 2016, 116, 1496–1539. <https://doi.org/10.1021/acs.chemrev.5b00303>.
201. Moxon, S.R.; Cooke, M.E.; Cox, S.C.; Snow, M.; Jeys, L.; Jones, S.W.; Smith, A.M.; Grover, L.M. Suspended Manufacture of Biological Structures. *Adv. Mater.* 2017, 29, 1605594. <https://doi.org/10.1002/adma.201605594>.
202. Li, H.; Liu, S.; Lin, L. Rheological study on 3D printability of alginate hydrogel and effect of graphene oxide. *Int. J. Bioprinting* 2016, 2, 80.
203. Chen, Z.; Zhao, D.; Liu, B.; Nian, G.; Li, X.; Yin, J.; Qu, S.; Yang, W. 3D Printing of Multifunctional Hydrogels. *Adv. Funct. Mater.* 2019, 29, 1900971. <https://doi.org/10.1002/adfm.201900971>.
204. Yan, C.; Pochan, D.J. Rheological properties of peptide-based hydrogels for biomedical and other applications. *Chem. Soc. Rev.* 2010, 39, 3528–3540.
205. Van Den Bulcke, A.I.; Bogdanov, B.; De Rooze, N.; Schacht, E.H.; Cornelissen, M.; Berghmans, H. Structural and rheological properties of methacrylamide modified gelatin hydrogels. *Biomacromolecules* 2000, 1, 31–38.
206. Jastram, A.; Claus, J.; Janmey, P.A.; Kragl, U. Rheological properties of hydrogels based on ionic liquids. *Polym. Test.* 2021, 93, 106943. <https://doi.org/10.1016/j.polymertesting.2020.106943>.
207. Zhao, W.; Jin, X.; Cong, Y.; Liu, Y.; Fu, J. Degradable natural polymer hydrogels for articular cartilage tissue engineering. *J. Chem. Technol. Biotechnol.* 2013, 88, 327–339. <https://doi.org/10.1002/jctb.3970>.
208. Derakhshanfar, S.; Mbeleck, R.; Xu, K.; Zhang, X.; Zhong, W.; Xing, M. 3D bioprinting for biomedical devices and tissue engineering: A review of recent trends and advances. *Bioact Mater* 2018, 3, 144–156. <https://doi.org/10.1016/j.bioactmat.2017.11.008>.
209. Ahmed, E.M. Hydrogel: Preparation, characterization, and applications: A review. *J. Adv. Res.* 2015, 6, 105–121. <https://doi.org/10.1016/j.jare.2013.07.006>.
210. Vedadghavami, A.; Minooei, F.; Mohammadi, M.H.; Khetani, S.; Rezaei Kolahchi, A.; Mashayekhan, S.; Sanati-Nezhad, A. Manufacturing of hydrogel biomaterials with controlled mechanical properties for tissue engineering applications. *Acta Biomater.* 2017, 62, 42–63. <https://doi.org/10.1016/j.actbio.2017.07.028>.
211. Iizawa, T.; Taketa, H.; Maruta, M.; Ishido, T.; Gotoh, T.; Sakohara, S. Synthesis of porous poly(N-isopropylacrylamide) gel beads by sedimentation polymerization and their morphology. *J. Appl. Polym. Sci.* 2007, 104, 842–850. <https://doi.org/10.1002/app.25605>.
212. Yang, L.; Chu, J.S.; Fix, J.A. Colon-specific drug delivery: New approaches and in vitro/in vivo evaluation. *Int. J. Pharm.* 2002, 235, 1–15. [https://doi.org/10.1016/S0378-5173\(02\)00004-2](https://doi.org/10.1016/S0378-5173(02)00004-2).
213. Maolin, Z.; Jun, L.; Min, Y.; Hongfei, H. The swelling behavior of radiation prepared semi-interpenetrating polymer networks composed of polyNIPAAm and hydrophilic polymers. *Radiat. Phys. Chem.* 2000, 58, 397–400. [https://doi.org/10.1016/S0969-806X\(99\)00491-0](https://doi.org/10.1016/S0969-806X(99)00491-0).
214. Hacker, M.C.; Mikos, A.G. Synthetic Polymers. In *Principles of Regenerative Medicine*; Academic Press: Cambridge, MA, USA, 2011; pp. 587–622. <https://doi.org/10.1016/b978-0-12-381422-7.10033-1>.
215. Ahangar, P.; Cooke, M.E.; Weber, M.H.; Rosenzweig, D.H. Current Biomedical Applications of 3D Printing and Additive Manufacturing. *Appl. Sci.* 2019, 9, 1713. <https://doi.org/10.3390/app9081713>.
216. Gupta, S.; Bissoyi, A.; Bit, A. A review on 3D printable techniques for tissue engineering.

- BioNanoScience 2018, 8, 868–883. <https://doi.org/10.1007/s12668-018-0525-4>.
217. Zhu, J. Bioactive modification of poly(ethylene glycol) hydrogels for tissue engineering. *Biomaterials* 2010, 31, 4639–4656. <https://doi.org/10.1016/j.biomaterials.2010.02.044>.
 218. Brandl, F.; Sommer, F.; Goepferich, A. Rational design of hydrogels for tissue engineering: Impact of physical factors on cell behavior. *Biomaterials* 2007, 28, 134–146. <https://doi.org/10.1016/j.biomaterials.2006.09.017>.
 219. Zhu, J.; Marchant, R.E. Design properties of hydrogel tissue-engineering scaffolds. *Expert Rev. Med. Devices* 2011, 8, 607–626. <https://doi.org/10.1586/erd.11.27>.
 220. Liang, Y.; Liu, W.; Han, B.; Yang, C.; Ma, Q.; Song, F.; Bi, Q. An in situ formed biodegradable hydrogel for reconstruction of the corneal endothelium. *Colloids Surf. B Biointerfaces* 2011, 82, 1–7. <https://doi.org/10.1016/j.colsurf.2010.07.043>.
 221. Kim, I.Y.; Seo, S.J.; Moon, H.S.; Yoo, M.K.; Park, I.Y.; Kim, B.C.; Cho, C.S. Chitosan and its derivatives for tissue engineering applications. *Biotechnol. Adv.* 2008, 26, 1–21. <https://doi.org/10.1016/j.biotechadv.2007.07.009>.
 222. Rosellini, E.; Cristallini, C.; Barbani, N.; Vozzi, G.; Giusti, P. Preparation and characterization of alginate/gelatin blend films for cardiac tissue engineering. *J. Biomed. Mater. Res. A* 2009, 91, 447–453. <https://doi.org/10.1002/jbm.a.32216>.
 223. Xing, Y.; Cheng, E.; Yang, Y.; Chen, P.; Zhang, T.; Sun, Y.; Yang, Z.; Liu, D. Self-assembled DNA hydrogels with designable thermal and enzymatic responsiveness. *Adv. Mater.* 2011, 23, 1117–1121. <https://doi.org/10.1002/adma.201003343>.
 224. Catoira, M.C.; Fusaro, L.; Di Francesco, D.; Ramella, M.; Boccafoschi, F. Overview of natural hydrogels for regenerative medicine applications. *J. Mater. Sci. Mater. Med.* 2019, 30, 115. <https://doi.org/10.1007/s10856-019-6318-7>.
 225. Gyles, D.A.; Castro, L.D.; Silva, J.O.C.; Ribeiro-Costa, R.M. A review of the designs and prominent biomedical advances of natural and synthetic hydrogel formulations. *Eur. Polym. J.* 2017, 88, 373–392. <https://doi.org/10.1016/j.eurpolymj.2017.01.027>.
 226. Li, L.; Yu, F.; Zheng, L.; Wang, R.; Yan, W.; Wang, Z.; Xu, J.; Wu, J.; Shi, D.; Zhu, L.; et al. Natural hydrogels for cartilage regeneration: Modification, preparation and application. *J. Orthop. Transl.* 2019, 17, 26–41. <https://doi.org/10.1016/j.jot.2018.09.003>.
 227. Miao, Z.; Lu, Z.; Wu, H.; Liu, H.; Li, M.; Lei, D.; Zheng, L.; Zhao, J. Collagen, agarose, alginate, and Matrigel hydrogels as cell substrates for culture of chondrocytes in vitro: A comparative study. *J. Cell. Biochem.* 2018, 119, 7924–7933. <https://doi.org/10.1002/jcb.26411>.
 228. Ngo, T.D.; Kashani, A.; Imbalzano, G.; Nguyen, K.T.Q.; Hui, D. Additive manufacturing (3D printing): A review of materials, methods, applications and challenges. *Compos. Part B Eng.* 2018, 143, 172–196. <https://doi.org/10.1016/j.compositesb.2018.02.012>.
 229. Kim, G.; Ahn, S.; Yoon, H.; Kim, Y.; Chun, W. A cryogenic direct-plotting system for fabrication of 3D collagen scaffolds for tissue engineering. *J. Mater. Chem.* 2009, 19, 8817–8823. <https://doi.org/10.1039/b914187a>.
 230. Lee, Y.B.; Polio, S.; Lee, W.; Dai, G.; Menon, L.; Carroll, R.S.; Yoo, S.S. Bio-printing of collagen and VEGF-releasing fibrin gel scaffolds for neural stem cell culture. *Exp. Neurol.* 2010, 223, 645–652. <https://doi.org/10.1016/j.expneurol.2010.02.014>.
 231. Asadi, N.; Del Bakhshayesh, A.R.; Davaran, S.; Akbarzadeh, A. Common biocompatible polymeric materials for tissue engineering and regenerative medicine. *Mater. Chem. Phys.* 2020, 242, 122528. <https://doi.org/10.1016/j.matchemphys.2019.122528>.
 232. Mimura, T.; Imai, S.; Okumura, N.; Li, L.; Nishizawa, K.; Araki, S.; Ueba, H.; Kubo, M.; Mori, K.; Matusue, Y. Spatiotemporal control of proliferation and differentiation of bone marrow-derived mesenchymal stem cells recruited using collagen hydrogel for repair of articular cartilage defects. *J. Biomed. Mater. Res. B Appl. Biomater.* 2011, 98, 360–368. <https://doi.org/10.1002/jbm.b.31859>.
 233. Chen, G.; Sato, T.; Ushida, T.; Ochiai, N.; Tateishi, T. Tissue engineering of cartilage using a hybrid scaffold of synthetic polymer and collagen. *Tissue Eng.* 2004, 10, 323–330. <https://doi.org/10.1089/107632704323061681>.
 234. Suesca, E.; Dias, A.M.A.; Braga, M.E.M.; de Sousa, H.C.; Fontanilla, M.R. Multifactor analysis on the effect of collagen concentration, cross-linking and fiber/pore orientation on chemical,

Design principles

- microstructural, mechanical and biological properties of collagen type I scaffolds. *Mater. Sci. Eng. C Mater. Biol. Appl.* 2017, 77, 333–341. <https://doi.org/10.1016/j.msec.2017.03.243>.
235. Rahmani Del Bakhshayesh, A.; Mostafavi, E.; Alizadeh, E.; Asadi, N.; Akbarzadeh, A.; Davaran, S. Fabrication of three-dimensional scaffolds based on nano-biomimetic collagen hybrid constructs for skin tissue engineering. *ACS Omega* 2018, 3, 8605–8611. <https://doi.org/10.1021/acsomega.8b01219>.
236. Tampieri, A.; Iafisco, M.; Sandri, M.; Panseri, S.; Cunha, C.; Sprio, S.; Savini, E.; Uhlarz, M.; Herrmannsdorfer, T. Magnetic bioinspired hybrid nanostructured collagen-hydroxyapatite scaffolds supporting cell proliferation and tuning regenerative process. *ACS Appl. Mater. Interfaces* 2014, 6, 15697–15707. <https://doi.org/10.1021/am5050967>.
237. Huang, S.; Fu, X. Naturally derived materials-based cell and drug delivery systems in skin regeneration. *J. Control. Release* 2010, 142, 149–159. <https://doi.org/10.1016/j.jconrel.2009.10.018>.
238. Silva, S.S.; Mano, J.F.; Reis, R.L. Potential applications of natural origin polymer-based systems in soft tissue regeneration. *Crit. Rev. Biotechnol.* 2010, 30, 200–221. <https://doi.org/10.3109/07388551.2010.505561>.
239. Djagny, V.B.; Wang, Z.; Xu, S. Gelatin: A valuable protein for food and pharmaceutical industries: Review. *Crit. Rev. Food Sci. Nutr.* 2001, 41, 481–492. <https://doi.org/10.1080/20014091091904>.
240. Aday, S.; Hasirci, N.; Deliloglu Gurhan, I. A cost-effective and simple culture method for primary hepatocytes. *Anim. Cells Syst.* 2011, 15, 19–27. <https://doi.org/10.1080/19768354.2011.555140>.
241. Wang, X.; Yan, Y.; Pan, Y.; XIONG, Z.; LIU, H.; CHENG, J.; LIU, F.; LIN, F.; WU, R.; ZHANG, R.; et al. Generation of Three-Dimensional Hepatocyte/Gelatin Structures with Rapid Prototyping System. *Tissue Eng.* 2006, 12, 83–90. <https://doi.org/10.1089/ten.2006.12.83>.
242. Klotz, B.J.; Gawlitta, D.; Rosenberg, A.; Malda, J.; Melchels, F.P.W. Gelatin-methacryloyl hydrogels: Towards biofabrication-based tissue repair. *Trends Biotechnol.* 2016, 34, 394–407. <https://doi.org/10.1016/j.tibtech.2016.01.002>.
243. Pepelanova, I.; Kruppa, K.; Scheper, T.; Lavrentieva, A. Gelatin-Methacryloyl (GelMA) Hydrogels with defined degree of functionalization as a versatile toolkit for 3D cell culture and extrusion bioprinting. *Bioengineering* 2018, 5, 55. <https://doi.org/10.3390/bioengineering5030055>.
244. Levett, P.A.; Melchels, F.P.; Schrobback, K.; Huttmacher, D.W.; Malda, J.; Klein, T.J. A biomimetic extracellular matrix for cartilage tissue engineering centered on photocurable gelatin, hyaluronic acid and chondroitin sulfate. *Acta Biomater.* 2014, 10, 214–223. <https://doi.org/10.1016/j.actbio.2013.10.005>.
245. Cooke, M.E.; Pearson, M.J.; Moakes, R.J.A.; Weston, C.J.; Davis, E.T.; Jones, S.W.; Grover, L.M. Geometric confinement is required for recovery and maintenance of chondrocyte phenotype in alginate. *APL Bioeng* 2017, 1, 016104. <https://doi.org/10.1063/1.5006752>.
246. Venkatesan, J.; Bhatnagar, I.; Manivasagan, P.; Kang, K.-H.; Kim, S.-K. Alginate composites for bone tissue engineering: A review. *Int. J. Biol. Macromol.* 2015, 72, 269–281. <https://doi.org/10.1016/j.ijbiomac.2014.07.008>.
247. George, M.; Abraham, T.E. Polyionic hydrocolloids for the intestinal delivery of protein drugs: Alginate and chitosan—A review. *J. Control. Release* 2006, 114, 1–14. <https://doi.org/10.1016/j.jconrel.2006.04.017>.
248. Kumar, A.; Lee, Y.; Kim, D.; Rao, K.M.; Kim, J.; Park, S.; Haider, A.; Lee, D.H.; Han, S.S. Effect of crosslinking functionality on microstructure, mechanical properties, and in vitro cytocompatibility of cellulose nanocrystals reinforced poly (vinyl alcohol)/sodium alginate hybrid scaffolds. *Int. J. Biol. Macromol.* 2017, 95, 962–973. <https://doi.org/10.1016/j.ijbiomac.2016.10.085>.
249. Augst, A.D.; Kong, H.J.; Mooney, D.J. Alginate hydrogels as biomaterials. *Macromol. Biosci.* 2006, 6, 623–633. <https://doi.org/10.1002/mabi.200600069>.
250. Ter Horst, B.; Chouhan, G.; Moiemmen, N.S.; Grover, L.M. Advances in keratinocyte delivery in burn wound care. *Adv. Drug Deliv. Rev.* 2018, 123, 18–32. <https://doi.org/10.1016/j.addr.2017.06.012>.
251. Chung, J.H.Y.; Naficy, S.; Yue, Z.; Kapsa, R.; Quigley, A.; Moulton, S.E.; Wallace, G.G. Bio-ink properties and printability for extrusion printing living cells. *Biomater. Sci.* 2013, 1, 763–773. <https://doi.org/10.1039/c3bm00012e>.
252. Duan, B.; Hockaday, L.A.; Kang, K.H.; Butcher, J.T. 3D bioprinting of heterogeneous aortic valve

- conduits with alginate/gelatin hydrogels. *J. Biomed. Mater. Res. A* 2013, 101, 1255–1264. <https://doi.org/10.1002/jbm.a.34420>.
253. Ferris, C.J.; Gilmore, K.J.; Beirne, S.; McCallum, D.; Wallace, G.G.; In Het Panhuis, M. Bio-ink for on-demand printing of living cells. *Biomater. Sci.* 2013, 1, 224–230. <https://doi.org/10.1039/c2bm00114d>.
 254. Skardal, A.; Atala, A. Biomaterials for integration with 3-D bioprinting. *Ann. Biomed. Eng.* 2015, 43, 730–746. <https://doi.org/10.1007/s10439-014-1207-1>.
 255. Dimitrova, M.; Corsalini, M.; Kazakova, R.; Vlahova, A.; Chuchulska, B.; Barile, G.; Capodiferro, S.; Kazakov, S. Comparison between conventional PMMA and 3D printed resins for denture bases: A narrative review. *J. Compos. Sci.* 2022, 6, 87. <https://doi.org/10.3390/jcs6030087>.
 256. Frazer, R.Q.; Byron Rt Fau–Osborne, P.B.; Osborne Pb Fau–West, K.P.; West, K.P. PMMA: An essential material in medicine and dentistry. *Natl. Cent. Biotechnol. Infomation* 2005, 15, 629–639. <https://doi.org/10.1615/JLongTermEffMedImplants.v15.i6.60>.
 257. Polzin, C.; Spath, S.; Seitz, H. Characterization and evaluation of a PMMA-based 3D printing process. *Rapid Prototyp. J.* 2013, 19, 37–43. <https://doi.org/10.1108/13552541311292718>.
 258. Liu, S.Q.; Tay, R.; Khan, M.; Rachel Ee, P.L.; Hedrick, J.L.; Yang, Y.Y. Synthetic hydrogels for controlled stem cell differentiation. *Soft Matter* 2010, 6, 67–81. <https://doi.org/10.1039/B916705F>.
 259. Hern, D.L.; Hubbell, J.A. Incorporation of adhesion peptides into nonadhesive hydrogels useful for tissue resurfacing. *J. Biomed. Mater. Res.* 1998, 39, 266–276. [https://doi.org/10.1002/\(sici\)1097-4636\(199802\)39:2<266::aid-jbm14>3.0.co;2-b](https://doi.org/10.1002/(sici)1097-4636(199802)39:2<266::aid-jbm14>3.0.co;2-b).
 260. Shin, H.; Jo, S.; Mikos, A.G. Biomimetic materials for tissue engineering. *Biomaterials* 2003, 24, 4353–4364. [https://doi.org/10.1016/s0142-9612\(03\)00339-9](https://doi.org/10.1016/s0142-9612(03)00339-9).
 261. Tan, H.; Marra, K.G. Injectable, biodegradable hydrogels for tissue engineering applications. *Materials* 2010, 3, 1746–1767. <https://doi.org/10.3390/ma3031746>.
 262. Buxton, A.N.; Zhu, J.; Marchant, R.; West, J.L.; Yoo, J.U.; Johnstone, B. Design and characterization of poly(ethylene glycol) photopolymerizable semi-interpenetrating networks for chondrogenesis of human mesenchymal stem cells. *Tissue Eng.* 2007, 13, 2549–2560. <https://doi.org/10.1089/ten.2007.0075>.
 263. Nguyen, K.T.; West, J.L. Photopolymerizable hydrogels for tissue engineering applications. *Biomaterials* 2002, 23, 4307–4314. [https://doi.org/10.1016/s0142-9612\(02\)00175-8](https://doi.org/10.1016/s0142-9612(02)00175-8).
 264. Lin, C.-C.; Metters, A.T. Hydrogels in controlled release formulations: Network design and mathematical modeling. *Adv. Drug Deliv. Rev.* 2006, 58, 1379–1408. <https://doi.org/10.1016/j.addr.2006.09.004>.
 265. Hoffman, A.S. Hydrogels for biomedical applications. *Adv. Drug Deliv. Rev.* 2002, 54, 3–12. [https://doi.org/10.1016/S0169-409X\(01\)00239-3](https://doi.org/10.1016/S0169-409X(01)00239-3).
 266. Schneider, G.B.; English, A.; Abraham, M.; Zaharias, R.; Stanford, C.; Keller, J. The effect of hydrogel charge density on cell attachment. *Biomaterials* 2004, 25, 3023–3028. <https://doi.org/10.1016/j.biomaterials.2003.09.084>.
 267. Hejčl, A.; Šedý, J.; Kapcalová, M.; Toro, D.A.; Amemori, T.; Lesný, P.; Likavčanová-Mašínová, K.; Krumbholcová, E.; Prádný, M.; Michálek, J. HPMA-RGD hydrogels seeded with mesenchymal stem cells improve functional outcome in chronic spinal cord injury. *Stem Cells Dev.* 2010, 19, 1535–1546.
 268. Beamish, J.A.; Zhu, J.; Kottke-Marchant, K.; Marchant, R.E. The effects of monoacrylated poly(ethylene glycol) on the properties of poly(ethylene glycol) diacrylate hydrogels used for tissue engineering. *J. Biomed. Mater. Res. A* 2010, 92, 441–450. <https://doi.org/10.1002/jbm.a.32353>.
 269. Higuchi, A.; Aoki, N.; Yamamoto, T.; Miyazaki, T.; Fukushima, H.; Tak, T.M.; Jyujyoji, S.; Egashira, S.; Matsuoka, Y.; Natori, S.H. Temperature-induced cell detachment on immobilized pluronic surface. *J. Biomed. Mater. Res. A* 2006, 79, 380–392. <https://doi.org/10.1002/jbm.a.30773>.
 270. Schmedlen, R.H.; Masters, K.S.; West, J.L. Photocrosslinkable polyvinyl alcohol hydrogels that can be modified with cell adhesion peptides for use in tissue engineering. *Biomaterials* 2002, 23, 4325–4332. [https://doi.org/10.1016/S0142-9612\(02\)00177-1](https://doi.org/10.1016/S0142-9612(02)00177-1).
 271. Ossipov, D.A.; Brännvall, K.; Forsberg-Nilsson, K.; Hilborn, J. Formation of the first injectable poly(vinyl alcohol) hydrogel by mixing of functional PVA precursors. *J. Appl. Polym. Sci.* 2007, 106, 60–70. <https://doi.org/10.1002/app.26455>.

Design principles

272. Lutolf, M.P. Biomaterials: Spotlight on hydrogels. *Nat. Mater.* 2009, 8, 451–453. <https://doi.org/10.1038/nmat2458>.
273. Lee, J.; Cuddihy, M.J.; Kotov, N.A. Three-dimensional cell culture matrices: State of the art. *Tissue Eng. Part B Rev.* 2008, 14, 61–86. <https://doi.org/10.1089/teb.2007.0150>.
274. Geckil, H.; Xu, F.; Zhang, X.; Moon, S.; Demirci, U. Engineering hydrogels as extracellular matrix mimics. *Nanomedicine* 2010, 5, 469–484. <https://doi.org/10.2217/nmm.10.12>.
275. Varghese, S.; Elisseeff, J.H. Hydrogels for musculoskeletal tissue engineering. In *Polymers for Regenerative Medicine*, Springer: Berlin/Heidelberg, Germany, 2006; pp. 95–144.
276. Sawhney, A.S.; Pathak, C.P.; Hubbell, J.A. Bioerodible hydrogels based on photopolymerized poly(ethylene glycol)-co-poly(alpha.-hydroxy acid) diacrylate macromers. *Macromolecules* 1993, 26, 581–587. <https://doi.org/10.1021/ma00056a005>.
277. Jiang, Z.; Hao, J.; You, Y.; Liu, Y.; Wang, Z.; Deng, X. Biodegradable and thermoreversible hydrogels of poly(ethylene glycol)-poly(epsilon-caprolactone-co-glycolide)-poly(ethylene glycol) aqueous solutions. *J. Biomed. Mater. Res. A* 2008, 87, 45–51. <https://doi.org/10.1002/jbm.a.31699>.
278. Clapper, J.D.; Skeie, J.M.; Mullins, R.F.; Guymon, C.A. Development and characterization of photopolymerizable biodegradable materials from PEG–PLA–PEG block macromonomers. *Polymer* 2007, 48, 6554–6564. <https://doi.org/10.1016/j.polymer.2007.08.023>.
279. Sanabria-DeLong, N.; Agrawal, S.K.; Bhatia, S.R.; Tew, G.N. Impact of Synthetic Technique on PLA–PEO–PLA Physical Hydrogel Properties. *Macromolecules* 2007, 40, 7864–7873. <https://doi.org/10.1021/ma071243f>.
280. Hudalla, G.A.; Eng, T.S.; Murphy, W.L. An approach to modulate degradation and mesenchymal stem cell behavior in poly(ethylene glycol) networks. *Biomacromolecules* 2008, 9, 842–849. <https://doi.org/10.1021/bm701179s>.
281. Rydholm, A.E.; Anseth, K.S.; Bowman, C.N. Effects of neighboring sulfides and pH on ester hydrolysis in thiol-acrylate photopolymers. *Acta Biomater.* 2007, 3, 449–455. <https://doi.org/10.1016/j.actbio.2006.12.001>.
282. Zhang, J.; Skardal, A.; Prestwich, G.D. Engineered extracellular matrices with cleavable crosslinkers for cell expansion and easy cell recovery. *Biomaterials* 2008, 29, 4521–4531. <https://doi.org/10.1016/j.biomaterials.2008.08.008>.
283. Deshmukh, M.; Singh, Y.; Gunaseelan, S.; Gao, D.; Stein, S.; Sinko, P.J. Biodegradable poly(ethylene glycol) hydrogels based on a self-elimination degradation mechanism. *Biomaterials* 2010, 31, 6675–6684. <https://doi.org/10.1016/j.biomaterials.2010.05.021>.
284. Zustiak, S.P.; Leach, J.B. Hydrolytically degradable poly(ethylene glycol) hydrogel scaffolds with tunable degradation and mechanical properties. *Biomacromolecules* 2010, 11, 1348–1357. <https://doi.org/10.1021/bm100137q>.
285. Li, Q.; Wang, J.; Shahani, S.; Sun, D.D.; Sharma, B.; Elisseeff, J.H.; Leong, K.W. Biodegradable and photocrosslinkable polyphosphoester hydrogel. *Biomaterials* 2006, 27, 1027–1034. <https://doi.org/10.1016/j.biomaterials.2005.07.019>.
286. Kaihara, S.; Matsumura, S.; Fisher, J.P. Synthesis and characterization of cyclic acetal based degradable hydrogels. *Eur. J. Pharm. Biopharm.* 2008, 68, 67–73. <https://doi.org/10.1016/j.ejpb.2007.05.019>.
287. Malkoch, M.; Vestberg, R.; Gupta, N.; Mespouille, L.; Dubois, P.; Mason, A.F.; Hedrick, J.L.; Liao, Q.; Frank, C.W.; Kingsbury, K.; et al. Synthesis of well-defined hydrogel networks using click chemistry. *Chem. Commun.* 2006, 26, 2774–2776. <https://doi.org/10.1039/b603438a>.
288. Chung, H.J.; Park, T.G. Self-assembled and nanostructured hydrogels for drug delivery and tissue engineering. *Nano Today* 2009, 4, 429–437. <https://doi.org/10.1016/j.nantod.2009.08.008>.
289. Deiber, J.A.; Ottone, M.L.; Piaggio, M.V.; Peirotti, M.B. Characterization of cross-linked polyampholytic gelatin hydrogels through the rubber elasticity and thermodynamic swelling theories. *Polymer* 2009, 50, 6065–6075. <https://doi.org/10.1016/j.polymer.2009.10.046>.
290. Freudenberg, U.; Hermann, A.; Welzel, P.B.; Stirl, K.; Schwarz, S.C.; Grimmer, M.; Zieris, A.; Panyanuwat, W.; Zschoche, S.; Meinhold, D. A star-PEG–heparin hydrogel platform to aid cell replacement therapies for neurodegenerative diseases. *Biomaterials* 2009, 30, 5049–5060.
291. Kopesky, P.W.; Vanderploeg, E.J.; Sandy, J.S.; Kurz, B.; Grodzinsky, A.J. Self-assembling peptide

- hydrogels modulate in vitro chondrogenesis of bovine bone marrow stromal cells. *Tissue Eng. Part A* 2010, 16, 465–477. <https://doi.org/10.1089/ten.TEA.2009.0158>.
292. Anderson, J.M.; Andukuri, A.; Lim, D.J.; Jun, H.-W. Modulating the gelation properties of self-assembling peptide amphiphiles. *ACS Nano* 2009, 3, 3447–3454. <https://doi.org/10.1021/nn900884n>.
 293. Auras, R.; Harte, B.; Selke, S. An overview of polylactides as packaging materials. *Macromol. Biosci.* 2004, 4, 835–864. <https://doi.org/10.1002/mabi.200400043>.
 294. Ulery, B.D.; Nair, L.S.; Laurencin, C.T. Biomedical Applications of Biodegradable Polymers. *J. Polym. Sci. B Polym. Phys.* 2011, 49, 832–864. <https://doi.org/10.1002/polb.22259>.
 295. Soares, J.S.; Moore, J.E.; Rajagopal, K.R. Constitutive framework for biodegradable polymers with applications to biodegradable stents. *ASAIO J.* 2008, 54, 295–301. <https://doi.org/10.1097/MAT.0b013e31816ba55a>.
 296. Wiebe, J.; Nef, H.M.; Hamm, C.W. Current Status of Bioresorbable Scaffolds in the Treatment of Coronary Artery Disease. *J. Am. Coll. Cardiol.* 2014, 64, 2541–2551. <https://doi.org/10.1016/j.jacc.2014.09.041>.
 297. Erne, P.; Schier, M.; Resink, T.J. The road to bioabsorbable stents: Reaching clinical reality? *CardioVascular Interv. Radiol.* 2006, 29, 11–16. <https://doi.org/10.1007/s00270-004-0341-9>.
 298. Maharana, T.; Mohanty, B.; Negi, Y.S. Melt–solid polycondensation of lactic acid and its biodegradability. *Prog. Polym. Sci.* 2009, 34, 99–124. <https://doi.org/10.1016/j.progpolymsci.2008.10.001>.
 299. Lim, J.Y.; Kim, S.H.; Lim, S.; Kim, Y.H. Improvement of flexural strengths of poly(L-lactic acid) by solid-state extrusion, 2: Extrusion through rectangular die. *Macromol. Mater. Eng.* 2003, 288, 50–57. <https://doi.org/10.1002/mame.200290033>.
 300. DeJong, L.T.C.E.S.; DeBerardino, L.T.C.T.M.; Brooks, D.E.; Judson, K. In vivo comparison of a metal versus a biodegradable suture anchor. Implants and implant instrumentation for this project were provided via material transfer agreement by Arthrex, Naples, Florida, U.S.A. *Arthrosc. J. Arthrosc. Relat. Surg.* 2004, 20, 511–516. <https://doi.org/10.1016/j.arthro.2004.03.008>.
 301. Soares, J. Constitutive Modeling of Biodegradable Polymers for Application in Endovascular Stents. PhD Thesis, Texas A&M University, College Station, TX, USA, 2008.
 302. Langer, R. Drug delivery and targeting. *Nature* 1998, 392, 5–10.
 303. Moravej, M.; Mantovani, D. Biodegradable Metals for Cardiovascular Stent Application: Interests and New Opportunities. *Int. J. Mol. Sci.* 2011, 12, 4250–4270.
 304. Garlotta, D. A literature review of poly(lactic acid). *J. Polym. Environ.* 2001, 9, 63–84. <https://doi.org/10.1023/A:1020200822435>.
 305. Drumright, R.E.; Gruber, P.R.; Henton, D.E. Polylactic acid technology. *Adv. Mater.* 2000, 12, 1841–1846. [https://doi.org/10.1002/1521-4095\(200012\)12:23<1841::AID-ADMA1841>3.0.CO;2-E](https://doi.org/10.1002/1521-4095(200012)12:23<1841::AID-ADMA1841>3.0.CO;2-E).
 306. Sawyer, D.J. Bioprocessing—No longer a field of dreams. *Macromol. Symp.* 2003, 201, 271–282. <https://doi.org/10.1002/masy.200351130>.
 307. Dorgan, J.R.; Lehermeier, H.J.; Palade, L.I.; Cicero, J. Polylactides: Properties and prospects of an environmentally benign plastic from renewable resources. *Macromol. Symp.* 2001, 175, 55–66. [https://doi.org/10.1002/1521-3900\(200110\)175:1<55::AID-MASY55>3.0.CO;2-K](https://doi.org/10.1002/1521-3900(200110)175:1<55::AID-MASY55>3.0.CO;2-K).
 308. Rasal, R.M.; Janorkar, A.V.; Hirt, D.E. Poly(lactic acid) modifications. *Prog. Polym. Sci.* 2010, 35, 338–356. <https://doi.org/10.1016/j.progpolymsci.2009.12.003>.
 309. Burg, K.J.L.; Holder, W.D.; Culberson, C.R.; Beiler, R.J.; Greene, K.G.; Loeb sack, A.B.; Roland, W.D.; Mooney, D.J.; Halberstadt, C.R. Parameters affecting cellular adhesion to polylactide films. *J. Biomater. Sci. Polym. Ed.* 1999, 10, 147–161. <https://doi.org/10.1163/156856299X00108>.
 310. Farah, S.; Anderson, D.G.; Langer, R. Physical and mechanical properties of PLA, and their functions in widespread applications—A comprehensive review. *Adv. Drug Deliv. Rev.* 2016, 107, 367–392. <https://doi.org/10.1016/j.addr.2016.06.012>.
 311. Rakovsky, A.; Gotman, I.; Rabkin, E.; Gutmanas, E.Y. β -TCP-polylactide composite scaffolds with high strength and enhanced permeability prepared by a modified salt leaching method. *J. Mech. Behav. Biomed. Mater.* 2014, 32, 89–98. <https://doi.org/10.1016/j.jmbbm.2013.12.022>.
 312. Kang, Y.; Yin, G.; Yuan, Q.; Yao, Y.; Huang, Z.; Liao, X.; Yang, B.; Liao, L.; Wang, H. Preparation

Design principles

- of poly (l-lactic acid)/ β -tricalcium phosphate scaffold for bone tissue engineering without organic solvent. *Mater. Lett.* 2008, 62, 2029–2032.
313. Prabakaran, M.; Rodriguez-Perez, M.; De Saja, J.; Mano, J. Preparation and characterization of poly (L-lactic acid)-chitosan hybrid scaffolds with drug release capability. *J. Biomed. Mater. Res. Part B Appl. Biomater.* 2007, 81, 427–434.
314. Nga, N.K.; Hoai, T.T.; Viet, P.H. Biomimetic scaffolds based on hydroxyapatite nanorod/poly(D,L) lactic acid with their corresponding apatite-forming capability and biocompatibility for bone-tissue engineering. *Colloids Surf. B Biointerfaces* 2015, 128, 506–514. <https://doi.org/10.1016/j.colsurfb.2015.03.001>.
315. Charles-Harris, M.; Koch, M.A.; Navarro, M.; Lacroix, D.; Engel, E.; Planell, J.A. A PLA/calcium phosphate degradable composite material for bone tissue engineering: An in vitro study. *J. Mater. Sci. Mater. Med.* 2008, 19, 1503–1513. <https://doi.org/10.1007/s10856-008-3390-9>.
316. Zhang, R.; Ma, P.X. Poly(alpha-hydroxyl acids)/hydroxyapatite porous composites for bone-tissue engineering. I. Preparation and morphology. *J. Biomed. Mater. Res.* 1999, 44, 446–455. [https://doi.org/10.1002/\(sici\)1097-4636\(19990315\)44:4<446::aid-jbm11>3.0.co;2-f](https://doi.org/10.1002/(sici)1097-4636(19990315)44:4<446::aid-jbm11>3.0.co;2-f).
317. Montjovent, M.-O.; Mathieu, L.; Hinz, B.; Applegate, L.L.; Bourban, P.-E.; Zambelli, P.-Y.; Månson, J.-A.; Pioletti, D.P. Biocompatibility of bioresorbable poly (L-lactic acid) composite scaffolds obtained by supercritical gas foaming with human fetal bone cells. *Tissue Eng.* 2005, 11, 1640–1649.
318. Liao, S.; Cui, F.; Zhang, W.; Feng, Q. Hierarchically biomimetic bone scaffold materials: Nano-HA/collagen/PLA composite. *J. Biomed. Mater. Res. Part B Appl. Biomater.* 2004, 69, 158–165.
319. Wang, D.; Lin, H.; Jiang, J.; Jin, Q.; Li, L.; Dong, Y.; Qu, F. Fabrication of long-acting drug release property of hierarchical porous bioglasses/poly(lactic acid) fibre scaffolds for bone tissue engineering. *IET Nanobiotechnol.* 2014, 9, 58–65.
320. Li, Y.; Li, D.; Lu, B.; Gao, D.; Zhou, J. Current status of additive manufacturing for tissue engineering scaffold. *Rapid Prototyp. J.* 2015, 21, 747–762.
321. Seck, T.M.; Melchels, F.P.; Feijen, J.; Grijpma, D.W. Designed biodegradable hydrogel structures prepared by stereolithography using poly (ethylene glycol)/poly (D, L-lactide)-based resins. *J. Control. Release* 2010, 148, 34–41.
322. Zhang, L.; Yang, G.; Johnson, B.N.; Jia, X. Three-dimensional (3D) printed scaffold and material selection for bone repair. *Acta Biomater.* 2019, 84, 16–33. <https://doi.org/10.1016/j.actbio.2018.11.039>.
323. Williams, J.M.; Adewunmi, A.; Schek, R.M.; Flanagan, C.L.; Krebsbach, P.H.; Feinberg, S.E.; Hollister, S.J.; Das, S. Bone tissue engineering using polycaprolactone scaffolds fabricated via selective laser sintering. *Biomaterials* 2005, 26, 4817–4827. <https://doi.org/10.1016/j.biomaterials.2004.11.057>.
324. Shuai, C.; Li, Y.; Wang, G.; Yang, W.; Peng, S.; Feng, P. Surface modification of nanodiamond: Toward the dispersion of reinforced phase in poly-l-lactic acid scaffolds. *Int. J. Biol. Macromol.* 2019, 126, 1116–1124.
325. Gayer, C.; Abert, J.; Bullemer, M.; Grom, S.; Jauer, L.; Meiners, W.; Reinauer, F.; Vučak, M.; Wissenbach, K.; Poprawe, R. Influence of the material properties of a poly (D, L-lactide)/ β -tricalcium phosphate composite on the processability by selective laser sintering. *J. Mech. Behav. Biomed. Mater.* 2018, 87, 267–278.
326. Guvendiren, M.; Molde, J.; Soares, R.M.; Kohn, J. Designing biomaterials for 3D printing. *ACS Biomater. Sci. Eng.* 2016, 2, 1679–1693.
327. Lanzotti, A.; Eujin Pei, D.; Grasso, M.; Staiano, G.; Martorelli, M. The impact of process parameters on mechanical properties of parts fabricated in PLA with an open-source 3-D printer. *Rapid Prototyp. J.* 2015, 21, 604–617. <https://doi.org/10.1108/rtpj-09-2014-0135>.
328. Casavola, C.; Cazzato, A.; Moramarco, V.; Pappalettere, C. Orthotropic mechanical properties of fused deposition modelling parts described by classical laminate theory. *Mater. Des.* 2016, 90, 453–458. <https://doi.org/10.1016/j.matdes.2015.11.009>.
329. Chacón, J.M.; Caminero, M.A.; García-Plaza, E.; Núñez, P.J. Additive manufacturing of PLA structures using fused deposition modelling: Effect of process parameters on mechanical properties and their optimal selection. *Mater. Des.* 2017, 124, 143–157. <https://doi.org/10.1016/j.matdes.2017.03.065>.

330. Ahmed, A.A.; Susmel, L. Static assessment of plain/notched polylactide (PLA) 3D-printed with different infill levels: Equivalent homogenised material concept and Theory of Critical Distances. *Fatigue Fract. Eng. Mater. Struct.* 2019, 42, 883–904. <https://doi.org/10.1111/ffe.12958>.
331. Song, Y.; Li, Y.; Song, W.; Yee, K.; Lee, K.Y.; Tagarielli, V.L. Measurements of the mechanical response of unidirectional 3D-printed PLA. *Mater. Des.* 2017, 123, 154–164. <https://doi.org/10.1016/j.matdes.2017.03.051>.
332. Ahmed, A.A.; Susmel, L. A material length scale-based methodology to assess static strength of notched additively manufactured polylactide (PLA). *Fatigue Fract. Eng. Mater. Struct.* 2018, 41, 2071–2098. <https://doi.org/10.1111/ffe.12746>.
333. Dave, H.K.; Rajpurohit, S.R.; Patadiya, N.H.; Dave, S.J.; Sharma, K.S.; Thambad, S.S.; Srinivasn, V.P.; Sheth, K.V. Compressive strength of PLA based scaffolds: Effect of layer height, infill density and print speed. *Int. J. Mod. Manuf. Technol.* 2019, 11, 21–27.
334. Ezeh, O.H.; Susmel, L. Fatigue strength of additively manufactured polylactide (PLA): Effect of raster angle and non-zero mean stresses. *Int. J. Fatigue* 2019, 126, 319–326. <https://doi.org/10.1016/j.ijfatigue.2019.05.014>.
335. Jerez-Mesa, R.; Travieso-Rodriguez, J.A.; Llumà-Fuentes, J.; Gomez-Gras, G.; Puig, D. Fatigue lifespan study of PLA parts obtained by additive manufacturing. *Procedia Manuf.* 2017, 13, 872–879. <https://doi.org/10.1016/j.promfg.2017.09.146>.
336. Afrose, M.F.; Masood, S.H.; Iovenitti, P.; Nikzad, M.; Sbarski, I. Effects of part build orientations on fatigue behaviour of FDM-processed PLA material. *Prog. Addit. Manuf.* 2016, 1, 21–28. <https://doi.org/10.1007/s40964-015-0002-3>.
337. Ezeh, O.H.; Susmel, L. On the notch fatigue strength of additively manufactured polylactide (PLA). *Int. J. Fatigue* 2020, 136, 105583. <https://doi.org/10.1016/j.ijfatigue.2020.105583>.
338. Ouhsti, M.; El Haddadi, B.; Belhouideg, S. Effect of printing parameters on the mechanical properties of parts fabricated with open-source 3D printers in PLA by fused deposition modeling. *Mech. Mech. Eng.* 2020, 22, 895–908.
339. Abbas, T.F.; Othman, F.M.; Ali, H.B. Influence of layer thickness on impact property of 3D-printed PLA. *Int. Res. J. Eng. Technol. (IRJET)* 2018, 5, 1–4.
340. Luzanin, O.; Movrin, D.; Stathopoulos, V.; Pandis, P.; Radusin, T.; Guduric, V. Impact of processing parameters on tensile strength, in-process crystallinity and mesostructure in FDM-fabricated PLA specimens. *Rapid Prototyp. J.* 2019, 25, 1398–1410. <https://doi.org/10.1108/RPJ-12-2018-0316>.
341. Yao, T.; Deng, Z.; Zhang, K.; Li, S. A method to predict the ultimate tensile strength of 3D printing polylactic acid (PLA) materials with different printing orientations. *Compos. Part B Eng.* 2019, 163, 393–402. <https://doi.org/10.1016/j.compositesb.2019.01.025>.
342. Murugan, R.; Mitilesh, R.; Singamneni, S. Influence of process parameters on the mechanical behaviour and processing time of 3D printing. *Int. J. Mod. Manuf. Technol.* 2019, 1, 21–27.
343. Grémare, A.; Guduric, V.; Bareille, R.; Heroguez, V.; Latour, S.; L’Heureux, N.; Fricain, J.C.; Catros, S.; Le Nihouannen, D. Characterization of printed PLA scaffolds for bone tissue engineering. *J. Biomed. Mater. Res. A* 2018, 106, 887–894. <https://doi.org/10.1002/jbm.a.36289>.
344. Alksne, M.; Simoliunas, E.; Kalvaityte, M.; Skliutas, E.; Rinkunaite, I.; Gendviliene, I.; Baltriukiene, D.; Rutkunas, V.; Bukelskiene, V. The effect of larger than cell diameter polylactic acid surface patterns on osteogenic differentiation of rat dental pulp stem cells. *J. Biomed. Mater. Res. Part A* 2019, 107, 174–186.
345. Donate, R.; Monzón, M.; Alemán-Domínguez, M.E. Additive manufacturing of PLA-based scaffolds intended for bone regeneration and strategies to improve their biological properties. *e-Polymers* 2020, 20, 571–599. <https://doi.org/10.1515/epoly-2020-0046>.
346. Teixeira, B.N.; Aprile, P.; Mendonça, R.H.; Kelly, D.J.; Thiré, R.M.d.S.M. Evaluation of bone marrow stem cell response to PLA scaffolds manufactured by 3D printing and coated with polydopamine and type I collagen. *J. Biomed. Mater. Res. Part B Appl. Biomater.* 2019, 107, 37–49.
347. Zhang, H.; Mao, X.; Du, Z.; Jiang, W.; Han, X.; Zhao, D.; Han, D.; Li, Q. Three dimensional printed macroporous polylactic acid/hydroxyapatite composite scaffolds for promoting bone formation in a critical-size rat calvarial defect model. *Sci. Technol. Adv. Mater.* 2016, 17, 136–148.
348. Zeng, S.; Cui, Z.; Yang, Z.; Si, J.; Wang, Q.; Wang, X.; Peng, K.; Chen, W. Characterization of highly

Design principles

- interconnected porous poly(lactic acid) and chitosan-coated poly(lactic acid) scaffold fabricated by vacuum-assisted resin transfer molding and particle leaching. *J. Mater. Sci.* 2016, 51, 9958–9970. <https://doi.org/10.1007/s10853-016-0203-2>.
349. Fernández-Cervantes, I.; Morales, M.A.; Agustín-Serrano, R.; Cardenas-García, M.; Pérez-Luna, P.V.; Arroyo-Reyes, B.L.; Maldonado-García, A. Polylactic acid/sodium alginate/hydroxyapatite composite scaffolds with trabecular tissue morphology designed by a bone remodeling model using 3D printing. *J. Mater. Sci.* 2019, 54, 9478–9496. <https://doi.org/10.1007/s10853-019-03537-1>.
350. Chen, Y.; Mak, A.F.T.; Wang, M.; Li, J.; Wong, M.S. PLLA scaffolds with biomimetic apatite coating and biomimetic apatite/collagen composite coating to enhance osteoblast-like cells attachment and activity. *Surf. Coat. Technol.* 2006, 201, 575–580. <https://doi.org/10.1016/j.surfcoat.2005.12.005>.
351. Kim, S.-H.; Oh, S.-A.; Lee, W.-K.; Shin, U.S.; Kim, H.-W. Poly(lactic acid) porous scaffold with calcium phosphate mineralized surface and bone marrow mesenchymal stem cell growth and differentiation. *Mater. Sci. Eng. C* 2011, 31, 612–619. <https://doi.org/10.1016/j.msec.2010.11.028>.
352. Kao, C.-T.; Lin, C.-C.; Chen, Y.-W.; Yeh, C.-H.; Fang, H.-Y.; Shie, M.-Y. Poly(dopamine) coating of 3D printed poly(lactic acid) scaffolds for bone tissue engineering. *Mater. Sci. Eng. C* 2015, 56, 165–173. <https://doi.org/10.1016/j.msec.2015.06.028>.
353. Lee, N.K.; Sowa, H.; Hinoi, E.; Ferron, M.; Ahn, J.D.; Confavreux, C.; Dacquin, R.; Mee, P.J.; McKee, M.D.; Jung, D.Y.; et al. Endocrine regulation of energy metabolism by the skeleton. *Cell* 2007, 130, 456–469. <https://doi.org/10.1016/j.cell.2007.05.047>.
354. Holmes, B.; Zhu, W.; Li, J.; Lee, J.D.; Zhang, L.G. Development of Novel Three-Dimensional Printed Scaffolds for Osteochondral Regeneration. *Tissue Eng. Part A* 2014, 21, 403–415. <https://doi.org/10.1089/ten.tea.2014.0138>.
355. Niaza, K.V.; Senatov, F.S.; Kaloshkin, S.D.; Maksimkin, A.V.; Chukov, D.I. 3D-printed scaffolds based on PLA/HA nanocomposites for trabecular bone reconstruction. *J. Phys. Conf. Ser.* 2016, 741, 012068. <https://doi.org/10.1088/1742-6596/741/1/012068>.
356. Esposito Corcione, C.; Gervaso, F.; Scalera, F.; Montagna, F.; Sannino, A.; Maffezzoli, A. The feasibility of printing polylactic acid–nanohydroxyapatite composites using a low-cost fused deposition modeling 3D printer. *J. Appl. Polym. Sci.* 2017, 134, 44656. <https://doi.org/10.1002/app.44656>.
357. Wei, Q.; Cai, X.; Guo, Y.; Wang, G.; Guo, Y.; Lei, M.; Song, Y.; Yingfeng, Z.; Wang, Y. Atomic-scale and experimental investigation on the micro-structures and mechanical properties of PLA blending with CMC for additive manufacturing. *Mater. Des.* 2019, 183, 108158.
358. Ferreira, B.; Pinheiro, L.; Nascente, P.; Ferreira, M.; Duek, E. Plasma surface treatments of poly (l-lactic acid)(PLLA) and poly (hydroxybutyrate-co-hydroxyvalerate)(PHBV). *Mater. Sci. Eng. C* 2009, 29, 806–813.
359. Yang, J.; Shi, G.; Bei, J.; Wang, S.; Cao, Y.; Shang, Q.; Yang, G.; Wang, W. Fabrication and surface modification of macroporous poly (L-lactic acid) and poly (L-lactic-co-glycolic acid)(70/30) cell scaffolds for human skin fibroblast cell culture. *J. Biomed. Mater. Res.* 2002, 62, 438–446.
360. Jacobs, T.; Morent, R.; De Geyter, N.; Dubruel, P.; Leys, C. Plasma surface modification of biomedical polymers: Influence on cell-material interaction. *Plasma Chem. Plasma Processing* 2012, 32, 1039–1073.
361. Scaffaro, R.; Lopresti, F.; Sutura, A.; Botta, L.; Fontana, R.M.; Gallo, G. Plasma modified PLA electrospun membranes for actinorhodin production intensification in *Streptomyces coelicolor* immobilized-cell cultivations. *Colloids Surf. B Biointerfaces* 2017, 157, 233–241. <https://doi.org/10.1016/j.colsurfb.2017.05.060>.
362. Jordá-Vilaplana, A.; Fombuena, V.; García-García, D.; Samper, M.D.; Sánchez-Nácher, L. Surface modification of polylactic acid (PLA) by air atmospheric plasma treatment. *Eur. Polym. J.* 2014, 58, 23–33. <https://doi.org/10.1016/j.eurpolymj.2014.06.002>.
363. Liu, X.; Holzwarth, J.M.; Ma, P.X. Functionalized synthetic biodegradable polymer scaffolds for tissue engineering. *Macromol. Biosci.* 2012, 12, 911–919.
364. van Manen, T.; Janbaz, S.; Jansen, K.; Zadpoor, A. 4D printing of reconfigurable metamaterials and devices. *Commun. Mater.* 2021, 2, 56.
365. Cuellar, J.S.; Plettenburg, D.; Zadpoor, A.A.; Breedveld, P.; Smit, G. Design of a 3D-printed hand prosthesis featuring articulated bio-inspired fingers. *Proc. Inst. Mech. Eng. Part H J. Eng. Med.* 2021,

- 235, 336–345.
366. Cuellar, J.S.; Smit, G.; Breedveld, P.; Zadpoor, A.A.; Plettenburg, D. Functional evaluation of a non-assembly 3D-printed hand prosthesis. *Proc. Inst. Mech. Eng. Part H J. Eng. Med.* 2019, 233, 1122–1131.
 367. Cuellar, J.S.; Smit, G.; Zadpoor, A.A.; Breedveld, P. Ten guidelines for the design of non-assembly mechanisms: The case of 3D-printed prosthetic hands. *Proc. Inst. Mech. Eng. Part H J. Eng. Med.* 2018, 232, 962–971.
 368. Nouri-Goushki, M.; Sharma, A.; Sasso, L.; Zhang, S.; Van der Eerden, B.C.; Staufer, U.; Fratila-Apachitei, L.E.; Zadpoor, A.A. Submicron patterns-on-a-chip: Fabrication of a microfluidic device incorporating 3D printed surface ornaments. *ACS Biomater. Sci. Eng.* 2019, 5, 6127–6136.
 369. Nouri-Goushki, M.; Mirzaali, M.; Angeloni, L.; Fan, D.; Minneboo, M.; Ghatkesar, M.; Staufer, U.; Fratila-Apachitei, L.; Zadpoor, A. 3D Printing of large areas of highly ordered submicron patterns for modulating cell behavior. *ACS Appl. Mater. Interfaces* 2019, 12, 200–208.
 370. Woodruff, M.A.; Hutmacher, D.W. The return of a forgotten polymer—Polycaprolactone in the 21st century. *Prog. Polym. Sci.* 2010, 35, 1217–1256. <https://doi.org/10.1016/j.progpolymsci.2010.04.002>.
 371. Labet, M.; Thielemans, W. Synthesis of polycaprolactone: A review. *Chem. Soc. Rev.* 2009, 38, 3484–3504. <https://doi.org/10.1039/B820162P>.
 372. Dwivedi, R.; Kumar, S.; Pandey, R.; Mahajan, A.; Nandana, D.; Katti, D.S.; Mehrotra, D. Polycaprolactone as biomaterial for bone scaffolds: Review of literature. *J. Oral Biol. Craniofacial Res.* 2020, 10, 381–388. <https://doi.org/10.1016/j.jobcr.2019.10.003>.
 373. Park, J.; Lee, S.J.; Jo, H.H.; Lee, J.H.; Kim, W.D.; Lee, J.Y.; Park, S.A. Fabrication and characterization of 3D-printed bone-like β -tricalcium phosphate/polycaprolactone scaffolds for dental tissue engineering. *J. Ind. Eng. Chem.* 2017, 46, 175–181. <https://doi.org/10.1016/j.jiec.2016.10.028>.
 374. Gomes, S.; Rodrigues, G.; Martins, G.; Henriques, C.; Silva, J.C. Evaluation of nanofibrous scaffolds obtained from blends of chitosan, gelatin and polycaprolactone for skin tissue engineering. *Int. J. Biol. Macromol.* 2017, 102, 1174–1185. <https://doi.org/10.1016/j.ijbiomac.2017.05.004>.
 375. Anderson, J.M.; Shive, M.S. Biodegradation and biocompatibility of PLA and PLGA microspheres. *Adv. Drug Deliv. Rev.* 1997, 28, 5–24. [https://doi.org/10.1016/S0169-409X\(97\)00048-3](https://doi.org/10.1016/S0169-409X(97)00048-3).
 376. Chen, J.-M.; Lee, D.; Yang, J.-W.; Lin, S.-H.; Lin, Y.-T.; Liu, S.-J. Solution Extrusion Additive Manufacturing of Biodegradable Polycaprolactone. *Appl. Sci.* 2020, 10, 3189. <https://doi.org/10.3390/app10093189>.
 377. Li, Y.; Li, X.; Zhao, R.; Wang, C.; Qiu, F.; Sun, B.; Ji, H.; Qiu, J.; Wang, C. Enhanced adhesion and proliferation of human umbilical vein endothelial cells on conductive PANI-PCL fiber scaffold by electrical stimulation. *Mater. Sci. Eng. C Mater. Biol. Appl.* 2017, 72, 106–112. <https://doi.org/10.1016/j.msec.2016.11.052>.
 378. Chen, Y.; Li, W.; Zhang, C.; Wu, Z.; Liu, J. Recent Developments of Biomaterials for Additive Manufacturing of Bone Scaffolds. *Adv. Healthc. Mater.* 2020, 9, e2000724. <https://doi.org/10.1002/adhm.202000724>.
 379. Kim, Y.B.; Kim, G.H. PCL/alginate composite scaffolds for hard tissue engineering: Fabrication, characterization, and cellular activities. *ACS Comb. Sci.* 2015, 17, 87–99. <https://doi.org/10.1021/co500033h>.
 380. Kim, M.S.; Kim, G. Three-dimensional electrospun polycaprolactone (PCL)/alginate hybrid composite scaffolds. *Carbohydr. Polym.* 2014, 114, 213–221. <https://doi.org/10.1016/j.carbpol.2014.08.008>.
 381. Vella, J.B.; Trombetta, R.P.; Hoffman, M.D.; Inzana, J.; Awad, H.; Benoit, D.S.W. Three dimensional printed calcium phosphate and poly(caprolactone) composites with improved mechanical properties and preserved microstructure. *J. Biomed. Mater. Res. Part A* 2018, 106, 663–672. <https://doi.org/10.1002/jbm.a.36270>.
 382. Diloksumpan, P.; de Ruijter, M.; Castilho, M.; Gbureck, U.; Vermonden, T.; van Weeren, P.R.; Malda, J.; Levato, R. Combining multi-scale 3D printing technologies to engineer reinforced hydrogel-ceramic interfaces. *Biofabrication* 2020, 12, 025014. <https://doi.org/10.1088/1758-5090/ab69d9>.

Design principles

383. Prasad, S.; Wong, R.C.W. Unraveling the mechanical strength of biomaterials used as a bone scaffold in oral and maxillofacial defects. *Oral Sci. Int.* 2018, 15, 48–55. [https://doi.org/10.1016/S1348-8643\(18\)30005-3](https://doi.org/10.1016/S1348-8643(18)30005-3).
384. Miranda, P.; Pajares, A.; Saiz, E.; Tomsia, A.P.; Guiberteau, F. Mechanical properties of calcium phosphate scaffolds fabricated by robocasting. *J. Biomed. Mater. Res. Part A* 2008, 85A, 218–227. <https://doi.org/10.1002/jbm.a.31587>.
385. Zocca, A.; Colombo, P.; Gomes, C.M.; Günster, J. Additive Manufacturing of Ceramics: Issues, Potentialities, and Opportunities. *J. Am. Ceram. Soc.* 2015, 98, 1983–2001. <https://doi.org/10.1111/jace.13700>.
386. Fares, M.M.; Shirzaei Sani, E.; Portillo Lara, R.; Oliveira, R.B.; Khademhosseini, A.; Annabi, N. Interpenetrating network gelatin methacryloyl (GelMA) and pectin-g-PCL hydrogels with tunable properties for tissue engineering. *Biomater. Sci.* 2018, 6, 2938–2950. <https://doi.org/10.1039/c8bm00474a>.
387. Kamaly, N.; Yameen, B.; Wu, J.; Farokhzad, O.C. Degradable Controlled-Release Polymers and Polymeric Nanoparticles: Mechanisms of Controlling Drug Release. *Chem. Rev.* 2016, 116, 2602–2663. <https://doi.org/10.1021/acs.chemrev.5b00346>.
388. Makadia, H.K.; Siegel, S.J. Poly Lactic-co-Glycolic Acid (PLGA) as Biodegradable Controlled Drug Delivery Carrier. *Polymers* 2011, 3, 1377–1397. <https://doi.org/10.3390/polym3031377>.
389. Song, T.H.; Jang, J.; Choi, Y.J.; Shim, J.H.; Cho, D.W. 3D-Printed Drug/Cell Carrier Enabling Effective Release of Cyclosporin A for Xenogeneic Cell-Based Therapy. *Cell Transpl.* 2015, 24, 2513–2525. <https://doi.org/10.3727/096368915x686779>.
390. Ge, Z.; Tian, X.; Heng, B.C.; Fan, V.; Yeo, J.F.; Cao, T. Histological evaluation of osteogenesis of 3D-printed poly-lactic-co-glycolic acid (PLGA) scaffolds in a rabbit model. *Biomed. Mater.* 2009, 4, 021001. <https://doi.org/10.1088/1748-6041/4/2/021001>.
391. Yousefi, A.M.; Powers, J.; Sampson, K.; Wood, K.; Gadola, C.; Zhang, J.; James, P.F. In vitro characterization of hierarchical 3D scaffolds produced by combining additive manufacturing and thermally induced phase separation. *J. Biomater. Sci. Polym. Ed.* 2020, 32, 454–476. <https://doi.org/10.1080/09205063.2020.1841535>.
392. Gentile, P.; Chiono, V.; Carmagnola, I.; Hatton, P.V. An overview of poly(lactic-co-glycolic) acid (PLGA)-based biomaterials for bone tissue engineering. *Int. J. Mol. Sci.* 2014, 15, 3640–3659. <https://doi.org/10.3390/ijms15033640>.
393. Montanheiro, T.L.d.A.; Ribas, R.G.; Montagna, L.S.; Menezes, B.R.C.d.; Schatkoski, V.M.; Rodrigues, K.F.; Thim, G.P. A brief review concerning the latest advances in the influence of nanoparticle reinforcement into polymeric-matrix biomaterials. *J. Biomater. Sci. Polym. Ed.* 2020, 31, 1869–1893. <https://doi.org/10.1080/09205063.2020.1781527>.
394. Dos Santos, V.I.; Merlini, C.; Aragones, Á.; Cesca, K.; Fredel, M.C. In vitro evaluation of bilayer membranes of PLGA/hydroxyapatite/ β -tricalcium phosphate for guided bone regeneration. *Mater. Sci. Eng. C Mater. Biol. Appl.* 2020, 112, 110849. <https://doi.org/10.1016/j.msec.2020.110849>.
395. Sequeira, J.A.; Santos, A.C.; Serra, J.; Veiga, F.; Ribeiro, A.J. Poly (lactic-co-glycolic acid)(PLGA) matrix implants. In *Nanostructures for the Engineering of Cells, Tissues and Organs*; Elsevier: Amsterdam, The Netherlands, 2018; pp. 375–402.
396. Puppi, D.; Chiellini, F. Wet-spinning of biomedical polymers: From single-fibre production to additive manufacturing of three-dimensional scaffolds. *Polym. Int.* 2017, 66, 1690–1696. <https://doi.org/10.1002/pi.5332>.
397. Meng, Z.X.; Zheng, W.; Li, L.; Zheng, Y.F. Fabrication, characterization and in vitro drug release behavior of electrospun PLGA/chitosan nanofibrous scaffold. *Mater. Chem. Phys.* 2011, 125, 606–611. <https://doi.org/10.1016/j.matchemphys.2010.10.010>.
398. Li, L.Y.; Cui, L.Y.; Zeng, R.C.; Li, S.Q.; Chen, X.B.; Zheng, Y.; Kannan, M.B. Advances in functionalized polymer coatings on biodegradable magnesium alloys—A review. *Acta Biomater.* 2018, 79, 23–36. <https://doi.org/10.1016/j.actbio.2018.08.030>.
399. Guo, T.; Holzberg, T.R.; Lim, C.G.; Gao, F.; Gargava, A.; Trachtenberg, J.E.; Mikos, A.G.; Fisher, J.P. 3D printing PLGA: A quantitative examination of the effects of polymer composition and printing parameters on print resolution. *Biofabrication* 2017, 9, 024101. <https://doi.org/10.1088/1758-5090/aa6370>.

400. Mironov, A.V.; Grigoryev, A.M.; Krotova, L.I.; Skaletsky, N.N.; Popov, V.K.; Sevastianov, V.I. 3D printing of PLGA scaffolds for tissue engineering. *J. Biomed. Mater. Res. Part A* 2017, 105, 104–109. <https://doi.org/10.1002/jbm.a.35871>.
401. Awad, A.; Trenfield, S.J.; Goyanes, A.; Gaisford, S.; Basit, A.W. Reshaping drug development using 3D printing. *Drug Discov. Today* 2018, 23, 1547–1555. <https://doi.org/10.1016/j.drudis.2018.05.025>.
402. Fu, J.; Yu, X.; Jin, Y. 3D printing of vaginal rings with personalized shapes for controlled release of progesterone. *Int. J. Pharm.* 2018, 539, 75–82. <https://doi.org/10.1016/j.ijpharm.2018.01.036>.
403. Goyanes, A.; Fina, F.; Martorana, A.; Sedough, D.; Gaisford, S.; Basit, A.W. Development of modified release 3D printed tablets (printlets) with pharmaceutical excipients using additive manufacturing. *Int. J. Pharm.* 2017, 527, 21–30. <https://doi.org/10.1016/j.ijpharm.2017.05.021>.
404. Goyanes, A.; Robles Martinez, P.; Buanz, A.; Basit, A.W.; Gaisford, S. Effect of geometry on drug release from 3D printed tablets. *Int. J. Pharm.* 2015, 494, 657–663. <https://doi.org/10.1016/j.ijpharm.2015.04.069>.
405. Khaled, S.A.; Alexander, M.R.; Wildman, R.D.; Wallace, M.J.; Sharpe, S.; Yoo, J.; Roberts, C.J. 3D extrusion printing of high drug loading immediate release paracetamol tablets. *Int. J. Pharm.* 2018, 538, 223–230. <https://doi.org/10.1016/j.ijpharm.2018.01.024>.
406. Khaled, S.A.; Burley, J.C.; Alexander, M.R.; Yang, J.; Roberts, C.J. 3D printing of tablets containing multiple drugs with defined release profiles. *Int. J. Pharm.* 2015, 494, 643–650. <https://doi.org/10.1016/j.ijpharm.2015.07.067>.
407. Vozi, G.; Flaim, C.; Ahluwalia, A.; Bhatia, S. Fabrication of PLGA scaffolds using soft lithography and microsyringe deposition. *Biomaterials* 2003, 24, 2533–2540. [https://doi.org/10.1016/s0142-9612\(03\)00052-8](https://doi.org/10.1016/s0142-9612(03)00052-8).
408. Minden-Birkenmaier, B.A.; Selders, G.S.; Fetz, A.E.; Gehrmann, C.J.; Bowlin, G.L. 7–Electrospun systems for drug delivery. In *Electrospun Materials for Tissue Engineering and Biomedical Applications*; Uyar, T., Kny, E., Eds.; Woodhead Publishing: 2017; pp. 117–145. <https://doi.org/10.1016/B978-0-08-101022-8.00011-9>.
409. Zhang, F.Y.; Ma, Y.; Liao, J.S.; Breedveld, V.; Lively, R.P. Solution-based 3D printing of polymers of intrinsic microporosity. *Macromol. Rapid Commun.* 2018, 39, 7. <https://doi.org/10.1002/marc.201800274>.
410. Chen, C.; Mehl, B.T.; Munshi, A.S.; Townsend, A.D.; Spence, D.M.; Martin, R.S. 3D-printed microfluidic devices: Fabrication, advantages and limitations-A mini review. *Anal. Methods* 2016, 8, 6005–6012. <https://doi.org/10.1039/c6ay01671e>.
411. Lee, B.K.; Yun, Y.H.; Choi, J.S.; Choi, Y.C.; Kim, J.D.; Cho, Y.W. Fabrication of drug-loaded polymer microparticles with arbitrary geometries using a piezoelectric inkjet printing system. *Int. J. Pharm.* 2012, 427, 305–310. <https://doi.org/10.1016/j.ijpharm.2012.02.011>.
412. Vozi, G.; Previti, A.; De Rossi, D.; Ahluwalia, A. Microsyringe-based deposition of two-dimensional and three-dimensional polymer scaffolds with a well-defined geometry for application to tissue engineering. *Tissue Eng.* 2002, 8, 1089–1098. <https://doi.org/10.1089/107632702320934182>.
413. Mota, C.; Puppi, D.; Dinucci, D.; Errico, C.; Bártolo, P.; Chiellini, F. Dual-scale polymeric constructs as scaffolds for tissue engineering. *Materials* 2011, 4, 527–542. <https://doi.org/10.3390/ma4030527>.
414. Naseri, E.; Butler, H.; MacNevin, W.; Ahmed, M.; Ahmadi, A. Low-temperature solvent-based 3D printing of PLGA: A parametric printability study. *Drug Dev. Ind. Pharm.* 2020, 46, 173–178. <https://doi.org/10.1080/03639045.2019.1711389>.
415. Mirzaali, M.; Pahlavani, H.; Yarali, E.; Zadpoor, A. Non-affinity in multi-material mechanical metamaterials. *Sci. Rep.* 2020, 10, 1–10.
416. Mirzaali, M.; Van Dongen, I.; Tümer, N.; Weinans, H.; Yavari, S.A.; Zadpoor, A. In-silico quest for bactericidal but non-cytotoxic nanopatterns. *Nanotechnology* 2018, 29, 43LT02.
417. Maleki, E.; Mirzaali, M.J.; Guagliano, M.; Bagherifard, S. Analyzing the mechano-bactericidal effect of nano-patterned surfaces on different bacteria species. *Surf. Coat. Technol.* 2021, 408, 126782.
418. Angeloni, L.; Ganjian, M.; Nouri-Goushki, M.; Mirzaali, M.; Hagen, C.; Zadpoor, A.; Fratila-Apachitei, L.; Ghatkesar, M. Mechanical characterization of nanopillars by atomic force microscopy. *Addit. Manuf.* 2021, 39, 101858.
419. Ganjian, M.; Modaresifar, K.; Ligeon, M.R.; Kunkels, L.B.; Tümer, N.; Angeloni, L.; Hagen, C.W.;

Design principles

- Otten, L.G.; Hagedoorn, P.L.; Apachitei, I. Nature helps: Toward bioinspired bactericidal nanopatterns. *Adv. Mater. Interfaces* 2019, 6, 1900640.
420. Modaresifar, K.; Azizian, S.; Ganjian, M.; Fratila-Apachitei, L.E.; Zadpoor, A.A. Bactericidal effects of nanopatterns: A systematic review. *Acta Biomater.* 2019, 83, 29–36.
421. Modaresifar, K.; Kunkels, L.B.; Ganjian, M.; Tümer, N.; Hagen, C.W.; Otten, L.G.; Hagedoorn, P.-L.; Angeloni, L.; Ghatkesar, M.K.; Fratila-Apachitei, L.E. Deciphering the roles of interspace and controlled disorder in the bactericidal properties of nanopatterns against *Staphylococcus aureus*. *Nanomaterials* 2020, 10, 347.
422. Ganjian, M.; Angeloni, L.; Mirzaali, M.J.; Modaresifar, K.; Hagen, C.W.; Ghatkesar, M.K.; Hagedoorn, P.L.; Fratila-Apachitei, L.; Zadpoor, A.A. Quantitative mechanics of 3D printed nanopillars interacting with bacterial cells. *Nanoscale* 2020, 12, 21988–22001.
423. Zagho, M.M.; Hussein, E.A.; Elzatahry, A.A. Recent overviews in functional polymer composites for biomedical applications. *Polymers* 2018, 10, 739.
424. Wang, X.; Jiang, M.; Zhou, Z.; Gou, J.; Hui, D. 3D printing of polymer matrix composites: A review and prospective. *Compos. Part B Eng.* 2017, 110, 442–458. <https://doi.org/10.1016/j.compositesb.2016.11.034>.
425. Nikzad, M.; Masood, S.H.; Sbarski, I. Thermo-mechanical properties of a highly filled polymeric composites for Fused Deposition Modeling. *Mater. Des.* 2011, 32, 3448–3456. <https://doi.org/10.1016/j.matdes.2011.01.056>.
426. Chung, H.; Das, S. Processing and properties of glass bead particulate-filled functionally graded Nylon-11 composites produced by selective laser sintering. *Mater. Sci. Eng. A* 2006, 437, 226–234.
427. Zhong, W.; Li, F.; Zhang, Z.; Song, L.; Li, Z. Short fiber reinforced composites for fused deposition modeling. *Mater. Sci. Eng. A* 2001, 301, 125–130.
428. Ning, F.; Cong, W.; Qiu, J.; Wei, J.; Wang, S. Additive manufacturing of carbon fiber reinforced thermoplastic composites using fused deposition modeling. *Compos. Part B Eng.* 2015, 80, 369–378.
429. Griffini, G.; Invernizzi, M.; Levi, M.; Natale, G.; Postiglione, G.; Turri, S. 3D-printable CFR polymer composites with dual-cure sequential IPNs. *Polymer* 2016, 91, 174–179.
430. Tekinalp, H.L.; Kunc, V.; Velez-Garcia, G.M.; Duty, C.E.; Love, L.J.; Naskar, A.K.; Blue, C.A.; Ozcan, S. Highly oriented carbon fiber-polymer composites via additive manufacturing. *Compos. Sci. Technol.* 2014, 105, 144–150.
431. Le Duigou, A.; Castro, M.; Bevan, R.; Martin, N. 3D printing of wood fibre biocomposites: From mechanical to actuation functionality. *Mater. Des.* 2016, 96, 106–114.
432. Wang, J.; Xie, H.; Weng, Z.; Senthil, T.; Wu, L. A novel approach to improve mechanical properties of parts fabricated by fused deposition modeling. *Mater. Des.* 2016, 105, 152–159.
433. Van Der Klift, F.; Koga, Y.; Todoroki, A.; Ueda, M.; Hirano, Y.; Matsuzaki, R. 3D printing of continuous carbon fibre reinforced thermo-plastic (CFRTP) tensile test specimens. *Open J. Compos. Mater.* 2016, 6, 18.
434. Tian, X.; Liu, T.; Yang, C.; Wang, Q.; Li, D. Interface and performance of 3D printed continuous carbon fiber reinforced PLA composites. *Compos. Part A Appl. Sci. Manuf.* 2016, 88, 198–205.
435. Lu, H.; Yao, Y.; Huang, W.M.; Leng, J.; Hui, D. Significantly improving infrared light-induced shape recovery behavior of shape memory polymeric nanocomposite via a synergistic effect of carbon nanotube and boron nitride. *Compos. Part B Eng.* 2014, 62, 256–261.
436. Sydney Gladman, A.; Matsumoto, E.A.; Nuzzo, R.G.; Mahadevan, L.; Lewis, J.A. Biomimetic 4D printing. *Nat. Mater.* 2016, 15, 413–418.
437. Shofner, M.; Lozano, K.; Rodríguez-Macías, F.; Barrera, E. Nanofiber-reinforced polymers prepared by fused deposition modeling. *J. Appl. Polym. Sci.* 2003, 89, 3081–3090.
438. Lin, D.; Jin, S.; Zhang, F.; Wang, C.; Wang, Y.; Zhou, C.; Cheng, G.J. 3D stereolithography printing of graphene oxide reinforced complex architectures. *Nanotechnology* 2015, 26, 434003.
439. Guo, S.-z.; Yang, X.; Heuzey, M.-C.; Therriault, D. 3D printing of a multifunctional nanocomposite helical liquid sensor. *Nanoscale* 2015, 7, 6451–6456.
440. Chung, H.; Das, S. Functionally graded Nylon-11/silica nanocomposites produced by selective laser sintering. *Mater. Sci. Eng. A* 2008, 487, 251–257.

441. Richerson, D.W. *The Magic of Ceramics*; John Wiley & Sons: Hoboken, NJ, USA, 2012.
442. Kingery, W.D.; Bowen, H.K.; Uhlmann, D.R. *Introduction to Ceramics*; John Wiley & Sons: Hoboken, NJ, USA, 1976; Volume 17.
443. Carter, C.B.; Norton, M.G. *Ceramic Materials Science and Engineering*; Springer: Berlin/Heidelberg, Germany, 2013.
444. Japan, T.C.S.o. *Advanced Ceramic Technologies & Products*; Springer Science & Business Media: Berlin, Germany, 2012.
445. Wang, G.; Wang, P.; Zhen, Z.; Zhang, W.; Ji, J. Preparation of PA12 microspheres with tunable morphology and size for use in SLS processing. *Mater. Des.* 2015, 87, 656–662.
446. Chawla, K.K. *Composite Materials: Science and Engineering*; Springer Science & Business Media: Berlin, Germany, 2012.
447. Bengisu, M. *Engineering Ceramics*; Springer Science & Business Media: Berlin, Germany, 2013.
448. Yan, C.; Shi, Y.; Hao, L. Investigation into the Differences in the Selective Laser Sintering between Amorphous and Semi-crystalline Polymers. *Int. Polym. Process.* 2011, 26, 416–423.
449. Zhou, F.; Molinari, J.-F. Stochastic fracture of ceramics under dynamic tensile loading. *Int. J. Solids Struct.* 2004, 41, 6573–6596. <https://doi.org/10.1016/j.ijsolstr.2004.05.029>.
450. Bene, P.; Bardaro, D. Numerical–experimental method to study the viscous behaviour of ceramic materials. *J. Eur. Ceram. Soc.* 2014, 34, 2617–2622. <https://doi.org/10.1016/j.jeurceramsoc.2014.01.034>.
451. Wachtman, J.B.; Cannon, W.R.; Matthewson, M.J. *Mechanical Properties of Ceramics*; John Wiley & Sons: Hoboken, NJ, USA, 2009.
452. Gogotsi, G.A. Deformational behaviour of ceramics. *J. Eur. Ceram. Soc.* 1991, 7, 87–92.
453. Lakhdar, Y.; Tuck, C.; Binner, J.; Terry, A.; Goodridge, R. Additive manufacturing of advanced ceramic materials. *Prog. Mater. Sci.* 2020, 116, 100736.
454. Yang, L.; Miyajima, H. Ceramic additive manufacturing: A review of current status and challenges. In *Proceedings of the 2017 International Solid Freeform Fabrication Symposium*, Austin, TX, USA, 7–9 August 2017; pp. 652–679.
455. Fielding, G.A.; Bandyopadhyay, A.; Bose, S. Effects of silica and zinc oxide doping on mechanical and biological properties of 3D printed tricalcium phosphate tissue engineering scaffolds. *Dent. Mater.* 2012, 28, 113–122. <https://doi.org/10.1016/j.dental.2011.09.010>.
456. Castilho, M.; Gouveia, B.; Pires, I.; Rodrigues, J.; Pereira, M. The role of shell/core saturation level on the accuracy and mechanical characteristics of porous calcium phosphate models produced by 3Dprinting. *Rapid Prototyp. J.* 2015, 21, 43–55.
457. Bourell, D.L.; Marcus, H.L.; Barlow, J.W.; Beaman, J.J. Selective laser sintering of metals and ceramics. *Int. J. Powder Metall.* 1992, 28, 369–381.
458. Chumnanklang, R.; Panyathanmaporn, T.; Sittthiseripratip, K.; Suwanprateeb, J. 3D printing of hydroxyapatite: Effect of binder concentration in pre-coated particle on part strength. *Mater. Sci. Eng. C* 2007, 27, 914–921.
459. Bergmann, C.; Lindner, M.; Zhang, W.; Koczur, K.; Kirsten, A.; Telle, R.; Fischer, H. 3D printing of bone substitute implants using calcium phosphate and bioactive glasses. *J. Eur. Ceram. Soc.* 2010, 30, 2563–2567.
460. Zocca, A.; Gomes, C.M.; Staude, A.; Bernardo, E.; Günster, J.; Colombo, P. SiOC ceramics with ordered porosity by 3D-printing of a preceramic polymer. *J. Mater. Res.* 2013, 28, 2243.
461. Zocca, A.; Elsayed, H.; Bernardo, E.; Gomes, C.M.; Lopez-Heredia, M.A.; Knabe, C.; Colombo, P.; Günster, J. 3D-printed silicate porous bioceramics using a non-sacrificial preceramic polymer binder. *Biofabrication* 2015, 7, 025008. <https://doi.org/10.1088/1758-5090/7/2/025008>.
462. Butscher, A.; Bohner, M.; Hofmann, S.; Gauckler, L.; Müller, R. Structural and material approaches to bone tissue engineering in powder-based three-dimensional printing. *Acta Biomater.* 2011, 7, 907–920. <https://doi.org/10.1016/j.actbio.2010.09.039>.
463. Yang, S.; Leong, K.-F.; Du, Z.; Chua, C.-K. The design of scaffolds for use in tissue engineering. Part II. Rapid prototyping techniques. *Tissue Eng.* 2002, 8, 1–11. <https://doi.org/10.1089/107632702753503009>.

Design principles

464. Deckers, J.; Vleugels, J.; Kruth, J.-P. Additive manufacturing of ceramics: A review. *J. Ceram. Sci. Technol.* 2014, 5, 245–260.
465. Kruth, J.P.; Levy, G.; Klocke, F.; Childs, T.H.C. Consolidation phenomena in laser and powder-bed based layered manufacturing. *CIRP Ann.* 2007, 56, 730–759. <https://doi.org/10.1016/j.cirp.2007.10.004>.
466. Juste, E.; Petit, F.; Lardot, V.; Cambier, F. Shaping of ceramic parts by selective laser melting of powder bed. *J. Mater. Res.* 2014, 29, 2086–2094.
467. Regenfuss, P.; Streek, A.; Hartwig, L.; Klötzer, S.; Brabant, T.; Horn, M.; Ebert, R.; Exner, H. Principles of laser micro sintering. *Rapid Prototyp. J.* 2007, 3, 204–212.
468. Subramanian, K.; Vail, N.; Barlow, J.; Marcus, H. Selective laser sintering of alumina with polymer binders. *Rapid Prototyp. J.* 1995, 21, 24–36.
469. Kruth, J.P.; Mercelis, P.; Van Vaerenbergh, J.; Froyen, L.; Rombouts, M. Binding mechanisms in selective laser sintering and selective laser melting. *Rapid Prototyp. J.* 2005, 11, 26–36.
470. Friedel, T.; Travitzky, N.; Niebling, F.; Scheffler, M.; Greil, P. Fabrication of polymer derived ceramic parts by selective laser curing. *J. Eur. Ceram. Soc.* 2005, 25, 193–197.
471. Kolan, K.C.R.; Leu, M.C.; Hilmas, G.E.; Brown, R.F.; Velez, M. Fabrication of 13-93 bioactive glass scaffolds for bone tissue engineering using indirect selective laser sintering. *Biofabrication* 2011, 3, 025004. <https://doi.org/10.1088/1758-5082/3/2/025004>.
472. Liu, F.-H.; Shen, Y.-K.; Lee, J.-L. Selective laser sintering of a hydroxyapatite-silica scaffold on cultured MG63 osteoblasts in vitro. *Int. J. Precis. Eng. Manuf.* 2012, 13, 439–444.
473. Simpson, R.L.; Wiria, F.E.; Amis, A.A.; Chua, C.K.; Leong, K.F.; Hansen, U.N.; Chandrasekaran, M.; Lee, M.W. Development of a 95/5 poly(L-lactide-co-glycolide)/hydroxylapatite and β -tricalcium phosphate scaffold as bone replacement material via selective laser sintering. *J. Biomed. Mater. Res. Part B Appl. Biomater.* 2008, 84B, 17–25. <https://doi.org/10.1002/jbm.b.30839>.
474. Tan, K.; Chua, C.; Leong, K.; Cheah, C.; Cheang, P.; Bakar, M.A.; Cha, S. Scaffold development using selective laser sintering of polyetheretherketone–hydroxyapatite biocomposite blends. *Biomaterials* 2003, 24, 3115–3123.
475. Wilkes, J.; Hagedorn, Y.C.; Meiners, W.; Wissenbach, K. Additive manufacturing of ZrO₂-Al₂O₃ ceramic components by selective laser melting. *Rapid Prototyp. J.* 2013, 19, 51–57. <https://doi.org/10.1108/13552541311292736>.
476. Griffith, M.L.; Halloran, J.W. Freeform fabrication of ceramics via stereolithography. *J. Am. Ceram. Soc.* 1996, 79, 2601–2608.
477. Zhou, W.; Li, D.; Wang, H. A novel aqueous ceramic suspension for ceramic stereolithography. *Rapid Prototyp. J.* 2010, 16, 29–35.
478. Kirihara, S. Creation of functional ceramics structures by using stereolithographic 3D printing. *Trans. JWRI* 2014, 43, 5–10.
479. Chu, T.M.G.; Orton, D.G.; Hollister, S.J.; Feinberg, S.E.; Halloran, J.W. Mechanical and in vivo performance of porous ceramic implants with controlled architectures. *Biomaterials* 2002, 23, 1283–1293. [https://doi.org/10.1016/S0142-9612\(01\)00243-5](https://doi.org/10.1016/S0142-9612(01)00243-5).
480. Bian, W.; Li, D.; Lian, Q.; Li, X.; Zhang, W.; Wang, K.; Jin, Z. Fabrication of a bio-inspired beta-Tricalcium phosphate/collagen scaffold based on ceramic stereolithography and gel casting for osteochondral tissue engineering. *Rapid Prototyp. J.* 2012, 18, 68–80.
481. Cesarano III, J.; Calvert, P.D. Freeforming Objects with Low-Binder Slurry. U.S. Patent 6027326A, 2000-02-22.
482. Genet, M.; Houmard, M.; Eslava, S.; Saiz, E.; Tomsia, A.P. A two-scale Weibull approach to the failure of porous ceramic structures made by robocasting: Possibilities and limits. *J. Eur. Ceram. Soc.* 2013, 33, 679–688. <https://doi.org/10.1016/j.jeurceramsoc.2012.11.001>.
483. Franco, J.; Hunger, P.; Launey, M.E.; Tomsia, A.P.; Saiz, E. Direct write assembly of calcium phosphate scaffolds using a water-based hydrogel. *Acta Biomater.* 2010, 6, 218–228. <https://doi.org/10.1016/j.actbio.2009.06.031>.
484. Miranda, P.; Pajares, A.; Saiz, E.; Tomsia, A.P.; Guiberteau, F. Fracture modes under uniaxial compression in hydroxyapatite scaffolds fabricated by robocasting. *J. Biomed. Mater. Res. Part A* 2007, 83, 646–655.

485. Fu, Q.; Saiz, E.; Tomsia, A.P. Bioinspired Strong and Highly Porous Glass Scaffolds. *Adv. Funct. Mater.* 2011, 21, 1058–1063. <https://doi.org/10.1002/adfm.201002030>.
486. Dellinger, J.G.; Cesarano III, J.; Jamison, R.D. Robotic deposition of model hydroxyapatite scaffolds with multiple architectures and multiscale porosity for bone tissue engineering. *J. Biomed. Mater. Res. Part A* 2007, 82, 383–394.
487. Grida, I.; Evans, J.R. Extrusion freeforming of ceramics through fine nozzles. *J. Eur. Ceram. Soc.* 2003, 23, 629–635.
488. Park, S.A.; Lee, S.H.; Kim, W.D. Fabrication of porous polycaprolactone/hydroxyapatite (PCL/HA) blend scaffolds using a 3D plotting system for bone tissue engineering. *Bioprocess Biosyst. Eng.* 2011, 34, 505–513. <https://doi.org/10.1007/s00449-010-0499-2>.
489. Kalita, S.J.; Bose, S.; Hosick, H.L.; Bandyopadhyay, A. Development of controlled porosity polymer-ceramic composite scaffolds via fused deposition modeling. *Mater. Sci. Eng. C* 2003, 23, 611–620.
490. Leukers, B.; Güllkan, H.; Irsen, S.; Milz, S.; Tille, C.; Seitz, H.; Schieker, M. Biocompatibility of ceramic scaffolds for bone replacement made by 3D printing. *Mater. Sci. Eng. Technol.* 2005, 36, 781–787.
491. Chhabra, M.; Singh, R. Rapid casting solutions: A review. *Rapid Prototyp. J.* 2011, 17. <https://doi.org/10.1108/13552541111156469>.
492. Detsch, R.; Uhl, F.; Deisinger, U.; Ziegler, G. 3D-Cultivation of bone marrow stromal cells on hydroxyapatite scaffolds fabricated by dispense-plotting and negative mould technique. *J. Mater. Sci. Mater. Med.* 2008, 19, 1491–1496. <https://doi.org/10.1007/s10856-007-3297-x>.
493. Woesz, A.; Rumpfer, M.; Stampfl, J.; Varga, F.; Fratzl-Zelman, N.; Roschger, P.; Klaushofer, K.; Fratzl, P. Towards bone replacement materials from calcium phosphates via rapid prototyping and ceramic gelcasting. *Mater. Sci. Eng. C* 2005, 25, 181–186.
494. Ahlhelm, M.; Günther, P.; Scheithauer, U.; Schwarzer, E.; Günther, A.; Slawik, T.; Moritz, T.; Michaelis, A. Innovative and novel manufacturing methods of ceramics and metal-ceramic composites for biomedical applications. *J. Eur. Ceram. Soc.* 2016, 36, 2883–2888.
495. Ahlhelm, M.; Fruhstorfer, J.; Moritz, T.; Michaelis, A. Die Herstellung von Feuerleichtsteinen über die Gefrier-Direktschäumungsmethode. *Keram. Z* 2011, 63, 6.
496. Ahlhelm, M.; Moritz, T.; Michaelis, A.; Fruhstorfer, J. The manufacturing of lightweight refractories by direct freeze foaming technique; Die Herstellung von Feuerleichtsteinen ueber die Gefrier-Direktschaeumungsmethode. *Keram. Z.* 2011, 63, 405–409.
497. Rieger, W. Ceramics in Orthopedics–30 Years of Evolution and Experience. In *Ceramics in Orthopedics–30 Years of Evolution and Experience*, World Tribology Forum in Arthroplasty; Hans Huber Verlag Bern: Bern, Switzerland; pp. 283–294.
498. Dressman, H. Über knochenplombierung. *Beitr. Klin. Chir.* 1892, 9, 804–810.
499. Chevalier, J.; Gremillard, L. Ceramics for medical applications: A picture for the next 20 years. *J. Eur. Ceram. Soc.* 2009, 29, 1245–1255.
500. Hench, L. An introduction to materials in medicine. *Bioceram. J. Am. Ceram. Soc.* 1998, 81, 1705–1727.
501. Daculsi, G.; Laboux, O.; Malard, O.; Weiss, P. Current state of the art of biphasic calcium phosphate bioceramics. *J. Mater. Sci. Mater. Med.* 2003, 14, 195–200. <https://doi.org/10.1023/a:1022842404495>.
502. Benaqqa, C.; Chevalier, J.; Saâdaoui, M.; Fantozzi, G. Slow crack growth behaviour of hydroxyapatite ceramics. *Biomaterials* 2005, 26, 6106–6112. <https://doi.org/10.1016/j.biomaterials.2005.03.031>.
503. Campbell, P.; Shen, F.W.; McKellop, H. Biologic and tribologic considerations of alternative bearing surfaces. *Clin. Orthop. Relat. Res.* 2004, 418, 98–111. <https://doi.org/10.1097/00003086-200401000-00017>.

Design considerations for patient-specific bone fixation plates

In orthopedic surgery, patient-specific bone plates are used for fixation when conventional bone plates do not fit the specific anatomy of a patient. However, plate failure can occur due to a lack of properly established design parameters that support optimal biomechanical properties of the plate. This review provides an overview of design parameters and biomechanical properties of patient-specific bone plates, which can assist in the design of the optimal plate. A literature search was conducted through PubMed and Embase, resulting in the inclusion of 71 studies, comprising clinical studies using patient-specific bone plates for fracture fixation or experimental studies that evaluated biomechanical properties or design parameters of bone plates. Biomechanical properties of the plates, including elastic stiffness, yield strength, tensile strength, and Poisson's ratio are influenced by various factors, such as material properties, geometry, interface distance, fixation mechanism, screw pattern, working length and manufacturing techniques. These factors affect the performance of bone plates and must be carefully considered during the design and manufacturing process to ensure optimal biomechanical properties and long-term stability. However, variations in boundary conditions of finite element analyses, experimental protocols, and bone types challenge comparison between studies and impede the translation of experimental results to clinical practice.

Brouwer de Koning, S.G., de Winter, N., Moosabeiki, V., Mirzaali, M.J., Berenschot, A., Witbreuk, M.M.E.H., Lagerburg, V., Design considerations for patient-specific bone fixation plates: A literature review, *Medical & Biological Engineering & Computing*, 61(12), pp.3233-3252, 2023.

3.1 Introduction

In the field of orthopedic surgery, plates play a vital role in fixating bones following traumatic injuries or osteotomies. These plates not only provide rigid fixation and accurate repositioning of the fractured parts, but also apply compressive stress and strain at the fracture site to stimulate bone healing [1-3]. During load bearing, plates need to maintain the fractured ends in position while appropriately distributing the load exposed to the fracture. The plate should also allow for more accurate distribution of mechanical signals (*i.e.*, compressive stress and strain) to promote bone healing and bone density adaptation. The plate should prevent stress shielding, that may occur when the plate handles most of the load, and the density of the bone declines [4, 5]. Furthermore, tight fixation of the plate to the bone may affect blood supply, leading to necrosis [6, 7]. To achieve stable bone fixation with satisfactory bone union and complete functional outcome, it is essential to consider these biomechanical requirements during plate design and manufacturing.

Currently, orthopedic surgeons rely primarily on conventional bone plates, which are manufactured using computer numerical control (CNC) techniques in standard shapes and sizes, allowing for immediate use in emergency surgeries and cost-effective production [8, 9]. These plates are typically made of biocompatible metals, such as titanium alloys or stainless steel, which can be sterilized and can withstand high loads [10, 11]. The conventional bone plates are an accepted solution with mostly satisfactory outcomes [10]. Despite this, they are not patient-specific and therefore do not precisely match individual anatomy. In some cases, they can be bent during surgery to improve the fit [2], but biomechanical or anatomical mismatch can still occur, leading to stress concentration and increasing the risk of plate or screw failure, or bone malunions. In such instances, revision surgery may be required [12-15].

Computer-aided-design/computer-aided-manufacturing (CAD/CAM) techniques offer a solution to the mismatch between conventional bone plates and the patient's specific anatomy associated with complex fractures or osteotomies [12, 16]. Using computed tomography, digital three-dimensional (3D) models of the patient's anatomy can be developed to virtually plan the surgery and design bone plates that fit the patient's anatomy precisely. These patient-specific bone plates can be manufactured, for example by 3D-printing, and can be used during surgery [16-19].

In order to achieve optimal bone-plate fixation, it is crucial to optimize the biomechanical properties of the patient-specific bone plate. Such properties include load distribution, elastic stiffness, Poisson's ratio, yield strength and tensile strength [5, 20]. The consideration of these properties is imperative for ensuring the mechanical stability and durability of bone-plate fixation. The modification of these plate biomechanical properties can be achieved by tuning several parameters, including the type of material,

type, number, and position of screws, plate geometry, working length, and gap between the bone and the plate. This literature review provides an overview of design parameters and their impact on biomechanical properties of patient-specific bone plates, to support designers to achieve the desired biomechanical properties for successful bone fixation.

3.2 Methods

A literature search was conducted in the PubMed and Embase databases on September 16th, 2020, and subsequently updated on December 6th, 2022 (PubMed) and December 30th, 2022 (Embase). The search strategy included both indexed and free terms related to computer-aided design, 3D-printing, and patient-specific bone plates, which were used to construct search queries. The resulting database was then de-duplicated. Figure 3.1 shows the process for study selection.

Studies that investigated the use of patient-specific bone plates for fracture fixation or evaluated design parameters through biomechanical testing or finite element analysis (FEA) were included. References of included articles were screened on eligibility for inclusion. Studies that were not medical or studies in which plates were not used for fixation, were excluded. In addition, studies that did not assess plate design or did not provide information on the design of the plate, were excluded. In addition, studies that focused on surgical guides, implants, screws, or total replacements were excluded. Clinical studies that utilized conventional rather than patient-specific bone plates, were ineligible. Also, studies that evaluated conventional bone plates that were pre-bent during surgery, or that presented operative techniques were excluded. Furthermore, studies related to maxillofacial, cranial, and animal studies were excluded. Finally, letters to the editor, review articles, conference abstracts, and studies not available in English were also excluded.

The included studies were systematically categorized according to various parameters that impact the biomechanical properties of the patient-specific bone plates, including material type, geometry, fixation mechanism and manufacturing techniques. Also, reported complications from relevant clinical studies were collected and analyzed.

3.3 Results

The initial search yielded a total of 1,321 articles. Through the screening of article titles and abstracts, 1,000 articles were excluded. Subsequently, the full texts of 295 studies were assessed, resulting in the inclusion of 71 articles, with an additional four identified through reference screening. Of these, 17 articles were clinical studies, while 54 described experimental studies focusing on biomechanical testing or FEA.

Design for fit

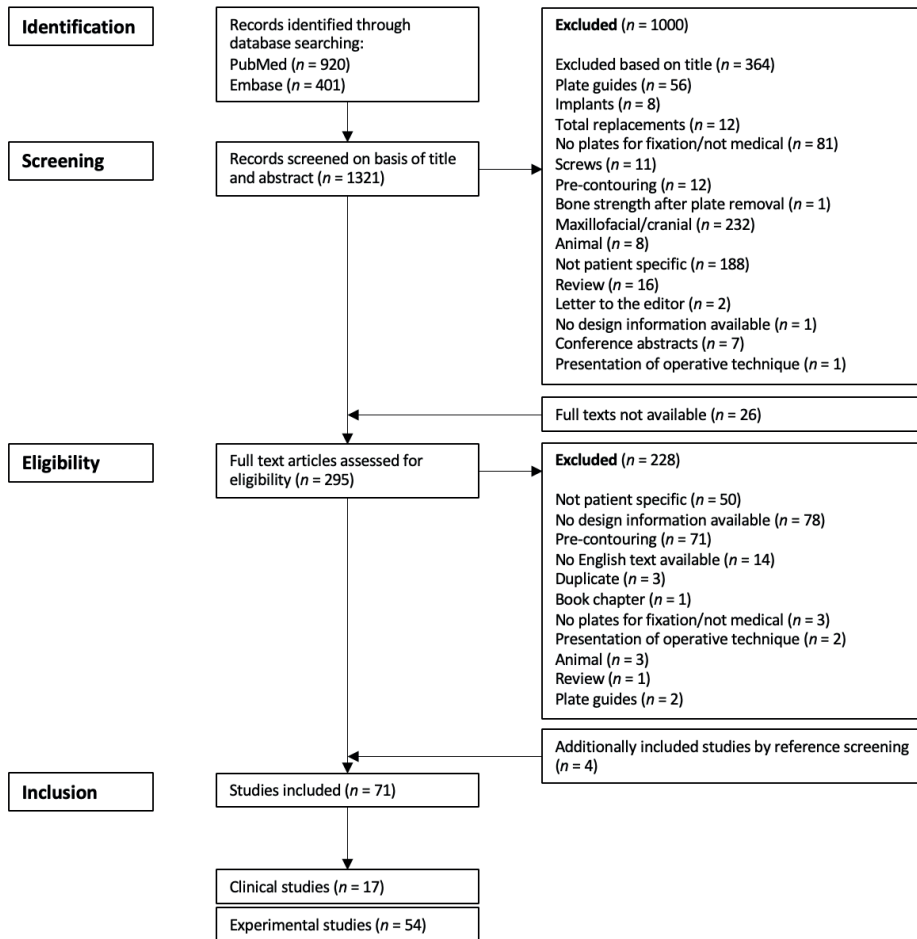


Figure 3.1. Flowchart of the literature search and study selection process

Experimental and FEA studies were conducted to analyze the relationship between design parameters and mechanical properties. The experimental studies included quasi-static and dynamic biomechanical load tests on patient-specific bone plates, using techniques such as axial compression, three-point bending, four-point bending, torsion, tensile testing, and simulations of muscle forces. Literature on patient-specific bone plates described a range of biomechanical properties, including load distribution, Young's modulus, Poisson's ratio, yield strength and tensile strength. Design parameters related to the bone plate include material properties, geometry, fixation mechanism (with details such as working length, interface distance and screw pattern) and manufacturing technique.

3.3.1 Material

The plates were made of various biocompatible materials, including titanium, stainless steel, E-glass/epoxy composite, Carbon Fiber Reinforced PolyEtherEtherKetone (CFR-PEEK), glass fiber reinforced polypropylene, cobalt chromium (Co-Cr), cobalt chromium molybdenum (Co-Cr-Mo), and nitinol (Table 3.1). Young's modulus, yield strength and ultimate tensile strength varied depending on the material, ranging from 1-280 GPa, 111-3,026 MPa, and 10-1,080 MPa, respectively. For example, titanium alloys had a Young's modulus of 105-193 GPa, a yield strength of 140-3,026 MPa and an ultimate tensile strength of 964-1080 MPa. The literature included patient-specific bone plate fixation in various parts of the body, including the femur, tibia, radius, ulna, humerus, spine, pelvis, clavicle and foot. Poisson's ratio, reported by 43 studies, ranged from 0.3 to 0.35 with a median 0.3.

3.3.2 Geometry

Literature on patient-specific bone plates provided information on the geometry of the plates, including shape, length, width, and thickness (Table 3.2). The shape of the plates varied based on the type of bone. For femur fixation, plate length ranged from 65- to 250-mm, whereas the width ranged from 8- to 35-mm and thickness ranged from 2- to 8-mm. For tibia fixation, plate length, width, and thickness ranged from 110- to 180-mm, 4.5- to 25-mm, and 2.5- to 6-mm, respectively. Pelvis plates had a thickness ranging from 3- to 3.5-mm, whereas plates for humerus fixation ranged in thickness from 2- to 4.5-mm. Radius plates were designed with a thickness ranging from 1.9- to 2.5-mm. For the rest of the bone types, only a few studies reported on geometry of the plates (Table 3.2).

3.3.3 Fixation

Studies investigating the biomechanical properties of patient-specific bone plates focused on fixation mechanisms for various bones (*e.g.*, femur, tibia, pelvis, humerus, radius, wrist, clavicle, spine and ulna) as documented in Table 3.3.

The plates were categorized into three main types based on their fixation mechanism: locking plates (LP), dynamic compression plates (DCP) and locking compression plates (LCP). LPs use threaded screw holes to lock the plate to the bone, while DCPs use non-threaded screw holes to allow for compressive loads [21]. LCPs feature both locking and compression screw holes, giving the surgeon greater flexibility to determine the optimal approach for each case [21]. All three types of fixations were utilized for various types of bone (Table 3.3). Pelvic fixation primarily used dynamic compression, while locking fixation was dominant in radius fixation. Clinical studies also evaluated all three types of plates across different types of bone.

The interface distance, *i.e.*, the distance between bone and plate after fixation, reported in literature ranged from 0.0 to 6.0 mm (Table 3.3).

Studies investigated surgical outcomes using different screw patterns (*e.g.*, straight in line, triangular or alternating patterns). In particular, conventional bone plates with a standard arrangement of screw holes (Figure 3.2a) were compared to plates with triangular patterns (Figure 3.2b) or an alternating pattern of screws, in terms of yield strength and stress distribution [1, 22]. In addition, different screw configurations were tested using a conventional straight in-line arrangement of screw holes [23-26].

The number of screw holes used in patient-specific bone plates ranged from 3 to 16 (Table 3.3). For example in femur plates, it was recommended to use 2-5 screw holes on either side of the fracture. Of particular interest was the number of screws used on either side of the fracture, and the working length, which is defined as the length between the first screw at each side of the fracture. The latter ranged from 5 to 102 mm.

Some studies have made recommendations on optimal screw patterns and working length for specific bone types. For example, in femur fixation, several studies recommend a significant working length with limited use of screws close to the gap [21, 24, 27]. An optimal working length for tibia fixation ranged between 38.5- and 62.5-mm [28, 29]. Studies that did not specify the bone type recommend a significant working length and report on an increased flexibility in compression and torsion, with unused holes nearby the gap [30]. This can also reduce the number of screws used significantly [31]. For humerus fixation, at least three screws on each side of the fracture and an increased working length are recommended [9, 32]. In radius fixation, it was found that the number of screws can be reduced to three, with only minor reduction of stiffness and strain when choosing an optimized configuration [33] (Figure 3.3).

3.3.4 Manufacturing techniques

Several studies have investigated manufacturing techniques for patient-specific bone plates, with five studies using conventional techniques in combination with milling ($n = 4$) and one un-specified method (Table 3.4). Besides conventional manufacturing techniques, 3D printing techniques were evaluated in 17 studies for the manufacturing of plates with complex geometries, with various types of powder bed fusion techniques utilized, including selective laser sintering or melting ($n = 10$), direct metal laser melting ($n = 1$), electron beam melting ($n = 2$), laser-based cutting and welding ($n = 1$) and three un-specified methods. Post-processing steps were required for 3D printed plates to enhance fatigue strength and reduce surface roughness [8, 10, 34], with anodizing, polishing, heat treatment, roll casting, acid pickling, and abrasive blasting (Table 3.4). The manufacturing and post-processing time ranged from 24 hours till 7 days.

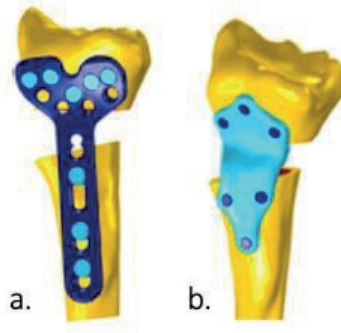


Figure 3.2. (a) Conventional screw pattern (b) triangular screw pattern [1]

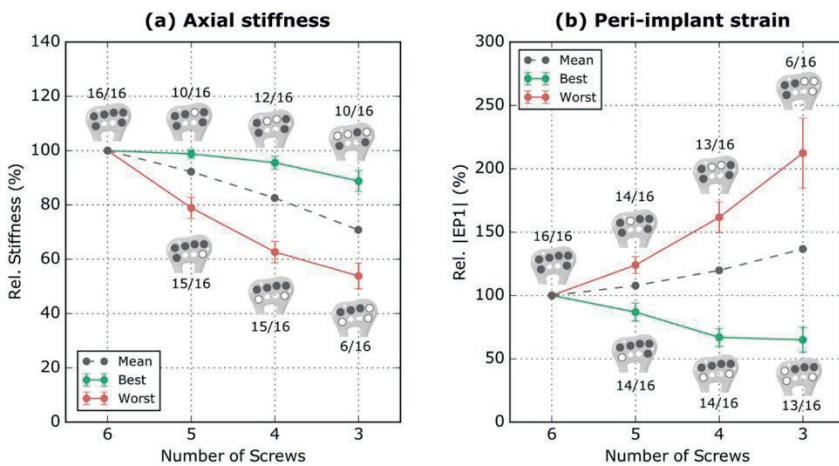


Figure 3.3. Best and worst configurations for each number of screws with respect to axial stiffness (a) and peri-implant strains (b) related to the number of subjects (10/16 means in 10 out of 16 subjects) [33]

3.3.5 Clinical complications

Clinical studies were conducted on various bone plate types, including the plates used for acetabulum/pelvis (104 patients), tibia (5 patients), wrist (30 patients), femur (8 patients), radius (24 patients) and humerus (18 patients). In these patients, patient-specific bone plates ($n = 127$) and conventional bone plates ($n = 65$) were used (Table 3.5). Complications associated with patient-specific bone plates included pain of scar and surrounding tissue, infection, nerve injury, screw loosening, thromboembolism, heterotopic bone ossification, and reduced physical function. For conventional bone plates, complications included wound infection, deep vein thrombosis, traumatic arthritis, nerve injury, and decrease in physical function.

Two studies comparing patient-specific and conventional bone plates showed a decrease in mean surgery time when patient-specific bone plates were used [35, 36].

3.4 Discussion

Orthopedic surgery is increasingly interested in using patient-specific bone plates to fix bones, particularly when conventional plates are not suitable for certain anatomies. Although patient-specific plates are associated with safe outcomes, there is a risk of plate failure due to the lack of established design parameters that support optimal biomechanical properties of the plate. This literature review provides an overview of design parameters and in this discussion section the impact of the design parameters on biomechanical properties of patient-specific bone plates will be discussed, to assist designers in manufacturing optimal bone plates.

To ensure optimal biomechanical properties, the patient-specific bone plate should ideally resemble the properties of bone. The properties of bone are modified on their function in the skeleton, which is dependent on the loading conditions applied to that specific bone. Similarly, the design and properties of a bone plate must match the biomechanical requirements of the specific bone and loading conditions to achieve optimal fixation. Physiological loading conditions on the plate vary per fixated bone, with higher loads to withstand for lower extremity plate fixation compared to upper extremity plate fixation. The daily life load ranges between 0.5 and 400% of the patient's bodyweight, *e.g.* 700 N for full weight bearing [27, 37-39, 61]. Unfortunately, this review found insufficient data on bone-specific studies to provide an accurate recommendation for Young's moduli per bone type. However, it is essential to consider bone-specific Young's modulus when developing plates with biomechanical properties that match the type of bone for future purposes. Studies report a higher range of yield- and tensile strength for titanium alloys compared to stainless steel, indicating that titanium alloys can tolerate a higher maximum stress before undergoing plastic deformation and can withstand a higher stress before failing. Composite materials, in general, have a lower yield- and tensile strength, making them less suitable for fixating high load-bearing bones (*e.g.*, femur and tibia), and are therefore not yet used in clinical practice [23, 41].

To promote bone union, it is important for the stiffness of bone plates to be as close as possible to that of bone, to reduce the risk of stress shielding. To achieve this, some studies have attempted to reduce the materials' stiffness to approximate that of bone. For example, Yan et al. performed a material sweep in FEA to reduce the elastic stiffness of a stainless-steel plate (with an original elastic stiffness of 193 GPa) to an elastic stiffness more closely resembling bone. When subjected to 100% body weight, a plate with an elastic stiffness of 20 GPa failed, while a 50 GPa plate was the limit of failure [22]. Composite materials have also been investigated to reduce plate (elastic) stiffness. Chakladar et al. reported a composite (E-glass/epoxy composite) with an elastic stiffness within 8% of bone (elastic) stiffness, in theory strong enough to allow for ulnar fixation but not for high weight-bearing bone types [23].

Poisson's ratio characterizes the deformation of a plate in response to strain and has an average value of 0.3 for both cortical and cancellous bone [1, 2, 9, 24, 27, 30, 31, 40]. The range of Poisson's ratio for the plates reported in the literature varied from 0.3 to 0.35 with a median 0.3. The Poisson's ratio can be achieved by careful design of the structure of the plate.

Geometry is another important factor affecting the biomechanical properties of bone plates. Plate length, width, and thickness all have an impact on plate compliance, interfragmentary strain, and callus formation. A short plate can result in increased stress concentration on both plate and bone, while a longer plate is more compliant and induces callus formation [1, 40, 42]. In addition, a thicker and wider plate generally results in a higher Young's modulus [23, 43]. From a clinical point of view, there is a trade-off between the stiffness and stability of the plate and its size, as a smaller plate is preferred to minimize the incision size and reduce the chances of infection of surrounding tissue [41, 44].

Carefully considering the geometry of a patient-specific bone plate can help reduce local stress concentrations on the plate. For example, MacLeod et al. increased the width and thickness of the plate around the screw holes and gave it a slight curve, resulting in a more even distribution of stress over the plate, and a reduction of strain per bone volume [31]. Other studies have investigated optimizing plate properties by using shapes such as a "dog bone" plate or a plate with increasing width from proximal to distal [8, 13, 43].

Different fixation mechanisms are used for bone plate fixation. The DCP is designed to be pressed tightly against the bone using non-threaded screw holes, promoting primarily healing. In contrast, the LP uses threaded screw holes for a secure fixation, resulting in a mechanically stable plate [36, 40, 45]. LPs also allow for an interface distance to promote callus formation and decrease the risk of bone necrosis [20, 22, 27, 38]. In addition, these plates do not require an exact patient-specific fit [22, 27]. LPs are less prone to screw loosening but may lead to prolonged healing [11, 45]. LCPs combine the benefits of both DCP and LP, allowing for compression and stable fixation. They have pre-drilled holes for both non-threaded and threaded screws [21, 45]. For example, Yan et al. designed a plate with locking screws for angular screw fixation, combination holes where both non-locking and locking screws could be used, in a design that allows an interface distance to maximize perfusion and callus forming [22]. Nevertheless, material type should be considered when selecting a fixation mechanism, as it was found that partially removing the threads of a titanium LP improved the plate's fatigue strength due to notch sensitivity [11, 46]. All three types of fixation mechanisms have been in use in practice, and plate failures and complications exist for each [27, 38, 45]. Kimsal et al. conducted a FEA to compare LPs and DCPs and found that an LP could withstand higher loads than a DCP [40]. However, it was not clear if this was a result of the fixation

mechanism or the geometrical differences between the plates. LPs are more expensive than DCPs [47], and an optimal fixation mechanism has not been established in literature.

The interface distance refers to the distance between the bone and plate after fixation and is dependent on the anatomical fit of the plate, anatomical location of the fracture, and the type of fixation mechanism used (*e.g.*, LP, DCP or LCP) [20]. A smaller interface distance increases stiffness but interferes with the vascularization of the periosteum, thereby increasing the risk of bone necrosis [20, 38]. On the other hand, a larger interface distance increases compliancy, inducing strain at the fracture gap and promoting callus formation [12, 34, 38, 48]. Fixated plates with interface distances smaller than 2.0 mm could withstand the applied mechanical loads [12, 20, 34, 38]. Ahmad et al. and Stoffel et al. reported on plate instability caused by a decline in axial stiffness and torsional rigidity resulting from a 5.0- and 6.0-mm interface distance [30, 38]. Ghimire et al. also found a delayed healing or even a non-union when an interface distance of 4.0 mm was found [34].

Enlarging the working length by removing the screw adjacent to the fracture resulted in a reduction of 64% and 36% of axial stiffness and torsional rigidity, respectively [25, 26, 30, 34]. Every subsequent screw removal reduced axial stiffness and torsional rigidity by an additional 10%. Maximum stress was observed around the screw holes closest to the fracture gap within the plate. By solidifying these screw holes, the working length increases and the stress that was initially concentrated around the holes closest to the fracture gap are now distributed over the whole working length of the plate instead [2, 12, 13, 22, 24, 31, 34]. In addition, the working length must be adjusted to the size of the fracture and the interface distance of the plate, as instability increases with a larger fracture combined with a longer working length, and a larger interface distance requires a smaller working length [34].

Yield strength and stress distribution improved when a triangular or alternating pattern of screws was used [1, 22]. There was no effect on axial stiffness when more than three screws were used proximally and distally from the fracture [30]. Torsional rigidity did not increase with more than four screws on both sides of the fracture.

Conventional plates were compared to 3D printed plates, and the latter showed comparable or increased elastic stiffness, yield strength and hardness [8-10, 44, 49, 50]. In terms of post-processing, *e.g.*, heat treatment of the 3D printed plates was necessary to achieve comparable fatigue strength to conventional plates [8]. Residual stresses in the 3D printed parts can occur because of the 3D printing process. This could affect the fatigue strength of the implant and can also result in warping. Heat treatment can reduce these residual stresses. Furthermore, 3D printed plates need to be polished to remove support structures of the printing and to obtain a smooth surface that prevents infection, friction at bone-plate interface, and bone ingrowth [10, 44]. Despite these positive results, 3D printing technology is still new, and further research is required to evaluate the

biomechanical behavior of 3D printed plates and establish optimal parameters (*e.g.*, build orientation, processing protocols, and post-processing techniques) [9, 37, 51]. However, 3D printed patient-specific implants have been used in surgery, with limited postoperative complications [37].

Three studies compared clinical outcomes between patients who received conventional bone plates and those who received patient-specific bone plates [35, 36, 50]. The rate of anatomical reduction was higher in the patient-specific bone plate group, and fewer complications were observed [36, 50, 52]. In addition, patients who underwent surgery with a patient-specific bone plate had a shorter mean operation time. This was attributed to the need for prebending of conventional bone plates during surgery [35, 36].

This review provides an overview of different design parameters for bone plates, but the results should be interpreted carefully for several reasons. The studies included in this literature review did not investigate a single parameter, but rather a combination of parameters to design the desired plate. The variations in the combination of parameters evaluated, challenge the establishment of the effect on biomechanical properties of the plate because of a single parameter. Also, the extend of simplification of boundary conditions in FEA and experimental protocol and setup, varied between studies, which challenges the comparison of outcomes between studies. Furthermore, it is yet unclear to what extent the experimental results are applicable to the clinical setting. The clinical papers showed safe and effective use of patient-specific bone plates [35, 53], but how the experimental findings relate to the clinic is not yet clear. Future studies should aim to establish standard protocols for testing and evaluating patient-specific bone plates to improve their clinical translation.

This paper focused on design parameters for patient-specific bone plates in orthopedic surgery, excluding findings reported by maxillofacial and cranial studies while these disciplines have a lot of experience with bone plate fixations. Also, the effect of screw length and diameter were not included in this study since the focus was on plate properties themselves.

3.5 Conclusion

The biomechanical properties of bone plates, including elastic stiffness, yield strength, tensile strength, and Poisson's ratio, are determined by a combination of factors, such as material properties, geometry, interface distance, fixation mechanism, screw placement, working length, and manufacturing techniques. This review serves as a useful reference guide for determining which parameters should be adjusted to achieve the desired biomechanical properties of a plate for fixation of a specific type of fracture.

Table 3.1. Biomechanical properties of bone plate materials reported in the literature based on experimental testing or finite element analysis (FEA)

Author, year	Type	Bone type	Young's modulus [GPa]	Poisson's ratio	Yield strength [MPa]	Tensile strength [MPa]	Experimental biomechanical testing	FEA
Titanium alloy								
Caiti <i>et al.</i> , 2019 [1]	Ti6Al4V	Radius	110	0.35	1060			Axial compression; Bending moments; Torsion
Chen <i>et al.</i> , 2018 [2]	Ti6Al7Nb	Femur	123	0.3				Axial compression
Chung <i>et al.</i> , 2018 [27]		Femur	110	0.3				Axial compression; Torsion
Fan <i>et al.</i> , 2017 [12]	Ti6Al4V	Femur	115	0.3	800			Muscle forces
Freitas <i>et al.</i> , 2021 [54]		Femur	193	0.33				Axial compression
Gupta <i>et al.</i> , 2021 [55]	Ti6Al4V	not specified			743	964	Tensile and 3 point bend tests	
Kaymaz <i>et al.</i> , 2022 [56]	Ti6Al4V	Humerus	110	0.31			Compression testing	Compression in x-, y- and z-direction
Kim <i>et al.</i> , 2017 [49]	Ti6Al4V	Radius			783-1114		Axial compression	
Kimshah <i>et al.</i> , 2015 [40]		Tibia	110	0.34	207			Axial compression
Lin <i>et al.</i> , 2018 [46]	Ti6Al4V				862	910	4 point bending test	
Liu <i>et al.</i> , 2014 [10]	Ti6Al4V	Clavicle			1347-3026		4 point bending test	

Table 3.1. (continued)

Author, year	Type	Bone type	Young's modulus [GPa]	Poisson's ratio	Yield strength [MPa]	Tensile strength [MPa]	Experimental biomechanical testing	FEA
Macleod <i>et al.</i> , 2018 [31]	Ti6Al4V	Tibia			789-1013		Axial compression	Muscle forces
Munch <i>et al.</i> , 2022 [29]		Tibia	110	0.3			Compression testing	Medial-lateral compression
Samsami <i>et al.</i> , 2022 [57]		Tibia					Quasistatic and cyclic loading	
Schader <i>et al.</i> , 2022 [58]		Humerus	105	0.3				Shoulder abduction and flexion in several degrees
Shams <i>et al.</i> , 2022 [59]	Ti6Al4V	Femur	113,8	0.33	839,9			Axial compression
Smith <i>et al.</i> , 2016 [8]	Ti6Al4V ELI	Foot			877-897	916-937	3 point bending test	
Sokol <i>et al.</i> , 2011 [47]		Radius				472-826	Axial compression	
Soni <i>et al.</i> , 2020 [39]	Ti6Al4V	Femur	110	0.33	825	1080		Axial compression
Stoffel <i>et al.</i> , 2003 [30]			115	0.34			Axial compression; Torsion	Axial compression; Torsion
Synek <i>et al.</i> , 2021 [33]		Radius	105	0.34				Axial compression
Reina-Romo <i>et al.</i> , 2014 [24]	Ti6Al7Nb	Femur	123	0.31				Muscle forces

Table 3.1. (continued)

Author, year	Type	Bone type	Young's modulus [GPa]	Poisson's ratio	Yield strength [MPa]	Tensile strength [MPa]	Experimental biomechanical testing	FEA
Thomrungriyathan <i>et al.</i> , 2021 [32]	Ti6Al4V	Humerus	110	0.34	1025			Axial compression
Tseng <i>et al.</i> , 2016 [11]	Ti6Al4V	Femur	110	0.3			4 point bending test	4 point bending test
Vancleef <i>et al.</i> , 2022 [60]	Ti6Al4V	Clavicle	115	0.3				Unloaded and loaded antelexion and abduction
Wang <i>et al.</i> , 2017 [44]	Ti6Al4V	Pelvis			900	1000	Hardness	
Wang <i>et al.</i> , 2020 [61]	Ti6Al4V	Tibia	110	0.3				700 N for full weight bearing
Wang <i>et al.</i> , 2022 [62]	Ti6Al4V	Spine	110	0.3				Axial compression
Yao <i>et al.</i> , 2021 [63]		Foot	110	0.3				Axial compression
Stainless steel								
Chakladar <i>et al.</i> , 2016 [23]		Ulna	280	0.33			3 point bending test	3 point bending test
Chung <i>et al.</i> , 2018 [27]		Femur	210	0.3				Axial compression; Torsion
Fan <i>et al.</i> , 2018 [12]		Femur	196	0.33	310			Muscle forces

Table 3.1. (continued)

Author, year	Type	Bone type	Young's modulus [GPa]	Poisson's ratio	Yield strength [MPa]	Tensile strength [MPa]	Experimental biomechanical testing	FEA
Kanchanomai <i>et al.</i> , 2010 [21]	316L	Femur	193			595	Axial compression; 4 point bending test	
Kimshah <i>et al.</i> , 2015 [40]	316L	Tibia	205	0.3	207			Axial compression
Murat <i>et al.</i> , 2021 [65]		Humerus	193	0.3			Axial compression	Axial compression
Olender <i>et al.</i> , 2011 [43]	AISI 304		193	0.3			4 point bending test	4 point bending test
Peleg <i>et al.</i> , 2006 [66]		Femur			111		Axial compression	Axial compression
Reina-Romo <i>et al.</i> , 2014 [24]	316L	Femur	193	0.3				Muscle forces
Soni <i>et al.</i> , 2020 [39]	316L	Femur	200	0.3	290	580		Axial compression
Stoffel <i>et al.</i> , 2003 [30]			220	0.34			Axial compression; Torsion	Axial compression; Torsion
Teo <i>et al.</i> , 2022 [67]	316L	Tibia					Loaded cyclically from 100 N to 3 times body weight	
Tilton <i>et al.</i> , 2020 [9]	316L	Humerus	193	0.3			Axial compression; Torsion	Axial compression; Torsion
Tseng <i>et al.</i> , 2016 [11]	F138, F1314	Femur	200	0.3			4 point bending test	4 point bending test

Table 3.1. (continued)

Author, year	Type	Bone type	Young's modulus [GPa]	Poisson's ratio	Yield strength [MPa]	Tensile strength [MPa]	Experimental biomechanical testing	FEA
Wee <i>et al.</i> , 2017 [25]		Femur	200	0.3			Axial compression; Torsion	Axial compression; Torsion
Yan <i>et al.</i> , 2020 [22]	316L	Tibia	193	0.3	690	860		Axial compression
Other								
Chakladar <i>et al.</i> , 2016 [23]	E-glass/epoxy	Ulna	15	0.3			3 point bending test	3 point bending test
Chung <i>et al.</i> , 2018 [27]	CFR-PEEK	Femur	50	0.3				Axial compression; Torsion
Kabiri <i>et al.</i> , 2021 [68]	Glass fiber reinforced	Tibia	1-20,1	0.1-0.35		10-400	Density, tensile, compression, four-point bending, shear and	
Nobari <i>et al.</i> , 2010 [42]	Cobalt-chromium	Femur	200	0.3				Mediolaral and anteroposterior force; Axial compression
Ren <i>et al.</i> , 2022 [69]	not specified	Tibia	110	0.3				Axial compression
Soni <i>et al.</i> , 2020 [39]	Co-Cr-Molybdenum	Femur	100	0.3		720		Axial compression
Olender <i>et al.</i> , 2011 [43]	Nitinol		23	0.33			4 point bending test	4 point bending test
Wang <i>et al.</i> , 2020 [70]	not specified	Femur	200	0.3				Axial compression

Table 3.2. Geometry of bone plates per bone type.

Bone type	Author, year	Shape	Recommended measures as a result of the research		
			Length [mm]	Width [mm]	Thickness [mm]
Femur	Amone <i>et al.</i> , 2013 [41]		5.5		
	Chen <i>et al.</i> , 2018 [2]		126.6 ± 6.5	3	
	Chen <i>et al.</i> , 2017 [13]	Three different widths for proximal, middle and distal	132.1	17, 22.5, 34.5	2, 4, 5
	Chung <i>et al.</i> , 2018 [27]		70	8	4
	Fan <i>et al.</i> , 2017 [12]				4.75 (Titanium); 5.25 (Stainless steel)
	Kanchanomai <i>et al.</i> , 2010 [21]		250		
	Nobari <i>et al.</i> , 2010 [42]	Short, wide and thick	65	35	07-Aug
	Shams <i>et al.</i> , 2022 [59]				5
	Tseng <i>et al.</i> , 2016 [11]		130	18	5.05
	Wee <i>et al.</i> , 2017 [25]			4.5	4

Table 3.2. (Continued)

Bone type	Author, year	Shape	Recommended measures as a result of the research		
			Length [mm]	Width [mm]	Thickness [mm]
Femur	CLINICAL: Ma et al., 2017 [52]				6
Tibia	Kabiri et al., 2021 [68]				5.5
	Kimshal et al., 2015 [40]	Short plates inferior to longer plates			3, 3.75
	Macleod et al., 2018 [31]	Thicker and wider around screw holes			
	Petersik et al., 2018 [20]				
	Ren et al., 2022 [69]	L-shaped			3.5
	Shin et al., 2022 [71]	Straight			2.5
	Wee et al., 2017 [25]			5	4
	Yan et al., 2020 [22]			5	
	Wang et al., 2020 [61]				4

Table 3.2. (Continued)

Bone type	Author, year	Shape	Recommended measures as a result of the research		
			Length [mm]	Width [mm]	Thickness [mm]
No type specified	Ghimire <i>et al.</i> , 2019 [34]			17.5	5.2
	Gupta <i>et al.</i> , 2021 [55]	Straight	70	17.5	3
	Lin <i>et al.</i> , 2018 [46]			18	5.05
	Olender <i>et al.</i> , 2011 [43]	Dogbone: thin in middle of the plate	53	6	
Pelvis	Stoffel <i>et al.</i> , 2003 [30]				4.5
	Wang <i>et al.</i> , 2017 [44]			10	3-3.5
	Wen <i>et al.</i> , 2020 [72]				3
	CLINICAL: Wang <i>et al.</i> , 2020 [50]				3-3.5
Wrist	CLINICAL: Del Pino <i>et al.</i> , 2014 [73]		94	6, 8.1	2.5
	CLINICAL: Sodl <i>et al.</i> , 2002 [74]			6, 8	

Table 3.2. (Continued)

Bone type	Author, year	Shape	Recommended measures as a result of the research		
			Length [mm]	Width [mm]	Thickness [mm]
Humerus	Ahmad <i>et al.</i> , 2007 [38]				4.5
	Murat <i>et al.</i> , 2021 [65]	Density variation in a porous plate			
	Thomrungruyathan <i>et al.</i> , 2021 [32]	Addition of a lateral brim with a lateral-medial linking screw	10		2
	Tilton <i>et al.</i> , 2020 [9]				3.5
Foot	Smith <i>et al.</i> , 2016 [8]	Dogbone: thin in middle of the plate			
	CLINICAL: Yao <i>et al.</i> , 2021 [63]	Increased bottom width			3.5
Clavicle	Liu <i>et al.</i> , 2014 [10]				3.5
	Vanceleef <i>et al.</i> , 2022 [60]				1.5
Spine	Peterson <i>et al.</i> , 2018 [75]	Material removed from center of the plate to lower stiffness			
	Wang <i>et al.</i> , 2022 [62]	Palm-leaf fan-shaped	32	22	5

Table 3.2. (Continued)

Bone type	Author, year	Shape	Recommended measures as a result of the research		
			Length [mm]	Width [mm]	Thickness [mm]
Radius	Caiti <i>et al.</i> , 2019 [1]				1.9
	Kim <i>et al.</i> , 2017 [49]				2.5
	Synek <i>et al.</i> , 2021 [33]				2
Ulna	Chakladar <i>et al.</i> , 2016 [23]		78	9—12	4.25, 4.85

Table 3.3. Fixation mechanisms, interface distance, screw pattern, working length, and final optimized geometry categorized per bone type.

Bone type	Author, year	Fixation mechanism	Interface distance [mm]	Screw Pattern	Number of screw holes	Working length [mm]	Final optimization
Femur	Chung <i>et al.</i> , 2018 [27]	Locking compression	0.0-2.0			May-40	Working length composite ≤ 20 mm vs titanium ≤ 15 mm vs steel ≤ 30 mm
	Amone <i>et al.</i> , 2013 [41]	Locking					
	Fan <i>et al.</i> , 2018 [12]	Locking	0.0; 1.0; 2.0				
	Freitas <i>et al.</i> , 2021 [54]			Sliding hip screw, L-shaped and L-shaped			Sliding hip screw and L-shaped with medial plate
	Kanchanomai <i>et al.</i> , 2010 [21]	Locking compression			14	1) 2 holes closest to gap	8 holes closest to gap unused
	Märdian <i>et al.</i> , 2015 [26]	Locking		Different configurations of 4 proximal screws	13 proximal and 7 distal	42; 62; 82; 102	3 screws on either side
	Nobari <i>et al.</i> , 2010 [42]				04-Oct		2-5 screw holes on either side
	Peleg <i>et al.</i> , [2006] [66]	Dynamic compression		Distal	2; 4		Long plate; 4 distal screws
	Reina-Romo <i>et al.</i> , 2014 [24]	Locking compression		Proximal: 3-6; Distal: 8	Nov-14		All holes used vs hole or 2 holes closest to gap unused
	Tseng <i>et al.</i> , 2016 [11]	Locking			3		Non-threaded holes
Wang <i>et al.</i> , 2020 [76]	Dynamic compression		Straight	2-hole, 4-hole and 6-hole		4-hole or 6-hole	

Table 3.3. (Continued)

Bone type	Author, year	Fixation mechanism	Interface distance [mm]	Screw Pattern	Number of screw holes	Working length [mm]	Final optimization
Femur	Wang <i>et al.</i> , 2021 [77]		0.16				
	Wee <i>et al.</i> , 2017 [25]	Locking compression	1	various	Aug-16	various	
Tibia	CLINICAL: Ma <i>et al.</i> , 2017 [52]	Locking					
	Kabiri <i>et al.</i> , 2021 [68]				6		
	Kimshah <i>et al.</i> , 2015 [40]	Dynamic compression Locking					
	Macleod <i>et al.</i> , 2018 [31]	Locking			7; 8	33; 50	7 screw holes; 50 mm working length
	Munch <i>et al.</i> , 2022 [29]	Locking					
	Petersik <i>et al.</i> , 2018 [20]	Locking compression	0.9-2.41				
	Samsami <i>et al.</i> , 2022 [57]	Locking					
	Shin <i>et al.</i> , 2022 [71]	non locking					
Teo <i>et al.</i> , 2021 [78]	Locking						

Table 3.3. (Continued)

Bone type	Author, year	Fixation mechanism	Interface distance [mm]	Screw Pattern	Number of screw holes	Working length [mm]	Final optimization
Tibia	Yan <i>et al.</i> , 2020 [22]	Locking compression		Straight/alternating	6	2 holes closest to gap unused	Alternating pattern and 2 holes closest to gap unused
	Wang <i>et al.</i> , 2020 [61]	Locking plate with locking and dynamic holes		Straight	8 or 10 holes	6.5 + 4 mm steps up to 62.5	Working length: >38.5 mm and <62.5 mm
	CLINICAL: Bastias <i>et al.</i> , 2014 [45]	Dynamic compression Locking compression					
	CLINICAL: Ma <i>et al.</i> , 2017 [52]	Locking					
No type specified	Gardner <i>et al.</i> , 2010 [79]	Locking compression Locking			10		Hole at gap unused and use of multi-holes
	Ghimire <i>et al.</i> , 2019 [34]	Locking compression	0.0; 2.0; 4.0		11	30; 100	100 mm working length with interface distance \leq 2 mm
	Lin <i>et al.</i> , 2018 [46]	Locking			3		Half or 1/3 of screw threads removed
	Stoffel <i>et al.</i> , 2003 [30]	Locking compression	2.0; 6.0	6; 8; 12 screws in various patterns	12		1) all holes used 3 screws on either side 2) twice as flexible compared to 1) in compression and torsion
Pelvis	Wang <i>et al.</i> , 2017 [44]	Dynamic compression					2) 2 holes closest to gap unused 3) 4 holes closest to gap unused
	Wen <i>et al.</i> , 2020 [72]	Dynamic compression					
	CLINICAL: Wu <i>et al.</i> , 2020 [36]	Dynamic compression					

Table 3.3. (Continued)

Bone type	Author, year	Fixation mechanism	Interface distance [mm]	Screw Pattern	Number of screw holes	Working length [mm]	Final optimization
Pelvis	CLINICAL: Xu <i>et al.</i> , Locking 2014 [80]						
Wrist	CLINICAL: Del Pino <i>et al.</i> , 2014 [73]	Locking compression					
	CLINICAL: Sodl <i>et al.</i> , 2002 [74]	Dynamic compression					
Humerus	Ahmad <i>et al.</i> , 2007 [38]	Dynamic compression Locking compression	0.0; 2.0; 5.0		7		
	Murat <i>et al.</i> , 2021 [65]			Straight	4		Subject-specific optimization of screw orientation leads to lower cutout risk and improved fixation
	Schader <i>et al.</i> , 2022 [58]	Locking		6 proximal screws with 3 shaft screws			
	Thomrungpiyathan <i>et al.</i> , 2021 [32]						
	Tilton <i>et al.</i> , 2020 [9]	Locking					
Clavicle	Liu <i>et al.</i> , 2014 [10]	Locking compression					
	Vancleef <i>et al.</i> , 2022 [60]		0.47	screws were positioned equidistance from each			
	Zhang <i>et al.</i> , 2019 [64]	Locking		Straight	6	2 holes closest to gap unused	2 holes closest to gap unused

Table 3.3. (Continued)

Bone type	Author, year	Fixation mechanism	Interface distance [mm]	Screw Pattern	Number of screw holes	Working length [mm]	Final optimization
Spine	Brodke <i>et al.</i> , 2001 [48]	Dynamic compression Locking					
	Peterson <i>et al.</i> , 2018 [75]	Dynamic compression			4		4 screw holes
	Wang <i>et al.</i> , 2022 [62]	Locking			4		
	Caiti <i>et al.</i> , 2019 [1]	Locking compression		Straight vs Triangular	9 vs 6		Triangular pattern, 6 screw holes
Radius	Kim <i>et al.</i> , 2017 [49]	Locking			11		Hole diameter of 2.5 mm
	Sokol <i>et al.</i> , 2011 [47]	Locking			10		10 screw holes
Ulna	Synek <i>et al.</i> , 2021 [33]	Locking		6, 5, 4, 3 distal screws			up to 3 screws could be removed with only minor reduction of stiffness and strain
	CLINICAL: Dobbe <i>et al.</i> , 2014 [37]	Locking					
	Chakladar <i>et al.</i> , 2016 [23]	Locking compression	0.5	15 combinations of 6	8		Pattern I an IX (Fig. 15)

Table 3.4. Manufacturing- and post-processing methods per bone type.

Bone type	Author, year	Manufacturing method	Post-processing	Time to develop
Femur	CLINICAL: Ma <i>et al.</i> , 2017 [52]	CNC with milling	Polishing; Anodizing	
Tibia	Kabiri <i>et al.</i> , 2021 [68]	Hot press or 3D print		
	Macleod <i>et al.</i> , 2018 [31]	Selective laser sintering		
	Shin <i>et al.</i> , 2022 [71]	Powder bed fusion	removal of supporter, surface finishing using hand piece and blasting with ceramic microbeat	24 hours and 7 min
	Teo <i>et al.</i> , 2021 [78]	Selective laser melting		24 hours
	Teo <i>et al.</i> , 2022 [67]		Support removal and beat blasting	
	CLINICAL: Jeong <i>et al.</i> , 2022 [81]	CNC with milling	Polishing; Anodizing	
No type specified	Gupta <i>et al.</i> , 2021 [55]	Selective laser melting	repeated cyclic heating and cooling below the β -transus temperature, and milling	
	Olender <i>et al.</i> , 2011 [43]	Laser cutting and welding		
Pelvis	Wang <i>et al.</i> , 2017 [44]	Selective laser melting	Vacuum heat treatment; Anodizing	24 hours

Table 3.4. (Continued)

Bone type	Author, year	Manufacturing method	Post-processing	Time to develop
Pelvis	Wen <i>et al.</i> , 2020 [72]	Selective laser melting		
	CLINICAL: Ijima <i>et al.</i> , 2021 [82]	5-axes milling		< 4 days
	CLINICAL: Merema <i>et al.</i> , 2017 [53]	CNC with milling		3 days
	CLINICAL: Wang <i>et al.</i> , 2020 [50]	Selective laser melting; CNC	Heat treatment; Roll casting; Acid pickling; Polishing; Anodizing	3.5 days
	CLINICAL: Xu <i>et al.</i> , 2014 [80]	CNC with milling	Polishing; Anodizing	
Humerus	Kaymaz <i>et al.</i> , 2022 [56]	Selective laser melting		
	Murat <i>et al.</i> , 2021 [65]	Selective laser melting		
	Thomrungriyathian <i>et al.</i> , 2021 [32]	Selective laser melting	Heat treatment	3-5 days
Clavicle	Tilton <i>et al.</i> , 2020 [9]	Laser powder bed fusion with forging	Heat treatment	13 hours
	Liu <i>et al.</i> , 2014 [10]	Electron beam melting		
Radius	Kim <i>et al.</i> , 2017 [49]	Direct metal laser melting	Abrasive blasting with zirconia	13 hours

Table 3.4. (Continued)

Bone type	Author, year	Manufacturing method	Post-processing	Time to develop
Foot	Edelmann <i>et al.</i> , 2020 [83]	Selective laser melting	Stress relief annealing	
	Smith <i>et al.</i> , 2016 [8]	Selective laser melting	Polishing; Anodizing	
	CLINICAL: Yao <i>et al.</i> , 2021 [63]	Electron beam melting	Trimmed, polished and anodized	3-7 days

Table 3.5. Clinical studies reporting on patient-specific bone plates used in patients with reported number of patients, mean follow-up, postoperative complications and mean surgery time.

Bone type	Author, year	Patient-specific/ conventional	Number of patients	Mean follow-up [months]	Postoperative complications	Mean surgery time [min]
Femur	Ma <i>et al.</i> , 2017 [52]	Patient-specific	8	29.3	1 infection and 1 nerve injury	272
	Jeong <i>et al.</i> , 2022 [81]	Patient-specific	1	1.5	None	65
Tibia	Ma <i>et al.</i> , 2017 [52]	Patient-specific	4	29.3	1 infection and 1 nerve injury	272
	Ijpm <i>et al.</i> , 2021 [82]	Patient-specific		12	1 deep wound infection; 1 plate removal at patients request; 4 patients reported some decrease in physical function after 1	
Pelvis	Merema <i>et al.</i> , 2017 [53]	Patient-specific	1	3	None	
	Wang <i>et al.</i> , 2020 [50]	Patient-specific			1 screw loosening	
Radius		Conventional			1 wound infection; 1 deep vein thrombosis; 1 traumatic arthritis; 2 obturator nerve injuries	223
	Wu <i>et al.</i> , 2020 [36]	Patient-specific		35.2	None	260
Humerus		Conventional		36.9	None	
	Xu <i>et al.</i> , 2014 [80]	Patient-specific		30.8	1 preoperative bending; 1 pneumonia; 1 thromboembolism; 1 sciatic nerve injury; 1 superficial infection; 1 heterotopic bone	
	Sodl <i>et al.</i> , 2002 [74]	Patient-specific	5	26	1 Carpal tunnel syndrome	

Table 3.5. (Continued)

Bone type	Author, year	Patient-specific/ conventional	Number of patients	Mean follow-up [months]	Postoperative complications	Mean surgery time [min]
Humerus	Shuang <i>et al.</i> , 2016 [35]	Patient-specific	6	10.6	None	70
		Conventional	7		1 poor Mayo elbow performance score	92
Wrist	Dobbe <i>et al.</i> , 2014 [37]	Patient-specific	1	20	Pain of scar and surrounding tissue	
	Dobbe <i>et al.</i> , 2021 [84]	Patient-specific		6	3 screw breakage; 4 hardware removal; 1 patient preference for corrective surgery	
	Del Pino <i>et al.</i> , 2014 [73]	Patient-specific	5	19	None	
	Schindele <i>et al.</i> , 2022 [85]	Patient-specific		12	1 plate removed because of pressure sensitivity; 1 wound dehiscence	92
Foot	Yao <i>et al.</i> , 2021 [63]	Patient-specific	1	36	None	
Rib	Ahmed <i>et al.</i> , 2021 [86]	Patient-specific	2	16 and 13	None	

Bibliography

1. Caiti G, Dobbe JGG, Bervoets E, Beerens M, Strackee SD, Strijkers GJ, et al. Biomechanical considerations in the design of patient-specific fixation plates for the distal radius. *Med Biol Eng Comput.* 2019;57(5):1099-107.
2. Chen X. Parametric design of patient-specific fixation plates for distal femur fractures. *Proc Inst Mech Eng H.* 2018;232(9):901-11.
3. Manić M, Stamenković Z, Mitković M, Stojković M, Shephard DE. Design of 3D model of customized anatomically adjusted implants. *Facta Universitatis, Series: Mechanical Engineering.* 2015;13(3):269-82.
4. Benli S, Aksoy S, Havitcioğlu H, Kucuk M. Evaluation of bone plate with low-stiffness material in terms of stress distribution. *J Biomech.* 2008;41(15):3229-35.
5. Fouad H. Effects of the bone-plate material and the presence of a gap between the fractured bone and plate on the predicted stresses at the fractured bone. *Medical Engineering & Physics.* 2010;32(7):783-9.
6. Uthoff HK, Poitras P, Backman DS. Internal plate fixation of fractures: short history and recent developments. *Journal of Orthopaedic Science.* 2006;11(2):118-26.
7. Saidpour SH. Assessment of carbon fibre composite fracture fixation plate using finite element analysis. *Annals of biomedical engineering.* 2006;34(7):1157-63.
8. Smith KE, Dupont KM, Safranski DL, Blair JW, Buratti DR, Zeetser V, et al. Use of 3D printed bone plate in novel technique to surgically correct hallux valgus deformities. *Techniques in Orthopaedics.* 2016;31(3):181-9.
9. Tilton M, Lewis GS, Wee HB, Armstrong A, Hast MW, Manogharan G. Additive manufacturing of fracture fixation implants: design, material characterization, biomechanical modeling and experimentation. *Additive manufacturing.* 2020;33:101137.
10. Liu PC, Yang YJ, Liu R, Shu HX, Gong JP, Yang Y, et al. A study on the mechanical characteristics of the EB3D-printed Ti-6Al-4V LCP plates in vitro. *J Orthop Surg Res.* 2014;9:106.
11. Tseng WJ, Chao CK, Wang CC, Lin J. Notch sensitivity jeopardizes titanium locking plate fatigue strength. *Injury.* 2016;47(12):2726-32.
12. Fan X, Chen Z, Jin Z, Zhang Q, Zhang X, Peng Y. Parametric study of patient-specific femoral locking plates based on a combined musculoskeletal multibody dynamics and finite element modeling. *Proc Inst Mech Eng H.* 2018;232(2):114-26.
13. Chen X, He K, Chen Z. A Novel Computer-Aided Approach for Parametric Investigation of Custom Design of Fracture Fixation Plates. *Comput Math Methods Med.* 2017;2017:7372496.
14. Dobbe JG, Vroemen JC, Strackee SD, Streekstra GJ. Patient-tailored plate for bone fixation and accurate 3D positioning in corrective osteotomy. *Med Biol Eng Comput.* 2013;51(1-2):19-27.
15. Gutwald R, Jaeger R, Lambers FM. Customized mandibular reconstruction plates improve mechanical performance in a mandibular reconstruction model. *Comput Methods Biomech Biomed Engin.* 2017;20(4):426-35.
16. Yang WF, Choi WS, Leung YY, Curtin JP, Du R, Zhang CY, et al. Three-dimensional printing of patient-specific surgical plates in head and neck reconstruction: A prospective pilot study. *Oral Oncol.* 2018;78:31-6.
17. Stokbro K, Bell RB, Thygesen T. Patient-Specific Printed Plates Improve Surgical Accuracy In Vitro. *J Oral Maxillofac Surg.* 2018;76(12):2647.e1-e9.
18. Willemsen K, Nizak R, Noordmans HJ, Castelein RM, Weinans H, Kruyt MC. Challenges in the design and regulatory approval of 3d-printed surgical implants: a two-case series. *The Lancet Digital Health.* 2019;1(4):e163-e71.
19. Xie P, Ouyang H, Deng Y, Yang Y, Xu J, Huang W. Comparison of conventional reconstruction plate versus direct metal laser sintering plate: an in vitro mechanical characteristics study. *J Orthop Surg Res.* 2017;12(1):128.
20. Petersik A, Homeier A, Hoare SG, von Oldenburg G, Gottschling H, Schröder M, et al. A numeric approach for anatomic plate design. *Injury.* 2018;49 Suppl 1:S96-s101.

Design for fit

21. Kanchanomai C, Muanjan P, Phiphobmongkol V. Stiffness and endurance of a locking compression plate fixed on fractured femur. *Journal of applied biomechanics*. 2010;26(1):10-6.
22. Yan L, Lim JL, Lee JW, Tia CSH, O'Neill GK, Chong DYR. Finite element analysis of bone and implant stresses for customized 3D-printed orthopaedic implants in fracture fixation. *Med Biol Eng Comput*. 2020;58(5):921-31.
23. Chakladar ND, Harper LT, Parsons AJ. Optimisation of composite bone plates for ulnar transverse fractures. *J Mech Behav Biomed Mater*. 2016;57:334-46.
24. Reina-Romo E, Giráldez-Sánchez M, Mora-Macias J, Cano-Luis P, Domínguez J. Biomechanical design of less invasive stabilization system femoral plates: computational evaluation of the fracture environment. *Proc Inst Mech Eng H*. 2014;228(10):1043-52.
25. Wee H, Reid JS, Chinchilli VM, Lewis GS. Finite Element-Derived Surrogate Models of Locked Plate Fracture Fixation Biomechanics. *Ann Biomed Eng*. 2017;45(3):668-80.
26. Mårdian S, Schaser K-D, Duda GN, Heyland M. Working length of locking plates determines interfragmentary movement in distal femur fractures under physiological loading. *Clinical Biomechanics*. 2015;30(4):391-6.
27. Chung C-Y. A simplified application (app) for the parametric design of screw-plate fixation of bone fractures. *Journal of the mechanical behavior of biomedical materials*. 2018;77(642-648).
28. Hwang BY, Lee JW. Lingual Application of Pre-Bent Reconstruction Plate for Segmental Mandibular Defect: Easy and Accurate Method Through the Buccal Drilling Approach Using Computer-Aided Design/Computer-Aided Manufacturing Surgical Guides. *J Craniofac Surg*. 2020;31(3):851-2.
29. Münch M, Barth T, Studt A, Dehoust J, Seide K, Hartel M, et al. Stresses and deformations of an osteosynthesis plate in a lateral tibia plateau fracture. *Biomedizinische Technik*. 2022;67(1):43-52.
30. Stoffel K, Dieter U, Stachowiak G, Gächter A, Kuster MS. Biomechanical testing of the LCP—how can stability in locked internal fixators be controlled? *Injury*. 2003;34:11-9.
31. MacLeod AR, Serranoli G, Fregly BJ, Toms AD, Gill HS. The effect of plate design, bridging span, and fracture healing on the performance of high tibial osteotomy plates: An experimental and finite element study. *Bone Joint Res*. 2018;7(12):639-49.
32. Thomrungrapiyathan T, Luenam S, Lohwongwatana B, Sirichativapee W, Nabudda K, Puncreobutr C. A custom-made distal humerus plate fabricated by selective laser melting. *Computer methods in biomechanics and biomedical engineering*. 2021;24(6):585-96.
33. Synek A, Baumbach SF, Pahr DH. Towards optimization of volar plate fixations of distal radius fractures: Using finite element analyses to reduce the number of screws. *Clinical biomechanics (Bristol, Avon)*. 2021;82:105272.
34. Ghimire S, Miramini S, Richardson M, Mendis P, Zhang L. Effects of dynamic loading on fracture healing under different locking compression plate configurations: A finite element study. *J Mech Behav Biomed Mater*. 2019;94:74-85.
35. Shuang F, Hu W, Shao Y, Li H, Zou H. Treatment of Intercondylar Humeral Fractures With 3D-Printed Osteosynthesis Plates. *Medicine (Baltimore)*. 2016;95(3):e2461.
36. Wu H-y, Shao Q-p, Song C-j, Shang R-r, Liu X-m, Cai X-h. Personalized three-dimensional printed anterior titanium plate to treat double-column acetabular fractures: A retrospective case-control study. *Orthopaedic surgery*. 2020;12(4):1212-22.
37. Dobbe JG, Vroemen JC, Strackee SD, Streekstra GJ. Patient-specific distal radius locking plate for fixation and accurate 3D positioning in corrective osteotomy. *Strategies Trauma Limb Reconstr*. 2014;9(3):179-83.
38. Ahmad M, Nanda R, Bajwa AS, Candal-Couto J, Green S, Hui AC. Biomechanical testing of the locking compression plate: when does the distance between bone and implant significantly reduce construct stability? *Injury*. 2007;38(3):358-64.
39. Soni A, Singh B. Design and Analysis of Customized Fixation Plate for Femoral Shaft. *Indian J Orthop*. 2020;54(2):148-55.
40. Kimsal J, Mercer D, Schenck R, DeCoster T, Bozorgnia S, Fitzpatrick J, et al. Finite element analysis of plate-screw systems used in medial opening wedge proximal tibial osteotomies. *International Journal of Biomedical Engineering and Technology*. 2015;19(2):154-68.
41. Arnone JC, Sherif El-Gizawy A, Crist BD, G.J. DR, Ward CV. Computer-aided engineering approach

- for parameteric investigation of locked plating systems design. *Journal of Medical Devices*. 2013;7(2).
42. Nobari S, Katoozian HR, Zomorodimoghadam S. Three-dimensional design optimisation of patient-specific femoral plates as a means of bone remodelling reduction. *Comput Methods Biomech Biomed Engin*. 2010;13(6):819-27.
 43. Olender G, Pfeifer R, Müller CW, Gössling T, Barcikowski S, Hurschler C. A preliminary study of bending stiffness alteration in shape changing nitinol plates for fracture fixation. *Ann Biomed Eng*. 2011;39(5):1546-54.
 44. Wang D, Wang Y, Wu S, Lin H, Yang Y, Fan S, et al. Customized a Ti6Al4V Bone Plate for Complex Pelvic Fracture by Selective Laser Melting. *Materials (Basel)*. 2017;10(1).
 45. Bastias C, Henriquez H, Pellegrini M, Rammelt S, Cuchacovich N, Lagos L, et al. Are locking plates better than non-locking plates for treating distal tibial fractures? *Foot Ankle Surg*. 2014;20(2):115-9.
 46. Lin CH, Chao CK, Ho YJ, Lin J. Modification of the screw hole structures to improve the fatigue strength of locking plates. *Clin Biomech (Bristol, Avon)*. 2018;54:71-7.
 47. Sokol SC, Amanatullah DF, Curtiss S, Szabo RM. Biomechanical properties of volar hybrid and locked plate fixation in distal radius fractures. *J Hand Surg Am*. 2011;36(4):591-7.
 48. Brodke DS, Gollogly S, Alexander Mohr R, Nguyen BK, Dailey AT, Bachus A K. Dynamic cervical plates: biomechanical evaluation of load sharing and stiffness. *Spine (Phila Pa 1976)*. 2001;26(12):1324-9.
 49. Kim SJ, Jo YH, Choi WS, Lee CH, Lee BG, Kim JH, et al. Biomechanical Properties of 3-Dimensional Printed Volar Locking Distal Radius Plate: Comparison With Conventional Volar Locking Plate. *J Hand Surg Am*. 2017;42(9):747.e1-e6.
 50. Wang C, Chen Y, Wang L, Wang D, Gu C, Lin X, et al. Three-dimensional printing of patient-specific plates for the treatment of acetabular fractures involving quadrilateral plate disruption. *BMC Musculoskelet Disord*. 2020;21(1):451.
 51. Das S, Bourell DL, Babu SS. Metallic materials for 3D printing. *MRS Bulletin*. 2016;41(10):729-41.
 52. Ma L, Zhou Y, Zhu Y, Lin Z, Chen L, Zhang Y, et al. 3D printed personalized titanium plates improve clinical outcome in microwave ablation of bone tumors around the knee. *Sci Rep*. 2017;7(1):7626.
 53. Merema BJ, Kraeima J, Ten Duis K, Wendt KW, Warta R, Vos E, et al. The design, production and clinical application of 3D patient-specific implants with drilling guides for acetabular surgery. *Injury*. 2017;48(11):2540-7.
 54. Freitas A, Bontempo RL, Azevedo FAR, Battaglion LR, Giordano MN, Barin FR, et al. New fixation method for Pauwels type III femoral neck fracture: a finite element analysis of sliding hip screw, L-shaped, and L-shaped with medial plate. *European Journal of Orthopaedic Surgery and Traumatology*. 2021;31(6):1069-75.
 55. Gupta SK, Shahidsha N, Bahl S, Kedaria D, Singamneni S, Yarlagadda P, et al. Enhanced biomechanical performance of additively manufactured Ti-6Al-4V bone plates. *Journal of the mechanical behavior of biomedical materials*. 2021;119:104552.
 56. Kaymaz I, Murat F, Korkmaz İH, Yavuz O. A new design for the humerus fixation plate using a novel reliability-based topology optimization approach to mitigate the stress shielding effect. *Clinical Biomechanics*. 2022;99.
 57. Samsami S, Pätzold R, Neuy T, Greinwald M, Müller PE, Chevalier Y, et al. Biomechanical Comparison of 2 Double Plating Methods in a Coronal Fracture Model of Bicondylar Tibial Plateau Fractures. *Journal of Orthopaedic Trauma*. 2022;36(4):E129-E35.
 58. Schader JF, Mischler D, Dauwe J, Richards RG, Gueorguiev B, Varga P. One size may not fit all: patient-specific computational optimization of locking plates for improved proximal humerus fracture fixation. *Journal of shoulder and elbow surgery*. 2022;31(1):192-200.
 59. Shams SF, Mehdizadeh A, Movahedi MM, Paydar S, Haghpanah SA. The comparison of stress and strain between custom-designed bone plates (CDBP) and locking compression plate (LCP) for distal femur fracture. *European journal of orthopaedic surgery & traumatology : orthopedie traumatologie*. 2022.
 60. Vanclief S, Wesseling M, Dufflou JR, Nijs S, Jonkers I, Vander Sloten J. Thin patient-specific clavicle fracture fixation plates can mechanically outperform commercial plates: An in silico approach.

- Journal of orthopaedic research : official publication of the Orthopaedic Research Society. 2022;40(7):1695-706.
61. Wang J, Zhang X, Li S, Yin B, Liu G, Cheng X, et al. Plating System Design Determines Mechanical Environment in Long Bone Mid-shaft Fractures: A Finite Element Analysis. *Journal of investigative surgery : the official journal of the Academy of Surgical Research*. 2020;33(8):699-708.
 62. Wang Y, Wang J, Tu S, Li S, Yi J, Zhao H, et al. Biomechanical Evaluation of an Oblique Lateral Locking Plate System for Oblique Lumbar Interbody Fusion: A Finite Element Analysis. *World Neurosurgery*. 2022;160:e126-e41.
 63. Yao Y, Mo Z, Wu G, Guo J, Li J, Wang L, et al. A personalized 3D-printed plate for tibiototalcalcaneal arthrodesis: Design, fabrication, biomechanical evaluation and postoperative assessment. *Computers in biology and medicine*. 2021;133:104368.
 64. Zhang X, Cheng X, Yin B, Wang J, Li S, Liu G, et al. Finite element analysis of spiral plate and Herbert screw fixation for treatment of midshaft clavicle fractures. *Medicine (United States)*. 2019;98(34).
 65. Murat F, Kaymaz I, Korkmaz IH. A new porous fixation plate design using the topology optimization. *Medical Engineering and Physics*. 2021;92:18-24.
 66. Peleg E, Mosheiff R, Liebergall M, Mattan Y. A short plate compression screw with diagonal bolts-- a biomechanical evaluation performed experimentally and by numerical computation. *Clin Biomech (Bristol, Avon)*. 2006;21(9):963-8.
 67. Teo AQA, Ng DQK, Ramruttun AK, O'Neill GK. Standard versus customised locking plates for fixation of schatzker ii tibial plateau fractures. *Injury*. 2022;53(2):676-82.
 68. Kabiri A, Liaghat G, Alavi F. Biomechanical evaluation of glass fiber/polypropylene composite bone fracture fixation plates: Experimental and numerical analysis. *Computers in Biology and Medicine*. 2021;132.
 69. Ren W, Zhang W, Jiang S, Peng J, She C, Li L, et al. The Study of Biomechanics and Clinical Anatomy on a Novel Plate Designed for Posterolateral Tibial Plateau Fractures via Anterolateral Approach. *Frontiers in bioengineering and biotechnology*. 2022;10:818610.
 70. Sheng X, Liu S, Wang J, Zhao L, Zhu Y, Zhang W, et al. Femoral neck fractures in middle-aged and young adults using femoral neck system assisted by 3D printed guide plate. *Chinese Journal of Tissue Engineering Research*. 2022;26(33):5290-6.
 71. Shin SH, Kim MS, Yoon DK, Lee JJ, Chung YG. Does a Customized 3D Printing Plate Based on Virtual Reduction Facilitate the Restoration of Original Anatomy in Fractures? *Journal of personalized medicine*. 2022;12(6).
 72. Wen X, Huang H, Wang C, Dong J, Lin X, Huang F, et al. Comparative biomechanical testing of customized three-dimensional printing acetabular-wing plates for complex acetabular fractures. *Adv Clin Exp Med*. 2020;29(4):459-68.
 73. del Pino JG. A new total wrist fusion locking plate for patients with small hands or with failed partial wrist fusion: preliminary experience. *J Wrist Surg*. 2014;3(2):148-53.
 74. Sodl JF, Kozin SH, Kaufmann RA. Development and use of a wrist fusion plate for children and adolescents. *J Pediatr Orthop*. 2002;22(2):146-9.
 75. Peterson JM, Chlebek C, Clough AM, Wells AK, Ledet EH. Stiffness Matters: Part I-The Effects of Plate Stiffness on the Biomechanics of ACDF In Vitro. *Spine (Phila Pa 1976)*. 2018;43(18):E1061-e8.
 76. Wang CC, Lee CH, Chin NC, Chen KH, Pan CC, Su KC. Biomechanical analysis of the treatment of intertrochanteric hip fracture with different lengths of dynamic hip screw side plates. *Technology and Health Care*. 2020;28(6):593-602.
 77. Wang L, Guo K, He K, Zhu H. Bone morphological feature extraction for customized bone plate design. *Scientific reports*. 2021;11(1):15617.
 78. Teo AQA, Ng DQK, Lee P, O'Neill GK. Point-of-Care 3D Printing: A Feasibility Study of Using 3D Printing for Orthopaedic Trauma. *Injury*. 2021;52(11):3286-92.
 79. Gardner MJ, Nork SE, Huber P, Krieg JC. Less rigid stable fracture fixation in osteoporotic bone using locked plates with near cortical slots. *Injury*. 2010;41(6):652-6.
 80. Xu M, Zhang LH, Zhang YZ, Zhang LC, He CQ, Wang Y, et al. Custom-made locked plating for

- acetabular fracture: a pilot study in 24 consecutive cases. *Orthopedics*. 2014;37(7):e660-e70.
81. Jeong SH, Samuel LT, Acuña AJ, Kamath AF. Patient-specific high tibial osteotomy for varus malalignment: 3D-printed plating technique and review of the literature. *European Journal of Orthopaedic Surgery and Traumatology*. 2022;32(5):845-55.
 82. FFA IJ, Meesters AML, Merema BBJ, Ten Duis K, de Vries JPM, Banierink H, et al. Feasibility of Imaging-Based 3-Dimensional Models to Design Patient-Specific Osteosynthesis Plates and Drilling Guides. *JAMA network open*. 2021;4(2):e2037519.
 83. Edelmann A, Dubis M, Hellmann R. Selective Laser Melting of Patient Individualized Osteosynthesis Plates-Digital to Physical Process Chain. *Materials (Basel, Switzerland)*. 2020;13(24).
 84. Dobbe JGG, Peymani A, Roos HAL, Beerens M, Streekstra GJ, Strackee SD. Patient-specific plate for navigation and fixation of the distal radius: a case series. *International journal of computer assisted radiology and surgery*. 2021;16(3):515-24.
 85. Schindele S, Oyewale M, Marks M, Brodbeck M, Herren DB. Three-Dimensionally Planned and Printed Patient-Tailored Plates for Corrective Osteotomies of the Distal Radius and Forearm. *The Journal of hand surgery*. 2022.
 86. Ahmed ADB, Prakash PS, Li Cynthia CM. Customized 3-dimensional printed rib plating in chest wall reconstruction. *JTCVS Techniques*. 2021;8:213-5

Semi-automated digital workflow to design and evaluate patient-specific mandibular reconstruction implants

The reconstruction of large mandibular defects with optimal aesthetic and functional outcomes remains a major challenge for maxillofacial surgeons. The aim of this study was to design patient-specific mandibular reconstruction implants through a semi-automated digital workflow and to assess the effects of topology optimization on the biomechanical performance of the designed implants. A fully porous implant (LA-implant) and a topology-optimized implant (TO-implant) both made of Ti-6Al-4V ELI were designed and additively manufactured using selective laser melting. The mechanical performance of the implants was predicted by finite element analysis (FEA) and was experimentally assessed by quasistatic and cyclic biomechanical tests. No statistically significant differences ($p < 0.05$) in the mean stiffness, mean ultimate load, or mean ultimate displacement were detected between the LA- and TO-implant groups. No implant failures were observed during quasi-static or cyclic testing under masticatory loads that were substantially higher (>1000 N) than the average maximum biting force of healthy individuals. Given its relatively lower weight (16.5%), higher porosity (17.4%), and much shorter design time (633.3%), the LA-implant is preferred for clinical application. This study clearly demonstrates the capability of the proposed workflow to develop patient-specific implants with high precision and superior mechanical performance, which will greatly facilitate cost- and time-effective pre-surgical planning and is expected to improve the surgical outcome.

Van Kootwijk, A., Moosabeiki, V., Saldivar, M.C., Pahlavani, H., Leeflang, M.A., Niar, S.K., Pellikaan, P., Jonker, B.P., Ahmadi, S.M., Wolvius, E.B. Tümer, N., Mirzaali, M.J., Zhou, J., Zadpoor, A.A., Semi-automated digital workflow to design and evaluate patient-specific mandibular reconstruction implants, *Journal of the Mechanical Behavior of Biomedical Materials*, 132, p.105291, 2022.

4.1 Introduction

Mandibular reconstruction is a routine surgical procedure for the restoration of mandibular continuity defects, which typically result from tumor resection (benign or malignant), trauma, osteomyelitis, or osteoradionecrosis [1-3]. Patients with untreated defects may at a later stage suffer from facial deformity, loss of speech, and reduced masticatory function, which will severely affect the patient's quality of life [3]. The ideal reconstruction procedure aims to optimize functional and cosmetic outcomes by restoring facial dimensions (*i.e.*, height, width, and projection), replacing compromised soft tissues, and providing a foundation for dental rehabilitation [2]. Even though the overall survival rate of free flap reconstructions is usually higher than 95%, there are several pivotal drawbacks associated with free tissue transfer, including the limited amount of available bone, donor site morbidity, and the need for high surgical expertise [4-6]. Moreover, a large variety of prostheses and osteosynthesis plates that are used for mandibular reconstruction have been reported to be associated with mechanical failure, usually resulting from premature fracture, loosening, or the exposure of either the implant itself or the screw fixation to the mandibular bone, as well as postoperative infections following wound dehiscence [7, 8]. These complications often result in extended surgical procedures, prolonged hospital stays, long recovery processes, and an increased risk of surgical revisions [9].

Clinical studies on customized metallic implant reconstructions using a cage (or crib) design with or without the insertion of bone grafts have shown promising results [5, 10-17]. First, no or limited harvesting of autologous tissue is involved, minimizing the risk of associated donor site morbidity. Second, there is no need for intra-operative bending of the implant components, which decreases their susceptibility to fatigue fracture. Third, the procedure does not require additional surgical training or special experience. Finally, the natural configuration of the mandible can be accurately reproduced, leading to better aesthetics and patient satisfaction.

Tuning the shape and mechanical properties of the implanted material to match the patient's specific situation is deemed crucial for an optimal reconstruction and has been a driving force for the application of additive manufacturing (AM) technologies and computational tools, such as finite element analysis (FEA) to produce patient-specific implants (PSIs) [18]. Over the past few years, the use of topology optimization (TO) in the development of mandibular reconstruction implants has been increasing [19-21]. The optimization of the implant designs for orthopedic and craniofacial applications has resulted in improved success rates of the surgeries [22]. Yet, only a few studies have reported the details of the design process of the customized reconstruction implants, including the implementation of TO. Moreover, hardly any study has evaluated the performance of the designed implants under physiologically relevant loading conditions

[23]. Consequently, a large variety of methodologies for implant design have been established, while standardized procedures regarding the design and testing of such implants have been lacking [24]. This leads to unpredictable and incomparable results. Moreover, the labor-intensive nature of the involved processes means that the treatment workflow is expensive, inefficient, and time-consuming [25]. There is, therefore, an urgent need for systematic and automated approaches to the design, fabrication, and (computational) testing of PSIs to pave the way for the integration of patient-specific cage-like reconstruction implants into routine care.

We, therefore, aimed to develop a semi-automated digital workflow for the design of patient-specific cage implants for mandibular reconstruction and to assess the effects of TO on the biomechanical performance of the implants through experimentally validated FEA models. The workflow proposed in this study was intended to help clinical engineers design reconstruction systems as a viable alternative to or in combination with the current standard free-flap approach in the treatment of mandibular continuity defects. Establishing a more systematic approach to the design of patient-specific mandibular reconstruction implants is expected to make pre-surgical planning more cost- and time-efficient while ensuring optimal aesthetics and minimizing morbidity. Furthermore, combining the design workflow with validated computational predictions regarding the implant performance provides a sound basis for the design decisions, leading to improved treatment outcomes.

4.2 Materials and methods

The digital workflow starts with the post-processing of computed tomography (CT) scans (Figure 4.1a-h) and runs towards a solid implant design (Figure 4.2b), ready to be exported to the FEA software for TO. All image processing and implant designing steps were compiled into a Python-based semi-automated workflow using the Mimics Research 21.0 (Materialise, Belgium) and 3-matic 15.0 (Materialise, Belgium) Scripting Modules. All scripts were written to be compatible with Python version 3.8.

4.2.1 Bone model generation

A polyurethane (PU) mandible (Model 8950, Synbone AG, Switzerland) was scanned using a Siemens Somatom Volume Zoom CT scanner at a slice thickness of 0.6 mm, a peak potential of 140 kVp, and a field-of-view of 512×512 pixels (Figure 4.1a). The segmentation and 3D part generation of the mandible were performed using Mimics Research 21.0 (Materialise, Belgium). The 3D mandible was then exported to 3-matic 15.0 (Materialise, Belgium) where resection, missing bone shape estimation, and implant designing procedures were carried out.

The resection area investigated in this study was a 4-cm long lateral defect that ranged from the canine tooth up to the mandibular angle (Figure 4.1c). The reason for

choosing this area was that a lateral defect type (*i.e.*, between the mandibular condyle and symphysis) corresponds to the region that is most frequently subjected to resection during the surgical treatment of advanced squamous cell carcinomas [26-30]. The osteotomy planes for resection were defined by positioning two datum planes (Figure 4.1b).

A combination of the segmental mirroring technique and anatomical extrusion technique was implemented in the current design workflow for shape estimation [31, 32]. First, the intact side was mirrored across the midsagittal plane onto the affected side (Figure 4.1d). Next, the missing segment was cut out of the mirrored side between the previously defined osteotomy planes, and teeth were trimmed off (Figure 4.1e). Three curves were then created around the surface of the mirrored segment, which served as intermediate contour profiles for the “sweep” operation (Figure 4.1f). A centerline was created between the two boundary surfaces of the remaining mandibular segments to provide a path for the sweep operation (Figure 4.1g). The estimated shape was generated by using a sweep-loft operation from one resection margin to the other, following the sweep path and the intermediate contour profiles (Figure 4.1h).

4.2.2 Implant designing

Two different implant designs were investigated in this study: a fully porous implant based on a lattice structure (*LA-implant*) and a topology-optimized design (*TO-implant*). A non-porous design (*solid-implant*) was used for the TO procedure.

The implant design procedure in 3-matic starts off by marking the manifold on the mandible that defines the outer shape of the implant (Figure 4.2a). An implant thickness of 1.5 mm was set to create the solid implant (Figure 4.2b). The general shape of the implant follows the contour of a cage or a tray. The implant height in the resected area was defined to be slightly smaller than the native mandible so that the implant can be covered with sufficient soft tissue without the need for an additional local flap [33]. Yet, the cage was designed with a sufficient height to allow for any required dental implants to be positioned atop the integrated bone graft at a later stage to restore masticatory performance. Then, the screw sizes (length and diameter) and screw positions were defined: eight 2.4 mm bicortical titanium cortex screws (MatrixMANDIBLE, DePuy Synthes, USA) were used to fixate each of the implants to the mandible. Four screws were placed on the anterior body and another four on the posterior lateral border of the ramus (Figure 4.2b). The four screws placed in the chin region were 14 mm long. Both screws on the posterior mandibular segment closest to the resection border were 8 mm long. The most distal screws on the posterior mandibular segment were both 6 mm long.

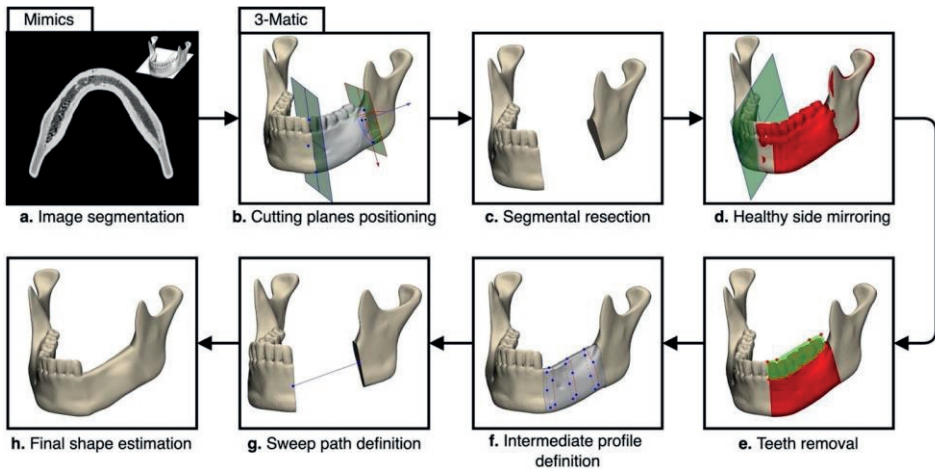


Figure 4.1. The image processing step as well as the workflow for the estimation of the shape of the missing bone implemented in Mimics and 3-matic: (a) a horizontal plane viewport of the Synbone mandible reconstructed from the CT images, (b) the positioning of the osteotomy planes, (c) the segmental resection, (d) the mirroring of the healthy side onto the affected side, (e) the segmental cut-out and trimming of teeth, (f) the definition of intermediate contour profiles, (g) the definition of a centerline as a sweep path, and (h) the final result after performing the sweep-loft operation.

A proper design of the porous structure is crucial for promoting osseointegration and angiogenesis, reducing implant stiffness, and disrupting fibrosis [34]. Lattice structures based on the ‘dode’ unit cell were used to implement porosity in the solid implant, as previous studies have found them to be promising [35, 36]. The implementation of the lattice structures was carried out using Magics 24.01 (Materialise, Belgium). Three default dode unit cell structures were initially considered, namely, ‘dode-thin’, ‘dode-medium’, and ‘dode-thick’ with stepwise increases in the strut thickness. The implant with the dode-thin structure resulted in a very high porosity (96%), a small strut thickness (110 μm), and poor strut connections, which would lead to a fragile implant with insufficient mechanical strength. The dode-medium and dode-thick unit cell structures met the design requirements, including a minimum pore size of 400 μm with a porosity of 70 to 90%, which are suggested to be optimal for bone regeneration [37, 38]. 3D printed implant samples with both unit cell structures showed that the permeability of the dode-thick lattice structure was impeded in various regions due to the fusion of powder particles in-between the struts. Hence, the 1.5-mm dode-medium unit cell (Figure 4.2c zoom-in) was selected for the lattice structure in the final implant design. These unit cells had an in-plane pore size, strut thickness, and porosity of 460 μm , 210 μm , and 87.5%, respectively.

Design workflow

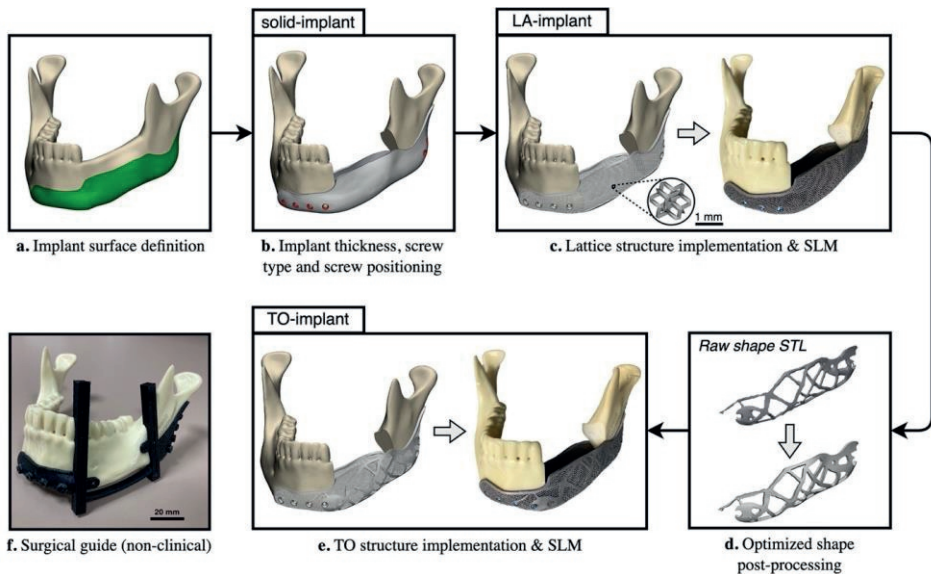


Figure 4.2. The implant design workflow implemented in 3-matic: (a) implant surface marking, (b) implant thickness, screw type, and position definition, (c) the implementation of a dode-medium lattice structure in the virtual (left) and 3D-printed (right) LA-implant design after reconstruction, (d) the post-processing step of the TO body, (e) the implementation of the TO body to create the virtual (left) and 3D-printed (right) TO-implant design after reconstruction, and (f) non-clinical surgical guide.

The LA-implant was entirely porous (Figure 4.2c) except for the solid edges around the screw holes and the implant extremities, which were maintained to provide the implant with additional mechanical strength and to protect the surrounding tissue from sharp strut ends. The topology optimized design resulting from the TO analysis was exported out of Abaqus as a raw STL part and was post-processed in 3-matic (Figure 4.2d) by reproducing this shape from the solid implant with a consistent thickness. The TO-implant (Figure 4.2e) was then obtained by combining the TO volume with the porous LA-implant through Boolean unification, as described by [39]. More details on TO are provided in Subsection 4.2.3.

4.2.3 FEA methods

All FE analyses were performed using Abaqus/CAE 2019 (Simulia, Dassault Systèmes, France). The TO was performed using Abaqus/CAE 2017 (Simulia, Dassault Systèmes, France). Before a complex musculatory system was implemented in the FE model, a simplified model that reproduced the experimental conditions (*EXP-FEA*) was developed. By doing so, two validation steps were integrated into the FEA process. First, the *EXP-FEA* model was validated against the experimental data. Afterwards, this model was extended to include more sophisticated physiological conditions (*PHY-FEA*), thereby simulating the clinical situation. The results of the *PHY-FEA* model were then compared

with the FEA data published in the literature. The healthy intact mandible was used for the validation of the *EXP-FEA* model using the digital image correlation (DIC) technique (see Section 4.2.4). Four different models were investigated under the *PHY-FEA* conditions, respectively representing the healthy intact mandible (*healthy-model*), the resected mandible model with the solid implant (*solid-implant-model*), the resected mandible model with the LA-implant (*LA-implant-model*), and the resected mandible model with the TO-implant (*TO-implant-model*) (Table 4.1).

Table 4.1. The study design for FEA modeling and experimental testing.

		FEA			Experimental testing				
		EXP-FEA	PHY-FEA		Quasi-static		Cyclic		
Loading condition		INC (I*)	INC (II*)	RMB (II)	INC (I)	INC (II)	RM B (II)	Constant-cyclic-method	Increment-cyclic-method
								INC (I)	INC (I)
Sample	Control**	EXP-FEA model	healthy-model	1***	2	2	-	-	
	Solid implant	-	solid-implant-model	-	-	-	-	-	
	LA implant	-	LA-implant-model	-	3	3	2	2	
	TO implant	-	TO-implant-model	-	3	3	2	2	

* 'I' indicates a 50%/50% healthy side/affected side load distribution while 'II' indicates a 70%/30% healthy side/affected side load distribution. INC: incisal clenching; RMB: right molar biting.

** The control specimens represent the intact (non-implanted) mandibles.

Numbers in the column "Experimental testing" indicate the number of the specimens used.

*** This control specimen was used for the DIC measurement.

Material assignment

In the case of *EXP-FEA*, the material properties were homogeneously assigned to the cancellous and cortical regions of the mandible. A negligible Young's modulus [E] of 1×10^{-6} GPa was assigned to the cancellous bone region, given that it does not significantly contribute to the stress distribution in the implant [40]. The Young's modulus of the cortical bone region was chosen such that the stiffness of the model would match the stiffness derived from the experimental data. By using this approach, a Young's modulus of 0.41 GPa was found for the cortical PU region (see subsection 4.3.1). The Poisson's ratio was set at $\nu = 0.3$.

Design workflow

In the case of *PHY-FEA*, the cancellous bone and cortical bone regions were respectively defined as those corresponding to $HU < 620$ and $HU > 620$, where HU is the Hounsfield unit. The empirical relationship between the density and elastic modulus of mandibular bone is available in the literature [41] and will be used in actual clinical use of the workflow. In the present study, however, we had to work with the HU values of the synthetic mandible, which are different from those of the real mandibular bone. The density-modulus relationships, therefore, had to be adjusted to obtain values that would match the average values of density [ρ] and elastic modulus [E] of the actual mandibular bone. For cancellous bone, the material properties were calculated using the following equations:

$$\rho = 5 + 0.005HU \quad (4.1)$$

$$E = 0.06 + 0.9\rho^2 \quad (4.2)$$

This resulted in ρ -values ranging between 0.08 and 1.70 g/cm³ and E -values ranging between 0.07 and 2.67 GPa. For the cortical bone, the material properties were calculated using the following equations:

$$\rho = 2.7 + 0.00165HU \quad (4.3)$$

$$E = 0.09 + 0.9\rho^{4.3} \quad (4.4)$$

This resulted in ρ -values ranging between 1.73 and 2.67 g/cm³ and E -values ranging from 9.61 to 43.46 GPa. The elastic modulus of the outer voxel layer was set to $E = 30.1$ GPa, which corresponds to the average elastic modulus of the dentulous mandibular cortex as determined by [41], to avoid issues related to the partial volume effect. The volume mesh of the healthy model and the corresponding material assignment are presented in Figure 4.3b-c. A similar process was followed in the case of the implanted mandibles. The implants, made of the Ti-6Al-4V ELI alloy, were assigned with an elastic modulus of 120 GPa (SLM Solutions, Material Data Sheet). A Poisson's ratio of 0.3 was assigned to all the volume elements of both the mandible and implant. All materials were modeled as linear elastic and isotropic.

Meshing

The mandible and implants (LA-implant and TO-implant) were discretized using 4-node tetrahedral elements (C3D4) and 10-node quadratic (C3D10) elements, respectively (Figure 4.3a). A mesh convergence study was performed to define the element sizes. Accordingly, the mandible and implants were discretized using $\approx 700,000$ and $\approx 3,500,000$ elements, respectively. For TO, the solid implant was discretized using $\approx 200,000$ C3D4 elements.

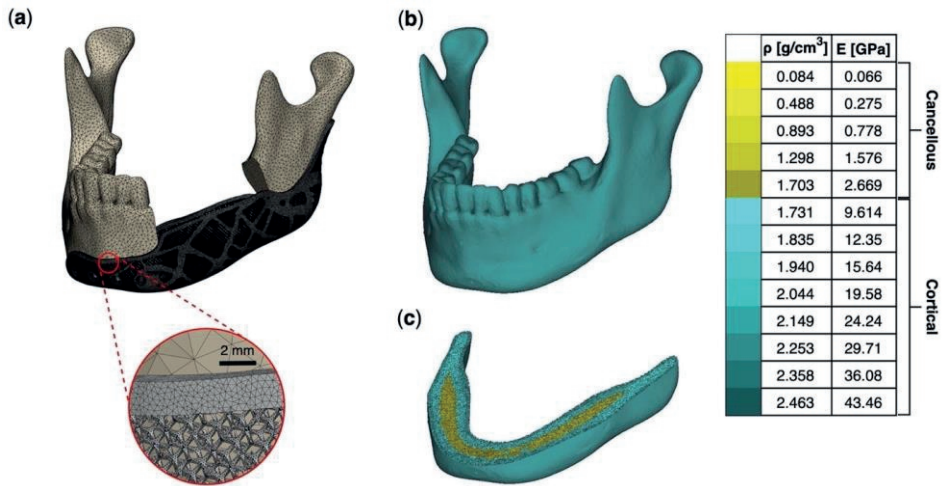


Figure 4.3. (a) An overview of the surface mesh applied to the mandible and TO-implant in the TO-implant-model, (b) the full and (c) cross-sectional views of the material assignment to the volume mesh of the healthy model. The color scale represents the corresponding values of the density and Young's modulus calculated for the cortical and cancellous regions of the mandible shown in (b) and (c).

Loads and boundary conditions

The loads and boundary conditions applied in the *EXP-FEA* model closely resembled those of the experimental setup (Figure 4.4a). The steel loading bar was modeled as an undeformable rigid object, given its high stiffness as compared to the PU bone specimen. It exerted an equal force on both sides of the mandible by displacing it 5 mm in the positive z -(*i.e.*, superior) direction while constraining all the other possible translations and rotations (Figure 4.4b). This displacement was enough to capture the linear part of the load-displacement curve obtained from the biomechanical experiments. Only incisal clenching (INC) of the jaw was evaluated in the *EXP-FEA* model. This was done by restraining the incisal surfaces of the central and lateral incisors from moving vertically (*i.e.*, perpendicularly to the occlusal plane) while restraining the movement of the articular surface of the temporomandibular joints in all directions. A friction coefficient of 0.2 was used at the interface of the bar and the bone.

Two types of clenching movements were simulated using the four models of the *PHY-FEA* group, including INC and right molar biting (RMB) at the unaffected side (Figure 4.4c). The same boundary conditions as described for *EXP-FEA* were used to create the INC condition. For RMB, the occlusal surfaces of the first and second molar were restrained from moving vertically while restraining all the possible movements of the articular surface of the temporomandibular joints.

Four different muscles (masseter, temporalis, medial pterygoid, and lateral pterygoid) were modeled bilaterally through three-dimensional force vectors [42]. In the

case of the healthy mandible, all four muscles were used bilaterally to create the required loading conditions. For some segmental resections, muscles can be (partially) reattached to the mandible, which can then continue to perform their function after implantation (to a limited extent). The residual muscle force after mandibular reconstruction is reported to be 60% of the average biting force of healthy adults [43]. The implant used in this study covered an area on the posterior mandibular segment that made the reattachment of both the left masseter and the left medial pterygoid unlikely. Therefore, the forces exerted by these muscles were excluded from the loading conditions in the solid-implant-model, LA-implant-model, and TO-implant-model.

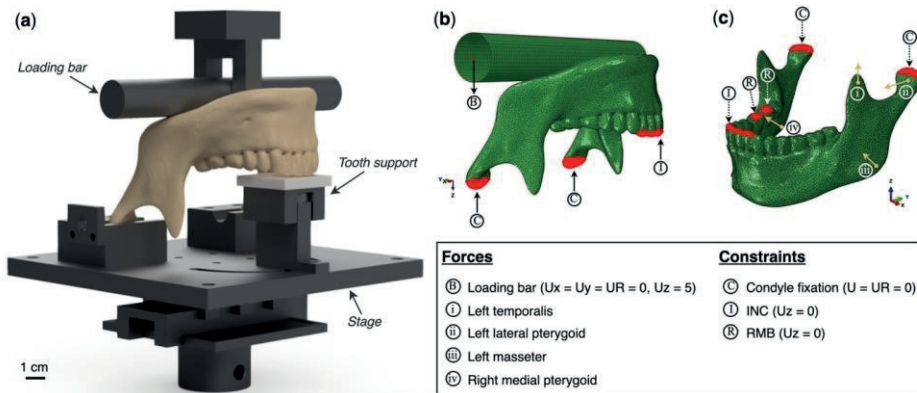


Figure 4.4. (a) The experimental setup, (b) the displacement (U) and rotation (UR) constraints in the *EXP-FEA* model, and (c) the constraints and resultant muscle force directions for the incisal clenching (INC) and right molar biting (RMB) conditions in the *PHY-FEA* group. For simplicity, the muscle force vectors are only partially shown on the left and right sides of the mandible.

Pinheiro and Alves [42] have described the expected reaction forces on the teeth involved in INC (570.90 N) and RBM (600.40 N). These forces were based on the average maximum single-tooth bite forces of young male adults. In the present study, the residual muscle force may be lower than 60% of the original maximum muscle force because two of the muscles are not going to be reattached to the affected side of the mandible. Since the exact reduction in the muscle forces could not be estimated, a general ‘worst-case’ scenario was simulated to ensure a good mechanical performance of the implant in the long term. To this end, the maximum biting forces described above were reduced by 40% as described by [43]. This resulted in the reaction forces of 342.54 and 360.24 N during INC and RMB, respectively. All individual muscle forces were scaled, depending on the desired biting conditions. The weighting factors of each muscle, the orthogonal directions, and the scaling factors that provided the muscle activation force are specified by [44] and are later adapted by [42]. The mandible models in this study were aligned with the reference frame used by Pinheiro and Alves, according to the cephalometric standards. The muscle forces could, therefore, be simply scaled uniformly until the teeth were subjected to the desired magnitude of reaction forces. For INC and RMB, those

scaling factors were 0.72 and 0.87, respectively. The displacement patterns in the healthy-model were compared with the displacements obtained by [44]. The three-dimensional force vectors of each muscle group for both loading cases, as well as the number of nodes to represent each muscle group are listed in Table S4.1 (Supplementary material) for the healthy-model and in Table S4.2 (Supplementary material) for the implanted models.

Topology optimization

The Abaqus Topology Optimization Module was used for the TO of the solid implant. Maximizing open space in the implant is beneficial for the healing process of the graft. Taking this and the benefits of implant weight reduction into account, the optimization constraint was set to constrain the final TO implant volume to 10% of the initial solid implant volume. The objective function was set to minimize the compliance of the system. Since the global shape of the implant had been defined earlier, no geometrical restrictions were applied to the optimization procedure.

4.2.4 Experimental methods

Ten LA-implants and ten TO-implants were 3D printed using grade 23 Ti-6Al-4V ELI powder. A selective laser melting (SLM) machine (SLM Solutions Group AG, Germany) was used. The chemical composition of the titanium alloy powder is listed in Table S4.3 (Supplementary material). The main SLM process parameters, powder particle sizes, and the physical properties of the as-built material are presented in Table S4.4 (Supplementary material). All the implanted specimens were prepared by using a customized surgical cutting and drilling guide (Figure 4.2f) to create nearly identical resections and screw holes in each mandible. Note that the surgical guide was not designed to be suitable for intra-operative clinical application. The screw holes were predrilled using a 1.8-mm drill bit and the resection area was cut out using an oscillating saw. The experimental test setup (Figure 4.4a) was designed both for quasi-static testing using a Lloyd Instruments LR5K testing machine and for cyclic fatigue testing using an INSTRON ElectroPuls™ E10000 machine. In order to create a specific clenching task, a distributed load was applied to both mandibular angles by means of a rigid seesaw device while fixing the translations of both condyles and constraining a certain region on the dental arch perpendicular to the plane of occlusion. Only the rotational movement of the condyles about the transverse horizontal axis was allowed. Several translational and rotational degrees of freedom were implemented in the designed fixture to enable the evaluation of the implant performance under various biting conditions, including INC and RMB. To enable an accurate comparison between the numerical and experimental results, the mandibles were positioned according to the cephalometric standards with their inferior border positioned at an angle of 26° with respect to the horizontal plane [45].

Quasi-static testing protocol

During both INC (Figure 4.5a) and RMB (Figure 4.5b), 70% and 30% of the load were applied to the mandibular angles of the healthy and affected sides, respectively [45-47]. Three LA-implant samples, three TO-implant samples, and two control specimens (*i.e.*, intact non-implanted mandibles) were tested in these two groups (Table 4.1). The specimens were subjected to continuous compressive loading at a rate of 1 mm/min until the specimen failed, which was defined as the fracture of the plate or mandible, failure at the screw-substrate interface, or a vertical displacement above 20 mm. A preload was set at 10 N [40]. For each sample, the failure or ultimate load (U. load) [N] of the construct, ultimate displacement (U. displacement) [mm], and the location of failure were recorded. The construct stiffness [N/mm] was determined from the slope of the best-fit line in the linear portion of the load-displacement curve. The one sample *t-test* with Bonferroni correction was used to determine the differences between both implant groups. $p < 0.05$ was set as the threshold of statistical significance.

Cyclic testing protocol

The cyclic testing setup is shown in Figure 4.5c. A 50%/50% INC loading configuration was used as this yielded the most stable setup while transferring the highest load through the implant. First, the fatigue performance of the implant was evaluated under physiological conditions (*constant-cyclic-method*) by cycling the stress over a constant range between the minimum (30 N) and maximum (340 N) compressive stresses (Figure 4.5e). The reconstruction system must survive up to a maximum of 250,000 loading cycles under this post-surgical ‘worst-case’ loading condition to guarantee the long-term mechanical function of the implant [29]. To detect any potential implant failures or screw loosening due to fatigue under higher loads, a second cyclic testing procedure (*increment-cyclic-method*) was used (Figure 4.5f). In this procedure, the maximum stress amplitude was increased incrementally (3 N per cycle) from the initial load of 340 N until the failure of the implanted sample or until a maximum load of 2,500 N was reached. For the tests with each of the two cyclic testing methods, four reconstructed samples were tested of which two contained the LA-implant and two contained the TO-implant (Table 4.1). The loading rate was set at 3 Hz [29, 47]. The number of cycles to failure and the failure load were registered.

DIC measurements

A Q-400 2x12MPixel digital image correlation (DIC) system (LIMESS GmbH, Krefeld, Germany) was used to measure the surface strains on the intact mandible during quasi-static testing employing an imaging frequency of 1 Hz.

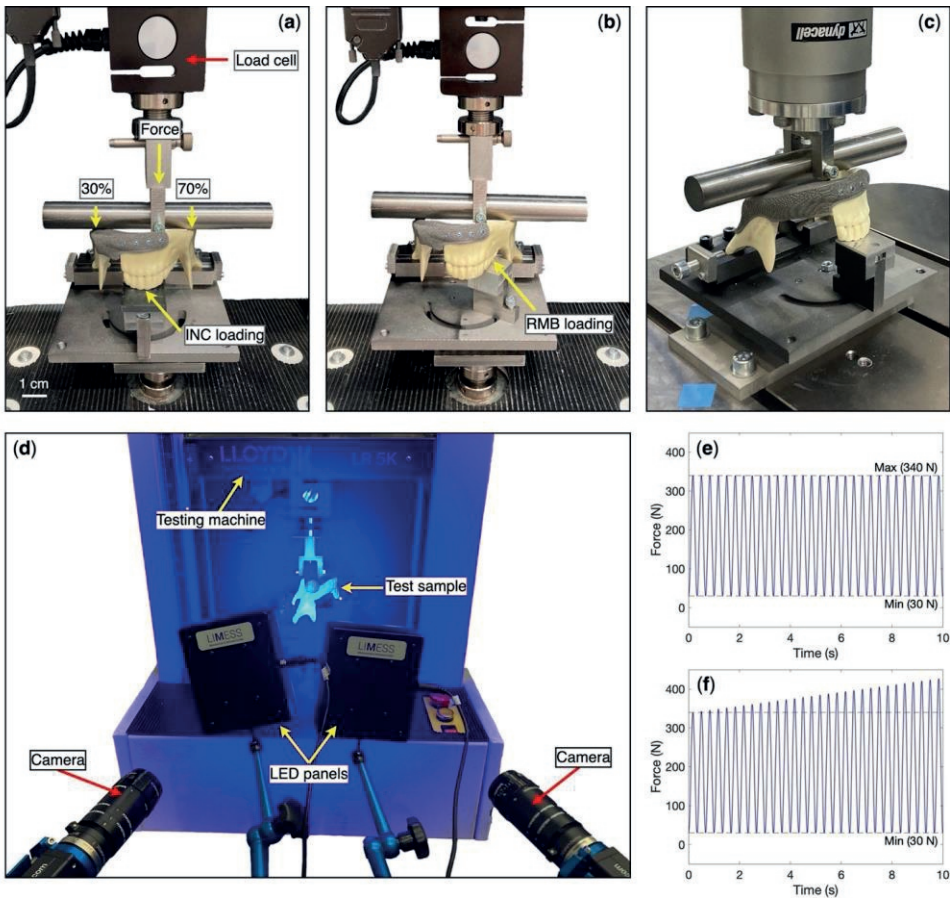


Figure 4.5. Quasi-static (a) INC and (b) RMB loading setup using a 70%/30% force distribution. (c) The cyclic testing setup using a 50%/50% force distribution. (d) The experimental setup for DIC measurements. The cyclic loading sine waves plotted against the applied force during the first 10 s of the cyclic tests with (e) the constant-cyclic-method and (f) the increment-cyclic-method.

The posterior segment of the mandible, corresponding to the implanted side in the case of the implanted mandibles, was selected as the area of interest, as it included the primary location of the specimen failure. A black dot speckle pattern was applied over a white paint background to cover the entire area of interest. Two digital cameras and light-emitting diode (LED) panels were placed at 0.8 m from the specimens to capture their images and illuminate them, respectively (Figure 4.5d). Image processing and strain calculations were performed using Istra4D x64 4.6.5 (Dantec Dynamics A/S, Skovunde, Denmark). Two enclosed polygonal regions, denoted as Polygon_1 and Polygon_2, were created within the anterior and posterior condylar neck regions of the mandibular bone, corresponding to the areas of the largest maximum and minimum principal strains, respectively. The mean strain values in each of these two areas were extracted and plotted

against the applied force. Similarly, both corresponding areas, denoted as Area_1 and Area_2, were identified in the FE model, and the average nodal strain values in both areas were plotted against the reaction force on the loading bar (Figure 4.4a). Only the linear elastic portion of the applied force was used for comparison with the DIC data, as plasticity was not considered in our FE analyses.

4.3 Results

4.3.1 FEA results

In *EXP-FEA*, the computational value of the stiffness (278.5 N/mm) agreed with the experimental value obtained using quasi-static testing (274.9 N/mm) (Figure 4.6d) when a Young's modulus of 0.41 GPa was assigned to the cortical PU region. Figure 4.6a shows the von Mises stress distribution within the intact mandible for a load of 800 N. The highest stress values were found at the posterior (12 MPa left and 16 MPa right) and anterior sides (14 MPa left and 16 MPa right) of the condylar neck, as well as along the external oblique line (8 MPa left and 9 MPa right). The deformations of the mandible as predicted by the *EXP-FEA* model (up to 1375 N) and as measured using the quasi-static experiments (up to fracture) are presented side by side in Supplementary Video 4.1.

The distributions of the maximum and minimum principal strain predicted by the FEA models and measured by DIC (load = 800 N) are presented in Figures 4.6b and 4.6c, respectively. The mean values of the maximum and minimum principal strains in the regions of interest were plotted against the applied force (Figure 4.6e and Figure 4.6f, respectively). In the linear elastic range (*i.e.*, between 150 and 850 N), the maximum principal strains measured by DIC within Polygon_1 were in good agreement with the strains predicted by the FE model within Area_1. The minimum principal strains in both regions were linearly correlated but slightly higher in Area_2 as compared to Polygon_2, with a difference of 31% at 800 N.

In *PHY-FEA* (healthy-model), the combined muscle forces resulted in the biting forces of 570.9 and 600.4 N during INC and RMB, respectively. The distributions of the von Mises stress within the healthy mandible subjected to the INC and RMB loading are presented in Figures 4.7a and 7c, respectively. Similar to results in [42], the high stresses under INC loading were observed below the condylar process in the mandibular notch (37 MPa), along the external oblique line (29 MPa), and at the posterior surface of the ramus (33 MPa). Consistent with the findings of [42], the high stresses under the RMB loading were found on the posterior surface of the contralateral ramus, when compared with the working (right) side, as well as along the external oblique lines on both sides.

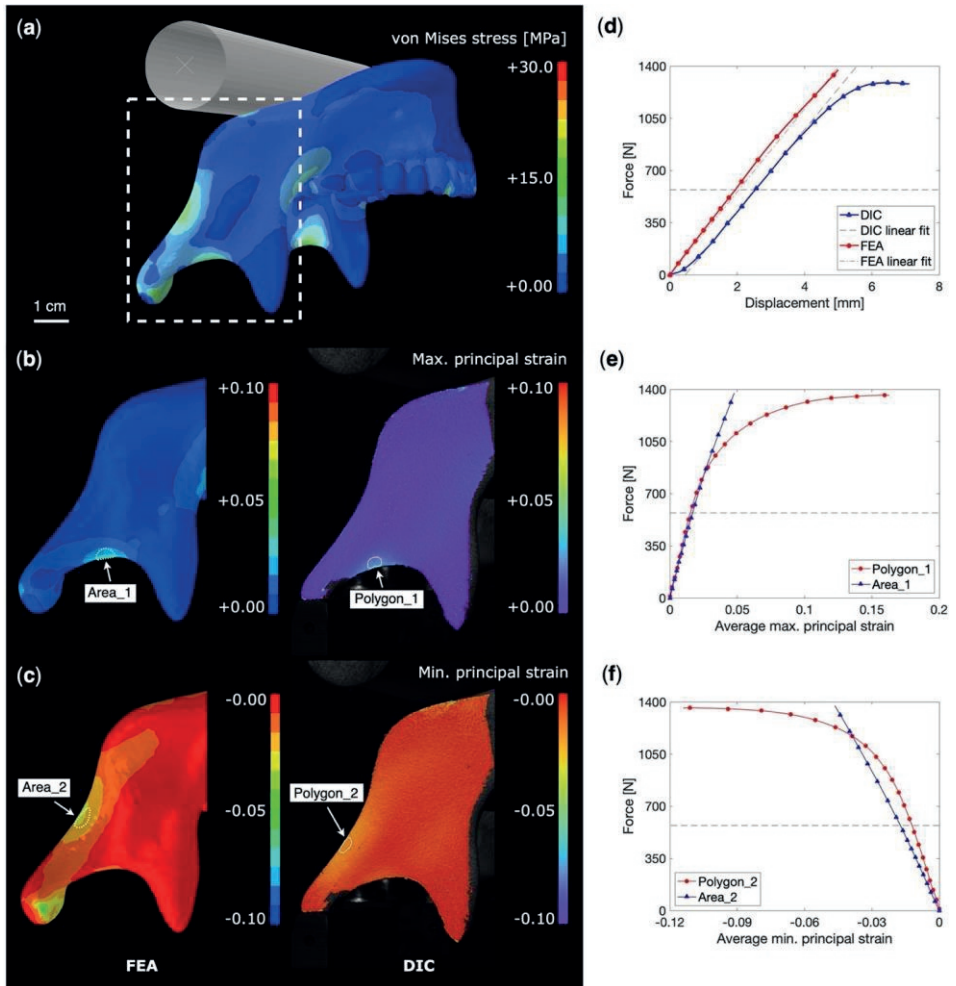


Figure 4.6. (a) The contour of the von Mises stress [MPa] within the intact mandible as predicted by the *EXP-FEA* model (800 N). (b) A comparison of the maximum principal strains within the intact mandible as obtained by the FEA model and DIC measurements. (c) A comparison between the minimum principal strains within the intact mandible predicted by the FEA model and the experimental values measured using DIC. The strain fields correspond to a load of 800 N. (d) The computational and experimental force-displacement curves of the intact mandible. The dotted and dashed lines represent the best-fit approximations of the linear portion of the curves. (e) The mean values of the maximum principal strain extracted from the surfaces in Area_1 and Polygon_1. (f) The mean values of the minimum principal strain extracted from the surfaces in Area_2 and Polygon_2. The horizontal dashed lines in (d-f) indicate the mean values of the maximum biting force of healthy individuals.

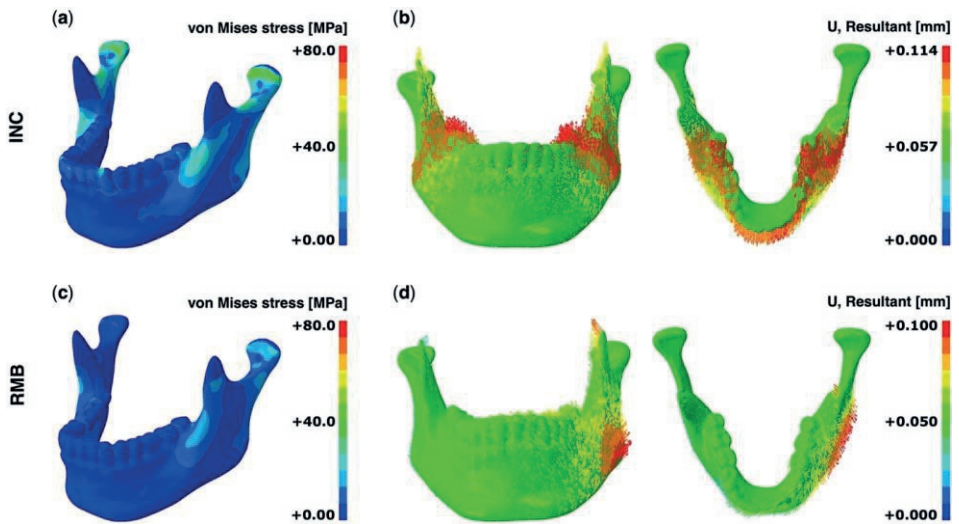


Figure 4.7. (a) The distribution of the von Mises stresses [MPa] and (b) the resulting deformation U [mm] in the healthy-model under the INC condition. (c) The distribution of the von Mises stresses [MPa] and (d) the resulting deformation U [mm] in the healthy-model under the RMB condition. The maximum deformations in (b) and (d) are magnified 50 times. Arrows in the vector plots represent the total displacement of each node. The color and length of the arrows indicate the magnitude and direction of the displacements, respectively.

The deformations in the healthy-model under INC and RMB loading are presented in Figure 4.7b and 4.7d, respectively. Under INC, most deformations occurred around the dental arch. The overall deformation patterns were very similar to those obtained by [44] with the molars moving up and slightly inward and the front teeth moving forward. The results corresponding to the RMB case agreed with the results in [44] too, including a counterclockwise torsional movement with a maximum deformation that was located at the left gonial angle.

Figure 4.8 shows the distribution of the von Mises stresses in the solid-implant-model, LA-implant-model, and TO-implant-model under the INC and RMB conditions. For all the three models, the stresses on the mandibular bone were mainly located on the anterior and posterior condylar neck and on the external oblique line of the contralateral side during INC and on the condylar neck of the lateral side during RMB. During both INC and RMB, the stresses around the contralateral condyle were similar in the three models (around 40 MPa), whereas the stresses on the lateral condyle were lower in the solid-implant-model (15 MPa for RMB) as compared to the TO-implant-model (23 MPa for RMB) and lattice-implant-model (55 MPa for RMB). The stress concentrations in the bone were noted in and around the first and second screw holes closest to the posterior resection margin, with a maximum value of 36 MPa observed in the TO-implant-model. The maximum von Mises stresses in the mandible bone in all the models were well below the mean compressive yield strengths of the cortical mandibular bone, which are reported

to be 200, 110, and 100 MPa along the longitudinal, tangential, and radial directions, respectively [48].

The von Mises stresses inside the implants were higher under the RMB condition as compared to the INC condition in all three implant reconstruction models. Some elevated stresses occurred around the anterior screw holes but the highest stress values were concentrated around the first posterior screw hole near the resection and to a lesser extent along the curved implant edge above that screw. The magnified views at the bottom of Figure 4.8 show that the elevated stress values in these critical areas during RMB stayed well below the yield strength of Ti-6Al-4V (*i.e.*, 800 MPa) [19].

4.3.2 Experimental testing results

The weights of the LA-implant and TO-implant after 3D printing were 15.8 and 18.4 g, respectively. These values are considerably lower than those of the implants used in previous studies (*e.g.*, implants with an average weight of 60 g in a study [13]). No problems were encountered during the preparation of the specimens. For all the specimens, excellent fit was obtained between the implant and the remaining mandibular segments, and tight screw fixation was established after the preparation of the samples using the surgical guide (Figure 4.2f).

Implant failure or failures at the screw-substrate interface were not observed in any of the samples during the quasi-static biomechanical testing. The force-displacement graphs for the INC and RMB loading conditions are presented in Figures 4.9a and 4.9b, respectively. The fracture occurred in the condylar neck region in all the cases, either on the implanted side or on the intact side, depending on the loading condition. In all the cases, the fracture occurred for loads (>1000 N) far above the maximum physiological biting force of healthy individuals (570.9 N during INC and 600.4 N during RMB). This provides the implant with a substantial safety margin in terms of the maximal loads that the reconstructed system can bear in the case of clinical application.

The stiffness, ultimate load, and ultimate displacement of the specimens are presented as grouped scatter plots in Figures 4.9c, 4.9d, and 4.9e, respectively. The intact mandibles and both implant designs exhibited comparable mechanical stiffness, ultimate loads, and ultimate displacements during the tests. No significant differences ($p < 0.05$) were found between the groups under INC and RMB loading conditions.

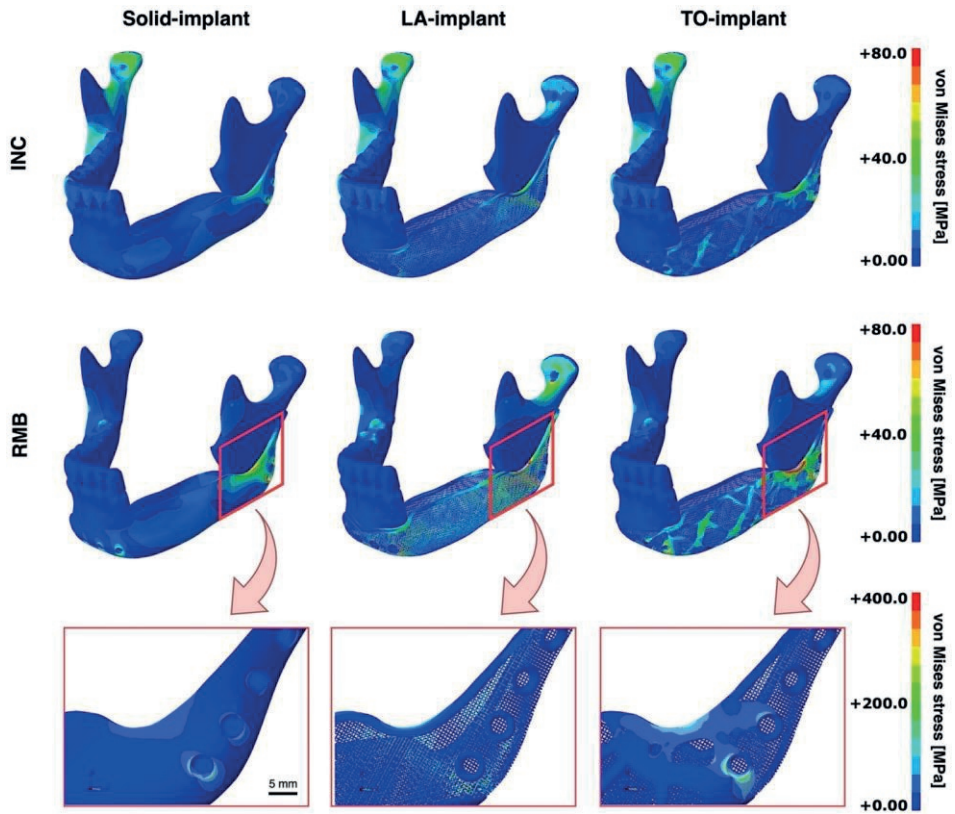


Figure 4.8. The distributions of the von Mises stresses [MPa] in the three implant models under the INC (top) and RMB (middle) conditions. The magnified views (bottom) illustrate the stress concentrations across the lateral mandibular angle region under the RMB condition.

All the cyclic tests of the specimens that were performed using the constant-cyclic-method ran their course up to the maximum number of cycles without any signs of bone failure, implant failure, or any visible changes in the screw fixations. During the subsequent removal of the implants, none of the screws were found to be loose. As for the tests with the increment-cyclic-method, no implant failures, or failures at the screw-substrate interface were observed. The number of cycles to failure and the failure load acting on each of the four samples are listed in Table 4.2. Similar to the quasi-static tests, the specimens tested using the increment-cyclic-method fractured in the condylar neck region of the mandible (three out of four specimens). One exception was identified (TO-implant, sample 2 in Table 4.2) where the mandible fractured in the region of the external oblique line and anterior mandibular angle.

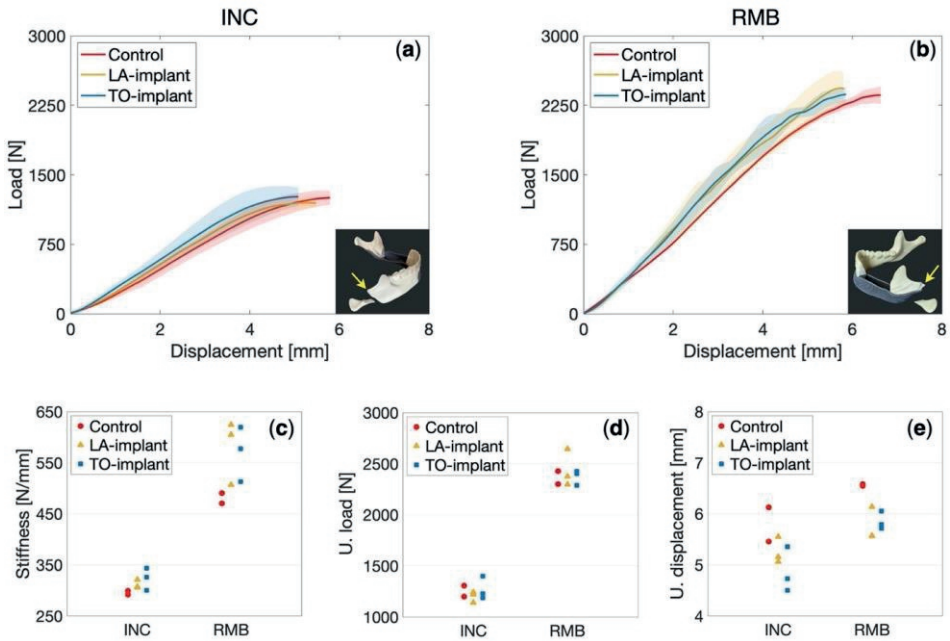


Figure 4.9. The load-displacement curves obtained from the quasi-static tests under the (a) INC and (b) RMB loading conditions. For each group, the lines and shaded areas indicate the mean and standard deviation, respectively. The small inset images on the bottom right indicate the fracture location in each group. The grouped scatter plots of the stiffness (c), ultimate load (d), and ultimate displacement (e) of the constructs. The control specimens represent the intact (non-implanted) mandibles.

Table 4.2. The results of the cyclic tests performed using the increment-cyclic-method.

Group	Sample	# Cycles to failure	Failure load [N]
LA-implant	1	501	1820
LA-implant	2	594	2099
TO-implant	1	579	2033
TO-implant	2	448	1647

The low von Mises stresses observed in the solid implant (Figure 4.8) indicate that the solid implant could perform well in the sense that no implant fractures are expected to occur under the applied loads. Yet, no experimental tests of the solid-implant-model were performed, as it was not considered suitable for clinical application. Its high stiffness and complete absence of implant permeability would almost certainly lead to the atrophy of the bone graft, thereby significantly reducing the implant longevity. Therefore, the main comparison in terms of the implant performance was performed between the LA and TO implant groups. Table 4.3 lists the most important findings of the study to enable a direct comparison between both design approaches.

Design workflow

Table 4.3. A comparison between the design outcomes and mechanical performances of the LA- and TO implants.

	LA-implant	TO-implant*
Design outcomes		
Implant weight [g]	15.8	18.4 (+ 16.5 %)
Implant porosity [%]	63.4	52.4 (- 17.4 %)
Estimated workflow time [h]	3	22 (+ 633.3 %)
Mechanical performance**		
Implant failure (static or fatigue)	No	No
Screw loosening (static or fatigue)	No	No
Mean construct stiffness [N/mm]	311.5 ± 8.3	323.3 ± 21.9 (+ 3.8 %)
Mean ultimate load [N]	1,200.9 ± 54.0	1,271.5 ± 112.0 (+ 5.9 %)
Mean ultimate displacement [mm]	5.3 ± 0.3	4.9 ± 0.4 (- 7.5 %)

* The values between brackets indicate the percentage of change with respect to the LA-implant.
** The values of the mean construct stiffness, mean ultimate load and mean ultimate displacement are presented for the INC 70%/30% loading condition.

4.4 Discussion

We developed a digital workflow for the design of patient-specific implants to restore lateral mandibular defects. Using this workflow, two proof-of-concept cage-shaped implants were designed to match the anatomy of a laterally resected synthetic mandible phantom. While one of the designed implants was fully porous, the other was topology-optimized. The excellent match between the screws and implant on the one hand and between the implant and the mandibular segments on the other confirms the capability of the developed workflow to design customized implants with accurate dimensions. The computationally predicted strains agreed with the DIC measurements. Moreover, the observed locations of specimen failure coincided with the computationally predicted ones. These observations confirm the reliability of the computational models. For both implant designs, the overall implant stresses under post-surgical chewing conditions stayed well below the yield stress of Ti-6Al-4V. Neither the implants nor screw-substrate fixations failed during the quasi-static or cyclic tests, meaning that the strengths of both implants exceeded the strengths needed to withstand the mean maximum bite forces experienced after mandibular resection. The comparison between both types of implants indicated that the fully porous implant may be preferable to the topology-optimized one as it offers a lower weight, a higher porosity, and a shorter design time.

4.4.1 Image processing, shape estimation, and implant designing

The software used for each of the processes in the current workflow (*i.e.*, image processing and implant designing) allows for the customization of their graphic user interface (GUI) through Python scripting. Abaqus/CAE offers a Python-based GUI toolkit too, making it possible to couple the design workflow with an FEA plugin in the near future.

The segmental mirroring of the mandible in combination with a “sweep” operation was the method of choice to estimate the shape of the missing part of the mandible after resection. Statistical shape models (SSM) can be considered as an alternative to estimate the missing bone shape. An advantage of using the mirroring technique compared to SSM is that no additional database with training samples is required, which makes the procedure easier to implement in the workflow. However, mirroring is not possible if both sides of the mandible are affected. For example, the mirroring technique is not applicable to central defects or lesions that cross the midline. Moreover, the presence of asymmetry in the mandibular body, rami, and condyles may hamper the accurate reconstruction of the resected areas. Shape estimation using SSM can address both of these limitations. Shape estimation through SSM is, therefore, a promising approach that could make it possible to treat a larger variety of pathologies and should be considered for inclusion in future versions of the developed workflow.

The implants used in this study were designed in the shape of a cage. Even though several case studies have produced successful clinical outcomes with reconstruction implants in the shape of a cage or tray, there are some potential disadvantages to construction with a cage and bone grafts. In particular, there are significant risks of bone resorption, wound dehiscence, extraoral implant exposure, and postoperative infection, leading to partial or total loss of the construction [2, 49]. This applies mainly to the patients who require the resection of malignant tumors together with a substantial amount of soft tissue. The approach used in this study could, nevertheless, be applied to patients who suffer from benign defects and those who have not (yet) been radiated, and to the situations where soft tissues are compromised only to a limited extent. To minimize the risks of infection and prevent contamination through the oral cavity, a two-stage intervention may be desirable. In such a scenario, first the resection is performed in combination with plate fixation. After healing, reconstruction can take place through the neck. It is important to realize that the application of the workflow proposed in this study is not limited to the design of cages. The workflow could also be used to create patient-specific reconstruction plates or any desired implant geometries for that matter. Since a mandible analog was used here, future studies should apply the developed workflow to actual patient cases.

4.4.2 FEA and experimental validation

The mechanical behavior of the materials involved in our analyses was simplified in various ways to reduce the complexity of the FEA models. Firstly, bone was modeled as an isotropic material even though bone is known to behave anisotropically. Secondly, all the materials present in our FEA models were assumed to be linear elastic while it is known that bone is a viscoelastic material [50] and that highly porous lattice structures may experience localized plastic deformation even when the effective stress is well below the yield stress of the architected material [51]. Finally, stress relaxation, hardening effects, and load redistributions that typically occur during dynamic loading are not considered in our FEA models. Because of these and other modeling simplifications, some discrepancies may be present between the absolute stress values obtained with FEA and the experimentally derived values, especially in the case of large deformations. The PU material used in the experiments is isotropic. It was, therefore, modeled correctly in the *EXP-FEA* model. To minimize the effects of plasticity on the predictions of the FEA models, the results of *EXP-FEA* were compared with the experimental data only within the linear elastic range of the associated force-displacement curves.

The elastic modulus of the PU mandible cortex in *EXP-FEA* was determined such that there was a good correspondence between the computational and experimental results. The selected value of the elastic modulus (0.41 GPa) was close to the value adopted by Koper *et al.* [40], who used the same synthetic mandible analog and estimated its elastic modulus with the elastic modulus of standard PU (0.50 GPa). In this study, experimental tests were performed on PU mandible specimens, and hence homogeneous material assignment with cortical PU properties was sufficient for the validation of the computational models. Density values and elastic moduli were translated to those of the actual bone for the *PHY-FEA* models to predict clinical scenarios accurately. The material properties in the latter case were scaled to those of the actual bone based on the grey values obtained from the CT images. The number of materials chosen to describe the cancellous and cortical bone may not be sufficient to reflect the variations in the material properties of the actual mandibular bone. In fact, the number of materials could theoretically be reduced to two, considering the way the mandibles are manufactured with two distinct regions of cancellous bone and cortical bone. However, a more diverse spread of *HU* values was obtained from the CT images, indicating that some transition regions between the cancellous bone and cortical bone may have existed as well as some higher-density areas in the cortical region. In the case of actual clinical applications, the material properties of the bone (*i.e.*, density and elastic modulus) will be obtained from the *HU* values of each patient's CT images. The correlation between the *HU* values and bone density can be established either by imaging hydroxyapatite phantoms or be derived from the average bone density data available in the literature. As for the mechanical properties, the empirical relationships available in the literature between the bone density and elastic

modulus could be employed [22, 52]. The patient-specific bone material properties would then be implemented in the FEA models to predict the mechanical and failure behaviors of both the bone and the entire construct.

Normally, a layer of periodontal ligament (PDL) is located between the tooth roots and the alveolar sockets, which is important for transferring the force to the alveolar bone. This very thin tissue cannot be easily captured with regular CT scanning protocols. Even though some other FEA studies have included this soft tissue layer between the teeth and the bone, it is often excluded from FEA models as it requires time-consuming manual segmentation steps and increases the processing time due to increased model complexity [53]. Several studies have, however, found that FEA models show a much higher stiffness and, thus, lower strains when teeth and bone are modeled as continuous objects as opposed to models where the PDL is included [53, 54]. It is, therefore, suggested that future studies perform a sensitivity analysis to determine the effect of PDL on the accuracy of the FEA model predictions.

The regions associated with the high values of the von Mises stress (Figure 4.6a) correspond well with the primary locations of failure observed during the mechanical tests, namely the condylar neck region. This suggests that the boundary conditions and forces are correctly implemented in the computational models. The compressive strength of the PU foam with densities between 0.240 – 0.641 g/cm³ ranges between 4.7 and 24.7 MPa [55]. A maximum stress of 16 MPa observed in the FE model (condylar neck region) falls within this range, assuming that the cortical PU is of high enough density. The agreement between the deformation patterns shown in Figures 4.7b and 4.7d indicates the correct implementation of the muscle force vector directions and the relative muscle force magnitudes. The good agreement in the stress patterns observed between Figures 4.7a and 4.7c and those reported by Pinheiro and Alves [42] indicates that the muscle forces are correctly scaled.

In all three implant models, the condylar neck on the contralateral side is stressed the most during INC whereas the condylar neck on the lateral side is stressed the most during RMB. This observation agrees well with the quasi-static testing results (Figures 4.9a-b) where the fracture under the INC loading conditions consistently occurred in the contralateral condyle. Under the RMB loading conditions, the fracture always occurred in the lateral condyle. While the stress levels on the contralateral side of the mandible are comparable in the three implant models, the stress levels on the lateral side of the mandible seem to increase as the stiffness of the implant decreases. The resistance of the implanted mandible to deformation depends on the stiffness of the implant. With a lower implant stiffness, the resistance to the deformation must be smaller. The equivalent stresses will, consequently, be higher in the bone surrounding the implant. The maximum stresses on the implants can be found just below the first screw hole near the posterior resection margin. The area of the mandibular angle, especially the area around the screws

close to the proximal resection margin, is known to represent a weak spot in reconstruction plates [29, 47, 56, 57].

The maximum and minimum principal strain values were extracted from two regions on the outer surface edges of the bone. When the surface on the outer edges is curved, the subtended angle of the camera view with respect to the sample will play an important role. As the curvature on the posterior surface of the condylar neck (Polygon_2) is relatively blunt, the back of the condylar neck may not be fully captured by the cameras (Figure 4.5d). Since the strain values are expected to be the largest in that area, it may be the case that Polygon_2 covers a region with lower maximum strain values than those covered by Area_2 in the FE model, which could explain the offset in the principal strain values in Figure 4.6-f. At the curved boundaries peak strains could be underestimated due to averaging errors given that the accuracy of the measurements depends on the pixel subset size used for the strain calculations [58]. Placing the cameras closer to the normal of the surfaces at the strain peak regions may improve the accuracy. Finally, a limitation regarding the comparison of the DIC measurements with the FEA results is that we only used one intact sample for DIC measurements. Comparing FEA with averaged DIC data from multiple specimens and taken at various camera angles may reduce the margin of error.

It is very challenging to mimic the *in vivo* three-dimensional loading configuration of the mandible. Simplifications are, therefore, needed. Seebach *et al.* [59] showed that the biting forces could be described by a resultant vector originating from the mandibular angles. This approach was translated into the current setup by applying uniaxial forces that act on both mandibular angles [40, 45-47, 60]. The various translational and rotational degrees of freedom integrated into the stage and the tooth supports of the experimental setup (Figure 4.4a) make it possible to test intact and reconstructed mandibles with different sizes and shapes and under almost any desired loading conditions. This is particularly useful if cadaveric studies are going to be performed. The muscle forces acting on the reconstructed side are often reduced to some extent, leading to an unequal distribution of biting forces between both sides [61, 62]. In the present study, the muscles that could not retain their function after reconstruction were removed from the FE model, whereas in the experimental setup, this loading imbalance was accounted for by distributing 70% and 30% of the total forces on the healthy and affected side, respectively [47]. It is important to mention is that this force distribution was selected because no reliable data could be found in the literature.

Two different methods were used to test the biomechanical performance of the reconstruction systems under cyclic loading, namely, the constant-cyclic-method and increment-cyclic-method. Methods like the former have been used by [47, 63], while the latter method was applied by [45, 46]. The fact that none of the implants failed during the quasi-static tests, either through fracture or screw/implant loosening, at loads far

exceeding the maximal physiological biting forces indicates that the reconstruction was stable. The fatigue tests performed with the constant-cyclic-method indicated that the reconstruction systems performed very well at least up to 250.000 cycles at relatively high chewing forces. The high resistance of the reconstruction systems to mechanical failure was also confirmed by the absence of fatigue failure in the osteosynthesis during the tests with the increment-cyclic-method. The reason that sample 2 in the TO-implant group fractured at a different location during the test with the increment-cyclic-method than the other specimens did was most likely minor manufacturing defects (cavities), which were observed at several locations along the fracture line.

A limitation regarding the data analysis approach can be identified. The fact that no large differences in the stiffness, ultimate load, or ultimate displacement were observed between the implanted and intact mandibles suggests that both implants will perform well in taking over the function of the original bone segment. This might also indicate that there is still a margin to further increase the porosity inside the implants. However, the low sample size per loading condition in the tests can be seen as a limitation, as it reduces the statistical power. Due to budget constraints, the sample sizes were minimized and determined such that the validation of the computational models could be established and the potentially (significant) differences between the two implant designs could still be revealed. Random sampling was applied within and between the experimental groups. All the samples were prepared in an identical fashion, followed by randomly allocating them to each of the experimental groups and random testing them for each loading condition. The variations between the specimens were minimized by using one type of mandible model, using a surgical guide for sample preparation, and ensuring an identical positioning of the samples during the mechanical tests. The level of variations within each group was, therefore, limited, making it safer to draw conclusions on the significance of the relative differences between the groups despite the low sample sizes. A Kruskal-Wallis non-parametric test ($p < 0.05$) with Bonferroni correction was performed to investigate the effects of any potential deviations from a normal distribution on the results of the performed statistical analysis. The results of the non-parametric test regarding statistical significance, however, matched those of the parametric t -test (*i.e.*, no significant differences in stiffness, ultimate load, or ultimate displacement were found between both implant designs).

Since the mechanical performances of the LA- and TO-implants were not found to be significantly different, the LA-implant may be preferable to the TO implant for clinical application due to the four following reasons. First, the weight of the LA-implant is slightly lower than that of the TO-implant, which will increase the patient comfort while reducing the material costs. Second, the LA-implant has a higher porosity, which is likely to result in a higher degree of osseointegration and bone tissue regeneration [17, 64]. Third, the increased porosity presumably leads to a lower implant stiffness, which is

beneficial for reducing stress shielding. Finally, the relatively time-consuming TO process (18 h for the implant designed here, excluding the additional post-processing time) can be omitted.

4.5 Conclusion

We demonstrated the capability of the proposed workflow to design and analyze patient-specific mandibular reconstruction cage implants with excellently reproduced mandibular contours and high resistance to mechanical failure. The proposed workflow will, after future incorporation of an FEA plugin, provide surgeons and medical engineers with a systematic approach and the tools to design and evaluate patient-specific reconstruction implants. This would enable cost- and time-effective pre-surgical planning and the design of customized implants that can maximize the aesthetic and functional outcomes while minimizing the associated morbidities.

4.6 Supplementary material

Table S4.1. Muscle forces acting in three directions during INC and RMB in the healthy-model. Resultant force vectors in their respective areas of exertion are shown in Figure 4.4.

Muscle name	# Nodes	INC			RMB		
		F_x [N]	F_y [N]	F_z [N]	F_x [N]	F_y [N]	F_z [N]
<i>Left lateral pterygoid</i>	21	-131.87	-146.00	-23.24	-30.89	-37.14	-8.50
<i>Left masseter</i>	24	88.25	-78.49	269.34	56.83	-34.19	155.75
<i>Left medial pterygoid</i>	24	-213.95	-164.23	348.19	-57.53	-44.17	93.54
<i>Left temporalis</i>	22	12.19	15.78	60.48	38.44	60.04	178.40
<i>Right lateral pterygoid</i>	24	131.87	-146.00	-23.24	14.23	-17.18	-3.90
<i>Right masseter</i>	23	-88.25	-78.49	269.34	-68.20	-41.13	186.90
<i>Right medial pterygoid</i>	22	213.95	-164.23	348.19	80.52	-61.78	131.02
<i>Right temporalis</i>	19	-12.19	15.78	60.48	-45.64	72.89	211.98

Table S4.2. Muscle forces acting in three directions during INC and RMB in the three implant reconstruction models. Resultant force vectors in their respective areas of exertion are shown in Figure 4.4.

Muscle name	# Nodes	INC			RMB		
		F_x [N]	F_y [N]	F_z [N]	F_x [N]	F_y [N]	F_z [N]
<i>Left lateral pterygoid</i>	21	-148.52	-164.43	-26.18	-24.64	-29.63	-6.78
<i>Left masseter</i>	-	-	-	-	-	-	-
<i>Left medial pterygoid</i>	-	-	-	-	-	-	-
<i>Left temporalis</i>	22	13.74	17.78	68.12	30.67	47.90	142.32
<i>Right lateral pterygoid</i>	24	148.52	-164.43	-26.18	11.35	-13.71	-3.12
<i>Right masseter</i>	23	-99.39	-88.40	303.33	-54.41	-32.81	149.11
<i>Right medial pterygoid</i>	22	240.95	-184.96	392.14	64.24	-49.29	104.53
<i>Right temporalis</i>	19	-13.74	17.78	68.12	-36.41	58.15	169.11

Design workflow

Table S4.3. Chemical composition [mass fraction in %] of the Ti-6Al-4V powder supplied by SLM Solutions (SLM Solutions, Material Data Sheet).

Ti	Al	V	C	O	N	Fe	H	Other each	Other each
Balance	5.50–6.50	3.50–4.50	0.08	0.13	0.03	0.25	0.0125	0.10	0.40

Table S4.4. Main 3D printing process parameters, powder particle sizes, and physical properties of the as-built Ti-6Al-4V material (SLM Solutions, Material Data Sheet).

Condition	Layer thickness/ laser power [μm / W]	Particle size [μm]	Mass density [g/cm^3]	Roughness average R_a [μm]	Mean roughness depth R_z [μm]
As-built	60 / 400	20 – 63	4.43	12 ± 1	71 ± 6

Supplementary movies

Supplementary Video 4.1. The deformations of the mandible during INC loading as predicted by the EXP-FEA model up to 1375 N (left) and as measured using the quasi-static experiments up to fracture (right) (see <https://doi.org/10.1016/j.jmbbm.2022.105291>)

Bibliography

1. B.T. Goh, S. Lee, H. Tideman, P.J. Stoelinga, Mandibular reconstruction in adults: a review, *International journal of oral and maxillofacial surgery* 37(7) (2008) 597-605.
2. B.P. Kumar, V. Venkatesh, K.J. Kumar, B.Y. Yadav, S.R. Mohan, Mandibular reconstruction: overview, *Journal of maxillofacial and oral surgery* 15 (2016) 425-441.
3. R.C. Wong, H. Tideman, M. Merckx, J. Jansen, S. Goh, K. Liao, Review of biomechanical models used in studying the biomechanics of reconstructed mandibles, *International journal of oral and maxillofacial surgery* 40(4) (2011) 393-400.
4. K. Kakarala, Y. Shnyder, T.T. Tsue, D.A. Girod, Mandibular reconstruction, *Oral Oncology* 77 (2018) 111-117.
5. W.-b. Lee, W.-h. Choi, H.-g. Lee, N.-r. Choi, D.-s. Hwang, U.-k. Kim, Mandibular reconstruction with a ready-made type and a custom-made type titanium mesh after mandibular resection in patients with oral cancer, *Maxillofacial plastic and reconstructive surgery* 40 (2018) 1-7.
6. A. Paré, A. Bossard, B. Laure, P. Weiss, O. Gauthier, P. Corre, Reconstruction of segmental mandibular defects: Current procedures and perspectives, *Laryngoscope Investigative Otolaryngology* 4(6) (2019) 587-596.
7. D. Radwan, F. Mobarak, Plate-related complications after mandibular reconstruction: observational study osteotomy, *Egyptian Journal of Oral and Maxillofacial Surgery* 9(1) (2018) 22-27.
8. G.-J. Seol, E.-G. Jeon, J.-S. Lee, S.-Y. Choi, J.-W. Kim, T.-G. Kwon, J.-Y. Paeng, Reconstruction plates used in the surgery for mandibular discontinuity defect, *Journal of the Korean Association of Oral and Maxillofacial Surgeons* 40(6) (2014) 266.
9. U. Vignesh, D. Mehrotra, D. Howlader, P.K. Singh, S. Gupta, Patient specific three-dimensional implant for reconstruction of complex mandibular defect, *Journal of Craniofacial Surgery* 30(4) (2019) e308-e311.
10. S. Kondo, H. Katsuta, A. Akizuki, Y. Kurihara, T. Kamatani, A. Yaso, M. Nagasaki, T. Shimane, T. Shirota, Computer-assisted surgery for mandibular reconstruction using a patient-specific titanium mesh tray and particulate cancellous bone and marrow, *Case Reports in Clinical Medicine* 4(3) (2015) 85-92.
11. Y.-W. Lee, H.-J. You, J.-A. Jung, D.-W. Kim, Mandibular reconstruction using customized three-dimensional titanium implant, *Archives of craniofacial surgery* 19(2) (2018) 152.
12. Z. Malekpour, F. Sarkarat, H. Hooshangi, Mandibular reconstruction using custom-made titanium mesh tray and autogenous bone graft: A case report, *Thrita* 3(4) (2014).
13. M. Mounir, A. Abou-ElFetouh, W. ElBeialy, R. Mounir, Patient-specific alloplastic endoprosthesis for reconstruction of the mandible following segmental resection: a case series, *Journal of Cranio-Maxillofacial Surgery* 48(8) (2020) 719-723.
14. J.-H. Park, M. Odkhuu, S. Cho, J. Li, B.-Y. Park, J.-W. Kim, 3D-printed titanium implant with pre-mounted dental implants for mandible reconstruction: a case report, *Maxillofacial Plastic and Reconstructive Surgery* 42 (2020) 1-4.
15. A. Rachmiel, D. Shilo, O. Blanc, O. Emodi, Reconstruction of complex mandibular defects using integrated dental custom-made titanium implants, *British Journal of Oral and Maxillofacial Surgery* 55(4) (2017) 425-427.
16. Y. Yamashita, Y. Yamaguchi, M. Tsuji, M. Shigematsu, M. Goto, Mandibular reconstruction using autologous iliac bone and titanium mesh reinforced by laser welding for implant placement, *International Journal of Oral & Maxillofacial Implants* 23(6) (2008).
17. L.-b. Zhou, H.-t. Shang, L.-s. He, B. Bo, G.-c. Liu, Y.-p. Liu, J.-l. Zhao, Accurate reconstruction of discontinuous mandible using a reverse engineering/computer-aided design/rapid prototyping technique: a preliminary clinical study, *Journal of Oral and Maxillofacial Surgery* 68(9) (2010) 2115-2121.
18. M. Oldhoff, M.J. Mirzaali, N. Tümer, J. Zhou, A. Zadpoor, Comparison in clinical performance of surgical guides for mandibular surgery and temporomandibular joint implants fabricated by additive manufacturing techniques, *journal of the mechanical behavior of biomedical materials* 119 (2021) 104512.

Design workflow

19. C.-H. Li, C.-H. Wu, C.-L. Lin, Design of a patient-specific mandible reconstruction implant with dental prosthesis for metal 3D printing using integrated weighted topology optimization and finite element analysis, *Journal of the mechanical behavior of biomedical materials* 105 (2020) 103700.
20. Y.-f. Liu, Y.-y. Fan, X.-f. Jiang, D.A. Baur, A customized fixation plate with novel structure designed by topological optimization for mandibular angle fracture based on finite element analysis, *Biomedical engineering online* 16 (2017) 1-17.
21. Y.-f. Liu, F.-d. Zhu, X.-t. Dong, W. Peng, Digital design of scaffold for mandibular defect repair based on tissue engineering, *Journal of Zhejiang University Science B* 12(9) (2011) 769-779.
22. K.-j. Cheng, Y.-f. Liu, R. Wang, J.-x. Zhang, X.-f. Jiang, X.-t. Dong, X. Xu, Topological optimization of 3D printed bone analog with PEKK for surgical mandibular reconstruction, *Journal of the Mechanical Behavior of Biomedical Materials* 107 (2020) 103758.
23. E. Abouel Nasr, A.M. Al-Ahmari, K. Moiduddin, M. Al Kindi, A.K. Kamrani, A digital design methodology for surgical planning and fabrication of customized mandible implants, *Rapid Prototyping Journal* 23(1) (2017) 101-109.
24. B.B.J. Merema, J. Kraeima, H.H. Glas, F.K. Spijkervet, M.J. Witjes, Patient-specific finite element models of the human mandible: Lack of consensus on current set-ups, *Oral diseases* 27(1) (2021) 42-51.
25. D.N. León, G.M. Flórez, C.L. Gualdrón, Low-cost mandibular reconstruction workflow, *Oral and Maxillofacial Surgery Cases* 6(2) (2020) 100146.
26. D.P. Coletti, R. Ord, X. Liu, Mandibular reconstruction and second generation locking reconstruction plates: Outcome of 110 patients, *International Journal of Oral and Maxillofacial Surgery* 38(9) (2009) 960-963.
27. J.M. Doty, D. Pienkowski, M. Goltz, R.H. Haug, J. Valentino, O.A. Arosarena, Biomechanical Evaluation of Fixation Techniques for Bridging Segmental Mandibular Defects, *Archives of Otolaryngology–Head & Neck Surgery* 130(12) (2004) 1388-1392.
28. T. Ettl, O. Driemel, B.V. Dresp, T.E. Reichert, J. Reuther, H. Pistner, Feasibility of alloplastic mandibular reconstruction in patients following removal of oral squamous cell carcinoma, *Journal of Cranio-Maxillofacial Surgery* 38(5) (2010) 350-354.
29. R. Gutwald, R. Jaeger, F.M. Lambers, Customized mandibular reconstruction plates improve mechanical performance in a mandibular reconstruction model, *Computer methods in Biomechanics and Biomedical engineering* 20(4) (2017) 426-435.
30. T. Shibahara, H. Noma, Y. Furuya, R. Takaki, Fracture of mandibular reconstruction plates used after tumor resection, *Journal of oral and maxillofacial surgery* 60(2) (2002) 182-185.
31. G.A. Khalifa, N.A. Abd El Moniem, S.A.-E. Elsayed, Y. Qadry, Segmental mirroring: does it eliminate the need for intraoperative readjustment of the virtually pre-bent reconstruction plates and is it economically valuable?, *Journal of Oral and Maxillofacial Surgery* 74(3) (2016) 621-630.
32. K. Moiduddin, A. Al-Ahmari, E.S.A. Nasr, M. Al Kindi, S. Ramalingam, A. Kamrani, Comparing 3-dimensional virtual reconstruction methods in customized implants, *Int J Adv Biotechnol Res* 7 (2016) 323-331.
33. Q. Qassemayr, N. Assouly, S. Temam, F. Kolb, Use of a three-dimensional custom-made porous titanium prosthesis for mandibular body reconstruction, *International Journal of Oral and Maxillofacial Surgery* 46(10) (2017) 1248-1251.
34. H.E. Koschwanetz, W.M. Reichert, Textured and porous materials, *Biomaterials Science*, Elsevier 2013, pp. 321-331.
35. K. Moiduddin, S.H. Mian, N. Ahmed, W. Ameen, H. Al-Khalefah, M.K. Mohammed, U. Umer, Integrative and multi-disciplinary framework for the 3D rehabilitation of large mandibular defects, *The International Journal of Advanced Manufacturing Technology* 106 (2020) 3831-3847.
36. K. Moiduddin, S.H. Mian, H. Alkhalefah, U. Umer, Digital design, analysis and 3D printing of prosthesis scaffolds for mandibular reconstruction, *Metals* 9(5) (2019) 569.
37. F.S.L. Bobbert, A.A. Zadpoor, Effects of bone substitute architecture and surface properties on cell response, angiogenesis, and structure of new bone, *Journal of Materials Chemistry B* 5(31) (2017) 6175-6192.
38. Z. Wang, C. Wang, C. Li, Y. Qin, L. Zhong, B. Chen, Z. Li, H. Liu, F. Chang, J. Wang, Analysis of

- factors influencing bone ingrowth into three-dimensional printed porous metal scaffolds: a review, *Journal of Alloys and Compounds* 717 (2017) 271-285.
39. W.-m. Peng, K.-j. Cheng, Y.-f. Liu, M. Nizza, D.A. Baur, X.-f. Jiang, X.-t. Dong, Biomechanical and Mechanostat analysis of a titanium layered porous implant for mandibular reconstruction: The effect of the topology optimization design, *Materials Science and Engineering: C* 124 (2021) 112056.
 40. D.C. Koper, C.A. Leung, L.C. Smeets, P.F. Laeven, G.J. Tuijthof, P.A. Kessler, Topology optimization of a mandibular reconstruction plate and biomechanical validation, *Journal of the mechanical behavior of biomedical materials* 113 (2021) 104157.
 41. M. Ay, T. Kubat, C. Delilbasi, B. Ekici, H.E. Yuzbasioglu, S. Hartomacioglu, 3D Bio-Cad modeling of human mandible and fabrication by rapid-prototyping technology, *Usak University Journal of Material Sciences* 2(2) (2016) 135-145.
 42. M. Pinheiro, J. Alves, The feasibility of a custom-made endoprosthesis in mandibular reconstruction: Implant design and finite element analysis, *Journal of Cranio-Maxillofacial Surgery* 43(10) (2015) 2116-2128.
 43. N.S. Moghaddam, A. Jahadakbar, A. Amerinatanz, M. Elahinia, M. Miller, D. Dean, Metallic fixation of mandibular segmental defects: Graft immobilization and orofacial functional maintenance, *Plastic and Reconstructive Surgery—Global Open* 4(9) (2016) e858.
 44. T. Koriath, A. Hannam, Deformation of the human mandible during simulated tooth clenching, *Journal of dental research* 73(1) (1994) 56-66.
 45. J. Gateno, C. Cookston, S.S.-P. Hsu, D.N. Stal, S.K. Durrani, J. Gold, S. Ismaily, J.W. Alexander, P.C. Noble, J.J. Xia, Biomechanical evaluation of a new MatrixMandible plating system on cadaver mandibles, *Journal of Oral and Maxillofacial Surgery* 71(11) (2013) 1900-1914.
 46. C. Rendenbach, K. Sellenschloh, L. Gerbig, M.M. Morlock, B. Beck-Broichsitter, R. Smeets, M. Heiland, G. Huber, H. Hanken, CAD–CAM plates versus conventional fixation plates for primary mandibular reconstruction: A biomechanical in vitro analysis, *Journal of cranio-maxillofacial surgery* 45(11) (2017) 1878-1883.
 47. W. Schupp, M. Arzdorf, B. Linke, R. Gutwald, Biomechanical testing of different osteosynthesis systems for segmental resection of the mandible, *Journal of oral and maxillofacial surgery* 65(5) (2007) 924-930.
 48. T. van Eijden, Biomechanics of the mandible, *Critical reviews in oral biology & medicine* 11(1) (2000) 123-136.
 49. H. Tideman, N. Samman, L. Cheung, Functional reconstruction of the mandible: a modified titanium mesh system, *International journal of oral and maxillofacial surgery* 27(5) (1998) 339-345.
 50. R.S. Lakes, J.L. Katz, S.S. Sternstein, Viscoelastic properties of wet cortical bone—I. Torsional and biaxial studies, *Journal of Biomechanics* 12(9) (1979) 657-678.
 51. M. Benedetti, A. du Plessis, R.O. Ritchie, M. Dallago, N. Razavi, F. Berto, Architected cellular materials: A review on their mechanical properties towards fatigue-tolerant design and fabrication, *Materials Science and Engineering: R: Reports* 144 (2021) 100606.
 52. M.B. Kucukguven, M. Akkocaoğlu, Finite element analysis of stress distribution on reconstructed mandibular models for autogenous bone grafts, *Technology and Health Care* 28(3) (2020) 249-258.
 53. F. Gröning, M. Fagan, P. O'higgins, Modeling the human mandible under masticatory loads: which input variables are important?, *The Anatomical Record: Advances in Integrative Anatomy and Evolutionary Biology* 295(5) (2012) 853-863.
 54. R. Marinescu, D.J. Daegling, A.J. Rapoff, Finite-element modeling of the anthropoid mandible: the effects of altered boundary conditions, *The Anatomical Record Part A: Discoveries in Molecular, Cellular, and Evolutionary Biology: An Official Publication of the American Association of Anatomists* 283(2) (2005) 300-309.
 55. K.L. Calvert, K.P. Trumble, T.J. Webster, L.A. Kirkpatrick, Characterization of commercial rigid polyurethane foams used as bone analogs for implant testing, *Journal of Materials Science: Materials in Medicine* 21(5) (2010) 1453-1461.
 56. S. Trainotti, S. Raith, M. Kesting, S. Eichhorn, F. Bauer, A. Kolk, B. Lethaus, F. Hölzle, T. Steiner, Locking versus nonlocking plates in mandibular reconstruction with fibular graft—a biomechanical ex vivo study, *Clinical oral investigations* 18 (2014) 1291-1298.

Design workflow

57. Z. Yi, Z. Jian-Guo, Y. Guang-Yan, L. Ling, Z. Fu-Yun, Z. Guo-Cheng, Reconstruction plates to bridge mandibular defects: a clinical and experimental investigation in biomechanical aspects, *International Journal of Oral & Maxillofacial Surgery* 28(6) (1999) 445-450.
58. S. Chanda, A. Dickinson, S. Gupta, M. Browne, Full-field in vitro measurements and in silico predictions of strain shielding in the implanted femur after total hip arthroplasty, *Proceedings of the Institution of Mechanical Engineers, Part H: Journal of Engineering in Medicine* 229(8) (2015) 549-559.
59. M. Seebach, F. Theurer, P. Foehr, C.v. Deimling, R. Burgkart, M.F. Zaeh, Design of bone plates for mandibular reconstruction using topology and shape optimization, *Advances in Structural and Multidisciplinary Optimization: Proceedings of the 12th World Congress of Structural and Multidisciplinary Optimization (WCSMO12) 12*, Springer, 2018, pp. 2086-2096.
60. S.C. Fontana, R.B. Smith, N. Nazir, B.T. Andrews, Biomechanical assessment of fixation methods for segmental mandible reconstruction with fibula in the polyurethane model, *Microsurgery* 36(4) (2016) 330-333.
61. D.A. Curtis, O. Plesh, A.G. Hannam, A. Sharma, T.A. Curtis, Modeling of jaw biomechanics in the reconstructed mandibulectomy patient, *The Journal of Prosthetic Dentistry* 81(2) (1999) 167-173.
62. M. Marunick, B. Mathes, B. Klein, Masticatory function in hemimandibulectomy patients, *Journal of oral rehabilitation* 19(3) (1992) 289-295.
63. C.-H. Wu, Y.-S. Lin, Y.-S. Liu, C.-L. Lin, Biomechanical evaluation of a novel hybrid reconstruction plate for mandible segmental defects: A finite element analysis and fatigue testing, *Journal of Cranio-Maxillofacial Surgery* 45(10) (2017) 1671-1680.
64. T. Schouman, M. Schmitt, C. Adam, G. Dubois, P. Rouch, Influence of the overall stiffness of a load-bearing porous titanium implant on bone ingrowth in critical-size mandibular bone defects in sheep, *Journal of the mechanical behavior of biomedical materials* 59 (2016) 484-496.

5

3D printed patient-specific fixation plates for the treatment of slipped capital femoral epiphysis: topology optimization vs. conventional design

Patient-specific orthopedic plates have recently emerged as a promising fixation device. However, it is unclear how various strategies used for the design of such plates perform in comparison with each other. Here, we compare the biomechanical performance of 3D printed patient-specific bone plates designed using conventional computer-aided design (CAD) techniques with those designed with the help of topology optimization (TO) algorithms, focusing on cases involving slipped capital femoral epiphysis (SCFE). We established a biomechanical testing protocol to experimentally assess the performance of the designed plates while measuring the full-field strain using digital image correlation. We also created an experimentally validated finite element model to analyse the performance of the plates under physiologically relevant loading conditions. The results indicated that the TO construct exhibited higher ultimate load and biomechanical performance as compared to the CAD construct, suggesting that TO is a viable approach for the design of such patient-specific bone plates. The TO plate also distributed stress more evenly over the screws, likely resulting in more durable constructs and improved anatomical conformity while reducing the risk of screw and plate failure during cyclic loading. In addition to enhancing the mechanical performance, the utilization of TO in plate design may also improve the surgical outcome and decrease the recovery time by reducing the plate and incision sizes.

Moosabeiki, V., de Winter, N., Saldivar, M.C., Leeflang, M.A., Witbreuk, M.M.E.H., Lagerburg, V., Mirzaali, M.J. and Zadpoor, A.A., 3D printed patient-specific fixation plates for the treatment of slipped capital femoral epiphysis: Topology optimization vs. conventional design, *Journal of the Mechanical Behavior of Biomedical Materials*, 148, p.106173, 2023.

5.1 Introduction

Slipped capital femoral epiphysis (SCFE) is a prevalent hip disorder in adolescents, where the growth plate, also known as physis, is disrupted and the metaphysis, the part of the bone located next to the growth plate, displaces in a posterior-inferior direction with respect to the capital femoral epiphysis (*i.e.*, femoral head) [1, 2]. Obesity, endocrine disorders, oblique physeal growth, and increased femoral retroversion increase the risk of SCFE due to either a weakening (endocrine) of the growth plate or an increased mechanical stress on the growth plate [3-5].

In situ pinning is the first step in preventing SCFE progression in mild cases. However, it has been linked to osteoarthritis later in life and does not restore normal anatomy or relieve pain, particularly in severe SCFE cases [5]. Corrective osteotomy surgery, commonly intertrochanteric osteotomy, is performed on patients with moderate SCFE. The proximal femur (*i.e.*, femur head) and femur shaft are realigned with a femoral head–neck osteotomy, then stabilized using a fixation plate [6, 7]. Intertrochanteric osteotomy restores hip motion and biomechanics while reducing the risk of avascular necrosis [8]. The surgery is considered successful when the mobility and pain level of the patient improve and no plate or screw failure occurs. The bone is expected to have adequately healed in six weeks, allowing for gradual hip loading. One year after the surgery, the plate is usually removed as it is no longer required for bone stability [9, 10]. However, reports indicate that plate failures do occur with 12.5% of these failures reported within the first six weeks [11], with most plate failures occurring between three to six months post-surgery [11-13]. These late failures are usually related to non-union of the bone after surgery.

In the field of orthopedic surgery, temporary fixation of bones following osteotomy is achieved using commercially available plates of standard size, which are bent to fit the bones as closely as possible. However, standard plates are not always suitable for complex cases, and a mismatch between the plate and bone can increase the risk of failure after surgery [14-17]. Patient-specific plates offer a better anatomical fit and reduce the risk of plate failure. These plates can be designed using virtual surgical planning tools and computationally enabled design methods, such as finite element analysis (FEA) and topology optimization (TO) [18-23], to optimize their shape, topology, and geometry, thereby limiting the incision size, minimizing the risk of infection, and promoting bone healing [24-28]. However, a smaller plate may also result in lower stiffness and decreased stability, compromising its effectiveness in supporting the affected area [24, 25]. A workflow that combines design optimization and computational/experimental testing is, therefore, required to facilitate the integration of patient-specific plates into routine medical practice.

Despite some studies reporting the design workflow for patient-specific femur fixation plates, there is a lack of research into their biomechanical performance under physiological loading conditions [29]. Moreover, while the mechanical properties of non-customized fixation plates have been studied, there is limited research into patient-specific bone plates for femur fixation and the optimal parameters for efficient and stable fracture fixation [25, 30].

In this study, we aimed to improve the biomechanical performance of a patient-specific proximal femur fixation plate through the incorporation of computational modelling and TO into the design process. Our objective was to optimize the plate size and enhance its biomechanical performance while maintaining its elastic stiffness. To accomplish this, we designed both above-mentioned types of fixation plates, manufactured them using 3D printing, and subjected them to mechanical loads while measuring the full-field strain patterns using digital image correlation. We also developed an experimentally validated FE model to evaluate the plates under two physiological loading conditions: two-leg stance (with a maximum reaction force of 1 time body weight (BW) and walking (with a maximum reaction force of 3 times BW). Our FE model considered a scenario in which bone healing is delayed, but gradual load bearing has already started, with a focus on the worst-case scenario of walking. The ultimate goal was to assist clinical engineers in designing more reliable and optimally sized patient-specific plates for the treatment of SCFE defects.

5.2 Materials and methods

A 13-year-old male patient with a body weight of 100 kg was referred to the OLVG Hospital (Amsterdam, the Netherlands) for the corrective osteotomy of the left proximal femur affected by SCFE (Ethical approval: OLVG Hospital institutional review board granted permission for the anonymized CT dataset (WO20.057)). A patient-specific CAD plate had been designed and utilized during surgery at OLVG. Here, we perform a retrospective study in which an alternative fixation plate is designed and compared with the actual implant in a laboratory setting. The workflow for creating a patient-specific bone plate using both conventional CAD techniques and TO is outlined in Figure 5.1. It starts from image acquisition and clinical diagnosis (Figure 5.1a-i). The 3D bone model is then generated from segmented CT images (Figure 5.1a-ii–iii). Consequently, virtual proximal femur osteotomies are performed (Figure 5.1b) and screw positions are defined (Figure 5.1c-i). Finally, a biomechanical engineer can design the patient-specific plate using computational tools, such as FEA software and TO (Figure 5.1c) or CAD software (Figure 5.1d).

5.2.1 Image segmentation and virtual reconstruction

Image acquisition was performed using a Revolution™ CT scanner (GE Healthcare, Milwaukee, WI, USA) at a tube voltage of 100 kVp, a current of 132 mA, and a slice thickness of 1.5 mm. Image segmentation and 3D model generation of the femur bone were done using Materialise Mimics® 21.0 (Materialise, Belgium) (Figure 5.1a-ii–iii). Foreground-background segmentation was applied with an optimal threshold of 226–3071 Hounsfield units (HU) to generate the 3D model of the femur. The CT images revealed a single pin with a high HU value in the proximal head of the femur, which had been placed to prevent further femoral head slippage. This pin was excluded from the 3D model as it was removed during the corrective surgery. The 3D bone model was then exported to 3-matic® 13.0 (Materialise, Belgium) for virtual reconstruction of the corrective osteotomy and plate design (Figure 5.1b-i).

The main objective of surgical treatment for SCFE is to realign the femoral head relative to the acetabulum and to secure stable fixation of proximal part of the femur, which requires at least 50% of the osteotomy to be in contact with each other to facilitate healing of the osteotomy. In virtual planning, the desired position of the femoral head can be determined based on the healthy opposite femur of the same patient, or, if both femurs are affected and cannot serve as a reference (as was the case in this study), the healthy femur of another patient can be used, in consultation with an orthopedic surgeon [6, 8]. A planar cut was first made between the lesser trochanter and the femoral neck (Figure 5.1b-ii). Next, the shaft and femoral head were rotated along the sagittal, axial, and coronal planes to obtain acceptable hip angles (Figures 3.1b-iii–v). The overlap between the femoral head and shaft was then cut (Figures 3.1b-vi–vii), and the wedge-shaped excess part was removed (Figure 5.1b-viii) to form the corrected femur model (Figure 5.1b-ix). The accuracy of the angles in the final model was confirmed by re-importing it into Materialise Mimics® and overlaying it on the CT images (Figure 5.1a-i).

5.2.2 Synthetic bone

We used a fused deposition modelling (FDM) 3D printer (Ultimaker S5, Ultimaker B.V., The Netherlands) and poly-lactic acid (PLA) filaments (Ultimaker PLA-white, 750 g Natural with a filament diameter of 2.85 mm) to additively manufacture a model of the SCFE-affected femur. We divided the 3D bone model into two sections, namely the compact and porous regions, and segmented the CT images to identify the areas whose gray values were indicative of cortical (> 226 HU) and cancellous bone (< 226 HU). These regions were then imported into the Ultimaker Cura software (V4.9.0) and were 3D printed using the printing parameters listed in Table S5.1 of the supplementary material.

5.2.3 Computational modelling

The finite element modelling and topology optimization in this study were performed using the commercial software suite Abaqus/CAE 2017 (Simulia, Dassault Systèmes, France). First, we created a simplified model to replicate the experimental conditions (Figure 5.2a and 5.3a–b). This model was then extended to include a musculoskeletal system and simulate more complex physiological loading conditions, such as two-leg stance and walking (Figure 5.3c). Next, we analyzed CAD plate designs featuring various screw positions, initially selected by the surgeon, under walking loading condition to establish the design domain for topology optimization (Figure 5.4a). The screw positions were altered in four configurations, including P3-D4 (three screws proximally in the head and four screws distally in the shaft) (Figure 5.4a-i), P3-D3 (Figure 5.4a-ii), P3-D2 (Figure 5.4a-iii), and P2-D4 (Figure 5.4a-iv). The design area was defined based on the screw configuration P3-D3 (Figure S3.1c) and was optimized to withstand the extreme loading conditions in this study, which was walking. A von Mises stress limit of 435 MPa (*i.e.*, a 50% safety margin from the yield strength of Ti-6Al-4V) was considered to be the maximum safe stress. The validity of the FE model was established by comparing its predictions with experimental data obtained using digital image correlation (DIC) for CAD plates (Figure 5.2c and the Supplementary Video 5.1).

Material assignment

We discretized the surfaces of the model with a maximum element edge length of 1.8 mm and generated the volume meshes with a maximum element edge length of 2.2 mm using 4-node tetrahedral (C3D4) elements (as illustrated in Figure 5.3a). Isotropic linear elastic material models were used for all the materials.

In the FE analysis of the experimental loading conditions, the material properties of PLA were assigned homogenously to the synthetic femur model. It has been reported that the elastic modulus (E) of 3D printed compact PLA can vary between 350 and 3500 MPa [31]. However, the mechanical properties of 3D printed PLA are very consistent as long as the filament batch, printing machine, and printing parameters are kept the same [32]. The variations in the mechanical properties of PLA are influenced by multiple factors, including manufacturing processes, material composition, and testing conditions. Additionally, its Poisson's ratio (ν) is recorded at 0.36, and its density (ρ) is $\sim 1240 \text{ kg/m}^3$ [31]. The material properties were then assigned based on the grey values obtained from CT images. The higher grey values ($> 226 \text{ HU}$) corresponded to an average value of $E = 350 \text{ MPa}$ and $\rho = 1240 \text{ kg/m}^3$, representing the cortical bone. The lower grey values ($< 226 \text{ HU}$) corresponded to $E = 140 \text{ MPa}$ and $\rho = 496 \text{ kg/m}^3$, representing the cancellous bone (Figure 5.3b).

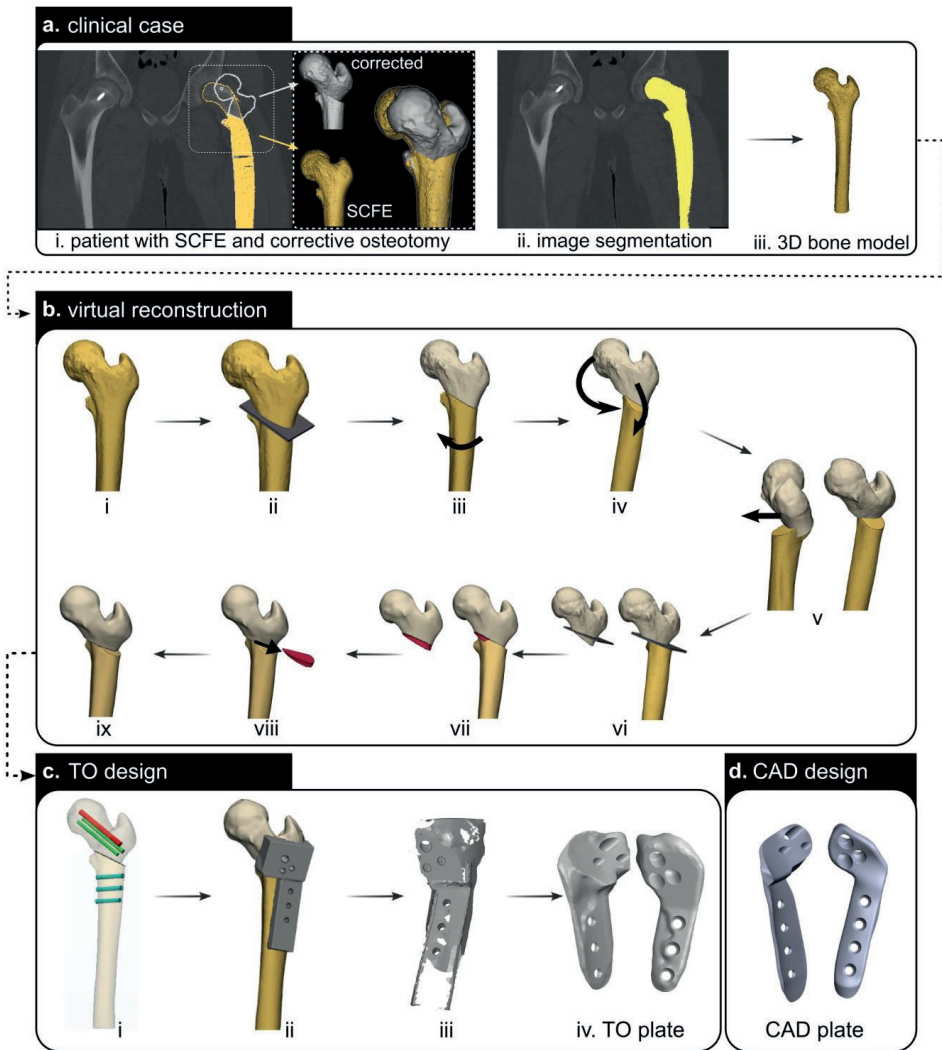


Figure 5.1. The workflow used for the design of a topology-optimized proximal femur fixation plate for the treatment of SCFE patients. The process starts with image acquisition and clinical diagnosis (a-i) followed by image segmentation (a-ii) and the generation of a 3D model of the affected bone (a-iii). The virtual reconstruction of the corrective osteotomy is carried out by cutting the bone along a plane placed between the femoral head and lesser trochanter (b-ii), rotating the bone shaft for physiological endo/exo rotation (b-iii), adjusting the rotation of the proximal part of the femur in the coronal and sagittal planes (b-iv), and translating it for proper placement in the acetabulum (b-v). The removal of the overlap between the proximal femur and shaft is achieved by creating a plane (b-vi), cutting the proximal femur (b-vii), removing the wedge (b-viii), and transferring the corrected bone model to the plate design stage (b-ix). The screw positions are defined (c-i) and the initial design area is placed on the bone after subtracting the bone surface (c-ii). The outcome of the topology optimization process (c-iii) is post-processed to produce the final product (c-iv). The design of the CAD plate used in this study is presented in subfigure (d).

To evaluate the performance of the plates under physiological loading conditions, we introduced the mechanical properties of the femur into the physiologically based FE model, using a grey-value-based approach. This method enabled us to model the effects of physiological loading conditions on the femur accurately, with a total of 15 material properties ranging between 14.2 and 19199.2 MPa for the Young's modulus (E) and 50 to 1573.1 kg/m³ for density (ρ) (Figure 5.3b). We assigned a homogeneous material value of $\rho = 50$ kg/m³ to all the negative HU-values up to 100 HU. To cover the HU values between 101 and 1840 HU, we used 14 materials ranging between $\rho_{min} = 107$ and $\rho_{max} = 1568$ Kg/m³. The material properties were calculated using the empirical expressions (*i.e.*, $E = 0.004\rho^{2.09}$) and $\nu = 0.3$ [33]. The proximal part of the femur required an additional material, as the CT scan included a pin in the proximal femur with a very high HU value. We assigned low mechanical properties (*i.e.*, $E = 14.2$ MPa and $\rho = 50$ kg/m³) to this area, since the pin was not included in our model. The following mechanical properties were assigned to the Ti-6Al-4V plates: $E = 110$ GPa, and $\nu = 0.3$ [34-36]. The yield strength (S_{Yield}) of the 3D-printed titanium alloy plates was considered to be 870 MPa [37].

Loads and boundary conditions

In the FE model, we imported the proximal femur fixture as an undeformable rigid object into the model to apply the load on the proximal femur head and distally fixated all the 6 degrees-of-freedom of the shaft ($U = UR = 0$) to represent the experimental setup (Figure 5.2a). The load was applied by displacing the fixture 6 mm inferiorly (*i.e.*, in the negative z -direction in Figure 5.2a), which was sufficient to capture the linear portion of the load-displacement curve obtained from the biomechanical experiments. Since the joint contact force on the femur is applied at a physiologically relevant angle, the bone-plate construct was rotated 3° around the x -axis (*i.e.*, flexion), 20° around the y -axis (*i.e.*, adduction), and -43.6° around the z -axis [38]. A friction coefficient of 0.3 [39] was assigned to the interfaces between the PLA parts (*i.e.*, shaft and the head) and the head and fixture, while a friction coefficient of 0.45 was assigned to model the contact between the synthetic bone and the plate[40, 41].

To assess the plates under physiological loading conditions, we considered joint reaction force and the major muscle groups, specifically the abductor forces on the greater trochanter, and the iliopsoas on the lesser trochanter [42-44]. During corrective surgery, the vastus lateralis, one of the most dominant quadriceps muscles, was detached and then reattached, leading to significant weakening and decreased load on the proximal femur. The decision to exclude it from the computational model was made in consultation with the surgeon. However, the muscles acting on the lesser and greater trochanters were stretched, not negatively affected, and were, thus, included in the model.

Design optimization

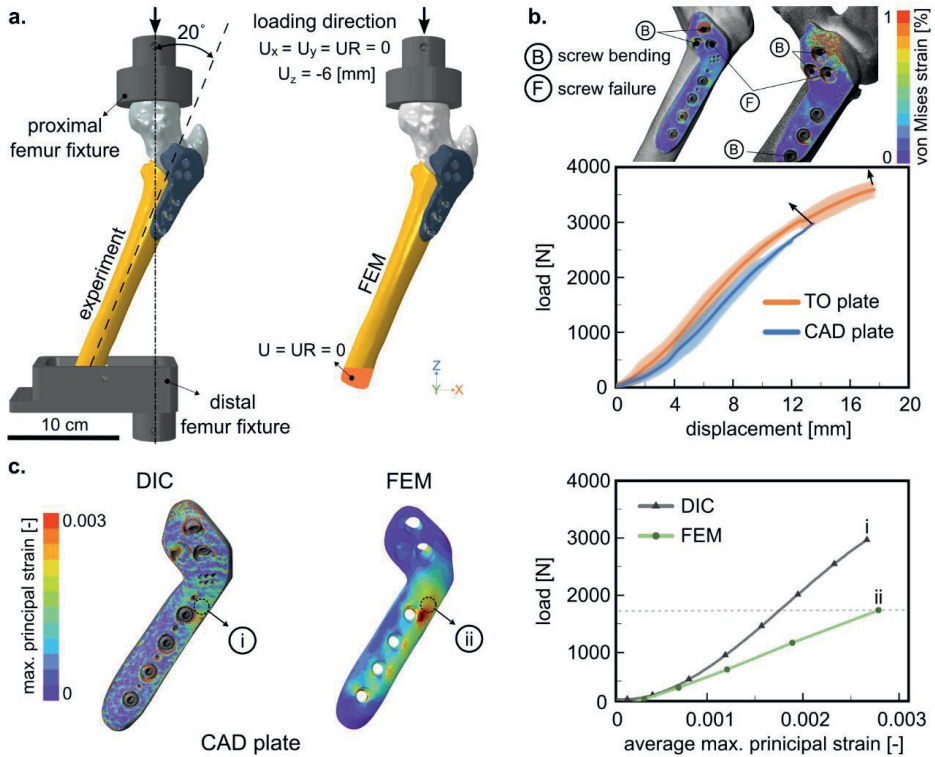


Figure 5.2. (a) The experimental setup (left) and displacement (U) and rotation (UR) constraints in the finite element model (right). (b) The force-displacement curves obtained from the quasi-static compression tests for the CAD and TO plates and the true effective (von Mises) strain fields of the plates prior to failure, measured by DIC. (c) A comparison between the true maximum principal strain values measured by DIC and the FEA-predicted values of the logarithmic (LE) maximum principal strain within the linear elastic region of the CAD plate (up to 1700 N).

To assess the plates under physiological loading conditions, we considered joint reaction force and the major muscle groups, specifically the abductor forces on the greater trochanter, and the iliopsoas on the lesser trochanter [42-44]. During corrective surgery, the vastus lateralis, one of the most dominant quadriceps muscles, was detached and then reattached, leading to significant weakening and decreased load on the proximal femur. The decision to exclude it from the computational model was made in consultation with the surgeon. However, the muscles acting on the lesser and greater trochanters were stretched, not negatively affected, and were, thus, included in the model.

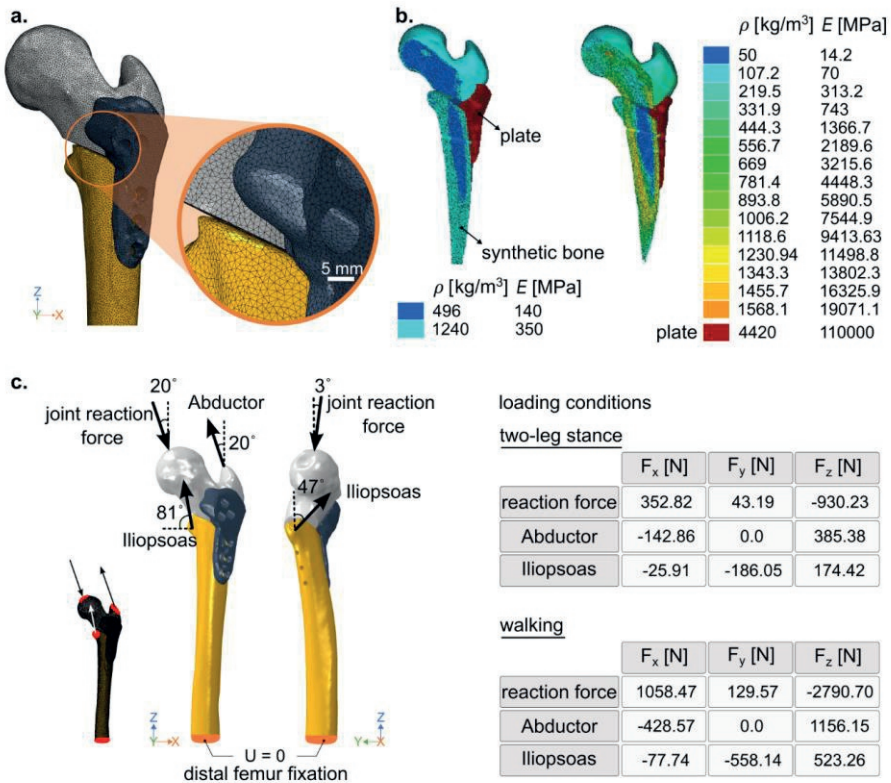


Figure 5.3. (a) Overview of surface mesh applied to bone and plate. (b) Cross-sectional views of material assignment to volume mesh of synthetic (PLA) bone (left) and patient's bone (right). The color scale represents the corresponding values of the density and Young's modulus calculated for bone and plate. (c) The constraints and muscle force directions for physiological loading conditions along with the muscle attachment regions (left) and the muscle forces in three directions during two-leg stance and walking (right).

To minimize the bending moments and achieve uniform stress distribution within the bone, the FEA model incorporated a joint contact force with an inclination angle of 20° with respect to the vertical direction (Figure 5.3c). This angle remains constant throughout the stance phase of the gait cycle, while supporting the maximum load during walking [45]. The physiological model necessitated adjustments to the interactions and constraints. Loading areas of 180 to 300 mm² were designated for joint reaction forces, abductor, and iliopsoas in accordance with literature and muscle attachment sites [14, 46, 47]. A friction coefficient of 0.45 was used at the contact interface between the femoral head and the shaft [48-50], while a penalty friction coefficient of 0.4 was utilized to model the interaction between the femur and Ti-6Al-4V plate [14, 40, 51, 52]. The distal surface of the femur was completely restricted from translation (Figure 5.3c) [25, 53, 54]. Non-locking screws were used in both experiments and were simulated in the computational

models. To simulate such screws, two reference points were defined: one at the middle of the hole in the plate and another at the bottom part of the hole within the bone. These reference points were kinematically coupled to the internal surfaces of each hole in the plate and in the bone cavity. This kinematic coupling condition restricted the movement between these reference points (*i.e.*, master) and their corresponding bone and plate surfaces (*i.e.*, slave) in all degrees of freedom. The two reference points were then linked together using a multi-point constraint (*i.e.*, beam) to represent the screw. Such a simulation approach reduces computational time by simplifying the interaction of the non-locking screw with its interfaces in the plate and bone (Figure S5.2 in the supplementary material). These constraints ensured that the components of the screw, bone, and plate components were appropriately connected and functioned as a unified system.

5.2.4 Plate design

We evaluated two different approaches for creating patient-specific femoral plates: computer-aided design (CAD plate) and topology optimization (TO plate). Our considerations for the TO plate were influenced by the previously designed CAD plate, which was successfully implanted in the patient. As a result, both approaches ensured that the plate size and shape were tailored to the patient's anatomy, making them effective for orthopedic plate design.

The CAD plate (Figure 5.1d) was developed at the OLVG hospital in collaboration with the orthopedic surgeon using SolidWorks® 2020 (Dassault Systèmes SolidWorks Corporation). The custom plate was modelled after the shape of pediatric hip plates and was adapted to the patient's anatomy. The distal part of the plate had a thickness ranging between 3.6 and 4.3 mm, with the proximal part having a thickness of up to 14.0 mm. The distal width was approximately 20.0 mm (19.5-20.2 mm). The CAD plate used in this study was slightly different from the version used in clinical practice. The plate was designed with small holes, strategically positioned along the lateral-distal part of the plate, to serve as internal markers for the purpose of monitoring print quality (Figure 5.2c). Three proximal and four distal cannulated dynamic compression screws (DePuy Synthes, West Chester, PA) were used to secure the plate to the bone. Six screws had a diameter of 4.5 mm, while the seventh (*i.e.*, the most proximal screw) had a diameter of 6.5 mm. The lengths of the screws varied between 32 and 38 mm distally and between 65 and 71 mm proximally. Further details regarding the CAD plate can be found in the supplementary Figures S5.1a–b.

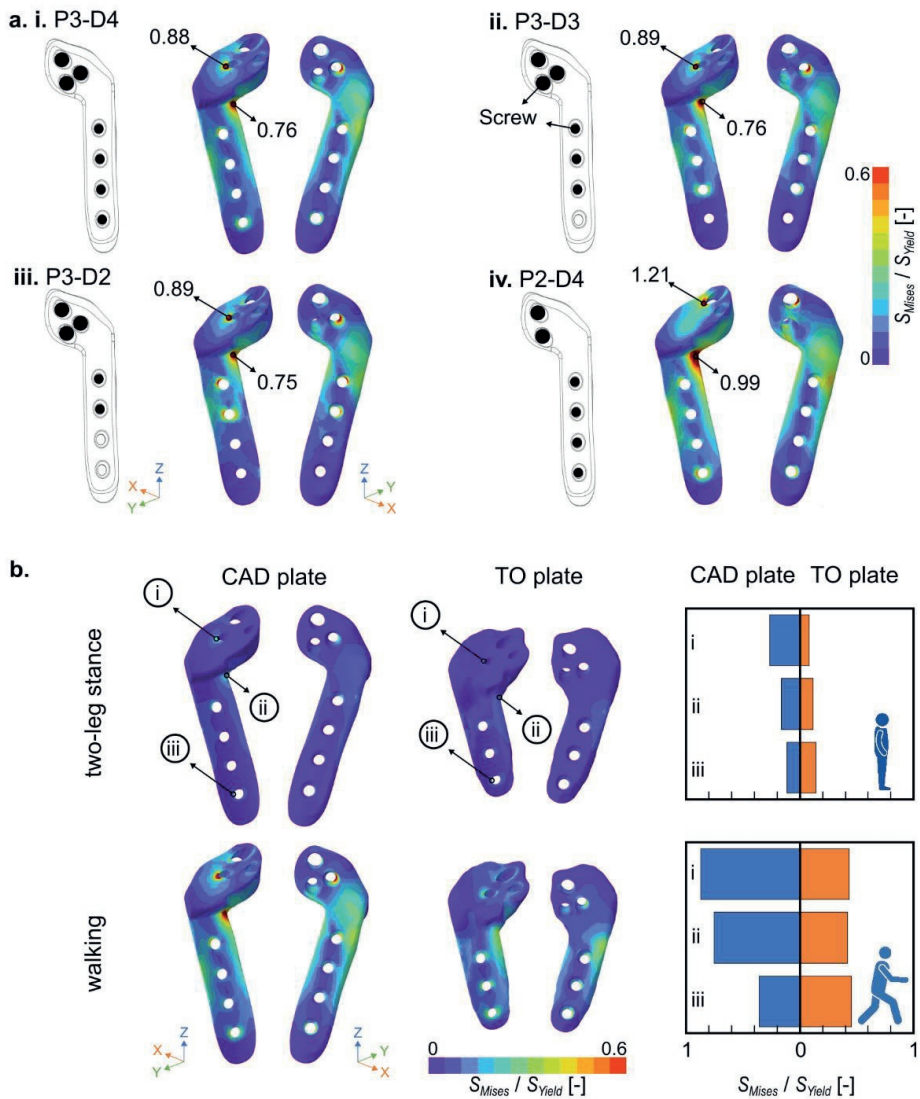


Figure 5.4. (a) A comparative analysis of the FEA-predicted von Mises stress (S_{Mises}) distributions normalized by the yield strength (S_{Yield}) of the 3D-printed titanium alloy across varying screw configurations. These configurations include (i) three proximal screws and four distal screws (P3-D4), (ii) three proximal screws and three distal screws (P3-D3), (iii) three proximal screws and two distal screws (P3-D2), and (iv) two proximal screws and four distal screws (P2-D4). (b) A comparative evaluation of the FEA-predicted von Mises stress distributions (S_{Mises}/S_{Yield}) for both CAD and TO plates under two distinct conditions: two-leg stance and walking.

The TO plate was generated by establishing an initial design domain that included six screws (three proximal and three distal), which was determined based on the results of comparing various screw configurations (*i.e.*, P3-D3 in Figure 5.4a). The design domain was defined with a maximum thickness of 8.0 mm distally and 18.0 mm proximally, and a portion of the medial side was subtracted from the bone surface to achieve a good fit with the femur (Figures 5.1c-i-ii and S1c of the supplementary material). The design area was 115.0 mm in length and 25.0 mm in width to cover the entire lateral side of the shaft (Figure S5.1c of the supplementary material). A total of 29 cycles of iterative general TO were performed using the TOSCA module within the Abaqus/CAE. We used the solid isotropic material with penalization (SIMP) method to describe how the density and stiffness of each element were related. The convergence criteria were set to 0.005 for element density changes and 0.001 for the objective function. The material distribution within the design domain was optimized for the extreme physiological loading condition (*i.e.*, walking) with the objective of minimizing the sum of strain energy while limiting the volume (the sum of the volumes of elements in the design area) to 30% of the design domain. The choice of a 30% volume constraint was made to find a balance between reducing material use and maintaining the integrity of the structure, while also avoiding potential convergence issues during the optimization process [55]. In addition to volume constraints, the model was subjected to geometrical constraints. To ensure that there was sufficient material available for screw fixation, the area surrounding the screw holes was frozen and was, thus, excluded from TO. Since the overall shape of the plate was already determined, no extra geometric limitations were imposed during the optimization stage.

The resulting TO plate (Figure 5.1c-iii) was then converted into a raw STL file using 3-matic® 13.0 (Materialise, Belgium) for post-processing. The raw STL file of the plate was imported and refined by removing any excess material and closing any openings that could potentially cause tissue integration, ensuring a solid plate structure. The edges were then rounded, and the final design was smoothed to minimize the risk of tissue irritation, friction between the plate and surrounding tissues, and bone ingrowth [24, 56]. The surface modifications were finalized after consultation with the orthopedic surgeon (Figure 5.1c-iv).

5.2.5 Experimental methods

CAD and TO plates were additively manufactured from Ti-6Al-4V ELI powder (grade 23), and were fixed to the synthetic bone using standard Ti-6Al-4V cannulated dynamic compression screws (MatrixMANDIBLE, DePuy Synthes, USA). The plates were manufactured using the direct metal printing (DMP) technique using a layer thickness of 60 μm (3D systems, Leuven) and were post-processed through hot isostatic pressing (HIP) (105 MPa, 1050 °C, dwell time = 120 min). The chemical composition

and mechanical properties of the used titanium alloy powder are listed in Tables S5.2 and S5.3 of the supplementary material, respectively.

The surgical cutting and drilling guide (Figure S5.1d of the supplementary material) was manufactured using the Formlabs surgical guide resin, which is a biocompatible photopolymer material specifically designed for use in surgical guide applications, and stereolithography (SLA) technique on a Form 3B printer (Formlabs, USA). The bone-plate construct was prepared in accordance with the virtual surgical plan by positioning the guide on the FDM 3D printed femur affected by SCFE. The screw holes were first predrilled with a 1.6-mm drill bit, and the wedge-shaped excess portion was removed using a hand saw. The plate was then screwed onto the proximal and distal femur sections with the aid of Kirschner wires inserted into the predrilled holes (Figure S5.1d of the supplementary material). During the screwing process, the applied torques were measured (Stahlwille Torque Screwdriver 760, Germany), and the maximum torque was set at 1.5 N.m[57-59].

The experimental test setup was devised to perform both quasi-static compression and cyclic testing (Figure 5.2a). The setup comprised a fixture consisting of a cup-shaped top and a box-shaped bottom to simulate the interaction between the head of the femur and the joint. The bone, which was fixed in place using epoxy resin (Poly-Pox epoxy THV 500 and hardener Poly-Pox 355, Poly-Service), was positioned at the bottom part of the fixture and angled at 20° in the coronal plane to replicate physiological posture. The cup's diameter was set to 47.0 mm to fit the sphere-shaped femoral head and its depth was set at 15.0 mm to minimize the risk of impingement. The fixture was designed using SolidWorks (Dassault Systèmes SolidWorks Corp., V2020) and was fabricated through milling. To imitate physiological posture during the curing process, a holder was utilized to maintain the constructs at a 20° angle in the coronal plane (Figure S5.1e of the supplementary material).

Quasi-static compression testing protocol

We conducted quasi-static compression tests on two CAD and three TO constructs using a mechanical testing bench (LLOYD instrument LR5K with a 5000 N load cell) at a rate of 0.3 mm/min with a preload of 1.0 N until failure occurred. The failure of the construct was determined as plate, screw, or bone failure or as screw loosening. The stiffness of the construct was calculated using the slope of the best-fit line in the linear portion of the load-displacement curve, while the strain energy stored in the construct was calculated as the area under the curve until the failure.

Compression-compression cyclic testing protocol

Three CAD and three TO constructs were subjected to cyclic loading under a constant range of compressive stresses between 150 N and 1500 N (equivalent to 1.5

times BW) using an INSTRON ElectroPuls™ E10000 machine with a 10 KN load cell (Figure 5.5a–b). To assess the long-term mechanical function of the plates, we evaluated them under a post-surgical worst-case loading condition within the first 150,000 cycles, which roughly corresponds to 15 minutes of walking with crutches per day for 5 months. To simulate this scenario, sinusoidal loads with 1 Hz oscillation were applied to the synthetic bone specimens for 150,000 cycles, based on physiological walking loading speeds and recovery times [60]. If no plate or construct failure was observed after 150,000 cycles, the test was extended to 1,000,000 cycles at 3 Hz to detect any potential plate or screw failures (Figure 5.5b).

DIC measurements

The local deformation and strain patterns during the experimental testing were measured using a Q-400 2x12 MPixel digital image correlation (DIC) system (LIMESS GmbH, Krefeld, Germany). The strain maps were obtained for both the CAD and TO plates at a frequency of 0.25 Hz and a facet size of 21–27 pixels. To study the full-field strain distribution of the bone plate, the plate itself was selected as the region of interest. A black dot speckle pattern was applied over a white paint background, covering the entire area of interest. Two digital cameras and LED panels were positioned at a distance of 0.8 m from the specimens to capture images and provide illumination, respectively. Image processing and strain calculations were performed using Istra4D x64 4.6.5 software (Dantec Dynamics A/S, Skovunde, Denmark). The logarithmic strain (LE) maps from FEA were then compared to the true principal strain maps measured with DIC within the linear region (Figure 5.2b).

5.3 Results

5.3.1 FEA results

The computational model was validated by comparing the logarithmic (LE) maximum principal strain in the linear elastic range (up to 1700 N) as predicted by the FEA model with the maximum principal true strain measured using DIC (Figure 5.2c). The comparison showed good agreement between the two, indicating that the FEA model is a valid representation of the experimentally obtained maximum principal strain fields. Both the DIC and FEA results revealed increased strain in the vicinity of the top screw in the shaft and towards the fracture gap at the lateral side of the CAD plate (Figure 5.2c). The DIC results also showed high strain fields at the top of the plate, which were not captured in the FEA.

Although the CAD plate was marked with small holes for monitoring print quality, these holes were not included in the FE model. However, the results of both experimental

testing and FE analysis were found to be comparable, suggesting that these small holes did not significantly affect the performance of the plate.

The FEA model was expanded to assess the performance of orthopedic plates with various designs and screw configurations under physiological loading conditions. The von Mises stress distribution resulted from the FEA were compared in two-leg stance and walking conditions (Figure 5.4b). Under both physiological loading conditions, the CAD plate showed the highest degrees of stresses concentration in the vicinity of the most lateral proximal screw, with maximum stress values of 233.0 MPa and 762.0 MPa ($S_{Mises}/S_{Yield} > 0.5$) in two-leg stance and walking, respectively (region i in Figure 5.4b). In contrast, the TO plate exhibited a more homogeneous stress distribution within the safety margin ($S_{Mises}/S_{Yield} < 0.5$) (Figure 5.4b-right). The CAD plate experienced higher stress concentration on the medial side near the fracture gap (region ii in Figure 5.2b), exceeding the safety margin for walking conditions. This result suggests that if walking loads are applied, the stress on the medial side of the CAD plate could potentially lead to plate fractures.

The stress distributions in the analyzed screw configurations were comparable with a variation of less than 5% in the maximum stress between configurations P3-D4, P3-D3, and P3-D2 (Figure 5.4a). However, a higher concentration of stress was noticed in the screw configuration P3-D2 at its most distal screw, resulting in a larger high stress area. The presence of fewer screws in the proximal part of the plate (*i.e.*, P2-D4) resulted in a significantly higher maximum von Mises stress, with a difference of 36% (~1055.0 MPa). All the configurations resulted in stress concentrations above the safety margin of 435 MPa in the plate. The configuration P3-D3 was ultimately selected for the topology optimization process.

The length of the TO plate was reduced by 18.1% in comparison to the CAD plate. The maximum thickness around the fracture gap, however, was increased by ~30%, and the lateral side of the distal plate was doubled (Figure S5.1 of the supplementary material). The final plate had a maximum length of 86.0 mm, a variable width of around 20.0 mm and a variable thickness ranging from 4.0–8.0mm distally (Figure S5.1c of the supplementary material). The TO plate weighed 62.6 grams, which was 23.1% heavier (50.86 grams) than the CAD plate. During two-leg stance loading, the maximum von Mises stress was recorded at 121.1 MPa near the bottom screw in the shaft. Walking loading resulted in a maximum von Mises stress of 390.7 MPa at the same location as observed in two-leg stance loading (Figure 5.4b). High stress areas were observed in the bone near the interface between both bone parts, with maximum stress values of 96.1 and 147.0 MPa for two-leg stance and walking, respectively. The von Mises stresses inside the plate remained below the yield strength of Ti-6Al-4V (*i.e.*, 870 MPa).

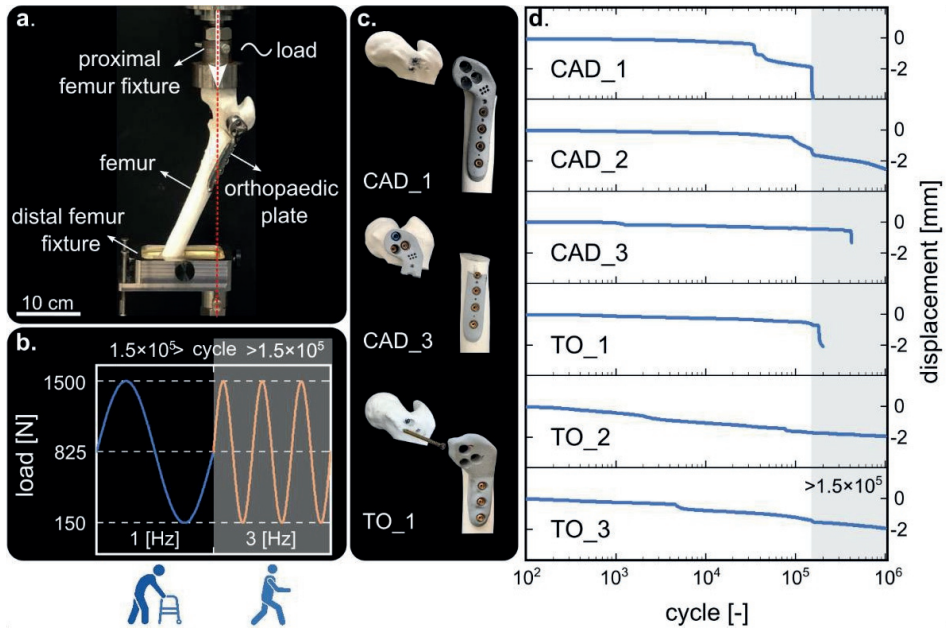


Figure 5.5. The setup used for cyclic loading tests and the corresponding experimental results. (a) The setup used for the cyclic loading tests, (b) the cyclic compressive load changed between a minimum of 150 N and a maximum of 1500 N with an initial frequency of 1 Hz until 150,000 cycles. The specimens surviving the first round of the cyclic test were subjected to cyclic loading with the same maximum and minimum loads applied with a frequency of 3 Hz until a total of 1,000,000 cycles (including the first round of tests), and (c) the different modes of failure observed in this study. (d) The displacement vs. number of cycles for both CAD and TO plates during the cyclic tests.

5.3.2 Experimental test results

As a part of this study, unpublished data was used to evaluate the impact of screw torque measurements on the results. Two scenarios were examined: fully tightened screwing and screwing with a maximum torque of 1.5 N.m. The findings indicated that including screw torque measurements significantly enhances the consistency of the results. Without torque measurement, the outcomes were found to be highly variable. Consequently, all the results presented in this study were obtained from the construct tightened to a maximum torque of 1.5 N.m. The force-displacement data was obtained from quasi-static compression tests until failure (Figure 5.2b). All the CAD constructs failed at loads lower than the maximum walking load of 3000 N (2814.4 ± 228.6 N), whereas all the three TO constructs failed at loads higher than the walking loading condition (> 3000 N) at 3603.3 ± 108.2 N.

The mean stiffness of the CAD and TO constructs was determined to have a difference of 11.7%. However, a discrepancy was observed between the experimental results and those obtained using FEA, with the CAD and TO constructs exhibiting a

14.76% and 4.9% difference, respectively. The results of the quasi-static test indicated that the ultimate load values for the TO constructs were significantly higher (*i.e.*, 24.6%) as compared to those for the CAD constructs. The ultimate displacement and stored strain energy in the TO plates were observed to be greater than those in the CAD plates with increase of 34.6% and 78.1%, respectively. This data substantiates the enhanced capability of the TO plates to sustain higher levels of deformation and absorb more energy.

The true effective (von Mises) strain fields of the plates were obtained from the DIC measurements before the plates failed (Figure 5.2b). In the CAD plate, the highest strain values were located near the fracture gap and the first distal screw due to bending moments. Conversely, the highest strain values in the TO plate were found in the proximal part of the plate, near the lateral screw hole. The CAD and TO constructs failed as a result of excessive bending, which led to the breakage of the lateral proximal screw. Bending was also visible at the remaining proximal screws in both the CAD and TO constructs and at the most distal screw in the shaft in two TO constructs (Figure 5.2b). Neither the CAD nor the topologically-optimized Ti-6Al-4V plates experienced plate failure.

In this study, the failures observed during the cyclic tests were categorized as screw failure, bending, or loosening, or as plate failure. Out of the three CAD constructs, two failed within 150,000 cycles, due to screw failure (*i.e.*, CAD_1 in Figure 5.5c–d) and screw bending (*i.e.*, CAD_2). All of the topologically optimized constructs, on the other hand, were able to withstand cyclic loading within the same timeframe. When the tests were continued until 1,000,000 cycles, CAD_3 failed at the most proximal screw hole in the shaft after 400,000 cycles, while TO_1 failed at the two most proximal screws after 180,000 cycles (Figure 5.5c). The other two TO constructs remained functional with slight displacement changes (< 2 mm) until the end of the 1,000,000 cycles. During the removal of the plates, no screws were found to be loose.

5.4 Discussion

We evaluated the biomechanical performance of patient-specific fixation plates designed using two different design strategies (*i.e.*, CAD and TO) used for temporary fixation of bones following osteotomy. An FE model was created, validated against experimental results including full-field strain measurements, and used to examine the behavior of these plates under clinically relevant loading scenarios.

While PLA does not entirely mimic the mechanical properties of cortical bone tissue, it does possess characteristics resembling those of cancellous bone [61]. Moreover, when comparing different design alternatives, the ranking of different designs in terms of their mechanical performance is not expected to be as much influenced by the absolute values of the mechanical properties of the bone phantom as it is by any inconsistencies (variabilities) in the geometry or mechanical properties of the bone phantom. Utilizing

PLA offers a homogeneous, bone-like 3D-printed structure with consistent mechanical properties and patient-specific geometry, which allows for a methodical assessment of the effectiveness of patient-specific metallic bone plates. This standardized setup facilitates the comparison of different plate designs under consistent conditions. The test results demonstrated that there was no occurrence of screw loosening or bone failure. Given that the synthetic bone used here has a lower strength than actual cortical bone, the results of the current study suggest that the bone-plate constructs are not expected to experience failure if real bone is used [62]. Although the findings are not directly translatable to clinical settings, previous research has established that the use of composite bone is a viable method for evaluating bone-plate constructs [46, 63].

The TO plate was designed with a smaller design area and a specific screw configuration that consisted of three distal and three proximal screws. The shape of the TO plate was similar to the CAD plate, but it was 20 mm shorter and thicker, with a maximum thickness of 8.0 mm distally and 18.0 mm proximally, compared to 4.0 mm and 14.0 mm in the CAD plate, respectively. The use of three distal screws, instead of the four used in the CAD plate, will likely reduce surgical incision size, surgery time while improving the patient recovery post-surgery [53, 54, 64]. The reduction in plate length also allows for better adaptation to the specific anatomy of the patient, enhancing the fit and reducing potential issues related to plate positioning. The increased thickness around the fracture gap helps to provide better stability and increase load-bearing capacity and support, particularly in areas where bending forces may be more prominent. This reinforcement helps to distribute the load more effectively and prevent stress concentrations, reducing the risk of plate failure. Although previous studies have shown that reducing the plate length and increasing its thickness can result in increased plate stiffness [30, 64, 65], these effects were minimal in the bone-plate constructs studied here. The stiffness of the construct differed by only 11.7% between the CAD and TO plates, with the TO construct displaying higher values of ultimate load, ultimate displacement, and stored strain energy as compared to the CAD construct.

The TO plate was 23.1% heavier than the CAD plate. The increased weight of the TO plate, although it may not be desirable in terms of implant weight, can contribute to improved stability and load distribution. A heavier plate can provide additional rigidity and resistance against deformations under load. After consultation with the surgeon, the extra weight was deemed acceptable.

We conducted a computational evaluation of the plates under simulated physiological loading conditions. Our results indicated that during walking and in the case of the CAD plate, the stress values within the areas of stress concentration exceeded the yield limit of 435 MPa ($S_{Mises}/S_{Yield} > 0.5$), while the TO plate remained below this limit in both two-leg stance and walking scenarios. This suggests that the CAD plate is at increased risk of failure, potentially leading to plastic deformation or crack initiation [66],

when subjected to a load of ≈ 3000 N. The computational findings are supported by the experimental results, including the cyclic and quasi-static loading tests, in which all the CAD constructs failed before reaching 3000 N.

The loading conditions applied to the hip joint were simplified in an effort to emulate the physiological loading conditions. Previous research has taken various approaches in representing the forces acting on the hip joint, including the inclusion of all muscles, only the primary muscles and joint forces, or just the hip contact force [14]. The distribution of stress and strain around the bone and plate can vary depending on the loading conditions used [14, 42]. Some studies have reported that including all the muscles in the hip joint leads to a more uniform distribution of strain along the femur [67], while others have found that only including the main muscles, such as the abductor and iliotibial tract, can cause increased strains at the distal part of the bone [68]. It is important to consider the contribution of muscle forces in FEA models, as neglecting them can lead to an overestimation of shear and bending forces [67, 68]. Including certain muscles, such as the obturator internus, iliopsoas, and superior and inferior gemellus, can help in decreasing the modeling errors [68]. However, in order to balance the complexity of the model with the accuracy of the results, it is necessary to make compromises and decisions about the inclusion of muscles in the FEA models. Further research is needed to better understand what impact these simplifications have on the simulation results.

The osteotomy procedure for patients with SCFE is intended to re-establish healthy loading conditions in the hip joint. It is, however, likely that these conditions remain weaker than normal after surgery due to reduced weight-bearing activities during the recovery period. In this study, forces generated by healthy muscles were used to analyze the forces acting on the femur, which may have resulted in an overestimation of these forces. This overestimation could have also been due to the simplified muscle model and the angle at which the muscle forces are applied [69]. Although the loading conditions used in this study may not precisely reflect the actual conditions encountered by the patient, the results of the plate strength analysis are likely still conservative, implying that the actual forces are probably lower than what was estimated. This offers a margin of safety, as the analysis results provide an indication of the minimum required strength for the plate to perform effectively.

The bone model was simplified by assuming isotropic linear elastic material properties, which is a commonly used assumption in biomechanical modelling of bones [66, 70], while the screws were modelled as fully constrained beam elements. Both the screws and the plate contribute to the deformation during the experiments. In the FEA model, however, the screws are considered rigid, causing the deformation from the screws to be transferred to the plate. This could result in higher strain values on the plate in the FEA as compared to the DIC measurements. In addition to the simplifications made in the FE model, this discrepancy may have been caused by the out-of-view motion of the

plate towards the DIC camera. However, the stiffness values obtained from the force-displacement curves were found to be similar between the experiments and the FEA, which may be because this method compares the deformation of the entire construct rather than just the plate.

During the quasi-static compression tests, the load was applied only to the head of the femur, which may lead to an overestimation of load transfer, particularly with respect to bending in bone-plate constructs [67, 68]. Some studies have attempted to incorporate tension at the greater trochanter in their loading device [60, 71]. However, this is a challenging task, and there are concerns that the synthetic bone 3D printed from PLA may fail at this location [71]. Despite these challenges, research has shown that acceptable results can still be obtained without incorporating more complex physiological loading conditions [25, 71].

The results of this study showed that the screws, particularly those located proximally, were the weakest part of all the tested constructs. The proximal cannulated screws of 4.5 mm diameter failed due to bending moments, a common mode of failure in bone plate constructs [30]. Bending was also observed in the other proximal screws in both plate constructs and in the most distal screw of the TO plate construct, which may be due to higher loads being applied to the TO plate construct prior to failure as compared to the CAD construct. To improve the performance of the constructs, it is suggested to consider increasing the diameter of the proximal screws and/or replacing cannulated screw with solid screws or other enhancements. In addition, this study highlighted the high variability in test results when screw torque was not measured. In our preliminary experimental tests, we observed that the torques applied to the screws can significantly influence the overall performance of the plates. Measuring screw torque resulted in more consistent outcomes. Moreover, excessive tightening torques have been identified in the literature as a major contributor to screw failure in bone plate constructs [59]. It is, therefore, recommended to take screw insertion torques into consideration during surgical procedures. Incorporating this variable in computational models could facilitate a parametric investigation of how varying torque levels applied to the screws affects the biomechanical performance of the plates. Such computational simulations can provide considerable added value particularly in surgical settings.

We also compared the performance of the CAD and TO plates under cyclic loading conditions. The results showed that the CAD plates are more likely to fail within 150,000 cycles of loading, due to screw bending and screw material failure. As cyclic loading continued (up to 1,000,000 cycles), the remaining CAD plate and one of the TO plates failed, while both other TO constructs performed well. The overall outcome indicated that the TO plates were more durable and more capable of withstanding cyclic loads as compared to the CAD plates. However, it is important to note that these findings are only applicable to the specific loading conditions tested and may not be generalizable to other

loading conditions. Moreover, the optimal design for a patient-specific plate may vary depending on various factors, such as bone anatomy, density, and osteotomy angle. Hence, further clinical testing is necessary to validate the strength of these plates in a clinical setting. The evaluation steps and finite element analysis used in this study can be applied in the design of patient-specific plates for SCFE patients. However, any design modifications should only be made after consulting with a qualified surgeon.

5.5 Conclusions

We present evidence that patient-specific bone plates designed using TO result in improved biomechanical performance, as demonstrated by higher ultimate loads and similar stiffness when compared to those designed using conventional CAD techniques. These results highlight the utility of TO as a valuable approach for designing custom bone plates for proximal femur fixation in patients with SCFE. The topology-optimized plates showed a more uniform stress distribution in the regions close to the screws, resulting in more durable constructs. While there were discrepancies between the results of the FEA models and experimental testing, the study showed that FEM data is a reliable tool for evaluating and optimizing bone plates for SCFE patients.

5.6 Supplementary material

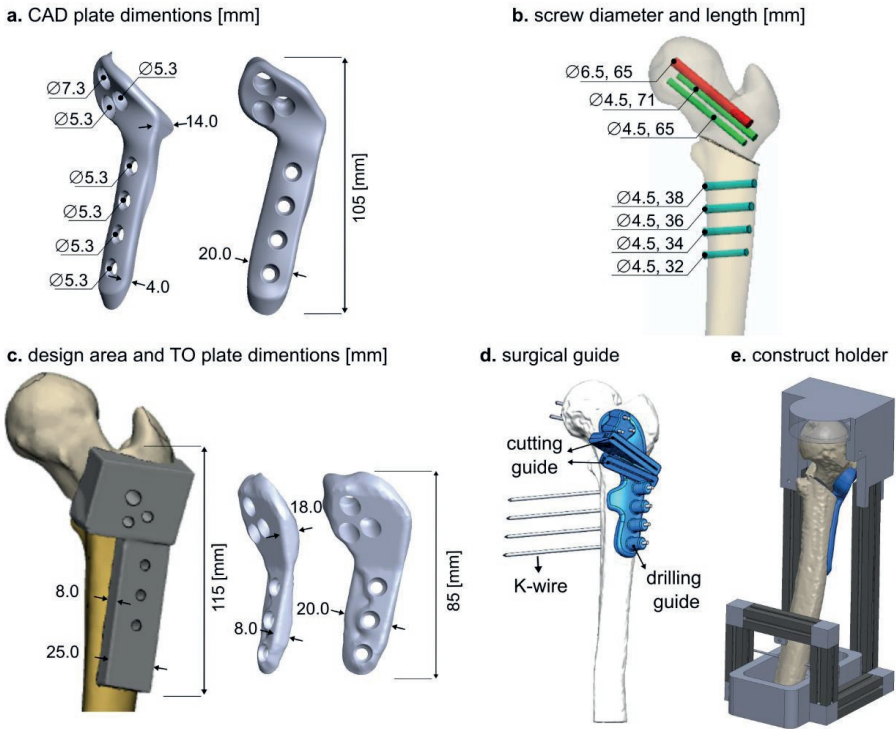


Figure S5.1. (a) dimensions of the CAD plate, (b) screw positions and screw hole dimensions in the bone, (c) initial design area for topology optimization process and dimensions of the TO plate, (d) surgical guide used in the study, and (e) construct holder for resin curing and fixing the distal part of the bone in the fixture.

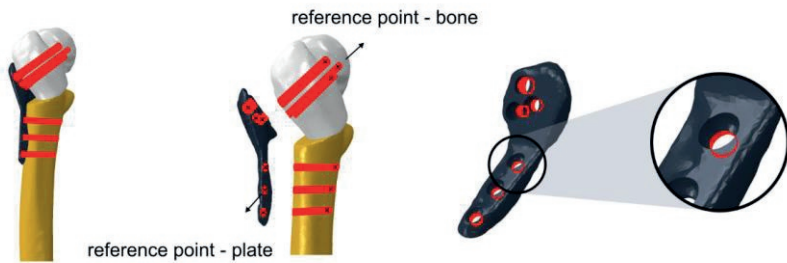


Figure S5.2. Simulation setup for non-locking screws. Two reference points represent the sections of the plate and bone that are in contact with the threaded part of the screws.

Table S5.1. Printing parameters for additively manufacturing femur bone models using PLA and an Ultimaker S5 FDM printer.

Parameters	Settings	Parameters	Settings
Layer height	0.15 mm	Nozzle size	0.4 mm
Line width	0.42 mm	Printing temperature	200 °C
Infill pattern/density cortical	Line / 100 %	Build plate temperature	60 °C
Infill pattern/density cancellous	Cubic / 40 %	Print speed	70 mm/s

Table S5.2. Chemical composition of Ti-6Al-4V ELI grade 23 powder (mass fraction in %) (3D Systems, Leuven, Belgium)

Element	Al	V	FE	O	C	N	H	Y	Others	Ti
Ti-6Al-4V	6.48	4.06	0.2	0.11	0.02	0.01	<0.001	<0.001	0.01	89.11

Table S5.3. Mechanical properties of Ti-6Al-4V ELI grade 23 (3D Systems, Leuven, Belgium)

Mechanical properties	Ultimate tensile strength [MPa]	Yield strength [MPa]	Plastic elongation [%]	Reduction of area [%]	Density [kg/m ³]
Ti-6Al-4V	975	870	17	45 ± 5	4420

Supplementary movies

Supplementary Video 5.1. True maximum principal strain field captured by FEA and DIC within the linear elastic region of the CAD plate (up to 1700 N)(see <https://doi.org/10.1016/j.jmbbm.2023.106173>)

Bibliography

1. E.M. Manoff, M.B. Banffy, J.J. Winell, Relationship Between Body Mass Index and Slipped Capital Femoral Epiphysis, *Journal of Pediatric Orthopaedics* 25(6) (2005).
2. E.N. Novais, M.B. Millis, Slipped capital femoral epiphysis: prevalence, pathogenesis, and natural history, *Clinical Orthopaedics and Related Research* 470(12) (2012) 3432-3438.
3. D.C. Perry, D. Metcalfe, S. Lane, S. Turner, Childhood obesity and slipped capital femoral epiphysis, *Pediatrics* 142(5) (2018).
4. B. Herngren, M. Stenmarker, L. Vavruch, G. Hagglund, Slipped capital femoral epiphysis: a population-based study, *BMC musculoskeletal disorders* 18(1) (2017) 1-12.
5. J.D. Wylie, E.N. Novais, Evolving Understanding of and Treatment Approaches to Slipped Capital Femoral Epiphysis, *Current Reviews in Musculoskeletal Medicine* 12(2) (2019) 213-219.
6. D.D. Aronsson, R.T. Loder, G.J. Breur, S.L. Weinstein, Slipped capital femoral epiphysis: current concepts, *JAAOS-Journal of the American Academy of Orthopaedic Surgeons* 14(12) (2006) 666-679.
7. M.M.E.H. Witbreuk, M. Bolkenbaas, M.G. Mullender, I.N. Sierevelt, P.P. Besselaar, The results of downgrading moderate and severe slipped capital femoral epiphysis by an early Imhauser femur osteotomy, *Journal of Children's Orthopaedics* 3(5) (2009) 405-410.
8. R.T. Loder, D.D. Aronsson, M.B. Dobbs, S.L. Weinstein, Slipped capital femoral epiphysis, *JBJS* 82(8) (2000) 1170.
9. L. Ma, Y. Zhou, Y. Zhu, Z. Lin, L. Chen, Y. Zhang, H. Xia, C. Mao, 3D printed personalized titanium plates improve clinical outcome in microwave ablation of bone tumors around the knee, *Scientific reports* 7(1) (2017) 1-10.
10. J.B. Erickson, W.P. Samora, K.E. Klingele, Treatment of chronic, stable slipped capital femoral epiphysis via surgical hip dislocation with combined osteochondroplasty and Imhauser osteotomy, *Journal of Children's Orthopaedics* 11(4) (2017) 284-288.
11. C.E. Henderson, L.L. Kuhl, D.C. Fitzpatrick, J. Marsh, Locking plates for distal femur fractures: is there a problem with fracture healing?, *Journal of orthopaedic trauma* 25 (2011) S8-S14.
12. T. Shibahara, H. Noma, Y. Furuya, R. Takaki, Fracture of mandibular reconstruction plates used after tumor resection, *Journal of oral and maxillofacial surgery* 60(2) (2002) 182-185.
13. R. Gutwald, R. Jaeger, F.M. Lambers, Customized mandibular reconstruction plates improve mechanical performance in a mandibular reconstruction model, *Computer methods in Biomechanics and Biomedical Engineering* 20(4) (2017) 426-435.
14. X. Fan, Z. Chen, Z. Jin, Q. Zhang, X. Zhang, Y. Peng, Parametric study of patient-specific femoral locking plates based on a combined musculoskeletal multibody dynamics and finite element modeling, *Proceedings of the Institution of Mechanical Engineers, Part H: Journal of Engineering in Medicine* 232(2) (2018) 114-126.
15. X. Chen, K. He, Z. Chen, A novel computer-aided approach for parametric investigation of custom design of fracture fixation plates, *Computational and Mathematical Methods in Medicine* 2017 (2017).
16. J.G. Dobbe, J.C. Vroemen, S.D. Strackee, G.J. Streekstra, Patient-tailored plate for bone fixation and accurate 3D positioning in corrective osteotomy, *Medical & biological engineering & computing* 51(1) (2013) 19-27.
17. S.G. Brouwer de Koning, N. de Winter, V. Moosabeiki, M.J. Mirzaali, A. Berenschot, M.M.E.H. Witbreuk, V. Lagerburg, Design considerations for patient-specific bone fixation plates: a literature review, *Medical & Biological Engineering & Computing* (2023).
18. A.A. Zadpoor, Design for additive bio-manufacturing: From patient-specific medical devices to rationally designed meta-biomaterials, *International Journal of Molecular Sciences* 18(8) (2017) 1607.
19. A. Van Kootwijk, V. Moosabeiki, M.C. Saldivar, H. Pahlavani, M. Leeflang, S.K. Niar, P. Pellikaan, B. Jonker, S. Ahmadi, E. Wolvius, Semi-automated digital workflow to design and evaluate patient-specific mandibular reconstruction implants, *journal of the mechanical behavior of biomedical materials* 132 (2022) 105291.

Design optimization

20. Y.-Y. Chen, K.-H. Lin, H.-K. Huang, H. Chang, S.-C. Lee, T.-W. Huang, The beneficial application of preoperative 3D printing for surgical stabilization of rib fractures, *PLoS One* 13(10) (2018) e0204652.
21. N. Wu, S. Li, B. Zhang, C. Wang, B. Chen, Q. Han, J. Wang, The advances of topology optimization techniques in orthopedic implants: A review, *Medical & Biological Engineering & Computing* 59(9) (2021) 1673-1689.
22. M.J. Mirzaali, V. Moosabeiki, S.M. Rajaai, J. Zhou, A.A. Zadpoor, Additive Manufacturing of Biomaterials—Design Principles and Their Implementation, *Materials*, 2022.
23. A. van Kootwijk, B.P. Jonker, E.B. Wolvius, M.C. Saldivar, M.A. Leeftang, J. Zhou, N. Tümer, M.J. Mirzaali, A.A. Zadpoor, Biomechanical evaluation of additively manufactured patient-specific mandibular cage implants designed with a semi-automated workflow: A cadaveric and retrospective case study, *Journal of the Mechanical Behavior of Biomedical Materials* 146 (2023) 106097.
24. D. Wang, Y. Wang, S. Wu, H. Lin, Y. Yang, S. Fan, C. Gu, J. Wang, C. Song, Customized a Ti6Al4V bone plate for complex pelvic fracture by selective laser melting, *Materials* 10(1) (2017) 35.
25. J.C. Arnone, A. Sherif El-Gizawy, B.D. Crist, G.J. Della Rocca, C.V. Ward, Computer-aided engineering approach for parametric investigation of locked plating systems design, *Journal of Medical Devices* 7(2) (2013).
26. M.J. Mirzaali, N. Shahriari, J. Zhou, A.A. Zadpoor, Chapter Sixteen - Quality of AM implants in biomedical application, in: J. Kadkhodapour, S. Schmauder, F. Sajadi (Eds.), *Quality Analysis of Additively Manufactured Metals*, Elsevier2023, pp. 689-743.
27. M.J. Mirzaali, A. Azamiya, S. Sovizi, J. Zhou, A.A. Zadpoor, 16 - Lattice structures made by laser powder bed fusion, in: I. Yadroitsev, I. Yadroitsava, A. du Plessis, E. MacDonald (Eds.), *Fundamentals of Laser Powder Bed Fusion of Metals*, Elsevier2021, pp. 423-465.
28. M. Mirzaali, F. Bobbert, Y. Li, A. Zadpoor, of Metals Using Powder Bed-Based Technologies, *Additive Manufacturing* (2019) 93.
29. A.A. Al-Tamimi, C. Quental, J. Folgado, C. Peach, P. Bartolo, Stress analysis in a bone fracture fixed with topology-optimised plates, *Biomechanics and modeling in mechanobiology* 19(2) (2020) 693-699.
30. K. Stoffel, U. Dieter, G. Stachowiak, A. Gächter, M.S. Kuster, Biomechanical testing of the LCP--how can stability in locked internal fixators be controlled?, *Injury* 34 (2003) B11-9.
31. S. Farah, D.G. Anderson, R. Langer, Physical and mechanical properties of PLA, and their functions in widespread applications—A comprehensive review, *Advanced drug delivery reviews* 107 (2016) 367-392.
32. I. Anderson, Mechanical properties of specimens 3D printed with virgin and recycled polylactic acid, *3D Printing and Additive Manufacturing* 4(2) (2017) 110-115.
33. M. Ciarelli, S. Goldstein, J. Kuhn, D. Cody, M. Brown, Evaluation of orthogonal mechanical properties and density of human trabecular bone from the major metaphyseal regions with materials testing and computed tomography, *Journal of Orthopaedic Research* 9(5) (1991) 674-682.
34. T. Sathish, S.D. Kumar, K. Muthukumar, S. Karthick, Temperature distribution analysis on diffusion bonded joints of Ti-6Al-4V with AISI 4140 medium carbon steel, *Materials Today: Proceedings* 21 (2020) 847-856.
35. A. Soni, B. Singh, Design and analysis of customized fixation plate for femoral shaft, *Indian Journal of Orthopaedics* 54(2) (2020) 148-155.
36. C.-Y. Chung, A simplified application (APP) for the parametric design of screw-plate fixation of bone fractures, *Journal of the mechanical behavior of biomedical materials* 77 (2018) 642-648.
37. P. Kobryn, S. Semiatiin, Mechanical properties of laser-deposited Ti-6Al-4V, 2001 International Solid Freeform Fabrication Symposium, 2001.
38. J. Simoes, M. Vaz, S. Blatcher, M. Taylor, Influence of head constraint and muscle forces on the strain distribution within the intact femur, *Med Eng Phys* 22(7) (2000) 453-459.
39. R. Aziz, M.I.U. Haq, A. Raina, Effect of surface texturing on friction behaviour of 3D printed polylactic acid (PLA), *Polymer Testing* 85 (2020) 106434.
40. H. Yu, Z. Cai, Z. Zhou, M. Zhu, Fretting behavior of cortical bone against titanium and its alloy, *Wear*

- 259(7-12) (2005) 910-918.
41. S. Zhiani Hervan, A. Altinkaynak, Z. Parlar, Hardness, friction and wear characteristics of 3D-printed PLA polymer, *Proceedings of the Institution of Mechanical Engineers, Part J: Journal of Engineering Tribology* 235(8) (2021) 1590-1598.
 42. M. Taylor, K. Tanner, M. Freeman, A. Yettram, Stress and strain distribution within the intact femur: compression or bending?, *Med Eng Phys* 18(2) (1996) 122-131.
 43. E.J. Cheal, M. Spector, W.C. Hayes, Role of loads and prosthesis material properties on the mechanics of the proximal femur after total hip arthroplasty, *Journal of orthopaedic research* 10(3) (1992) 405-422.
 44. E. Reina-Romo, M. Giráldez-Sánchez, J. Mora-Macías, P. Cano-Luis, J. Domínguez, Biomechanical design of Less Invasive Stabilization System femoral plates: computational evaluation of the fracture environment, *Proceedings of the Institution of Mechanical Engineers, Part H: Journal of Engineering in Medicine* 228(10) (2014) 1043-1052.
 45. G. Bergmann, A. Bender, J. Dymke, G. Duda, P. Damm, Standardized Loads Acting in Hip Implants, *PLoS One* 11(5) (2016) e0155612.
 46. A. MacLeod, G. Serrancoli, B.J. Fregly, A. Toms, H. Gill, The effect of plate design, bridging span, and fracture healing on the performance of high tibial osteotomy plates: an experimental and finite element study, *Bone & Joint Research* 7(12) (2018) 639-649.
 47. P. Yang, T.-Y. Lin, J.-L. Xu, H.-Y. Zeng, D. Chen, B.-L. Xiong, F.-X. Pang, Z.-Q. Chen, W. He, Q.-S. Wei, Finite element modeling of proximal femur with quantifiable weight-bearing area in standing position, *Journal of Orthopaedic Surgery and Research* 15(1) (2020) 1-10.
 48. J. Von Fraunhofer, L. Schaper, D. Seligson, The rotational friction characteristics of human long bones, *Surface technology* 25(4) (1985) 377-383.
 49. M. Tilton, A. Armstrong, J. Sanville, M. Chin, M.W. Hast, G.S. Lewis, G.P. Manogharan, Biomechanical testing of additive manufactured proximal humerus fracture fixation plates, *Annals of Biomedical Engineering* 48(1) (2020) 463-476.
 50. J. Shockey, J. Von Fraunhofer, D. Seligson, A measurement of the coefficient of static friction of human long bones, *Surface Technology* 25(2) (1985) 167-173.
 51. J. Cordey, M. Borgeaud, S. Perren, Force transfer between the plate and the bone: relative importance of the bending stiffness of the screws and the friction between plate and bone, *Injury* 31 (2000) 21-92.
 52. M. Pendergast, R. Rusovici, A finite element parametric study of clavicle fixation plates, *International Journal for Numerical Methods in Biomedical Engineering* 31(6) (2015) e02710.
 53. S. Nobari, H. Katoozian, S. Zomorodimoghadam, Three-dimensional design optimisation of patient-specific femoral plates as a means of bone remodelling reduction, *Computer Methods in Biomechanics and Biomedical Engineering* 13(6) (2010) 819-827.
 54. E. Peleg, R. Mosheiff, M. Liebergall, Y. Mattan, A short plate compression screw with diagonal bolts—a biomechanical evaluation performed experimentally and by numerical computation, *Clinical Biomechanics* 21(9) (2006) 963-968.
 55. D.K. Gupta, F. van Keulen, M. Langelaar, Design and analysis adaptivity in multiresolution topology optimization, *International Journal for Numerical Methods in Engineering* 121(3) (2020) 450-476.
 56. P.-c. Liu, Y.-j. Yang, R. Liu, H.-x. Shu, J.-p. Gong, Y. Yang, Q. Sun, X. Wu, M. Cai, A study on the mechanical characteristics of the EBM-printed Ti-6Al-4V LCP plates in vitro, *Journal of Orthopaedic Surgery and Research* 9 (2014).
 57. B. Kincaid, L. Schroder, J. Mason, Measurement of orthopedic cortical bone screw insertion performance in cadaver bone and model materials, *Experimental Mechanics* 47(5) (2007) 595-607.
 58. S. Yerby, C.C. Scott, N.J. Evans, K.L. Messing, D.R. Carter, Effect of cutting flute design on cortical bone screw insertion torque and pullout strength, *Journal of orthopaedic trauma* 15(3) (2001) 216-221.
 59. T.K. Daftari, W.C. Horton, W.C. Hutton, Correlations between screw hole preparation, torque of insertion, and pullout strength for spinal screws, *Clinical Spine Surgery* 7(2) (1994) 139-145.
 60. C. Kanchanomai, P. Muanjan, V. Phiphobmongkol, Stiffness and Endurance of a Locking Compression Plate Fixed on Fractured Femur, *Journal of Applied Biomechanics* 26(1) (2010) 10-16.

Design optimization

61. D. Wu, A. Spanou, A. Diez-Escudero, C. Persson, 3D-printed PLA/HA composite structures as synthetic trabecular bone: A feasibility study using fused deposition modeling, *Journal of the mechanical behavior of biomedical materials* 103 (2020) 103608.
62. K.A. Egol, E.N. Kubiak, E. Fulkerson, F.J. Kummer, K.J. Koval, Biomechanics of locked plates and screws, *Journal of orthopaedic trauma* 18(8) (2004) 488-493.
63. J. Elfar, S. Stanbury, R.M.G. Menorca, J.D. Reed, Composite bone models in orthopaedic surgery research and education, *The Journal of the American Academy of Orthopaedic Surgeons* 22(2) (2014) 111.
64. A. Petersik, A. Homeier, S.G. Hoare, G. von Oldenburg, H. Gottschling, M. Schröder, R. Burgkart, A numeric approach for anatomic plate design, *Injury* 49 (2018) S96-S101.
65. N. Chakladar, L.T. Harper, A. Parsons, Optimisation of composite bone plates for ulnar transverse fractures, *Journal of the mechanical behavior of biomedical materials* 57 (2016) 334-346.
66. G. Caiti, J.G. Dobbe, E. Bervoets, M. Beerens, S.D. Strackee, G.J. Strijkers, G.J. Streekstra, Biomechanical considerations in the design of patient-specific fixation plates for the distal radius, *Medical & biological engineering & computing* 57(5) (2019) 1099-1107.
67. G.N. Duda, M. Heller, J. Albinger, O. Schulz, E. Schneider, L. Claes, Influence of muscle forces on femoral strain distribution, *Journal of biomechanics* 31(9) (1998) 841-846.
68. G.N. Duda, E. Schneider, E.Y. Chao, Internal forces and moments in the femur during walking, *Journal of biomechanics* 30(9) (1997) 933-941.
69. C. Bitsakos, J. Kerner, I. Fisher, A.A. Amis, The effect of muscle loading on the simulation of bone remodelling in the proximal femur, *Journal of biomechanics* 38(1) (2005) 133-139.
70. H. Yang, X. Ma, T. Guo, Some factors that affect the comparison between isotropic and orthotropic inhomogeneous finite element material models of femur, *Med Eng Phys* 32(6) (2010) 553-560.
71. J. Cordey, M. Borgeaud, M. Frankle, Y. Harder, O. Martinet, Loading model for the human femur taking the tension band effect of the ilio-tibial tract into account, *Injury* 30 (1999) SA26-SA30.

6

Multi-material 3D printing of functionally graded soft-hard interfaces for enhancing mandibular kinematics of temporomandibular joint replacement prostheses

Temporomandibular joint (TMJ) replacement prostheses often face limitations in accommodating translational movements, leading to unnatural kinematics and loading conditions, which affect functionality and longevity. Here, we investigate the potential of functionally graded materials (FGMs) in TMJ prostheses to enhance mandibular kinematics and reduce joint reaction forces. We develop a functionally graded artificial cartilage for the TMJ implant and evaluate five FGM designs: hard, hard-soft, and three FGM gradients with gradual transitions from 90% hard material to 0%, 10%, and 20%. These designs are 3D printed, mechanically tested under quasi-static compression, and simulated under physiological conditions. Results from computational modeling and experiments are compared to an intact mandible during incisal clenching and left group biting. The FGM design with a transition from 90% to 0% hard material improves kinematics by 19% and decreases performance by 3%, reduces joint reaction forces by 8% and 10%, and increases mandibular movement by 20% and 88% during incisal clenching and left group biting, respectively. These findings provide valuable insights for next-generation TMJ implants.

Moosabeiki, V., Khan, A., Cruz Saldivar, M., Van Paepegem, W., Jonker, B.P., Wolvius, E.B., Zhou, J., Tumer, N., Mirzaali, M.J. and Zadpoor, A.A., Multi-material 3D printing of functionally graded soft-hard interfaces for enhancing mandibular kinematics of temporomandibular joint replacement prostheses, *Communications Materials*, 5, 226, 2024.

6.1 Introduction

The temporomandibular joint (TMJ) is an important part of the human masticatory system. It supports such functions as chewing, speaking, swallowing, and facial expressions [1, 2]. Anatomically, the TMJ is a complex structure including the mandibular condyle, articular disc, and temporal bone socket, all working together to facilitate smooth and coordinated movements [3]. The TMJ allows for rotational movement in the sagittal plane and translational movement along its own axis. Proper functioning of the TMJ is necessary for maintaining overall oral health and well-being [4, 5]. However, disorders and injuries can impact the TMJ, leading to significant pain and dysfunction [5, 6] and, thus, might require surgical interventions with the use of TMJ prostheses.

Current TMJ total joint replacement (TJR) prostheses have several clinical limitations [7]. These prostheses typically allow primarily rotational movements but have limitations in accommodating translational movements, which leads to unnatural kinematics and inefficient loading conditions for the prosthetic joint [8-15]. Furthermore, while these prostheses offer an adequate movement range for daily activities, they do not achieve the mobility levels seen in healthy individuals [16, 17]. This gap highlights the necessity for developing advanced TMJ prostheses that can more accurately replicate the natural joint mechanics and improve the functional outcomes for patients. Moreover, many current TMJ prosthesis designs include a metallic structure (*i.e.*, the mandibular component which is typically made of a titanium alloy for the shaft and a cobalt-chromium-molybdenum alloy for the articulating surface) and a polymeric fossa component (*e.g.*, ultra-high molecular weight polyethylene (UHMWPE)), which can lead to issues, such as wear, slippage, and degradation over time, thereby affecting the longevity and functionality of such prostheses [8, 10, 18]. The functional outcomes of TMJ arthroplasty are evaluated mainly in terms of restoring function, maintaining prosthesis fixation, and minimizing the degradation of the prosthetic components and surrounding bone and soft tissue [11]. It is expected that addressing the limitations of the current TMJ prostheses will considerably improve their functional outcomes.

Functionally graded materials (FGMs) have emerged as a generation of engineered materials to serve the specific needs of many structural parts and may offer a promising solution to address the limitations of the current TMJ prostheses [19, 20]. These materials are found in biological structures, such as bone, teeth, and interface tissues, such as cartilage-to-bone interfaces at the end of the condyle in the mandible [20-27]. FGMs are characterized by a gradual variation in composition and/or structure over their volume, which allows for the tailoring of their properties to meet specific functional requirements [28]. This gradation can be achieved through various means, including porosity gradients, compositional or chemical, and/or microstructural gradients [29]. One of the key advantages of FGMs over traditional composites, such as layered composites, is their

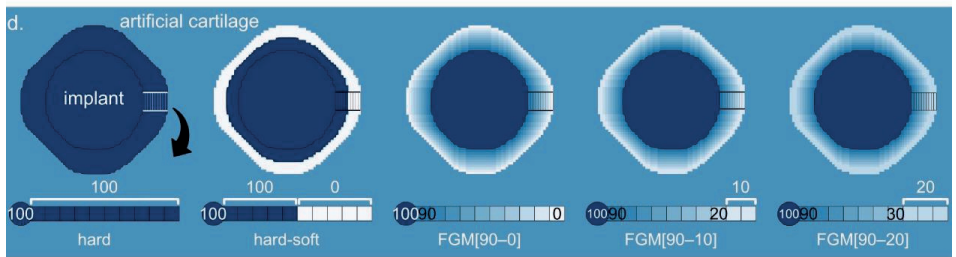
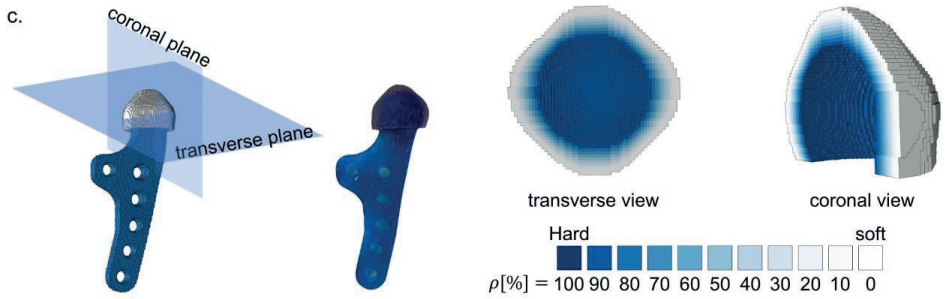
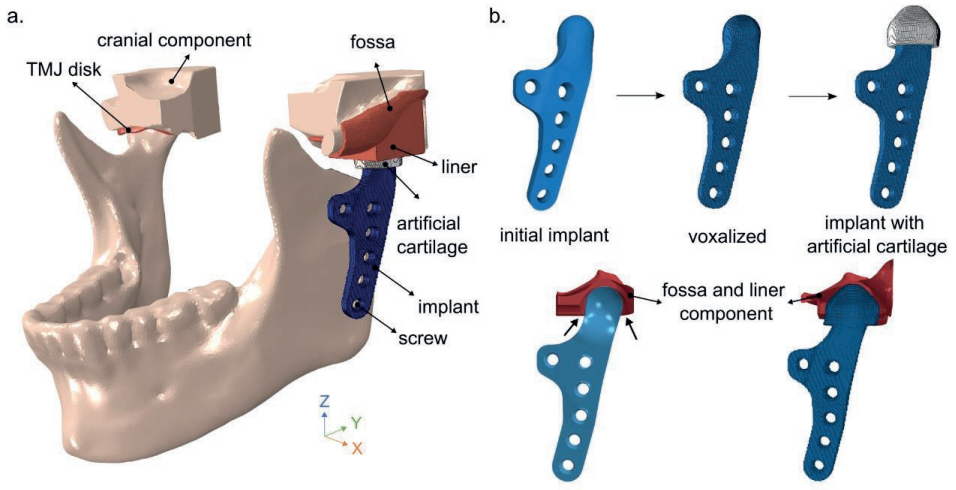
ability to eliminate abrupt hard-soft interfaces [22, 23]. Discrete interfaces in layered composites often lead to stress concentrations, which can compromise the structural integrity and longevity of the composites [30-32]. FGMs, on the other hand, provide a smoother transition between different material properties, thereby mitigating the stress concentrations and enhancing the overall performance of such materials, especially under repetitive loading conditions. While the concept of FGMs for implants is well known, including dental [33] and other joint implants (*e.g.*, knee and ankle prostheses [34, 35] and hip stem implants [36, 37]), their clinical implementation has been limited due to the obstacles related to the fabrication costs and difficulties of applying FGMs to complexly shaped implants. The feasibility of applying FGMs to TMJ replacement prostheses for alloplastic reconstruction of the mandible is yet to be explored [38].

Here, we propose a methodology to incorporate FGM design concepts into TMJ prostheses. We hypothesized that such an implementation enhances the mandibular kinematics and reduces joint reaction forces. Toward this purpose, we designed, additively manufactured, and mechanically tested various FGM configurations with different material property distributions, and identified designs that better replicate the natural movements of the TMJ while maintaining the distribution of the stresses more evenly across the joint. We also employed experimentally validated finite element models to evaluate the performance of those TMJ prosthesis designs under relevant physiological conditions corresponding to the incisal clenching (INC) and left group biting (LGF). Finally, using finite element analysis (FEA) we investigated the stress and strain distributions and potential points of failure when incorporating such FGM concepts in the design of TMJ prostheses.

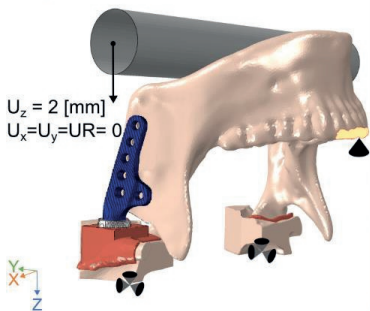
The significance of this study lies in its potential to contribute to the development of more tissue-mimetic TMJ implants for future clinical applications. By addressing the current limitations and exploring these design strategies, we aim to improve the functional outcomes for the patients requiring TMJ replacement through the design and implementation of FGM-incorporated prostheses for TMJ reconstruction.

6.2 Results and discussion

In this study, we explored how FGMs could enhance the biomechanical performance of TMJ prostheses, focusing on the kinematics and reaction forces of prostheses. We developed and implemented various designs of artificial cartilage attached to the proximal part of the TMJ implants (Figure 6.1a). The modifications in those designs aimed to enhance the contact interface between the TMJ implant and the fossa component, based on the structurally optimized TMJ implant designs introduced in a previous study [39]. The initial TMJ implant design had a gap between the implant head and the liner, which could cause some rigid body movements of the implant (Figure 6.1b) [12].



e. experimental condition



f. physiological condition

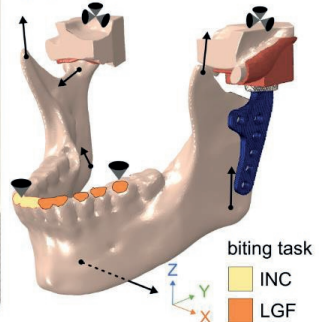


Figure 6.1. Design and material composition of TMJ Implants— (a) The implanted mandible with artificial cartilage. (b) Initial and modified designs of the TMJ implants and artificial cartilage. (c) The voxelized model with 10 additional layers of materials acting as artificial cartilage to ensure close-fitting contact between the articulating surfaces and prevent rigid body movements. (d) Various material property distributions within the artificial cartilage, including hard, hard-soft, and multiple FGM designs (*e.g.*, $\rho=90\%$ to $\rho=0\%$) (transverse cut view). (e) Experimental configuration (EXP-FEA) and (f) muscle force vectors and constraints used in physiological FEA (PHY-FEA).

To resolve this issue, we added ten layers of materials with different elastic moduli to act as artificial cartilage and ensure a close-fitting contact between the articulating surfaces, thereby limiting any rigid body movement of the TMJ implant head (Figures 1b, c). Consequently, the liner was also modified to fit the layers and avoid any gaps or clearances between the TMJ implant head and the liner (Figure 6.1b).

The computational model was validated by using three methods. First, we compared the maximum principal logarithmic strain in the linear elastic range (corresponding to a bar displacement of 1.5 mm), as predicted by the FEA model with the maximum principal true strain measured using DIC (Figures 2a and 2c). Second, we compared the force-displacement graphs (Figure 6.2b). Lastly, we compared the x and y displacements of the sixth screw (Figure 6.2a) relative to the bar displacement (*i.e.*, the z -displacement) between FEA and DIC (Figure 6.2d).

High strains were observed on the implants together with the cartilage-mimicking component around the condylar neck and near the resection border on the superior side of the first and second screws (Figure 6.2a). The strain contour plots from DIC and FEA on the ramus area showed similar distributions, with strain values in the three regions (*i.e.*, sigmoid notch, posterior border of the ramus, and mandibular angle) closely matching by factors of 1.07 and 1.3 for the intact mandible and the implant with a hard-soft cartilage-mimicking component, respectively (Figure 6.2c). The Pearson's correlation coefficients of $r = 0.99$ for the intact mandible and $r = 0.94$ for the implant with the hard-soft cartilage indicated a strong linear correlation between DIC measurements and FEA predictions (Figure 6.2c).

6.2.1 Prosthesis performance

When comparing the strain distribution among the three designs of the cartilage-mimicking component (*i.e.*, hard, hard-soft, and FGM [90–0]), the FGM designs demonstrated the evenest strain distribution in the mandibular angle (Figure 6.2a) and the cartilage-mimicking component (Figure 6.2e). In the hard-soft design, which featured an abrupt transition between the hard and soft materials, stress concentrations were detected at the interface of both materials, as evidenced by a more than ninefold increase of the stress value (from 0.37 to 3.42 MPa) (Figure 6.2e). This stress concentration could initiate cracks and delamination at the interfaces, thereby affecting the long-term performance and durability of the prosthesis [29, 32].

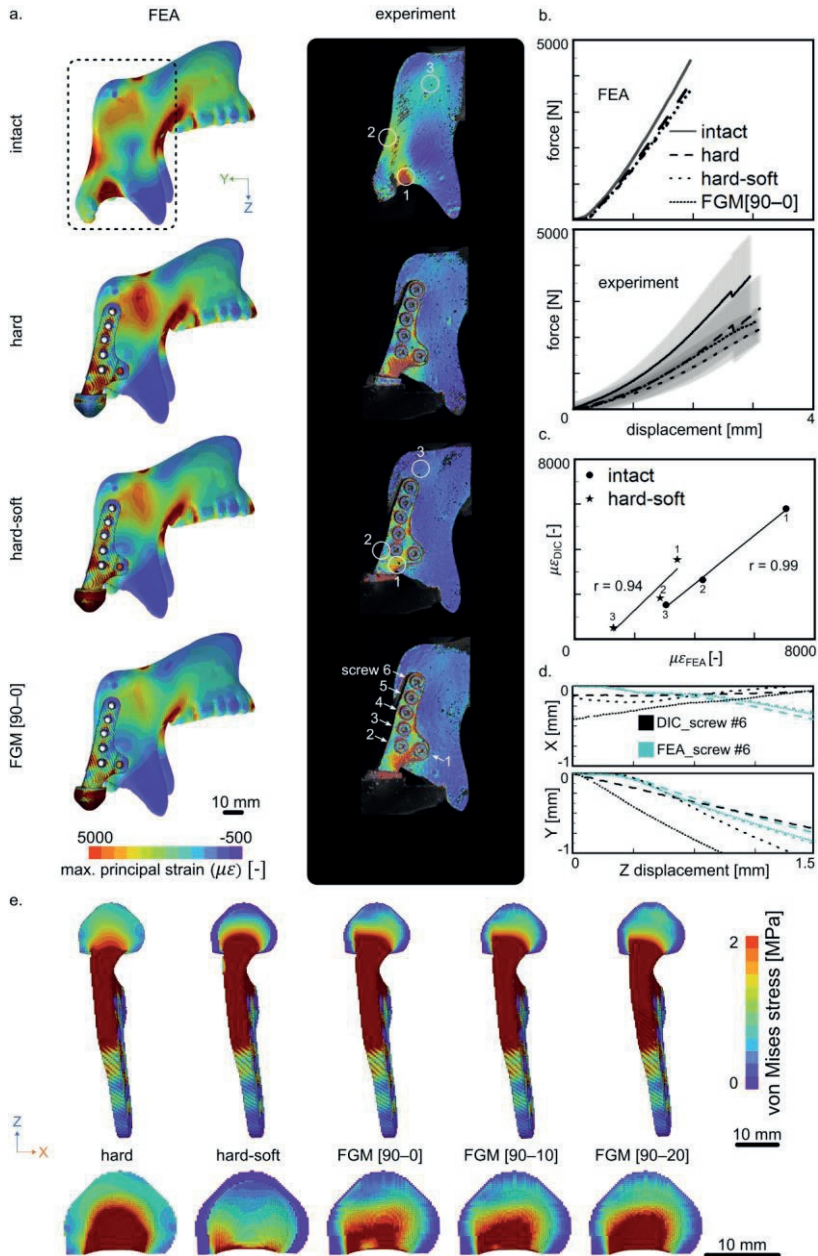


Figure 6.2. Strain/stress distributions and biomechanical testing— (a) Comparisons between digital image correlation (DIC) and FEA in the strain distributions on the surface of the implant (together with the artificial cartilage), around the condylar neck, and resection border. (b) The results obtained from the quasi-static compression testing for biomechanical evaluation. (c) The Pearson similarity between FEA and DIC in three different regions chosen in (a). (d) Comparisons in the x and y displacements of screw No. 6 with respect to the bar displacement (in the z-direction) between FEA and DIC. (e) Von Mises stress distributions of different cartilage designs. The legends in (b) apply to (d) as well.

The force-displacement results obtained from the quasi-static biomechanical testing and FEA are shown in Figure 6.2b. The stiffness values of the implanted mandibles were similar between computational results and experimental measurements, and all were consistently lower than the value of the intact mandible. Specifically, the stiffness of the FGM-implanted mandible was 14% lower than the intact mandible in the FEA and 31% lower in the experimental setup. The forces predicted by the FEA were 1.9 times higher than those measured in the experiment (Figure 6.2b). These differences could be attributed to the variations in material properties, as the mechanical properties used in the FEA may not perfectly match those of the actual materials used in the experimental setup. Additionally, variations in experimental measurements and the 3D printing process could contribute to these differences [40].

While this study primarily focused on INC and LGF biting tasks, where bending is more dominant, we acknowledge that twisting (torsional) movements of the mandible may also play an important role in mandibular biomechanics. Twisting can occur during more complex or asymmetric chewing patterns and may introduce additional stress distributions that could further impact the performance of TMJ prostheses. Although our study focused on designing an artificial cartilage and did not explicitly consider twisting movements, future research should incorporate both bending and twisting to provide a more comprehensive understanding of the mechanical behavior of TMJ prostheses under various functional conditions.

Additionally, we acknowledge that while this study reports peak stress values, the effects of bone remodeling were not considered. Bone remodeling can influence stress distribution and implant stability over time, and screw loosening may result from regional bone resorption around the screws, which was not evaluated [41]. Future research should incorporate bone remodeling to better assess long-term stress distribution and screw stability.

6.2.2 Kinematics analysis

We assessed the kinematics of four designs of cartilage-mimicking components, *i.e.*, hard, FGM [90–0], FGM [90–10], and FGM [90–20], during the INC task using PHY-FEA, and compared the kinematics of the implanted mandible to that of the intact mandible (Figure 6.3). The FGM [90–10] and FGM [90–20] designs were specifically used to evaluate the effect of harder materials. Subsequently, we examined the implanted mandible with hard and FGM [90–0] cartilage-mimicking components and compared them with the intact mandible during the LGF task (Figure 6.4).

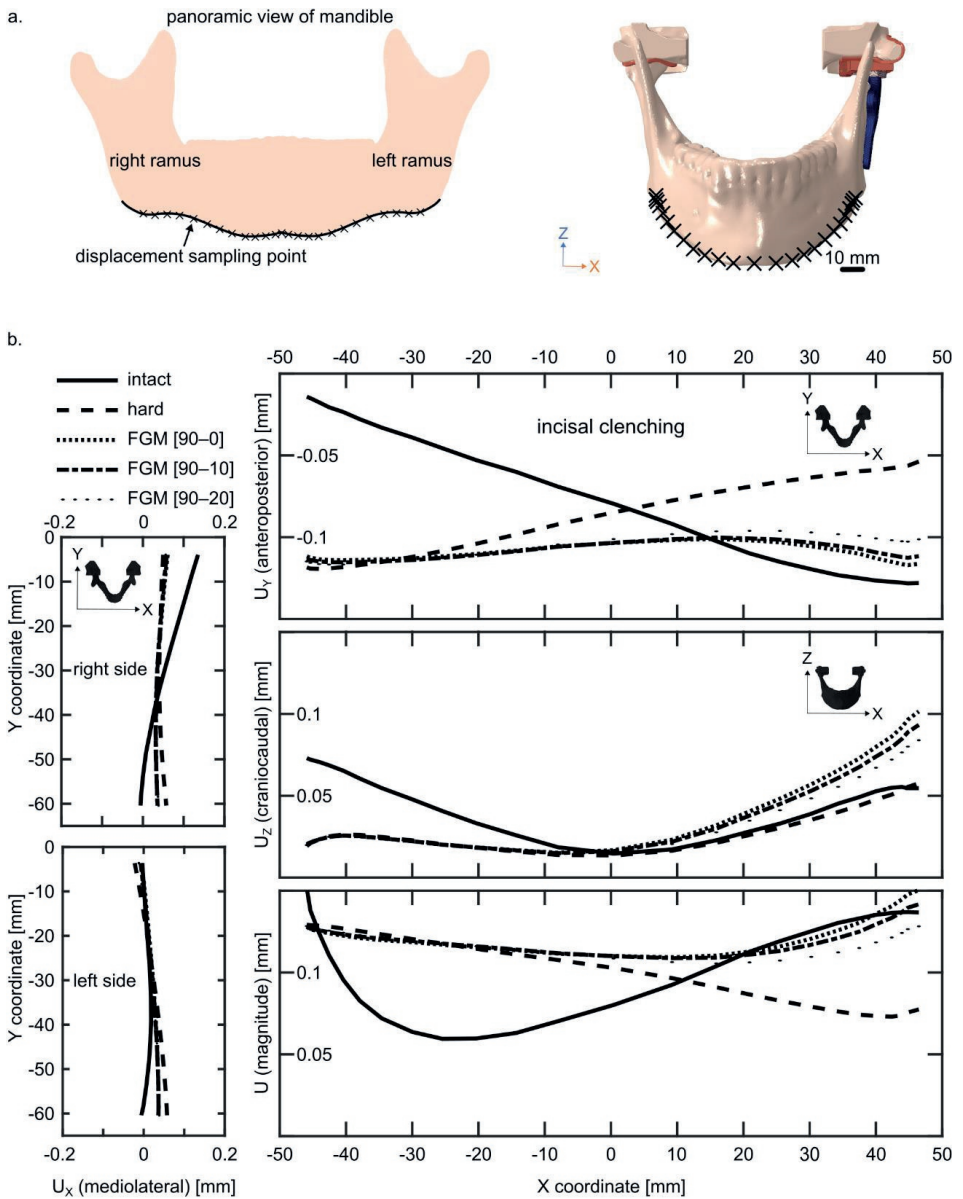


Figure 6.3. Mandibular kinematics during incisal clenching— (a) The sampling points along the mandible. (b) The mediolateral (U_x), anteroposterior (U_y), craniocaudal (U_z), and magnitude displacements of the mandible during incisal clenching for different cartilage designs (hard, FGM [90-0], FGM [90-10], FGM [90-20]).

During the INC, due to the morphological asymmetry of the mandible, the intact mandible tended to move toward the left side. The PHY-FEA showed around a 0.15 mm larger mediolateral (U_X) displacement of the right ramus as compared to the left side (Figure 6.3b-left). Moreover, the left side of the mandible moved more anteriorly (U_Y) than the right side during incisal biting, with a displacement of around 0.1 mm (Figure 6.3b-right).

Achieving symmetric movement of the mandible is crucial to ensure an even distribution of forces throughout the mandibular structure and its joint [14]. The FGM-incorporated prostheses reduced the asymmetry in mediolateral (U_X) movement on the right side and showed a leftward movement in the vicinity of the mandible mental tubercles. They also showed relatively better similarity and closeness to the intact mandible on the left (implanted) side (Figure 6.3b-left). In particular, the FGM [90–0] prosthesis achieved a recovery rate of approximately 72% ($\alpha = 0.72$) in the intact mandibular displacement patterns, while the hard cartilage-mimicking components resulted in a recovery rate of only 28% ($\alpha = 0.28$) (Figure 6.4b). Furthermore, the mandibular displacement of the FGM [90–0] prosthesis was 4% closer to that of the intact mandible, compared to the prosthesis with a hard cartilage-mimicking component, as indicated by the Euclidean distance values of 0.16 mm for the FGM [90–0] prosthesis and 0.20 mm for the prosthesis with a hard cartilage-mimicking component (Figure 6.4b).

During the INC, the anteroposterior (U_Y) movement of the mandibles showed that the hard cartilage-mimicking components resulted in greater anterior movement on the right side (0.12 mm) as compared to the left side (0.05 mm). In contrast, the FGM-incorporated prostheses facilitated anterior movement on the left side, resulting in more symmetrical anteroposterior movements of the mandible. Both the left (implanted) and right (intact) sides demonstrated nearly equal anterior movements (0.12 mm) (Figure 6.3b-right).

As compared to the prosthesis with the hard cartilage, the FGM-incorporated prostheses, particularly FGM [90–0], reduced the asymmetry in anteroposterior (U_Y) movement (Figure 6.3b-right) and demonstrated 28% less dissimilarity ($\alpha = 0.28$) and 7% closer alignment with the displacement patterns of the intact mandible (Figure 6.4b). The normalized cross-correlation increased from -1 to -0.28 while the Euclidean distance decreased from 0.35 mm to 0.28 mm when comparing the displacements of the intact mandible with those of the prostheses incorporating a hard and an FGM [90–0] cartilage-mimicking component, respectively (Figure 6.4b).

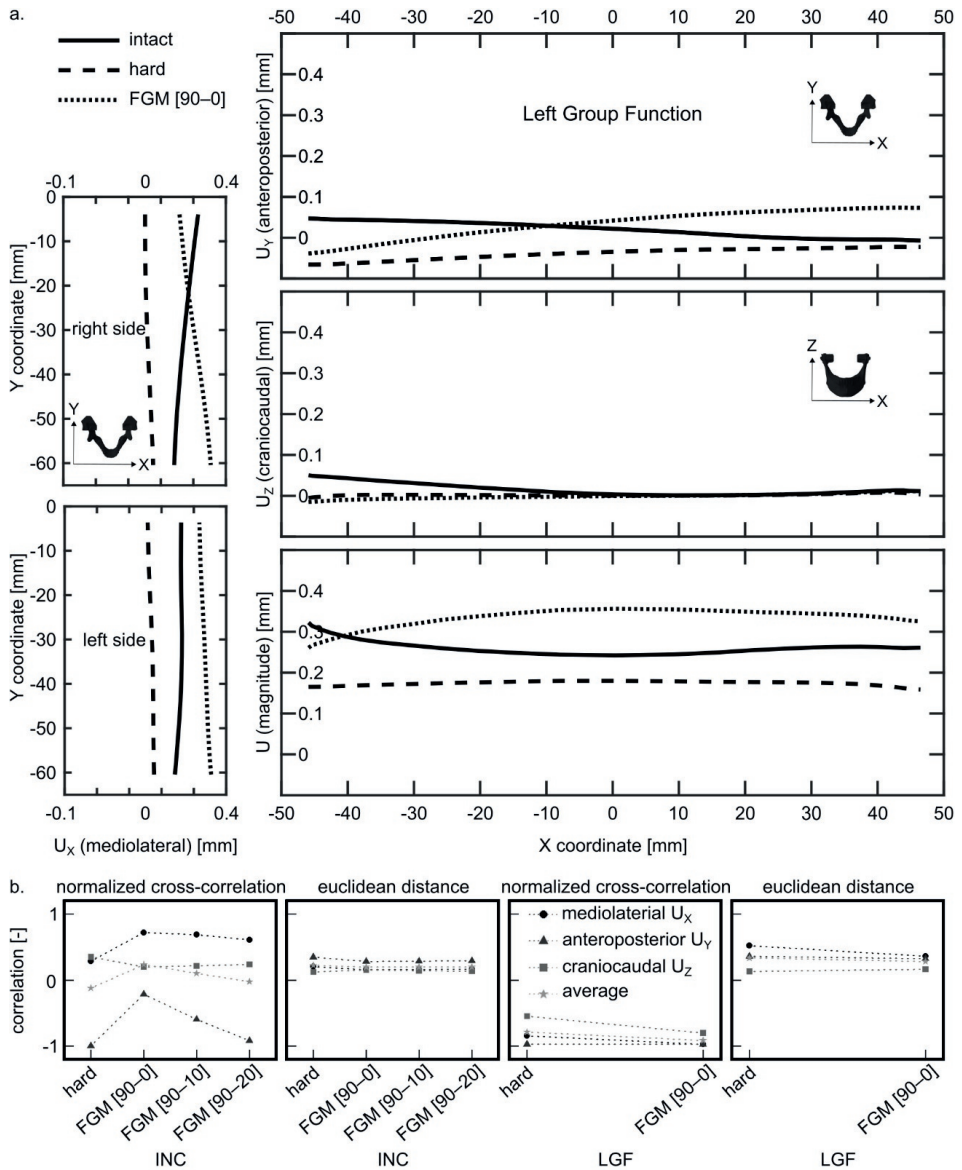


Figure 6.4. Mandibular kinematics during left group biting— (a) The displacement patterns of hard and FGM [90-0] prostheses (mediolateral, anteroposterior, craniocaudal, and magnitude) during left group biting. (b) The correlation and Euclidean distance between the displacement patterns of the hard, FGM [90-0], FGM [90-10], and FGM [90-20] designs against the intact mandible during the INC and LGF biting tasks.

The TMJ prosthesis with a hard cartilage-mimicking component showed superior craniocaudal (U_z) displacement performance during the INC as compared to those with FGM cartilage-mimicking components. The FGM designs of the prostheses, particularly FGM [90–0], resulted in a larger craniocaudal (U_z) displacement (0.09 mm) on the left side as compared to the design with a hard cartilage-mimicking component (0.05 mm), thus increasing the asymmetry in this specific mandibular movement (Figure 6.3b-right). The prosthesis with a hard cartilage-mimicking component resulted in a higher degree of symmetry in the motion of the implanted mandible and enhanced its similarity to the movement pattern observed in the intact mandible. Specifically, the TMJ prosthesis with a hard cartilage-mimicking component recovered 15% more of the intact mandibular displacement patterns than the FGM [90–0] prosthesis (Figure 6.4b). Moreover, the prosthesis with a hard cartilage-mimicking component brought this specific movement 3% closer to that of the intact mandible, as indicated by the corresponding Euclidean distances in Figure 6.4b.

Among the four designs of the cartilage-mimicking component (Figure 6.4b), the FGM [90–0] demonstrated, on average, 36% less dissimilarity and 2% closer alignment to the displacement patterns of the intact mandible as compared to the ones with a hard cartilage-mimicking component. In general, the mandibular movement range during the INC increased when FGM-incorporated prostheses were used, as is clear from the corresponding displacement magnitudes (Figure 6.3b-right). The FGM design [90–0] increased the mandibular movement range by 20% (0.02 mm) as compared to the prosthesis with a hard cartilage-mimicking component. The results presented in Figure 6.4b also indicate that mandibular displacements could be regulated through a rational distribution of material properties and that the displacement magnitudes increase when the outer layer of the cartilage-mimicking component is relatively softer. Additionally, the reaction forces on the prosthetic joint decreased from 167 N for the hard design of the cartilage-mimicking component to 153 N for the FGM [90–0] design, corresponding to a reduction of > 8%.

We further examined the performance of the hard and FGM [90–0] designs of the cartilage-mimicking components during the LGF biting task. Given that mandibular movement during LGF is inherently asymmetric, the concept of symmetry is not applicable here. The intact mandible demonstrated mediolateral (U_x) displacement towards the left side on both the right and left sides (Figure 6.4a-left). The right side experienced a greater craniocaudal (U_z) displacement of 0.05 mm as compared to the left side, which exhibited a displacement of 0.01 mm (Figure 6.4a-right). Additionally, the right side moved posteriorly (U_y) by 0.05 mm, while the left side showed a slight anterior displacement of 0.01 mm (Figure 6.4a-right).

Regarding mediolateral (U_x) displacement during LGF, the hard design of the cartilage-mimicking component decreased the tendency of the implanted mandible to

Design transitions

move toward the left (U_x), while the FGM [90–0] design increased it (Figure 6.4a-left). As compared with the FGM [90–0] design, the hard design of the cartilage-mimicking component showed a 13% reduction in dissimilarity from the displacement patterns observed in the intact mandible, as indicated by the normalized cross-correlation in Figure 6.4b. Conversely, the displacements of the FGM [90–0] design demonstrated a 16% greater degree of proximity to the displacement pattern of the intact mandible, as compared to the hard cartilage design, as shown by the Euclidean distance presented in Figure 6.4b.

There is an inversely proportional relationship between the anteroposterior (U_y) displacements exhibited by the implanted mandibles and those of the intact mandible during LGF. The hard and FGM [90–0] designs showed nearly equal dissimilarity to the displacement field of the intact mandible, with a correlation coefficient (α) of approximately -0.97. However, the FGM [90–0] design demonstrated 4% greater proximity to the displacements of the intact mandible as compared to the hard design (Figure 6.4b).

For craniocaudal (U_z) displacement during LGF, the hard design performed better than the FGM [90–0] design. The hard design exhibited 25% less dissimilarity to the displacement patterns of the intact mandible, as compared to the FGM [90–0] design. The normalized cross-correlation between the intact mandible and the implanted mandible with a hard cartilage-mimicking component was -0.55, while it was -0.80 between the intact mandible and implanted mandible and the FGM [90–0] design (Figure 6.4b). Additionally, the displacement pattern of the hard design was 3% closer to that of the intact mandible as compared to the FGM [90–0] design, as indicated by the corresponding Euclidean distances presented in Figure 6.4b.

In the LGF scenario, the FGM [90–0] design showed better mediolateral (U_x) and anteroposterior (U_y) displacements, while the hard cartilage design excelled in craniocaudal (U_z) displacement. The displacement magnitudes showed that the FGM [90–0] design enhanced the mandibular movement range as compared to the hard design, with an average increase of 88%. The average displacement magnitude increased from 0.17 mm for the hard design to 0.32 mm for the FGM [90–0] design. Although the prosthesis with a hard cartilage-mimicking component exhibited 12% less dissimilarity from the displacement patterns observed in the intact mandible, as compared to the FGM [90–0] prosthesis (Figure 6.4b), the FGM [90–0] design displayed a smaller average Euclidean distance (0.28 mm) to the intact mandible as compared to the hard design (0.34 mm). This indicates that the displacement of the FGM [90–0] design was 6% closer to the intact mandible (the average Euclidean distances in Figure 6.4b). Consequently, with the FGM [90–0] design, there was an average performance increase of 19% during the INC and an average performance decrease of 3% during LGF. Additionally, the reaction

forces on the prosthetic joint decreased from 151 N for the hard design to 137 N for the FGM [90–0] design, representing a reduction of nearly 10%.

The excessive mandibular displacements observed mediolaterally (U_x) and anteroposteriorly (U_y) during biting, particularly during LGF, are due to the absence of the lateral pterygoid muscle, which controls the precise horizontal movement of the mandible [42]. Following TMJ replacement, translational movements are often the most impacted. The primary factors contributing to reduced mandibular translation include the detachment of the lateral pterygoid muscle, the geometry of the articular surface, and the development of fibrosis in the articular and muscular tissues [12].

Comparing the displacement patterns of implanted mandibles to that of the intact mandible during mastication is challenging, mainly due to their dependency on the prosthetic joint design approach [12, 43, 44]. The prosthetic joint is often simplified to be a spherical or ball-and-socket joint with a clearance between the articulating surfaces [2, 12]. However, in this study, the prosthetic joint was designed with tight surface-to-surface contact. Since the TMJ is a bilateral joint, where the movement of one side affects the other, the implantation alters the kinematics of both the implanted and healthy sides of the mandible [9]. This interdependence complicates a direct comparison between the implanted and intact mandibles.

For a comparative analysis of various prosthesis designs, each implanted mandible can be positioned alongside an intact mandible [39]. The similarity (measured by α) and proximity (measured by the Euclidean distance) between the displacements of the intact and implanted mandibles largely depend on the design and modeling approach of the prosthetic joint. Ideally, α should be close to 1 and the Euclidean distance close to 0 when comparing the intact and implanted mandibles. However, it is important to recognize that α will not be exactly 1 and the Euclidean distance will not be exactly 0, as complete functional restoration of the TMJ is practically not achievable even with an effective replacement [45].

In this study, we designed artificial cartilage-mimicking components using FGMs, ranging from hard material properties to those of a softer material. In the actual TMJ prostheses, however, the implant is made of a cobalt-chromium-molybdenum alloy, a titanium alloy, or both, while the fossa component is typically made of polyethylene (UHMWPE) [46, 47]. The resulting hard-soft contact interface without any gradual transitions poses risks of wear, slippage, and degradation over time [8, 10, 18]. Fabricating FGMs that transition from the metallic implant to the fossa component made of a soft material, such as polyethylene, is quite challenging.

To address this challenge, we suggest the use of multi-layer coatings on the metal implant to create functional gradation. Coatings can provide a softer region on the implant head, and reduce the risks associated with soft-hard contact while maintaining the

structural integrity and durability of the metal implant. Additionally, introducing cellular structures made from the same material as the implant, with variations in porosity on the top of the implant using additive manufacturing techniques, such as directed energy deposition, could further enhance the gradation. This could be followed by the infiltration of a polymeric material to create FGMs.

Future research should focus on the development and testing of coating techniques and advanced manufacturing methods to enhance the performance and longevity of TMJ prostheses. Furthermore, performing fatigue tests on these designs will be crucial to evaluate their long-term durability and performance under physiological cyclic loading conditions. This will help in assessing the wear resistance and structural integrity of the prostheses over an extended period.

6.3 Methods

6.3.1 TMJ prosthesis design and manufacturing

The initial TMJ implant design was voxelized to fine voxel sizes of $0.25 \times 0.25 \times 0.25$ mm³ using a MATLAB code described in [48] (Figure 6.1b). Subsequently, ten (voxel) layers of materials, each with a thickness of 0.25 mm and an overall thickness of 2.5 mm (10×0.25 mm), were added onto the proximal part of the implant head to mimic the presence of the artificial cartilage (Figure 6.1c). This design thickness falls within the average range measured for articular cartilage covering the temporomandibular joint disc, which varies between 2.0 to 2.8 mm in the central, lateral, medial, and posterior regions [49]. Each layer was then assigned a value of ρ , representing the volume fraction of the hard phase (Figures 1c, d). In the original TMJ implant design, all voxels were consistently assigned a volume fraction of $\rho=100\%$, indicating that they were entirely composed of the hard phase material. In the added ten layers positioned above the TMJ implant head, however, we assigned varied volume fractions of the hard phase, assigning values from $\rho=90\%$ to $\rho=0\%$ (Figures 1c, d). This gradation in volume fraction created a functionally graded material, transitioning from the hard material of the implant to a softer material, thereby mimicking the function of natural cartilage.

We created five FGM artificial cartilages with varied material property distributions of $\rho=0, 10, 20, 30, 40, 50, 60, 70, 80,$ and 90% of the hard material, including (i) FGM [90–0] where the material distribution from the implant body toward the liner component was 90, 80, 70, 60, 50, 40, 30, 20, 10, and 0%, (ii) FGM [90–10] with a distribution of 90, 80, 70, 60, 50, 40, 30, 20, 10, and 10%, and (iii) FGM [90–20] with a distribution of 90, 80, 70, 60, 50, 40, 30, 20, 20, and 20%. We compared these designs with (iv) a cartilage-mimicking component having an abrupt hard-soft connection in the middle (denoted as ‘hard-soft’) with a distribution of 100, 100, 100, 100, 100, 0, 0, 0, 0, and 0%,

and (v) a cartilage-mimicking component without a material gradient and with a volume fraction of $\rho=100\%$ (denoted as ‘hard’) (Table 6.1 and Figure 6.1d).

All the specimens were fabricated using a multi-material Polyjet 3D printer (ObjetJ735 Connex3, Stratasys® Ltd., USA) with a print resolution of $0.042 \text{ mm} \times 0.084 \text{ mm}$ and a layer thickness of 0.027 mm [48]. Specimen preparation for printing was carried out using the GrabCAD Print software (Stratasys® Ltd., USA, version 1.76.10.25761). A rigid opaque photopolymer, VeroCyan™ (RGD841, Stratasys® Ltd., USA), was utilized to represent the hard phase, while a rubber-like photopolymer, Agilus30™ Clear (FLX935, Stratasys® Ltd., USA), was used for the soft phase. These materials, which are available in the 3D printer with different Shore hardness values, were automatically mixed by the 3D printer according to the specified volume fractions to achieve the desired material gradient.

Table 6.1. FGM artificial cartilages with ten layers of varied material property distributions $\rho(\%)$ of the hard material. The values are presented from left to right (L1–L10), indicating the distribution from the implant body toward the liner component.

FGM design	material distribution $\rho(\%)$ within layers									
	L1	L2	L3	L4	L5	L6	L7	L8	L9	L10
FGM [90–0]	90	80	70	60	50	40	30	20	10	0
FGM [90–10]	90	80	70	60	50	40	30	20	10	10
FGM [90–20]	90	80	70	60	50	40	30	20	20	20
hard-soft	100	100	100	100	100	0	0	0	0	0
hard	100	100	100	100	100	100	100	100	100	100

6.3.2 Biomechanical testing

The healthy intact mandible and three prosthesis designs (*i.e.*, hard, hard-soft, and FGM [90–0]) were tested with three replications. To secure the connection of the TMJ implant to the mandible, we utilized universal flat head stainless-steel screws with dimensions of $3.0 \times 12.0 \text{ mm}$. The torque applied during the screw insertion process was measured using a Stahlwille Torque Screwdriver 760 (Germany), with the maximum torque set at 0.3 Nm [50]. This ensured precise and controlled fixation of the implant.

The implanted and intact mandibles were biomechanically tested under quasi-static compressive loading using a mechanical testing bench (LLOYD instrument LR5K equipped with a 5000 N load cell) at a crosshead speed of 1 mm/min and with a preload of 10 N until failure occurred. The specimens were positioned upside down on the test setup proposed in [51] (Figure 6.1e). The load from the machine was distributed evenly in the region of the mandibular angle through a rigid steel bar. The cranial component with an (artificial) TMJ disk was used to support the condyle, constraining its translational movement while allowing rotational movement. The INC task was executed using a support structure that constrained the incisal region perpendicularly to the occlusion plane (*i.e.*, the z -direction) (Figure 6.1e). Failure criteria included fractures of the mandible, the

implant with the artificial cartilage, failure at the screw-substrate interface, or a crosshead displacement exceeding 10 mm after the preload.

The full-field strain and local deformation during the experimental testing were recorded using a Q-400 2×12 MPixel digital image correlation (DIC) system (LIMESS GmbH, Krefeld, Germany). Strain maps were generated at a frequency of 1 Hz with facet sizes ranging from 21 to 27 pixels. The lateral surface of the ramus bone and the TMJ implant together with the cartilage were designated as the region of interest (Figure 6.2a). A black dot speckle pattern was applied over a white-painted background to cover the entire area of interest. Two digital cameras, along with LED panels for illumination, were positioned 0.7 m from the specimen to capture the images. Image processing and strain calculations were conducted using Istra4D x64 4.6.5 software (Dantec Dynamics A/S, Skovunde, Denmark). The maximum principal strain maps obtained from FEA were then compared to those measured with DIC within the linear region (Figure 6.2a).

6.3.3 Computational modeling

The finite element analysis (FEA) was performed using the commercial software suite (implicit solver, Abaqus 2019, Dassault Systems Simulia, France). The model was developed based on the randomly selected and anonymized computed tomographic (CT) scan of a mandible described in reference [12]. The CT data had a spatial resolution of $0.52 \times 0.52 \times 1.0$ mm³. The mandible segmentation was performed using Materialise Mimics® v21.0 (Materialise Inc., Leuven, Belgium), and Materialise 3-matic® v14.0 (Materialise Inc., Leuven, Belgium) was used for mesh generation. A quadratic tetrahedron (C3D10) element was used for both the implanted and intact mandibles. A model was accordingly created and accounted for nonlinear geometry to replicate the experimental condition (EXP-FEA) (see section 6.3.1 and Figure 6.1e). Subsequently, the model was expanded to include a musculoskeletal system and simulate more complex physiological loading conditions (PHY-FEA), such as INC and LGF, according to the musculoskeletal model proposed by Koriath et al. [52] (Figure 6.1f).

6.3.4 Material property assignments

The material properties of the hard phase (*i.e.*, $\rho=100\%$) were assigned to the implant body, while those of the FGM artificial cartilage were determined by the locally assigned volume fraction of the hard phase (ρ) to each individual layer. The constitutive model, which can predict both linear elastic and hyperelastic mechanical behaviors and accommodate both hardening or softening nonlinear regimes for a given volume fraction of the hard phase was obtained in our previous study [48]. However, here, we only focused on the linear elastic part of these material properties.

In the EXP-FEA, all the components, including the mandible, fossa component, cranial component, and TMJ disc, were assumed to be isotropic and homogeneous and

had linear elastic material properties ($E = 2697.3$ MPa and $\nu = 0.4$) for the hard phase (*i.e.*, $\rho = 100\%$). In the PHY-FEA, the mandible was assumed to be isotropic and non-homogeneous, and have linear elastic material properties derived from the CT image data using Materialise Mimics® (Materialise Inc., Leuven, Belgium) as described in [12]. The material properties of the TMJ disc and cranial component were set to be homogeneous, isotropic, and linearly elastic, as described in [12, 39].

6.3.5 Loads and boundary conditions

The model was constrained at the superior surfaces of both cranial sections in all directions (Figure 6.1e, f). Biting tasks were simulated by constraining the teeth in the direction perpendicular to the plane of occlusion (*i.e.*, the z -direction) (Figure 6.1e, f). In other words, no vertical movements of the lateral and central incisors were allowed during INC.

The interactions between the cartilage (*i.e.*, TMJ disc) and cranial component and between the fossa component and cranial component were modeled with a tie constraint. The contacts between the cartilage (TMJ disc) and mandibular condyle and between the mandible and the TMJ implant were assumed to be frictionless. Fixation screws were modeled by applying a rigid beam constraint to the adjacent screw hole surfaces of the TMJ implant and the bone. A bar-to-bone contact was modeled using a friction coefficient (penalty) of 0.2 and a finite sliding formulation without surface smoothing [51].

In EXP-FEA, a steel loading bar was simulated as an analytically rigid and, thus, non-deformable object. The bar was placed to transmit distributed forces similar to those applied in the experiments (Figure 6.1e). A displacement of 2 mm was imposed on the bar along the positive z -direction (craniocaudal axis) with all the rotations constrained except for those around the y -axis (anteroposterior axis).

In PHY-FEA, the FGM-incorporated prostheses were subjected to conditions under INC and LGF biting tasks. Table 6.2 lists the muscle force components for each biting task. To ensure that the TMJ prosthesis experiences a maximum stress level below the yield stress of the soft material, we considered 25% of the maximum muscle forces for INC and LGF from the literature [12, 39]. Moreover, the left lateral pterygoid muscle was detached in the implanted model. Each muscle force was applied as a concentrated load at the corresponding insertion point (Figure 6.1f). Nodes within a 2 mm radius of each insertion point were kinematically coupled to the corresponding node to simulate realistic muscle forces. These boundary conditions were selected based on their widespread use and recognition in the literature for accurately simulating TMJ function under physiological loading conditions [9, 12, 39, 51, 52].

6.3.6 Kinematic performance evaluation

We assessed the functional performance of the designs by analyzing mandibular displacement during INC and LGF biting tasks, and compared mediolateral, anteroposterior, and craniocaudal displacements (Figures 3 and 4). Moreover, we evaluated the joint reaction forces for each design by measuring the forces exerted at the artificial joint interfaces during these tasks using the finite element model.

To do this, we selected a series of sampling points along the lower contour of the mandible. For a symmetrical configuration, points on one half of the mandible were chosen at nearly equal distances, and these points were then mirrored across the sagittal plane to ensure symmetry (Figure 6.3a). We calculated the displacements at each sampling point using the finite element model. We then compared the displacement of each sampling point between the intact and implanted mandibles using normalized cross-correlation, represented by Pearson's correlation coefficient (α),

$$\alpha = \frac{\sum_i^n (U_i^{intact} - \bar{U}^{intact})(U_i^{implanted} - \bar{U}^{implanted})}{\sqrt{\sum_i^n (U_i^{intact} - \bar{U}^{intact})^2 \sum_i^n (U_i^{implanted} - \bar{U}^{implanted})^2}} \quad (5.1)$$

, where U_i^{intact} represents the displacement of i^{th} sampling point out of n sampling points on the intact mandible, $U_i^{implanted}$ represents the displacement of i^{th} sampling point on the implanted mandible, \bar{U}^{intact} is the mean displacement of all the sampling points on the intact mandible, and $\bar{U}^{implanted}$ is the mean displacement of all the sampling points on the implanted mandible.

Furthermore, to quantify the spatial differences between the corresponding displacement sampling points of the intact and implanted mandibles, the Euclidean distance was calculated (Figure 6.4b):

$$Euclidean\ distance = \sqrt{\sum_i (U_i^{intact} - U_i^{implanted})^2} \quad (5.2)$$

Table 6.2. Muscle force components (25% of maximum bite force) for the incisal clenching (INC) and left group (LGF) biting tasks.

Muscle name	Incisal clenching (INC)			Left group biting (LGF)		
	F _x [N]	F _y [N]	F _z [N]	F _x [N]	F _y [N]	F _z [N]
<i>Right masseter</i>	-30.46	-27.09	92.89	-24.80	-15.57	68.66
<i>Left masseter</i>	30.46	-27.09	92.89	25.81	-4.30	58.65
<i>Right temporalis</i>	-4.22	5.46	20.85	-4.31	6.99	19.95
<i>Left temporalis</i>	4.22	5.46	20.85	43.38	73.77	196.93
<i>Right lateral pterygoid</i>	45.48	-50.35	-8.02	8.53	-9.56	-1.63
<i>Left lateral pterygoid</i>	-45.48	-50.35	-8.02	-32.62	-37.47	-7.19
<i>Right medial pterygoid</i>	73.76	-56.61	120.06	72.02	-55.27	117.21
<i>Left medial pterygoid</i>	-73.76	-56.61	120.06	-6.63	-5.09	10.80
<i>Right anterior digastric</i>	-5.44	20.95	-5.28	-4.14	15.95	-4.02
<i>Left anterior digastric</i>	5.44	20.95	-5.28	5.56	21.41	-5.40

6.4 Conclusions

This study investigated the incorporation of FGMs into TMJ prostheses to enhance mandibular kinematics and reduce prosthesis reaction forces. We tested various FGM configurations with different material property distributions and compared them with the designs featuring an abrupt soft-hard transition and no gradient. An experimentally validated finite element model was used to evaluate the designs under INC and LGF tasks. The results demonstrate that the prosthesis with an abrupt hard-soft connection in the cartilage suffers from stress concentrations; the stress at the interface is increased by up to nine times as high as that of the FGM [90–0] cartilage design. The FGM [90–0] cartilage design improves the performance by 19% during the INC and decreases performance by 3% during LGF in terms of mandibular kinematics and reduces the joint reaction force by 8% and 10% at the artificial joint interfaces during the INC and LGF, respectively. Additionally, the FGM [90–0] design makes the mandibular movement less asymmetric during the INC. The FGM [90–0] cartilage design significantly increases the mandibular movement range by 20% during the INC and 88% during LGF as compared to the hard design. Although FGM-incorporated prostheses show great promise in enhancing TMJ functionality, achieving a complete replication of the natural TMJ function remains challenging and the fabrication technology for such prostheses are yet to be developed.

Bibliography

1. L. Guarda-Nardini, D. Manfredini, G. Ferronato, Temporomandibular joint total replacement prosthesis: current knowledge and considerations for the future, *International Journal of Oral and Maxillofacial Surgery* 37(2) (2008) 103-110.
2. H. Sinno, Y. Tahiri, M. Gilardino, D. Boby, Engineering alloplastic temporomandibular joint replacements, *McGill Journal of Medicine: MJM* 13(1) (2011) 63.
3. G. Wilkie, Z. Al-Ani, Temporomandibular joint anatomy, function and clinical relevance, *British Dental Journal* 233(7) (2022) 539-546.
4. G. Minervini, R. Franco, S. Crimi, M. Di Blasio, C. D'Amico, V. Ronsivalle, G. Cervino, A. Bianchi, M. Cicciù, Pharmacological therapy in the management of temporomandibular disorders and orofacial pain: a systematic review and meta-analysis, *BMC Oral Health* 24(1) (2024) 78.
5. A.U. Yap, J. Lei, C. Liu, K.-Y. Fu, Comparison of painful temporomandibular disorders, psychological characteristics, sleep quality, and oral health-related quality of life of patients seeking care before and during the Covid-19 pandemic, *BMC Oral Health* 23(1) (2023) 438.
6. A. Ilgunas, A. Fjellman-Wiklund, B. Häggman-Henrikson, F. Lobbezoo, C.M. Visscher, J. Durham, A. Lövgren, Patients' experiences of temporomandibular disorders and related treatment, *BMC Oral Health* 23(1) (2023) 653.
7. A. Westermark, D. Koppel, C. Leiggner, Condylar replacement alone is not sufficient for prosthetic reconstruction of the temporomandibular joint, *International Journal of Oral and Maxillofacial Surgery* 35(6) (2006) 488-492.
8. B. Gonzalez-Perez-Somarriba, G. Centeno, C. Vallengano, L.M. Gonzalez-Perez, On the Analysis of the Contact Conditions in Temporomandibular Joint Prostheses, *Advances in Materials Science and Engineering* 2018(1) (2018) 2687864.
9. J.-P. van Loon, E. Otten, C.H. Falkenström, L.G.M. de Bont, G.J. Verkerke, Loading of a unilateral temporomandibular joint prosthesis: A three-dimensional mathematical study, *Journal of Dental Research* 77(11) (1998) 1939-1947.
10. M. Dolwick, Reconstruction of the TMJ using an alloplastic stock total joint prostheses, *International Journal of Oral and Maxillofacial Surgery* 40(10) (2011) 1015.
11. L.G. Mercuri, *Temporomandibular joint total joint replacement—TMJ TJR*, Switzerland: Springer Int Pub (2016).
12. M. Pinheiro, R. Willaert, A. Khan, A. Krairi, W. Van Paepegem, Biomechanical evaluation of the human mandible after temporomandibular joint replacement under different biting conditions, *Scientific Reports* 11(1) (2021) 14034.
13. H. Pinto-Borges, O. Carvalho, B. Henriques, F. Silva, A. Ramos, J.C.M. Souza, A preliminary analysis of the wear pathways of sliding contacts on temporomandibular joint total joint replacement prostheses, *Metals* 11(5) (2021) 685.
14. C. Leiggner, S. Erni, L. Gallo, Novel approach to the study of jaw kinematics in an alloplastic TMJ reconstruction, *International Journal of Oral and Maxillofacial Surgery* 41(9) (2012) 1041-1045.
15. J.-P. Van Loon, C. Falkenström, L. De Bont, G. Verkerke, B. Stegenga, The theoretical optimal center of rotation for a temporomandibular joint prosthesis: a three-dimensional kinematic study, *Journal of dental research* 78(1) (1999) 43-48.
16. D. Perez, L. Perez, H. Mahgoub, N. Hernandez, Subjective and functional outcomes following TMJ reconstruction with custom-made total joint prostheses, *Journal of Oral and Maxillofacial Surgery* 72(9) (2014) e15.
17. S. Quan, L. Kaide, L. Lei, Progress of temporomandibular joint prosthesis, *West China Journal of Stomatology* 32(4) (2014) 422-425.
18. H. Pinto-Borges, O. Carvalho, B. Henriques, F. Silva, A. Ramos, J.C. Souza, A preliminary analysis of the wear pathways of sliding contacts on temporomandibular joint total joint replacement prostheses, *Metals* 11(5) (2021) 685.
19. H.T. Idogava, P.Y. Noritomi, G.B. Daniel, Numerical model proposed for a temporomandibular joint prosthesis based on the recovery of the healthy movement, *Computer Methods in Biomechanics and Biomedical Engineering* 21(8) (2018) 503-511.

Design transitions

20. M.J. Mirzaali, V. Moosabeiki, S.M. Rajaai, J. Zhou, A.A. Zadpoor, Additive manufacturing of biomaterials—Design principles and their implementation, *Materials* 15(15) (2022) 5457.
21. M.C. Saldívar, S. Salehi, R.P.E. Veeger, E. Tay, M. Fenu, A. Cantamessa, M. Klimopoulou, G. Talò, M. Moretti, S. Lopa, Rational positioning of 3D-printed voxels to realize high-fidelity multifunctional soft-hard interfaces, *Cell Reports Physical Science* 4(9) (2023).
22. M.J. Mirzaali, A. Herranz de la Nava, D. Gunashekar, M. Nouri-Goushki, R.P.E. Veeger, Q. Grossman, L. Angeloni, M.K. Ghatkesar, L.E. Fratila-Apachitei, D. Ruffoni, E.L. Doubrovski, A.A. Zadpoor, Mechanics of bioinspired functionally graded soft-hard composites made by multi-material 3D printing, *Composite Structures* 237 (2020) 111867.
23. M.J. Mirzaali, M. Cruz Saldívar, A. Herranz de la Nava, D. Gunashekar, M. Nouri-Goushki, E.L. Doubrovski, A.A. Zadpoor, Multi-Material 3D Printing of Functionally Graded Hierarchical Soft-Hard Composites, *Advanced Engineering Materials* 22(7) (2020) 1901142.
24. Y.X. Liu, S. Thomopoulos, V. Birman, J.S. Li, G.M. Genin, Bi-material attachment through a compliant interfacial system at the tendon-to-bone insertion site, *Mechanics of Materials* 44 (2012) 83-92.
25. G.M. Genin, A. Kent, V. Birman, B. Wopenka, J.D. Pasteris, P.J. Marquez, S. Thomopoulos, Functional grading of mineral and collagen in the attachment of tendon to bone, *Biophysical Journal* 97(4) (2009) 976-985.
26. A. Sola, D. Bellucci, V. Cannillo, Functionally graded materials for orthopedic applications—an update on design and manufacturing, *Biotechnology Advances* 34(5) (2016) 504-531.
27. M.C. Saldívar, E. Tay, A. Isaakidou, V. Moosabeiki, L.E. Fratila-Apachitei, E.L. Doubrovski, M.J. Mirzaali, A.A. Zadpoor, Bioinspired rational design of bi-material 3D printed soft-hard interfaces, *Nature Communications* 14(1) (2023) 7919.
28. L. Ren, Z. Wang, L. Ren, Z. Han, Q. Liu, Z. Song, Graded biological materials and additive manufacturing technologies for producing bioinspired graded materials: An overview, *Composites Part B: Engineering* 242 (2022) 110086.
29. P.M. Pandey, S. Rathee, M. Srivastava, P.K. Jain, *Functionally Graded Materials (FGMs): Fabrication, properties, Applications, and Advancements*, CRC Press 2021.
30. G. Knoppers, J. Gunnink, J. Van Den Hout, W. Van Vliet, The reality of functionally graded material products, *Proceedings of the 2004 International Solid Freeform Fabrication Symposium*, Austin, TX, August 2004, pp. 38-43.
31. S.K. Bohidar, R. Sharma, P.R. Mishra, Functionally graded materials: A critical review, *International Journal of Research* 1(4) (2014) 289-301.
32. M. Naebe, K. Shirvanimoghaddam, Functionally graded materials: A review of fabrication and properties, *Applied Materials Today* 5 (2016) 223-245.
33. S. Elleuch, H. Jrad, M. Wali, F. Dammak, Mandibular bone remodeling around osseointegrated functionally graded biomaterial implant using three dimensional finite element model, *International Journal for Numerical Methods in Biomedical Engineering* 39(9) (2023) e3750.
34. M.R. Ayatollahi, M.H. Davari, H.A. Shirazi, A. Asnafi, To Improve Total Knee Prostheses Performance Using Three-Phase Ceramic-Based Functionally Graded Biomaterials, *Frontiers in Materials* 6 (2019).
35. Jyoti, R. Ghosh, Printable functionally graded tibial implant for TAR: FE study comparing implant materials, FGM properties, and implant designs, *Computers in Biology and Medicine* 177 (2024) 108645.
36. H.S. Hedia, S.M. Aldousari, A.K. Abdellatif, N. Fouda, A new design of cemented stem using functionally graded materials (FGM), *Bio-Medical Materials and Engineering* 24 (2014) 1575-1588.
37. A. Najibi, T. Mokhtari, Functionally graded materials for knee and hip arthroplasty; an update on design, optimization, and manufacturing, *Composite Structures* 322 (2023) 117350.
38. M. Mehrali, F.S. Shirazi, M. Mehrali, H.S.C. Metselaar, N.A.B. Kadri, N.A.A. Osman, Dental implants from functionally graded materials, *Journal of Biomedical Materials Research Part A* 101(10) (2013) 3046-3057.
39. M. Pinheiro, A. Krairi, R. Willaert, M.C. Costa, W. Van Paepegem, Structural optimization of patient-specific temporomandibular joint replacement implants for additive manufacturing: novel metrics for

- safety evaluation and biomechanical performance, *Bio-Design and Manufacturing* 5(2) (2022) 333-347.
40. K. Szykiedans, W. Credo, Mechanical Properties of FDM and SLA Low-cost 3-D Prints, *Procedia Engineering* 136 (2016) 257-262.
 41. D. Lin, Q. Li, W. Li, M. Swain, Dental implant induced bone remodeling and associated algorithms, *Journal of the Mechanical Behavior of Biomedical Materials* 2(5) (2009) 410-432.
 42. G.M. Murray, I. Phanachet, S. Uchida, T. Whittle, The role of the human lateral pterygoid muscle in the control of horizontal jaw movements, *Journal of Oral & Facial Pain and Headache* 15(4) (2001) 279-92.
 43. S. Madhavan, M. Dhanraj, A.R. Jain, Methods of recording mandibular movements-A review, *Drug Invention Today* 10(7) (2018) 1254-1259.
 44. X. Xu, D. Luo, C. Guo, Q. Rong, A custom-made temporomandibular joint prosthesis for fabrication by selective laser melting: Finite element analysis, *Med Eng Phys* 46 (2017) 1-11.
 45. M. Oldhoff, M.J. Mirzaali, N. Tümer, J. Zhou, A. Zadpoor, Comparison in clinical performance of surgical guides for mandibular surgery and temporomandibular joint implants fabricated by additive manufacturing techniques, *Journal of the Mechanical Behavior of Biomedical Materials* 119 (2021) 104512.
 46. N. De Meurechy, A. Braem, M.Y. Mommaerts, Biomaterials in temporomandibular joint replacement: current status and future perspectives—a narrative review, *International Journal of Oral and Maxillofacial Surgery* 47(4) (2018) 518-533.
 47. R.J. McCoy, D.J. Psutka, *Alloplastic Temporomandibular Total Joint Replacement, Diagnosing and Managing Temporomandibular Joint Conditions*, Edited by Vladimir Machon (2024).
 48. M.C. Saldívar, E.L. Doubrovski, M.J. Mirzaali, A.A. Zadpoor, Nonlinear coarse-graining models for 3D printed multi-material biomimetic composites, *Additive Manufacturing* 58 (2022) 103062.
 49. F. Mirahmadi, J.H. Koolstra, F. Lobbezoo, G.H. van Lenthe, V. Everts, Ex vivo thickness measurement of cartilage covering the temporomandibular joint, *Journal of Biomechanics* 52 (2017) 165-168.
 50. A. Ramos, R.J. Duarte, M. Mesnard, Strain induced in the condyle by self-tapping screws in the Biomet alloplastic temporomandibular joint: a preliminary experimental study, *International Journal of Oral and Maxillofacial Surgery* 44(11) (2015) 1376-1382.
 51. A. van Kootwijk, V. Moosabeiki, M.C. Saldívar, H. Pahlavani, M.A. Leeftang, S. Kazemivand Niar, P. Pellikaan, B.P. Jonker, S.M. Ahmadi, E.B. Wolvius, N. Tümer, M.J. Mirzaali, J. Zhou, A.A. Zadpoor, Semi-automated digital workflow to design and evaluate patient-specific mandibular reconstruction implants, *Journal of the Mechanical Behavior of Biomedical Materials* 132 (2022) 105291.
 52. T.W.P. Korioto, A.G. Hannam, Deformation of the Human Mandible During Simulated Tooth Clenching, *Journal of Dental Research* 73(1) (1994) 56-66.

7

Additively manufactured shape-morphing implants for the treatment of acetabular defects

Acetabular defects pose significant challenges in orthopedic surgery, particularly in revision total hip arthroplasty (THA). Here, we design, additively manufacture, and evaluate shape-morphing porous implants with kinematic structures to address these defects. Three defect types were examined using synthetic hemipelvis models: posterior wall, cranial-posterior combination, and central-posterior defects. The implants were secured with screws and bone cement, and their surface conformity was assessed through micro computed tomography (μ CT). Biomechanical performance was evaluated under quasi-static compression and cyclic loading conditions. Results demonstrated excellent surface conformity of the flexible mesh across all defect types, with minimal differences from healthy acetabula (< 10 mm). The mesh implants exhibited strong load-bearing capacity, with failures occurring only in the pubic region of the hemipelvis, while both the implants and mesh-cement interfaces remained intact. The implants withstood cyclic loading simulating half the body weight of a 80 kg patient for more than 1,000,000 loading cycles with no evidence of fatigue failure, further confirming their durability. These findings suggest that the flexible mesh implant provides a reliable and adaptable solution for complex acetabular defects, offering anatomical conformity and mechanical stability, even in cases where conventional mesh grafts might be inadequate. Future studies, including cadaveric testing and clinical trials, are necessary to further validate these results in (pre-)clinical settings.

Moosabeiki, V., Leeflang, M.A., Gerbers, J.G., de Jong, P.H., Broekhuis, D., Agarwal, Y., Ganaesan, J.N., Kaptein, B.L., Nelissen, R.G.H.H., Mirzaali, M.J., Zadpoor, A.A., Additively manufactured shape-morphing implants for the treatment of acetabular defects, *Acta Biomaterialia*, Revised, 2025.

7.1 Introduction

Acetabular defects, involving structural damage or deformities in the acetabulum, pose significant challenges in orthopedic surgery. These defects can result from trauma, infection, or previous procedures like total hip arthroplasty (THA) [1, 2]. Addressing bone deficiency during revision THA is particularly challenging for surgeons, especially when managing severe acetabular deficiencies or performing complex primary hip replacements after post-infective or post-traumatic complications [3]. The primary goals of acetabular reconstruction are to achieve stable and durable fixation of the new socket, restore the center of rotation, and, where possible, rebuild bone stock [4, 5]. Effective management of these defects is essential to restore hip joint function and improve patient mobility [4, 6-12]. However, traditional approaches, including standard implants and grafting techniques, often fail to achieve precise anatomical fit and stable fixation, leading to less favorable outcomes and higher revision rates [13, 14].

Standard revision hardware (cups, shells, crosses, and augmentations) are generally designed to fit a wide range of patients but lack the necessary customization for unique anatomical variations. This often results in poor implant fit, instability, and increased wear, compromising surgical outcomes [15]. In response to these challenges, recent advancements in acetabular implant design, mainly through additive manufacturing (=3D printing) technology, have shown promise in managing complex acetabular defects [16-20]. Custom-made 3D printed acetabular components in THA have demonstrated encouraging results, especially in patients with severe bone defects [21-24]. Custom 3D printed triflange implants have also been evaluated for massive acetabular defects, both with and without pelvic discontinuity, resulting in high implant survivorship and significant functional improvements [5, 19, 24, 25]. Custom 3D printed implants have demonstrated excellent osseointegration and implant stability, particularly in complex revision surgeries, providing a reliable solution for challenging cases [5, 24, 26].

Despite the benefits, patient-specific implants present challenges. Although they offer superior anatomical conformity, they are often time-consuming and costly to produce [27, 28]. The manufacturing process requires extensive preoperative planning, detailed imaging, and modeling, which can delay surgery and increase overall treatment costs [27, 29]. Furthermore, the high cost of producing a unique implant for each patient may not be feasible in many healthcare settings, limiting their widespread adoption. Additionally, unlike bone impaction grafting (BIG) with mesh backing, patient-specific implants do not replenish bone stock, which is essential for long-term structural integrity and support [30].

Recent developments in shape-matching implants have sought to improve functional performance and production efficiency [27, 31] to overcome these limitations. One such innovation involves shape-morphing implants, which adapt to complex anatomical

geometries using advanced 3D and 4D printing techniques [32-36]. These implants conform to the patient's unique anatomy during surgery and lock into place, providing a customized fit without requiring extensive preoperative planning [37-39]. This approach blends the advantages of patient-specific and standard implants, offering a tailored fit and enhanced mechanical stability while reducing production time and costs. Shape-matching implants hold significant potential to advance orthopedic reconstruction by optimizing anatomical conformity and streamlining production processes. Additionally, they offer the possibility of expanding the use of bone impaction grafting (BIG) to address larger defects such as Paprosky IIIA and B.

We proposed the concept of "metallic clay", a design approach that enables medical devices, particularly orthopedic implants, to exhibit both shape-morphing and shape-locking capabilities [37]. Using this concept, this study aims to design and evaluate a 3D printed shape-morphing mesh implant with kinematic structures that combines the benefits of both standard and patient-specific implants. The kinematic mesh is designed as a generic implant capable of conforming to various patient anatomies, providing a patient-specific fit without the need for individualized manufacturing. This approach offers a versatile, cost-effective, and timely solution for managing acetabular defects.

The 3D printed flexible mesh implant was designed to adapt to the contours of the acetabulum and be effectively fixed using screws and bone cement. This design aimed to provide superior surface conformity and mechanical stability compared to conventional implants. To evaluate this approach, a series of experiments under physiologically relevant conditions were conducted using synthetic hemipelvis models with three distinct types of defects: a large posterior acetabular wall defect, a combination of cranial and posterior acetabular wall defects, and both central and posterior defects to replicate a Paprosky IIIB defect. These models simulated the surgical procedure and implant placement. Post-operative evaluations included CT scanning to assess mesh conformity to the acetabular surface and mechanical testing to evaluate the implants' biomechanical performance under quasi-static and cyclic loading.

This research addresses the critical need for innovative solutions in managing acetabular defects by leveraging 3D printing technology. By creating a flexible, generic implant capable of adapting to individual anatomical variations, we aimed to overcome the limitations of standard and patient-specific implants. The outcomes of this study have the potential to enhance clinical practice by providing a customizable, effective, and economically viable option for patients with complex acetabular defects.

7.2 Materials and methods

7.2.1 Implant design and manufacturing

The shape-morphing implant was designed using computer-aided design (CAD) software, SolidWorks 2023 (Dassault Systèmes, France), to conform to various acetabular geometries (Figures 7.1a and b). The design process involved creating a mesh structure with flexibility and strength suitable for anatomical adaptation and high enough load-bearing capacity. Specific design parameters such as strut length, strut thickness, tolerance, body size, and overall geometry were optimized to balance shape-morphing and mechanical stability (Figure 7.1b).

The mesh implants were 3D printed using plasma atomized Titanium alloy (Ti-6Al-4V ELI) powder (AP&C Inc, Canada), with particle sizes ranging from 10 to 45 μm . A high-resolution selective laser melting (SLM) 3D printer (ReaLizer SLM125, ReaLizer GmbH, Paderborn, Germany) was employed to manufacture the implants at the Additive Manufacturing Lab at Delft University of Technology. Considering the constraints of the additive manufacturing process, the implants were positioned in the supine orientation, ensuring that the functional surfaces of the joint could be printed concomitantly without requiring support structures. Additionally, the cross-sections of the rod end, connecting the spherical components, were designed in a rhombus shape to prevent warping. The specimens were fully functional after removing the build plate and completing ultrasonic cleaning.

7.2.2 Synthetic hemipelvis models

For this study, synthetic structurally calibrated hemipelvis models representing the left side of the pelvis, each with an acetabular diameter of 52 mm, were used to simulate realistic clinical scenarios and evaluate the performance of the 3D printed flexible mesh implants. The choice of synthetic models ensured consistency in experimental conditions and allowed for precise control over the defect types.

Three different types of defects were represented to cover a range of clinical situations, from moderate to severe acetabular defects (Figure 7.2). The first model simulated a posterior acetabular wall defect (Model 4122, Synbone AG, Switzerland). The second model featured a combination of cranial and posterior acetabular wall defects (Model 4123, Synbone AG, Switzerland), representing a more complex scenario involving extensive bone loss across multiple regions of the acetabulum. The third model was a modified healthy hemi-pelvis (Model 4032, Synbone AG, Switzerland) with central and posterior defects to replicate a Paprosky IIIB defect. Paprosky IIIB defects are characterized by substantial bone loss,

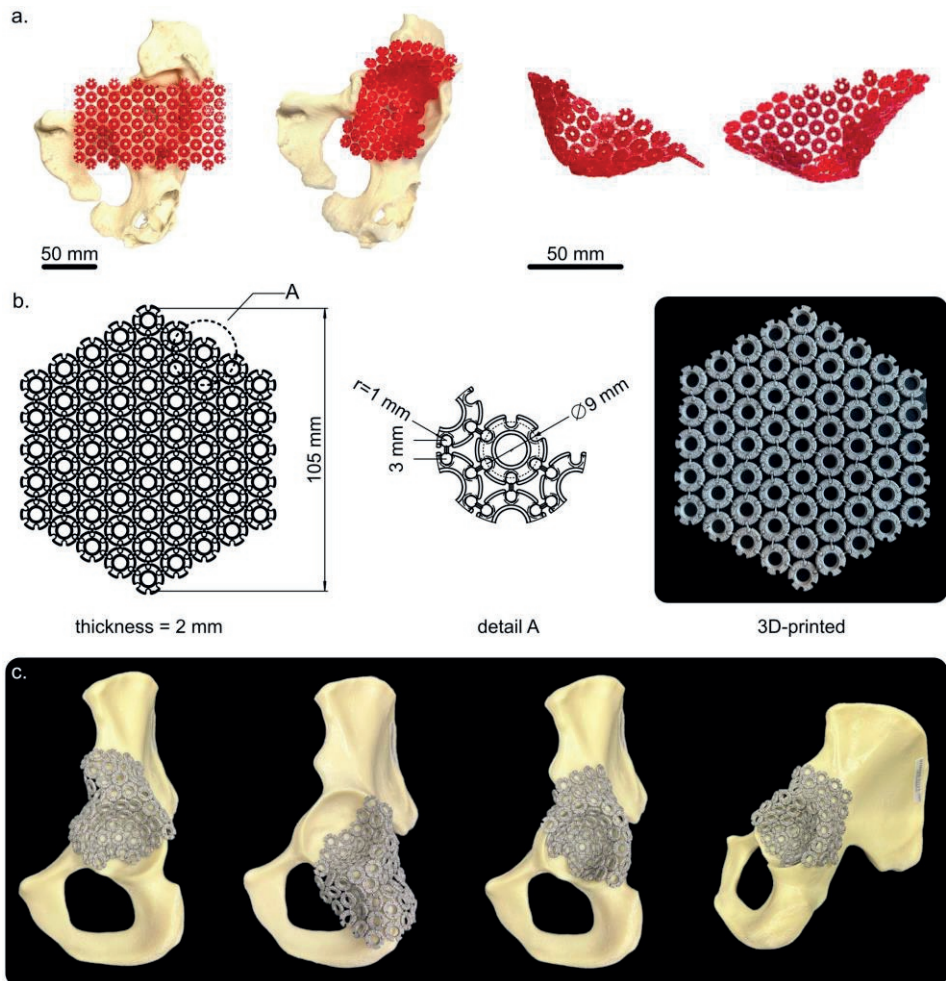


Figure 7.1. Design and application of the flexible mesh implant for acetabular reconstruction— (a) Perspective view of the flexible mesh illustrating its adaptability and conformity to the acetabular defect. The mesh was fabricated using PolyJet printing technology. (b) A detailed schematic drawing of the mesh design. The right panel shows a 3D printed version of the mesh structure. (c) The flexible mesh implant integrated into different regions of the acetabulum of synthetic pelvis models, demonstrating surface conformity and coverage.

compromising the structural integrity of the acetabulum and surrounding pelvic regions [10, 23]. These defects pose significant challenges in reconstruction due to the extensive nature of bone loss and the difficulty in achieving stable fixation.

7.2.3 Surgical implementation

An experienced hip surgeon (JGG) performed the simulated surgeries. The surgical procedure for implanting the flexible mesh involved securing the mesh to the acetabulum

of the synthetic hemipelvis models (Figure 7.2 and Supplementary Video 7.1). The acetabulum was prepared, and reamed using increasing size reamers to suitable depth (*i.e.*, final reamer size of 56 mm). To improve cement integration and ensure a secure fit, ten to fifteen holes were drilled to a depth of 5-10 mm within the acetabular surface. The mesh was then carefully positioned over the defect area to ensure optimal coverage and fit. Once positioned correctly, the mesh was fixed in place using titanium cortical screws (AO large fragment screws, Depuy Synthes, Switzerland) with a diameter of 4.5 mm. The length of the screws varied between 24 mm and 40 mm, depending on the specific anatomical requirements of each defect model. The acetabulum was then carefully cleaned to remove any loose debris.

Bone cement (Polymethyl methacrylate, PMMA, Optimac® 60 Refobacin® Bone Cement R, Zimmer Biomet, BIOMET France, France) was applied to the prepared acetabular surface. Since this was a synthetic model, no bone impaction was performed. The bone cement was introduced, followed by pressurization to ensure optimal distribution. Cup placement was simulated using a punch (46 mm in diameter), representing the size of a acetabular cup suitable for this reconstruction. Applying bone cement helped lock the mesh securely, providing additional mechanical support and ensuring the implant remained stable under load. After cement hardening the punch was retracted.

7.2.4 CT scanning and analysis

CT images were acquired using a TESCAN CorTOM CT scanner (TESCAN, Brno, Czech Republic), and the resulting images were analyzed and segmented using Dragonfly image processing software (version 2022.1.1249), applying Otsu method to optimize the thresholding for segmentation accuracy. Each specimen was scanned over a full 360° rotation, with an isotropic voxel size of 45 µm and an angular rotation step of 0.08°. The CT images were acquired under a voltage of 150 kV and a current of 300 µA, with each imaging cycle taking ~14 minutes to complete.

The shape-matching performance of the flexible mesh implants was assessed by comparing post-surgery CT scans of the reconstructed acetabulum for three different defect types (*i.e.*, posterior defect, a combination of posterior and cranial defects, and a combination of central and posterior defects) (Figure 7.3a), with a healthy, intact acetabulum model featuring a 52 mm femoral head.

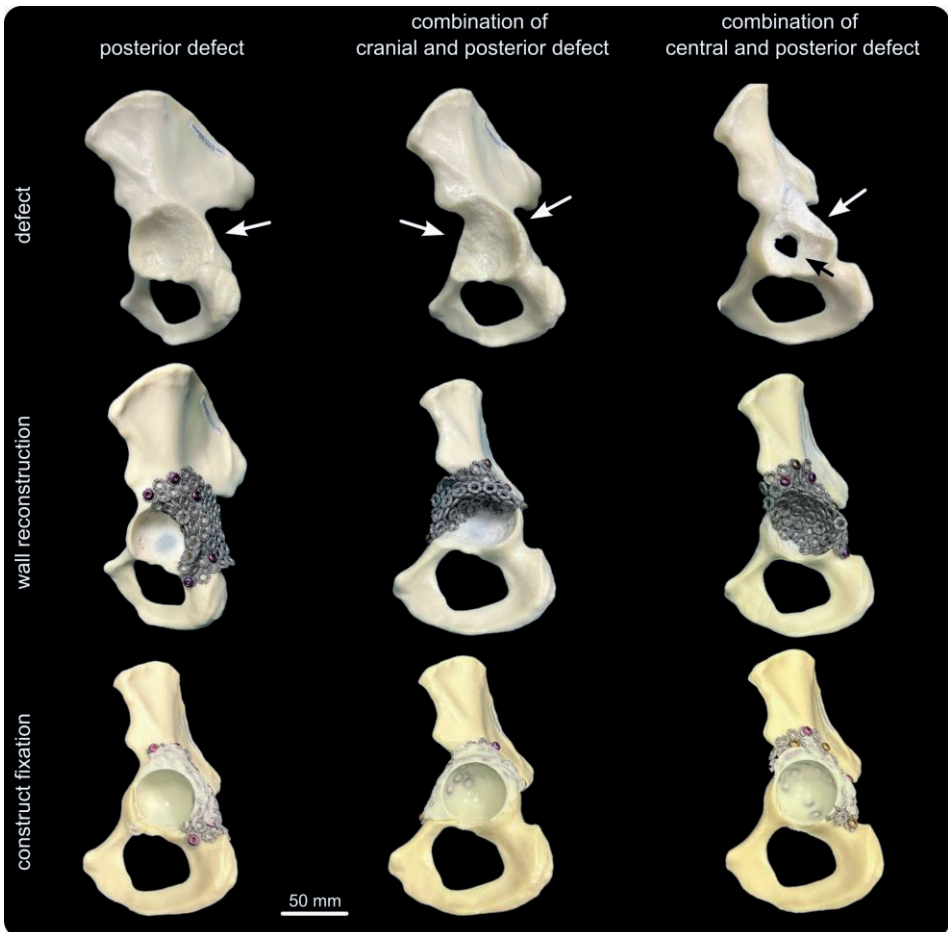


Figure 7.2. Reconstruction of acetabular defects using the shape-morphing mesh implant— The flexible mesh implant reconstructed three types of acetabular defects (posterior, cranial, posterior combination, and central and posterior combination). The top row shows the original defects (indicated by arrows), the middle row shows the mesh-based wall reconstruction, and the bottom row illustrates the final construct fixation with an acetabular cup.

To evaluate the surface conformity of the mesh implants to the acetabulum, the degree of conformity was quantified by measuring the distance between the implant and the bone surface of a healthy, intact hemipelvis model. CloudCompare software (V.2.9.1) was used to align the implanted hemipelvis with the healthy model, and the distance between the two surfaces was calculated (Figure 7.3b). In addition, a sphere-fitting method was applied by selecting 30 points within the acetabular cavity to determine the maximum size of a sphere that could be fitted into the reconstructed acetabulum (Figure 7.3c). This sphere-fitting process provided additional insights into the volumetric accuracy and fit of the implant within the acetabular structure.

7.2.5 Biomechanical testing

Biomechanical testing was carried out using 18 samples to evaluate the load-bearing capacity and durability of the implants. These samples were equally divided between quasi-static and cyclic loading tests, with three samples dedicated to each defect type. A custom setup (Synbone AG, Switzerland) was used for all the tests to ensure consistent positioning and alignment of the synthetic hemipelvis models. The hemipelvis models were secured at both the ilium and pubic regions, with the acetabular cavity oriented upward to facilitate uniaxial compression testing (Figure 7.4a). The vertical compressive load was applied directly onto the acetabulum, simulating the forces experienced during weight-bearing activities.

A mechanical testing machine (LLOYD Instrument LR5K, Hampshire, United Kingdom) equipped with a 5 kN load cell was employed for the quasi-static uniaxial compression tests. Each sample was compressed at a 1 mm/min rate, ensuring precise alignment and stability through the custom setup. Displacement, force, and time were continuously recorded at a sampling rate of 100 Hz. The tests were conducted until either the implant or hemipelvis failed or a vertical displacement of 30 mm was reached. A preload of 10 N was applied at the start of each test. For each sample, the maximum load, displacement, and failure modes were collected to assess the initial mechanical stability of the implants.

Cyclic compression-compression testing was performed using an electrodynamic mechanical testing machine (ElectroPulse™ E10000, Instron, MA, USA) with a 10 kN load cell. Each sample was subjected to cyclic loading at a frequency of 2 Hz, following two loading scenarios: an initial maximum load of 350 N, followed by a 25% increase to 437.5 N. A constant load ratio of 0.1 (*i.e.*, the ratio of minimum to maximum loads in each cycle) was applied, and each step consisted of 500,000 cycles (Figure 7.4e). Displacement, signs of fatigue failure, and implant migration were continuously monitored to evaluate the long-term durability of the mesh implants.

7.2.1 Statistical analysis

Statistical analysis was performed using OriginPro (2023, OriginLab Corporation, Northampton, MA, USA) to analyze the maximum difference between the reconstructed acetabulum and the healthy model, mechanical strength, and sphere-fitting data. Mean values and standard deviations were calculated to summarize the data. Due to the small sample size ($n=3$ per group), non-parametric tests (*i.e.*, Kruskal-Wallis test) were employed where appropriate, with a significance level of 0.05 used for comparisons. The results should be interpreted with caution, and future studies with larger sample sizes are recommended to validate these findings.

7.3 Results

7.3.1 Shape-matching performance

For the posterior defect, the shape-morphing implant demonstrated close conformity, with a maximum distance of 9.5 mm (± 0.6) from the healthy acetabulum. In the combination defect, where both cranial and posterior walls were compromised, the maximum distance was 10.1 mm (± 0.6), reflecting a comparable level of fit despite the increased complexity. The mesh exhibited the highest level of conformity for the central and posterior defect, with a maximum distance of 8.3 mm (± 1.3), indicating a more precise adaptation to the defect geometry (Figure 7.3b). In all cases, the maximum distances were observed at the edges of the acetabulum.

In addition to surface gap measurements, a sphere-fitting analysis was conducted to determine the maximum sphere size that could be accommodated within the reconstructed acetabulum for each defect type. For the posterior defect, the maximum sphere diameter was 50.3 mm (± 2.8), closely matching the capacity of the healthy acetabulum and closely approximating the capacity of the healthy acetabulum. The sphere size remained consistent at 50.4 mm (± 1.5) in the cranial and posterior combination defect. For the central and posterior defect, the sphere size was slightly reduced to 49.5 mm (± 0.7), indicating that the mesh restored a significant portion of the acetabular volume.

7.3.2 Biomechanical performance

Quasi-static uniaxial compression tests demonstrated that the pelvic constructs with flexible mesh implants could withstand substantial loads before failure. The mean maximum load capacities were 1890.9 N (± 112.3) for the posterior defect, 1501.6 N (± 142.5) for the cranial-posterior combination defect, and 1923.7 N (± 199.3) for the central-posterior defect. The corresponding stiffness values for the mesh-pelvis constructs were 239 N/mm (± 0.8) for the posterior defect, 237.8 N/mm (± 0.9) for the cranial-posterior combination defect, and 198 N/mm (± 0.2) for the central-posterior defect. Displacement at both the maximum load and the point of failure was consistent across all the specimens, indicating a uniform response to applied loading. Failure modes observed in all the tested specimens primarily involved fractures of the synthetic bone, specifically starting at the superior ramus of the pubis, followed by fractures at the pubic tubercle (Figure 7.4c).

a.

posterior defect

combination of
cranial and posterior defect

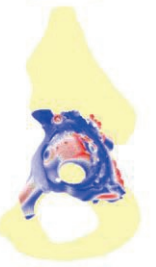
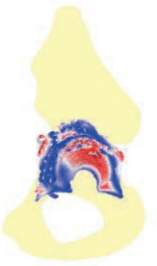
combination of
central and posterior defect



50 mm

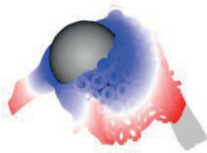
b.

distance from
healthy pelvis [mm]

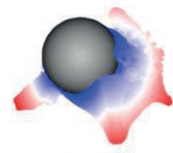


c.

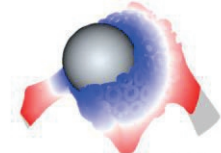
distance from
sphere [mm]



$D_{\text{sphere}} = 50.3 \text{ mm} \pm 2.8$



$D_{\text{sphere}} = 50.4 \text{ mm} \pm 1.5$



$D_{\text{sphere}} = 49.5 \text{ mm} \pm 0.7$

Figure 7.3. Shape-matching performance and sphere-fitting analysis of the shape-morphing mesh implants— (a) 3D reconstructions of the flexible mesh implants from μ CT images, fitted to the posterior, cranial-posterior, and central-posterior acetabular defects post-surgery. (b) The distance between each defect type's reconstructed acetabulum and the healthy pelvis. (c) A sphere-fitting analysis showing the maximum sphere diameter (D_{sphere}) that the reconstructed acetabulum for each defect type can accommodate.

The tests were extended to identify additional failure points and potentially weak areas within the pelvis-mesh construct. For both the posterior defect and the central and posterior defect, increased displacement revealed subsequent weak points at the screw locations, particularly those in the superior ischial ramus (Figure 7.4d-top). In contrast, for the combination defect, where no screws were positioned in the ischium, fractures occurred at the superior ischial ramus after the initial breakage at the pubis (Figure 7.4d-bottom). No cracks or visible changes were observed in the flexible mesh or the bone cement throughout the testing.

During cyclic testing, the mesh implants maintained their structural integrity under two loading phases, with maximum loads of 350 N and 437.5 N for up to 500,000 cycles per phase (*i.e.*, a total of $>1,000,000$ loading cycles). Displacement changes were minimal at each step, and no sign of implant migration, screw loosening, or crack on the bone cement was observed throughout the test cycles (Figure 7.4f).

7.4 Discussion

This study evaluated the effectiveness of a 3D printed shape-morphing implant designed with kinematic structures to address complex acetabular defects. The results demonstrated that the flexible mesh provided a high degree of anatomical conformity, mechanical stability, and adaptability, which are critical factors in the success of acetabular reconstruction [40, 41]. By focusing on three distinct defect types (*i.e.*, posterior wall, cranial-posterior combination, and central-posterior defects), the research provides comprehensive insights into the performance of the mesh in a range of clinically relevant scenarios.

The flexible nature of the mesh allowed it to conform closely to the irregular surfaces of the acetabulum (Figure 7.1c). Minimal differences were observed between the reconstructed and healthy acetabula, with maximum surface discrepancies of 9.5 mm (± 0.6) for the posterior defect, 10.1 mm (± 0.6) for the cranial-posterior combination defect, and 8.3 mm (± 1.3) for the central-posterior defect. The most significant discrepancies occurred at the acetabular edges, where the reconstructed wall was slightly higher than the natural acetabulum (Figure 7.3b). This additional height enhances the acetabular cup's support, improving overall stability. The other more significant discrepancies observed at the acetabulum corresponded to the defect regions, which were absent compared to the healthy acetabulum (Figure 7.3b).

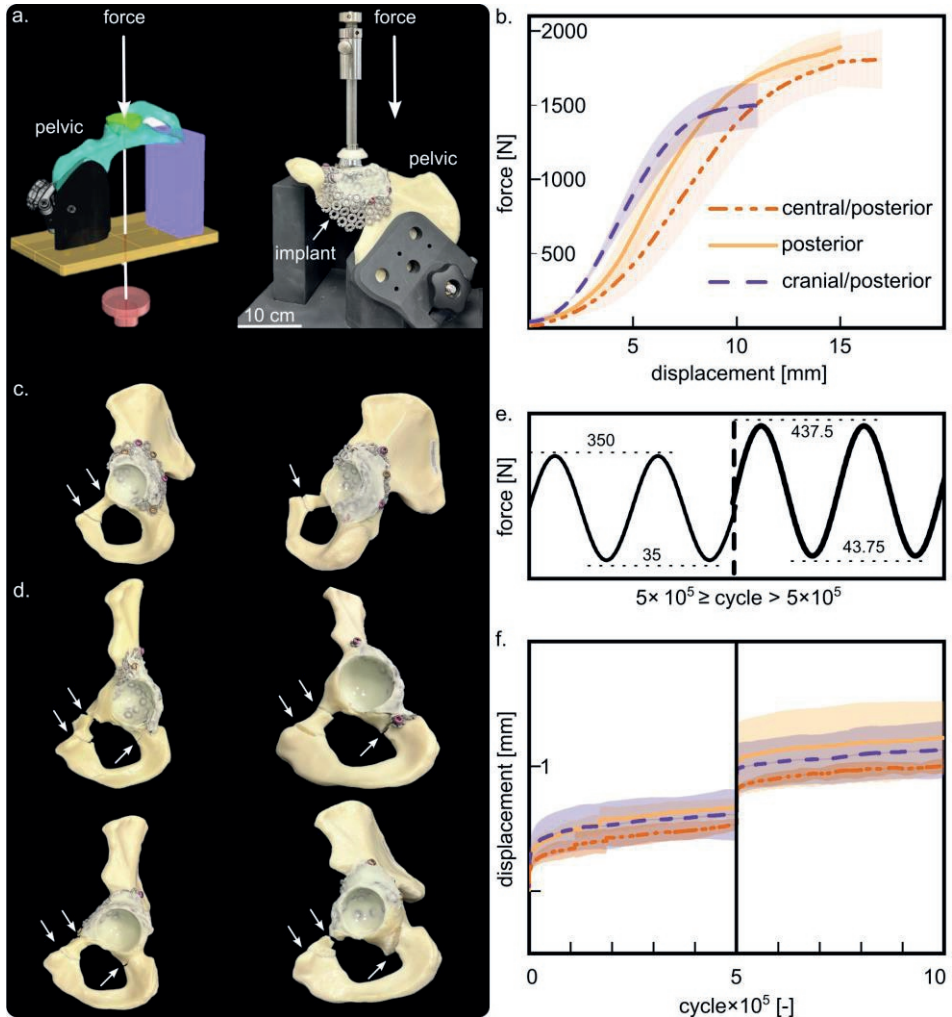


Figure 7.4. Biomechanical testing of shape-morphing implants for acetabular defects— (a) A schematic drawing and experimental setup for uniaxial compression testing of the synthetic hemipelvis models with flexible mesh implants. The compressive force was applied vertically to the acetabulum. (b) Force-displacement curves for the three acetabular defect types (central/posterior, posterior, and cranial/posterior) during quasi-static compression testing. (c) First observed failure points under compression testing, with fractures occurring in the pubic region while the mesh and bone cement remained intact. (d) After initial failure, compression testing was extended to observe further failure points. All the specimens exhibited subsequent fractures in the synthetic bone without damage to the mesh or cement interfaces. (e) The protocol for the cyclic testing of the mesh-pelvis constructs, which was conducted in two phases (each up to 500,000 cycles) with forces of 350 N and 437.5 N at a frequency of 2 Hz. (f) Results from the cyclic testing, represented by extension-cycle curves, highlighting the durability and long-term performance of the flexible mesh implants under repetitive loading conditions.

Additionally, the sphere-fitting analysis further confirmed the capacity of the mesh design to restore acetabular volume with near-identical sphere sizes compared to the healthy model (Figure 7.3c). However, no statistically significant difference was observed in sphere sizes between the defect groups. Similarly, there was no statistically significant difference in surface conformity between the different models. This level of shape-matching performance across varying defect types demonstrates the versatility of the mesh in adapting to different anatomical challenges while providing a secure and anatomically accurate fit. However, due to the volumetric effect of the mesh, selecting a slightly smaller cup is recommended to maintain an optimal cement layer thickness. These outcomes suggest that the flexible mesh can closely replicate the anatomical structure, which is vital for the long-term success of THA in patients with significant bone loss [45, 46].

The biomechanical tests indicated that the mesh implants could withstand high compressive loads, similar to the forces experienced in the hip joint (Figure 7.4b). Importantly, none of the samples failed at the mesh, cement, or mesh-cement interfaces. Instead, all failures occurred in the synthetic bone at the superior pubic ramus and pubic tubercle (Figure 7.4c). After the initial failure, the quasi-static tests were extended until a deflection of 30 mm, and subsequent failures consistently occurred in the pubic region of the synthetic bone, confirming that the mesh, cement, and mesh-cement interfaces remained intact throughout (Figure 7.4d). In the cranial-posterior defect, the presence of screws in the pubic region resulted in earlier fractures at this location, and this statistically significant difference in mechanical strength for the cranial-posterior defect was attributed to the use of screws in the pubic region. However, this occurred at the same location as the other defects, indicating that the mesh provided consistent performance across different anatomical scenarios.

Cyclic loading tests further validated the durability of the mesh implants, revealing minimal performance degradation over time. After 1,000,000 cycles (equivalent to the approximate number of cycles experienced by active patients in one year [47]), no signs of fatigue failure, screw loosening, or cement cracking were observed. Conducted at two loading levels (350 N and 437.5 N), the tests demonstrated that the mesh implants maintained their structural integrity under conditions that simulate long-term, repetitive loading in the hip joint.

In cases like Paprosky type IIIB defects, acetabular fixation is particularly challenging due to the lack of superior dome support and proximal migration of the acetabular component [41]. Studies have demonstrated that using a hemispherical porous-coated component alone often leads to failure in these scenarios, primarily due to micro-motion and superolateral migration, especially when structural grafts or augmentations are not employed [48, 49]. The standard BIG with mesh technique is unsuitable for type IIIB defects and is likely to have higher failure rates in type IIIA reconstructions [30].

Design for morphing

The flexible mesh used in this study addresses these limitations by improving both conformity and stability. However, successful reconstruction still requires bone grafts, particularly in complex defects where restoring bone stock is crucial for long-term success [4, 46, 50].

A significant advantage of the flexible mesh design is its ability to accommodate bone grafts during surgery (Supplementary Video 7.1). The mesh allows easy manipulation, enabling precise placement within the defect while incorporating bone graft material beneath and between the mesh layers. This flexibility promotes better graft integration with surrounding tissue, enhancing long-term mechanical support and stability. During surgery, the mesh facilitates free movement, allowing for accurate positioning and even distribution of the bone graft, further improving osseointegration.

Compared to conventional acetabular wire mesh (commonly called “chicken wire”) [51, 52], our flexible mesh design may significantly improve anatomical conformity, mechanical stability, and overall surgical outcomes. Traditional wire mesh, rigid and manually shaped during surgery, often struggle to conform precisely to the complex geometry of acetabular defects, leading to uneven load distribution and gaps between the mesh and bone. In contrast, our flexible mesh is designed to conform more naturally to the defect, potentially improving fit and stability. Additionally, the flexibility of our mesh allows for the accommodation of more bone graft material even after the initial fixation of the mesh, promoting better graft integration and long-term stability (Supplementary Video 7.1). This adaptability could enhance osseointegration and structural support in large or complex defects where conventional wire mesh may fall short.

The ability of our flexible mesh implants to conform to different acetabular geometries and provide stable fixation has significant clinical implications. While severe defects, such as those we addressed in this study, typically require patient-specific meshes due to their complexity, our flexible mesh effectively covered these defects without requiring individualized manufacturing. This adaptability allows surgeons to use these implants in a broader range of patients, reducing the necessity for custom solutions and decreasing surgical wait times and overall treatment costs [5, 53]. Future studies could enhance implant performance by exploring diverse network geometries and incorporating variable strut lengths within the structure. These adjustments could improve anatomical conformity and optimize load distribution, allowing the implants to better align with individual anatomical curvatures.

Despite the promising results, our study has limitations. The evaluation was conducted on synthetic hemipelvis models, which, while useful for controlled testing, do not fully replicate the complexities of the human bone. Notably, synthetic bone lacks cancellous bone, critical in integrating bone cement. In real-world scenarios, proper integration with cancellous bone can significantly enhance implant stability, a factor not represented in our study. Further research using cadaveric models and clinical trials is

necessary to further validate these findings and assess the added stability provided by bone-cement integration.

This study also focused on a single loading scenario during mechanical testing. Future research should consider various loading conditions that simulate the dynamic forces experienced in the hip joint during daily activities such as walking and running to evaluate the flexible mesh implants' performance fully. Moreover, the long-term in vivo performance of the shape-morphing implants was not assessed. Future research should also focus on the biocompatibility and durability of the implants over extended periods in living subjects.

7.5 Conclusions

This study successfully designed and evaluated 3D printed shape-morphing implants with kinematic structures for managing acetabular defects. The flexible mesh implants demonstrated excellent surface conformity and robust mechanical stability, adapting closely to the acetabulum and withstanding significant compressive loads. This flexible mesh offers improved adaptability and reduced need for extensive bone preparation, addressing critical limitations of standard and custom implants. The 3D printed flexible mesh implants offer a cost-effective and efficient solution for acetabular defects, potentially significantly improving clinical outcomes in orthopedic reconstruction surgeries. Further research and clinical validation are essential to realize this innovative design's benefits fully.

7.6 Supplementary material

Supplementary Video 1. The surgical procedure for treating an acetabular defect using the flexible mesh implant. The procedure includes acetabular reaming, mesh implantation, and bone cementing.

Bibliography

1. M. Baauw, M.L. van Hooff, M. Spruit, Current Construct Options for Revision of Large Acetabular Defects: A Systematic Review, *JBJS Reviews* 4(11) (2016) e2.
2. F. Mancino, G. Cacciola, V. Di Matteo, D. De Marco, A. Greenberg, C. Perisano, M. Ma, P.K. Sculco, G. Maccauro, I. De Martino, Reconstruction options and outcomes for acetabular bone loss in revision hip arthroplasty, (2035-8237 (Print)).
3. A.G. Chen, Total Hip Arthroplasty in Young Patients, The University of Western Ontario (Canada), 2022.
4. W.Y. Shon, S.S. Santhanam, J.W. Choi, Acetabular Reconstruction in Total Hip Arthroplasty, (2287-3260 (Print)).
5. D. Broekhuis, W.M.H. Meurs, B.L. Kaptein, S. Karunaratne, R.L. Carey Smith, S. Sommerville, R. Boyle, R.G.H.H. Nelissen, High accuracy of positioning custom triflange acetabular components in tumour and total hip arthroplasty revision surgery, *Bone & Joint Open* 5(4) (2024) 260-268.
6. J.A. Shaw, A. Bailey Jh Fau - Bruno, R.B. Bruno A Fau - Greer, 3rd, R.B. Greer, 3rd, Threaded acetabular components for primary and revision total hip arthroplasty, (0883-5403 (Print)).
7. P.K. Sculco, T. Wright, M.A. Malahias, A. Gu, M. Bostrom, F. Haddad, S. Jerabek, M. Bolognesi, T. Fehring, A. Gonzalez DellaValle, W. Jiranek, W. Walter, W. Paprosky, D. Garbuz, T. Sculco, The Diagnosis and Treatment of Acetabular Bone Loss in Revision Hip Arthroplasty: An International Consensus Symposium, (1556-3316 (Print)).
8. D.G. Allan, A. Bell Rs Fau - Davis, F. Davis A Fau - Langer, F. Langer, Complex acetabular reconstruction for metastatic tumor, (0883-5403 (Print)).
9. B.N. Trumm, S.S. Callaghan Jj Fau - Liu, D.D. Liu Ss Fau - Goetz, R.C. Goetz Dd Fau - Johnston, R.C. Johnston, Revision with cementless acetabular components: a concise follow-up, at a minimum of twenty years, of previous reports, (1535-1386 (Electronic)).
10. C.L. Sheth Np Fau - Nelson, B.D. Nelson Cl Fau - Springer, T.K. Springer Bd Fau - Fehring, W.G. Fehring Tk Fau - Paprosky, W.G. Paprosky, Acetabular bone loss in revision total hip arthroplasty: evaluation and management, (1067-151X (Print)).
11. B.T. Barlow, G.H. McLawhorn As Fau - Westrich, G.H. Westrich, The Cost-Effectiveness of Dual Mobility Implants for Primary Total Hip Arthroplasty: A Computer-Based Cost-Utility Model, (1535-1386 (Electronic)).
12. S.G. Brouwer de Koning, N. de Winter, V. Moosabeiki, M.J. Mirzaali, A. Berenschot, M.M.E.H. Witbreuk, V. Lagerburg, Design considerations for patient-specific bone fixation plates: a literature review, *Medical & Biological Engineering & Computing* 61(12) (2023) 3233-3252.
13. M.D. Ries, Reconstruction and Management Options for Acetabular Bone Loss, *Fundamentals of Revision Hip Arthroplasty*, CRC Press 2024, pp. 91-101.
14. P.S. Issack, M. Nousiainen, B. Beksac, D.L. Helfet, T.P. Sculco, R.L. Buly, Acetabular component revision in total hip arthroplasty. Part II: management of major bone loss and pelvic discontinuity, *Am J Orthop (Belle Mead NJ)* 38(11) (2009) 550-556.
15. J.-A. Lee, Y.-G. Koh, K.-T. Kang, Biomechanical and Clinical Effect of Patient-Specific or Customized Knee Implants: A Review, *Journal of Clinical Medicine* 9(5) (2020) 1559.
16. L. Dall'Ava, H. Hothi, A. Di Laura, J. Henckel, A. Hart, 3D printed acetabular cups for total hip arthroplasty: a review article, *Metals* 9(7) (2019) 729.
17. S.-H. Woo, M.-J. Sung, K.-S. Park, T.-R. Yoon, Three-dimensional-printing technology in hip and pelvic surgery: current landscape, *Hip & pelvis* 32(1) (2020) 1-10.
18. O. Okolie, I. Stachurek, B. Kandasubramanian, J. Njuguna, 3D printing for hip implant applications: a review, *Polymers* 12(11) (2020) 2682.
19. V. Goriainov, L.J. King, R.O. Oreffo, D.G. Dunlop, Custom 3D-printed triflange implants for treatment of severe acetabular defects, with and without pelvic discontinuity: early results of our first 19 consecutive cases, *JBJS Open Access* 6(4) (2021) e21.
20. A. Taninaka, T. Kabata, Y. Kajino, D. Inoue, T. Ohmori, Y. Yamamuro, T. Kataoka, Y. Saiki, Y. Yanagi, M. Ima, Accurate implant placement in THA using Three-dimensional printed custom-made acetabular component for massive defects, *Proceedings of The 22nd Annual*

- Meeting of the Interna, 2024, pp. 110-114.
21. S. Fang, Y. Wang, P. Xu, J. Zhu, J. Liu, H. Li, X. Sun, Three-dimensional-printed titanium implants for severe acetabular bone defects in revision hip arthroplasty: short-and mid-term results, *International orthopaedics* 46(6) (2022) 1289-1297.
 22. Z. Li, Y. Luo, M. Lu, Y. Wang, T. Gong, X. Hu, X. He, Y. Zhou, L. Min, C. Tu, 3D-printed Personalized Porous Acetabular Component to Reconstruct Extensive Acetabular Bone Defects in Primary Hip Arthroplasty, *Orthopaedic Surgery* (2024).
 23. C. Xiao, S. Zhang, Z. Gao, C. Tu, Custom-made 3D-printed porous metal acetabular composite component in revision hip arthroplasty with Paprosky type III acetabular defects: A case report, *Technology and Health Care* 31(1) (2023) 283-291.
 24. S. Callary, J. Barends, L.B. Solomon, R. Nelissen, D. Broekhuis, B. Kaptein, Virtual biomechanical assessment of custom triflange and trabecular metal components to treat large acetabular defects, *Orthopaedic Proceedings* 105-B(SUPP_12) (2023) 6-6.
 25. S.J. Lee, J.J. Shea, Acetabular apparatuses for hip revision surgery, Google Patents, 2023.
 26. A.A.-O. Di Laura, J. Henckel, A. Hart, Custom 3D-Printed Implants for Acetabular Reconstruction: Intermediate-Term Functional and Radiographic Results. LID - 10.2106/JBJS.OA.22.00120 [doi. LID - e22.00120, (2472-7245 (Electronic))].
 - [27. A.A. Zadpoor, Design for Additive Bio-Manufacturing: From Patient-Specific Medical Devices to Rationally Designed Meta-Biomaterials, *International Journal of Molecular Sciences*, 2017.
 - [28. A. van Kootwijk, V. Moosabeiki, M.C. Saldivar, H. Pahlavani, M.A. Leeflang, S. Kazemivand Niar, P. Pellikaan, B.P. Jonker, S.M. Ahmadi, E.B. Wolvius, N. Tümer, M.J. Mirzaali, J. Zhou, A.A. Zadpoor, Semi-automated digital workflow to design and evaluate patient-specific mandibular reconstruction implants, *Journal of the Mechanical Behavior of Biomedical Materials* 132 (2022) 105291.
 29. V. Moosabeiki, N. de Winter, M. Cruz Saldivar, M.A. Leeflang, M.M.E.H. Witbreuk, V. Lagerburg, M.J. Mirzaali, A.A. Zadpoor, 3D printed patient-specific fixation plates for the treatment of slipped capital femoral epiphysis: Topology optimization vs. conventional design, *Journal of the Mechanical Behavior of Biomedical Materials* 148 (2023) 106173.
 30. M.-A. Malahias, F. Mancino, A. Gu, M. Adriani, I. De Martino, F. Boettner, P.K. Sculco, Acetabular impaction grafting with mesh for acetabular bone defects: a systematic review, *HIP International* 32(2) (2022) 185-196.
 31. M.J. Mirzaali, V. Moosabeiki, S.M. Rajaai, J. Zhou, A.A. Zadpoor, Additive Manufacturing of Biomaterials—Design Principles and Their Implementation, *Materials*, 2022.
 32. M.A. Leeflang, F.S.L. Bobbert, A.A. Zadpoor, Additive manufacturing of non-assembly deployable mechanisms for the treatment of large bony defects, *Additive Manufacturing* 46 (2021) 102194.
 33. T. van Manen, S. Janbaz, K.M.B. Jansen, A.A. Zadpoor, 4D printing of reconfigurable metamaterials and devices, *Communications Materials* 2(1) (2021) 56.
 34. V. Moosabeiki, E. Yarali, A. Ghalayaniesfahani, S.J.P. Callens, T. van Manen, A. Accardo, S. Ghodrat, J. Bico, M. Habibi, M.J. Mirzaali, A.A. Zadpoor, Curvature tuning through defect-based 4D printing, *Communications Materials* 5(1) (2024) 10.
 35. F.S.L. Bobbert, S. Janbaz, T. van Manen, Y. Li, A.A. Zadpoor, Russian doll deployable meta-implants: Fusion of kirigami, origami, and multi-stability, *Materials & Design* 191 (2020) 108624.
 36. P.H. de Jong, A.L. Schwab, M.J. Mirzaali, A.A. Zadpoor, A multibody kinematic system approach for the design of shape-morphing mechanism-based metamaterials, *Communications Materials* 4(1) (2023) 83.
 37. S. Leeflang, S. Janbaz, A.A. Zadpoor, Metallic clay, *Additive Manufacturing* 28 (2019) 528-534.
 38. P.H. de Jong, Y. Salvatori, F. Libonati, M.J. Mirzaali, A.A. Zadpoor, Shape-locking in architected materials through 3D printed magnetically activated joints, *Materials & Design* 235 (2023) 112427.
 39. F.S.L. Bobbert, S. Janbaz, A.A. Zadpoor, Towards deployable meta-implants, *Journal of Materials Chemistry B* 6(21) (2018) 3449-3455.
 40. G.W. Fryhofer, S. Ramesh, N.P. Sheth, Acetabular reconstruction in revision total hip

- arthroplasty, *Journal of Clinical Orthopaedics and Trauma* 11(1) (2020) 22-28.
41. A.Q. Ahmad, R. Schwarzkopf, Clinical evaluation and surgical options in acetabular reconstruction: A literature review, *Journal of Orthopaedics* 12 (2015) S238-S243.
 42. J. Thanner, The acetabular component in total hip arthroplasty: evaluation of different fixation principles, *Acta Orthopaedica Scandinavica* 70(sup286) (1999) i-41.
 43. P.K. Sculco, T. Wright, M.-A. Malahias, A. Gu, M. Bostrom, F. Haddad, S. Jerabek, M. Bolognesi, T. Fehring, A. Gonzalez DellaValle, The diagnosis and treatment of acetabular bone loss in revision hip arthroplasty: an international consensus symposium, *HSS Journal* 18(1) (2022) 8-41.
 44. P.C. Krause, J.L. Braud, J.M. Whatley, Total hip arthroplasty after previous fracture surgery, *Orthopedic Clinics* 46(2) (2015) 193-213.
 45. F.S. Fröschen, T.M. Randau, G.T.R. Hischebeth, N. Gravius, S. Gravius, S.G. Walter, Mid-term results after revision total hip arthroplasty with custom-made acetabular implants in patients with Paprosky III acetabular bone loss, *Archives of Orthopaedic and Trauma Surgery* 140(2) (2020) 263-273.
 46. F. Mancino, G. Cacciola, V. Di Matteo, D. De Marco, A. Greenberg, C. Perisano, M. Malahias, P.K. Sculco, G. Maccauro, I. De Martino, Reconstruction options and outcomes for acetabular bone loss in revision hip arthroplasty, *Orthopedic reviews* 12(Suppl 1) (2020).
 47. M. Morlock, E. Schneider, A. Bluhm, M. Vollmer, G. Bergmann, V. Müller, M. Honl, Duration and frequency of every day activities in total hip patients, *Journal of Biomechanics* 34(7) (2001) 873-881.
 48. S. Avcı, N. Connors, W. Petty, 2-to 10-year follow-up study of acetabular revisions using allograft bone to repair bone defects, *The Journal of arthroplasty* 13(1) (1998) 61-69.
 49. M. Jasty, W.H. Harris, Total hip reconstruction using frozen femoral head allografts in patients with acetabular bone loss, *Orthopedic Clinics of North America* 18(2) (1987) 291-299.
 50. E. Garcia-Rey, L. Saldaña, E. Garcia-Cimbrelo, Impaction bone grafting in hip re-revision surgery: bone stock restoration and radiological migration of the acetabular component, *The Bone & Joint Journal* 103(3) (2021) 492-499.
 51. Y.-Y. Lian, F.-X. Pei, J.-Q. Cheng, W. Feng, H. Zhang, Reconstruction of acetabular defect with wire mesh and impacted bone graft in cemented acetabular revision., *Zhonghua Yi Xue Za Zhi* 87(23) (2007) 1603-1606.
 52. W.H. Harris, W.N. Jones, The Use of Wire Mesh in Total Hip Replacement Surgery, *Clinical Orthopaedics and Related Research* 106 (1975).
 53. B.T. Barlow, A.S. McLawhorn, G.H. Westrich, The Cost-Effectiveness of Dual Mobility Implants for Primary Total Hip Arthroplasty: A Computer-Based Cost-Utility Model, *JBJS* 99(9) (2017).

Curvature tuning through defect-based 4D printing

Emerging 4D printing techniques have enabled the realization of smart materials whose shape or properties can change with time. Two important phenomena play important roles in the 4D printing of shape memory polymeric materials. First, the anisotropic deformation of the printed filaments due to residual stresses can be harnessed to create out-of-plane shape transformations. Second, the unavoidable formation of micro-defects during the printing processes often affects the programmability of the printed object. Here, we propose a design approach that harnesses these two effects occurring during fused deposition modeling to create tailor-made curved geometries from initially 2D flat disks. We first determined the size and distribution of the imperfections formed within printed structures by varying two printing parameters namely the printing speed and the number of printed materials. Spatially varying the printing speed and combining polylactic acid filaments with a softer material without shape memory properties allowed us to cover a variety of shapes from negative to positive values of the mean and Gaussian curvature. We propose an analytical model to calculate the magnitude of the maximum out-of-plane deformation from the anisotropic expansion factor of the constituting microstructures. Furthermore, we develop computational models to predict the complex shape-changing of thermally actuated 4D printed structures given the distribution of rationally introduced imperfections and we demonstrate the potential applications of such defect-based metamaterials in drug delivery systems.

8.1 Introduction

Shape-changing phenomena frequently occur in our everyday life: a flat leaf curls after falling from a tree due to drying, or a thin slice of fresh wood undergoes an irreversible shape transformation from a flat state into a dome-like shape due to a drying process [1, 2] (Figure 8.1a). More often than not, however, shape-shifting in nature is a reversible dynamic process and follows differential growth morphogenesis patterns [3, 4]. Examples are cuttlefish [5], squids [6], and Bauhinia pods [7] whose complex biological microstructures enable them to adapt their body shape, stiffness, and behavior to create elaborate shape changes, once triggered by external stimuli. Mimicking natural shape-shifting principles [8] has led to the emergence of a new class of engineered materials with tailor-made shape-morphing capabilities that have numerous applications in soft matter (*e.g.*, soft actuators [9] and soft robotics [10]), programmable materials (*e.g.*, mechanical metamaterials [11-16] and reconfigurable materials [17, 18]), and medical devices (*e.g.*, drug delivery vehicles [19] and microfluidic systems [20]).

Successful spatiotemporal planning of an arbitrary shape morphing behavior depends on two main factors. First, one needs to select the proper type of actuation (*e.g.*, thermal, light, electromagnetic, swelling, or pH) and stimuli-responsive material (*e.g.*, shape memory polymers [21, 22], magneto-rheological elastomers [23, 24], liquid crystal polymers [25], or hydrogels [26, 27]). Second, the microscale geometry of the involved materials should be rationally designed to achieve local deformations that collectively give rise to the desired global shape-shifting behavior [21, 28, 29]. Several approaches based on origami [30, 31] and kirigami [32-34] as well as a number of theoretical models [35, 36]) have been proposed in the past for the rational and predictable design of such shape-shifting behaviors.

The emergence of additive manufacturing in general and multi-material 3D printing, in particular, has provided unparalleled opportunities to fabricate 4D printed structures with complex shape morphing capabilities. Among different 3D printing technologies, fused deposition modeling (FDM) is one of the most widely available technologies that has been used for the fabrication of 4D printed structures [37, 38]. Tuning the printing parameters, such as the bed temperature, nozzle temperature, printing speed, and printing patterns, is shown to be an easy yet effective way to control the final shape of the 4D printed structures. From a microstructural viewpoint, these different parameters have two impacts: influencing the residual stresses stored in the polymeric material and affecting the level of fusion and bonding between individual filament strands or between the consecutive layers making up the printed structure. Residual stress, which is in general undesired, is related to the elongation of polymeric molecules along the printing direction during their extrusion through the printer nozzle and is a result of the quick solidification of the filament in its elongated state. If the printed material is brought to a temperature

close to its glass transition temperature (T_g), polymeric molecules tend to relax by creep, leading to an in-plane contraction of the material in the direction of the filament. Because of this anisotropic deformation, initially flat structures can adopt a 3D doubly curved shape [21, 28, 39, 40]. In mathematical terms, metric distortions induce a change of the Gaussian curvature. However, if this relaxation is not uniform across the thickness, the structure also tends to bend due to the classical Timoshenko bilayer effect [41]. In addition to residual stresses, printing parameters dictate the quality of the bonding between adjacent filament strands. Poor bonding between filaments or layers may create undesired local imperfections that modify the local mechanical properties and, thus, the direction of (local) deformations. These imperfections can, consequently, cause arbitrary shape transformations under external stimuli. However, little is known about the exact formation mechanisms of such local micro-scale imperfections and how their morphological features (*e.g.*, size and distribution) can be linked to the printing parameters. Moreover, such printing imperfections have been primarily seen as undesired, leading to their potential as a design tool for shape transformation remaining unexploited. It is, therefore, unclear how such imperfections in addition to residual stresses can be harvested as a design tool to create complex yet fully predictable and controllable shape transformations. Here, we turn the tables around by proposing to see imperfections and residual stresses distribution not as a threat to the success of 4D printing but rather as a design tool.

To put this in the context of the available literature, several studies have established that different types of curvatures can be achieved by modifying the geometrical design of the 4D printed object (*e.g.*, layer thickness), through the use of multi-layer materials, as well as by introducing specific rationally designed printing patterns [42-44]. Local curvature tuning can also be accomplished by using multiple types of materials and by incorporating multiple stimuli [43, 45]. However, the currently existing techniques impose serious limitations regarding the specimen design, specimen dimensions, and printing patterns. As main contributions of the current study, we propose an approach based on the synergistic effect of micro-scale imperfections and stress relaxation for introducing programmed shape transformations into the fabrication of 4D printed materials. The rational introduction of micro-scale imperfections has the advantage that it does not impose too many constraints regarding the geometry, material/layer composition, and printing patterns of 4D printed objects.

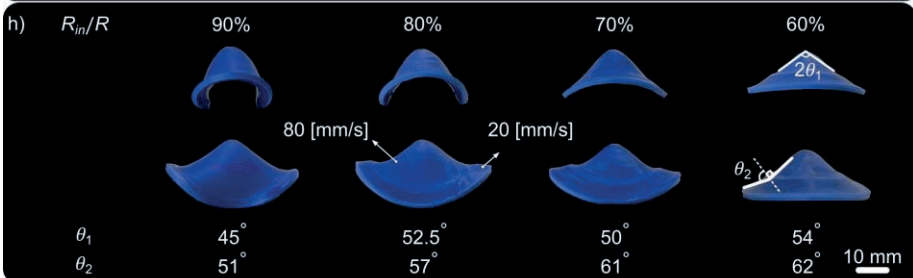
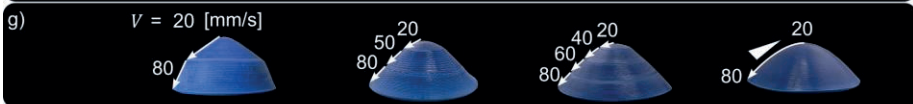
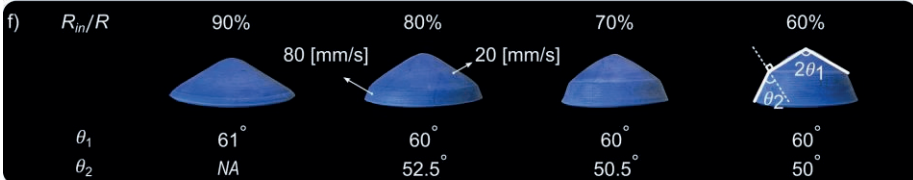
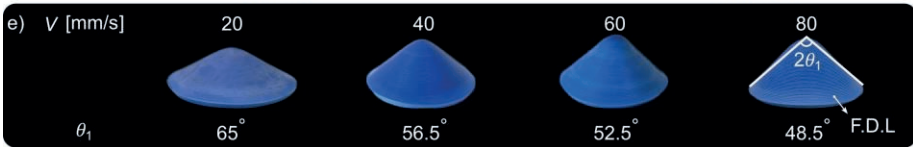
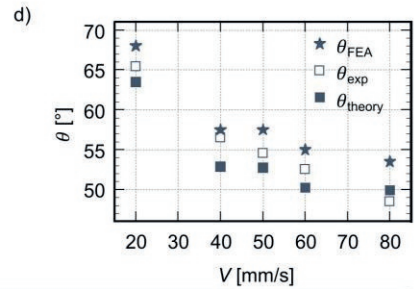
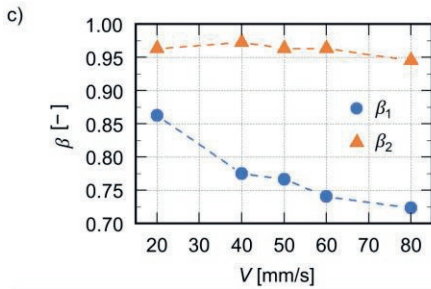
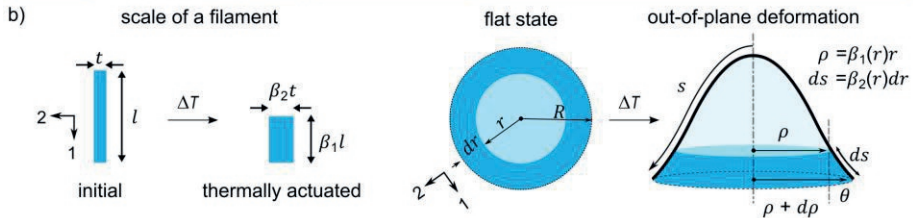
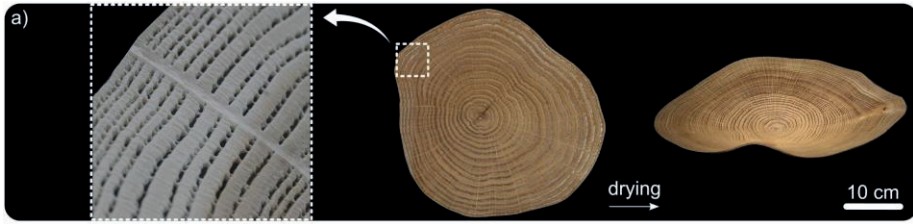


Figure 8.1. Shape-Shifting phenomena in nature and 4D printed disks— Shape-shifting frequently occurs in nature because of drying processes and material shrinkage. A freshly cut slice of wood, with its orthotropic mechanical properties [62], transforms from a flat state into a dome-like shape upon drying [1, 2] (a). Similar out-of-plane shape transformations take place when a 4D printed disk made of shape memory polymers is exposed to high temperatures (b). Based on the empirical Equation (8.2), the out-of-plane deformation of the disk and the resulting cone angle depend on the equivalent lateral and longitudinal expansion factors (β_1 and β_2) (c). By changing the printing speed, one can adjust the equivalent longitudinal and transverse expansion factors and, thus, the deformation angle (θ) (d). The angles calculated from the empirical Equation (8.2) for different printing speeds were compared to experimental and numerical results (d). We 4D printed disks with various printing speeds, including a constant printing speed (e), a step-wise printing speed in which the inner part of the disk was printed at a speed of 20 mm s^{-1} while the outer part was printed at 80 mm s^{-1} (f), a gradually increasing the printing speed from 20 mm s^{-1} at the center to 80 at the peripheral edge of the disk (g), and a step-wise printing speed in which the inner part of the disk was printed with a speed of 80 mm s^{-1} while the outer was printed at 20 mm s^{-1} (h). The surfaces shown in (e–h) are the first deposited layers (F.D.L).

This further expands the space of achievable shape transformations and makes the approach applicable to a wider range of materials, microarchitectural designs, and overall geometries. We will demonstrate the utility of the proposed approach both in its own right and in combination with some of the already existing approaches. Toward that ambition, we elucidate the role of undesired microstructural imperfections occurring during the FDM printing process and propose a design strategy to exploit them, in combination with multi-material printing, to fully control and tailor the shape transformation of 4D printed parts. We will specifically focus on curved surfaces and will apply the developed methodology to transform flat plates into curved 3D surfaces with a wide range of positive and negative values of the mean and Gaussian curvatures.

8.2 Results and discussion

The role of residual stresses and micro-defects positioning— Polymeric filaments (in our case, polylactic acid (PLA)) generally exhibit residual stresses after the printing process. When the material is heated up to a temperature close to its glass transition temperature (typically 74°C for PLA), residual stresses tend to relax, leading to longitudinal contraction and transverse expansion. The rest length and thickness of a filament with an initial length of l and an initial thickness of t are then given by: $l' = \beta_1 l$ and $t' = \beta_2 t$, where β_1 and β_2 are the longitudinal and transverse expansion factors, respectively (Figure 8.1b). Both factors are expected to depend on the specific polymer properties and on the printing process, namely the printing speed (the higher the velocity, the higher the residual stress). Nevertheless, the proposed relaxation mechanism imposes $\beta_1 < 1$ and $\beta_2 > 1$ at the scale of an individual filament. Note that this effect differs from thermal expansion as the structures are eventually cooled down to their initial room temperature. Nevertheless, these transformations may be numerically treated as standard thermal expansion with anisotropic heat expansion coefficients.

Let us consider a flat disk 3D printed as a succession of concentric rings (in practice the printing path follows a single concentric ring). When heated up ($\Delta T = \text{cte}$), the disk

will undergo anisotropic strains leading to out-of-plane deformations. In such an axisymmetric configuration, the expansion factors β_1 and β_2 may depend on the radial coordinate r in the reference flat disk. In the absence of any geometrical incompatibility and if the bending stiffness can be neglected, an initially flat annulus of inner radius r and width dr in the flat transforms into a tilted annulus of inner radius $\rho = \beta_1(r)r$, an outer radius of $\rho + d\rho = \beta_1(r + dr) \cdot (r + dr) = \beta_1(r)r + (\beta_1(r) + r \frac{\partial \beta_1}{\partial r})dr$ and a width of $\beta_2(r)dr$ (Figure 8.1b).

Therefore, the tilt angle of the annulus is given by:

$$\sin(\theta) = \frac{\beta_1(r) + r \frac{\partial \beta_1}{\partial r}}{\beta_2(r)} \quad (8.1)$$

If the expansion factors are uniform, the expected shape is a cone with a characteristic angle:

$$\sin(\theta) = \frac{\beta_1}{\beta_2} \quad (8.2)$$

To probe this relation, several disks of thicknesses $h = 2$ mm were printed from PLA with different speeds ranging between 20 mm s^{-1} and 80 mm s^{-1} (the printing speed was uniform for each specimen). Once the heat stimulus is applied, the disks deform into cones with the most acute one corresponding to the highest printing speed, in qualitative agreement with Equation (8.2) (Figure 8.1 c-d). We measured the longitudinal expansion coefficients of the specimens printed at different printing speeds (Figure 8.1c). Our experimental results confirmed that increasing the printing speed decreased the magnitude of the longitudinal expansion factor of the specimens (Figure 8.1c). This can be explained by the fact that increasing the printing speed results in elongated filaments with smaller diameters. Interestingly, the effective values measured for β_2 are not larger than 1 as expected at the scale of a filament. We interpret this observation by the presence of void defects between the deposited filaments as described later. We also found an excellent agreement between the experimentally determined cone angles and the cone angles predicted analytically using Equation (8.2) (Figure 8.1d, e).

These results show that the printing speed can be considered as a design parameter to control the overall deformation of the printed disks. To obtain more complex shapes, we decomposed the disks into two regions (*i.e.*, inner disk and outer annulus) (Figure 8.1f), which were printed with the constant printing speeds of 20 and 80 mm s^{-1} , respectively (Figure 8.1f). We fixed the radius of the inner (R_{in}) and outer (R) disks at four levels: $R_{in}/R = 90\%$, 80% , 70% , and 60% . In theory, abruptly changing the printing speed should induce a geometrical discontinuity in the local radius of the structure. Such discontinuities are, however, smoothed out by the material and the observed slope is close to the one predicted by Equation (8.2).

To achieve a smoother deformation curve, we gradually increased the printing speed from the center to the periphery of the specimens using stepwise and linear functions (Figure 8.1g). The stepwise functions were defined such that either three equal regions were printed at 20, 50, and 80 mm s⁻¹ or four equal regions were printed at 20, 40, 60, and 80 mm s⁻¹. When the printing speed was linearly increased, we obtained the smoothest shape-transformed curvature (Figure 8.1g).

Furthermore, we 3D printed and tested square plates that were respectively printed at two distinct printing speeds: the minimum (*i.e.*, 20 mm s⁻¹) and the maximum (*i.e.*, 80 mm s⁻¹). The plate printed at the lower printing speed exhibited longitudinal shrinkage along the printing direction and transverse expansion (Supplementary Figure S8.1a). Importantly, in this case, no out-of-plane deformation was observed in the overall deformation. Indeed, since the direction of contraction remains parallel and the contraction rate is uniform, Gaussian curvature is not expected to occur [25]. In contrast, the plate printed at the higher printing speed exhibited an unexpected out-of-plane deformation, appearing as a bending feature (Supplementary Figure S8.1a). This observation highlighted that plates printed at a higher speed experience not only an in-plane stress but also a stress gradient through the plate thickness. The interplay between these two stress components contributes to different behavior when subjected to elevated temperatures. As a matter of fact, the layers printed at the vicinity of printer build-plate apparently accumulates less residual stress than the upper layers. As a consequence, standard bilayer effect tends to induce a concavity on the opposite side of the build-plate to the different structures that were printed with a uniform speed across the thickness [41]. Although this bending effect is not significant in the thicker specimens (beyond selecting the side where the concavity appears), bending is observed for thinner specimens (Supplementary Figure S8.2).

To further confirm the role of the printing speed on the final shape of the disks, we inverted the printing speed of the inner and outer disks (*i.e.*, the inner disk was printed at a speed of 80 mm s⁻¹ while the outer section was printed at 20 mm s⁻¹) (Figure 8.1h). The deformation angles were nearly constant for the disks with the equal inner to outer ratios (*i.e.*, $R_{in}/R = 60\%$ and 70%) and were close to those calculated using Equation 8.2 (Figure 8.1h). However, for $R_{in}/R = 90\%$, the inner disk dominated the final deformation, resulting in a more complex shape. For this ratio, the proposed analytical equation is not anymore valid.

To put this relationship into a broader perspective, we printed PLA disks with various thicknesses. For very thin disks (*i.e.*, $h < 2$ mm), the contribution of cross-sectional stresses caused the specimens to fold or roll when triggered by external thermal energy (Figure 8.2a, and Supplementary Figure S8.2). The overall bending deformation of the plates was optimum for a thickness of $h = 2$ mm, which is considered as the reference plate thickness throughout this study. For the specimens with larger thicknesses

(*i.e.*, $h = 4$ mm), the increase in the bending stiffness of the plates prevented them from fully bending (Figure 8.2a, and Supplementary Figure S8.2). The expansion factors (β_1, β_2) of the disks were not constant among disks with different thicknesses, although these variations decreased with the out-of-plane thickness of the specimens (Figure 8.2b). These results were surprising, because we had not changed the printing parameters of the disks with different thicknesses. This can be attributed to changes in various factors, such as the change in the bending stiffness and the distribution of defects during the 3D printing process when changing the thickness of the disk. Furthermore, we 3D printed square-shaped specimens at speeds of 20 and 80 mm s⁻¹. The results showed that $\beta_2 \approx 1$ in the transverse direction, independent of the printing speed (Supplementary Figure S8.1a). To explain this behavior, we further analyzed the mechanical properties of the constituent PLA as well as the morphological features of the 4D printed disks.

We calculated the dynamic mechanical properties of the PLA cuboid bar-like specimens printed at two extreme printing speeds (*i.e.*, 20 and 80 mm s⁻¹) in the longitudinal direction (Figure 8.2c). The storage and loss moduli of the PLA printed using two different speeds showed a similar trend (Figure 8.2c), with the materials printed at the highest printing speed (*i.e.*, 80 mm s⁻¹) exhibiting slightly higher storage moduli beyond the glass transition temperature (Figure 8.2c–top). This observation suggests that changing the printing speed has only limited impact on the mechanical properties of the material along the longitudinal direction. The glass transition temperatures of the specimens printed at the highest printing speed were also slightly higher (Figure 8.2c–bottom).

The microstructural properties of the specimens printed at the highest printing speed were, however, significantly different (Figure 8.2d–f, Supplementary Movie 1). We used micro-computed tomography to non-destructively measure the level of porosity (φ) in the disks printed at different printing speeds. The PLA disks printed at the lowest printing speed (*i.e.*, 20 mm s⁻¹) were almost free of defects (Figure 8.2e), showing near-perfect bonding between their filaments and layers during the printing process. Printing at the highest printing speed (*i.e.*, 80 mm s⁻¹), on the other hand, resulted in the formation of micro-defects not only across the thickness of the disk but also radially (Figure 8.2d–f). The initial printing layers, which were closer to the printing bed, were almost free of defects, while the amount of porosity linearly increased until it reached an asymptote $\varphi \approx 30\%$ for the top printing layers (Figure 8.2e, Supplementary Movie 8.1). Micro-voids had also formed in the material in the form of concentric rings. The void fraction was smallest at the center of the disks and increased along the disk radius (Figure 8.2f, Supplementary Movie 8.1).

The behavior of the 4D printed specimens is influenced by the distribution of micro-defects within the specimens. As illustrated in Figure 8.2a, the impact of non-uniform distribution of micro-defects across the thickness is more pronounced for thinner

specimens (*i.e.*, $h < 2$ mm) with a lower bending stiffness. These specimens are more likely to exhibit folding or rolling behaviors. Additionally, fewer defects and non-uniformities occur in the initial layers during the printing process (Figure 8.2e–f). These characteristics collectively result in greater radial expansion, yielding an expansion factor (β_2) greater than 1 (Figure 8.2b). However, when the specimen thickness reaches 2 mm, other factors such as in-plane stresses, bending stiffness, and printing-induced non-uniformities become more significant. This leads to reduced transverse expansion and a decrease in the β_2 value (Figure 8.2b). The specimens then become less susceptible to bending while shrinkage in the radial printing direction (β_1) becomes more dominant.

We developed non-linear finite element models to simulate the shape-shifting behavior of the PLA disks. We defined the thermo-mechanical properties of its constituting elements based on the expansion factors measured in the experiments (Figures 8.1c and 2b) and the dynamic mechanical tests (Figure 8.2c) performed on pure PLA. We also implemented the experimentally observed geometrical imperfections (*i.e.*, the level of porosity and its distribution) in our computational models (Figure 8.2d–f). The distribution of the imperfections and their sizes (Supplementary Figure S8.3) were compatible with what was observed using micro-computed tomography (Figure 8.2d–f). The deformation angles predicted by our computational models for the disks printed using different printing speeds were close to the experimentally measured values (Figure 8.1d), confirming the validity of the proposed numerical approach. This also shows that the final shape of the 4D printed PLA disks depends not only on the proper distribution of anisotropic thermo-mechanical properties but also on the specific distribution of geometrical imperfections within the numerical model (Supplementary Figure S8.3). We used the developed computational model to predict the shape-shifting behavior of other designs.

To highlight the interplay between the mechanical properties and microstructural features of the PLA disks, we analyzed the local curvatures of heat-actuated specimens. The specimens were divided into two regions with the inner part printed at the lowest printing speed (*i.e.*, 20 mm s^{-1}) and the outer at the highest speed (*i.e.*, 80 mm s^{-1}). For such specimens, the overall transformed shape (*i.e.*, dome-like geometries) remained constant (Figure 8.3a–left), exhibiting an overall negative mean curvature (*i.e.*, H) and a positive Gaussian curvature (*i.e.*, K) (Figure 8.3a–right) at any point of the deformed disk. The discontinuity of the printing speed at the interface of two regions created a discontinuous deformation field at those regions, resulting in a local increase of the Gaussian curvature (Figure 8.3a–left).

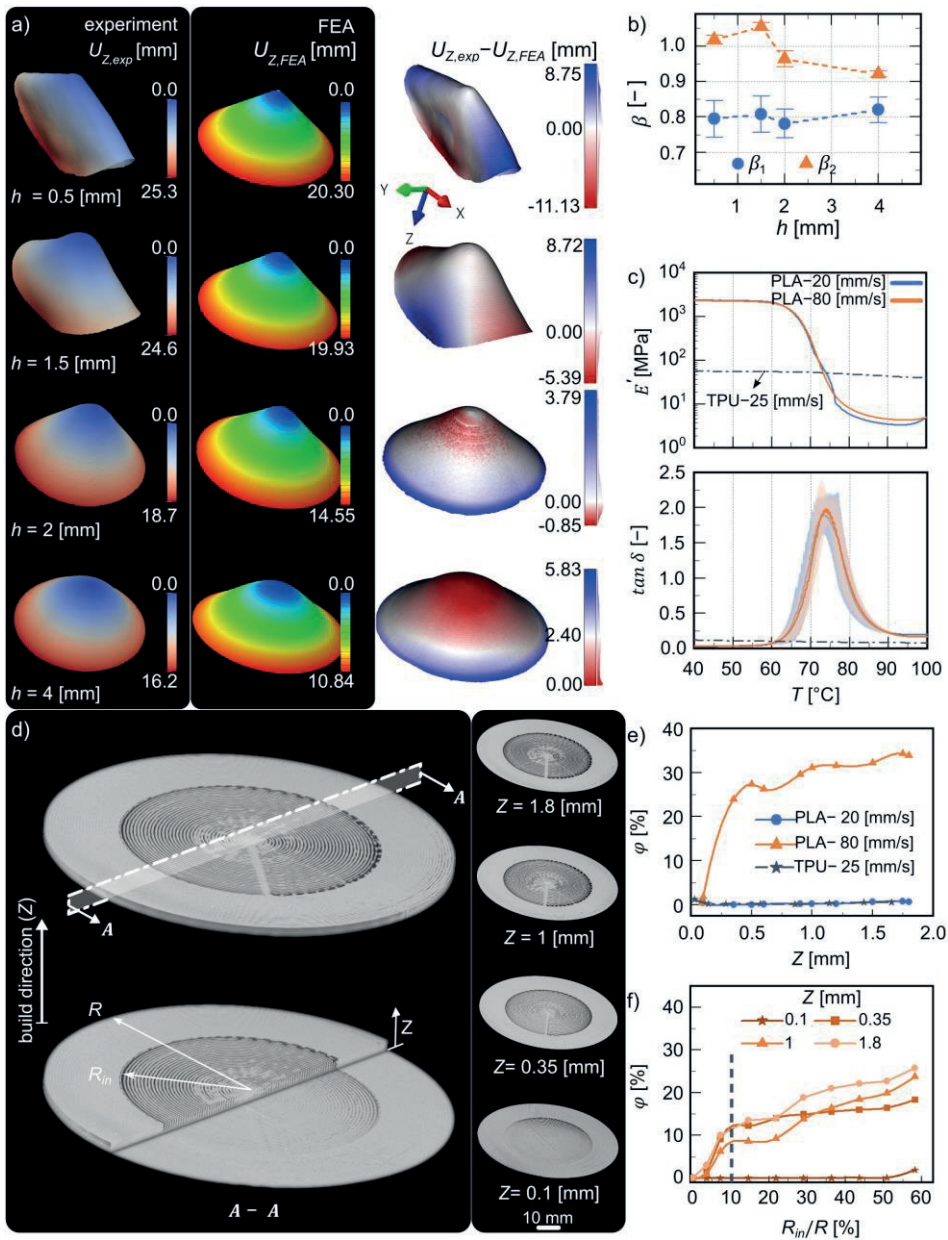


Figure 8.2. Thermo-mechanical behavior and microstructural analysis of PLA and TPU disks— PLA disks of varying thicknesses behave differently when exposed to an external thermal stimulus (a). Disks with $h = 2$ mm thickness are considered as the reference specimens in this study because in-plane stresses dominate the shape-shifting behavior in thinner disks (*i.e.*, $h < 2$ mm), causing the disk to fold or roll. When the sheet thicknesses are large enough (*i.e.*, $h \geq 4$ mm), the increased bending stiffness prevents the disks from fully bending (a). The experimentally measured expansion factors (β_1, β_2) were used in our computational models (b). The results of dynamic mechanical tests (*i.e.*, storage moduli in a logarithmic scale (c–top), and $\tan \delta$ (c–bottom)) performed on the PLA specimens printed with the maximum (*i.e.*, 80 mm s^{-1}) and minimum (*i.e.*, 20 mm s^{-1}) printing speeds and for the TPU specimens printed with a speed of 25 mm s^{-1} . Constructed μCT images of a PLA disk were used to analyze the formation of micro-voids during the 4D printing process (d). A μCT image of a disk whose inner and outer parts were printed at 80 mm s^{-1} and 20 mm s^{-1} , respectively. A morphological analysis of these specimens showed virtually no porosity for the PLA disks printed with the lowest speed (*i.e.*, 20 mm s^{-1}) and TPU while the level of porosity was significantly higher for the disks printed at 80 mm s^{-1} (e). The level of porosity also increased in the radial direction for the PLA disks printed at 80 mm s^{-1} (f). See Supplementary Movie 1 for the visualization of the defect distribution in the specimens printed at different speeds. The lines in subfigures e and f are to guide the eyes of readers.

Moreover, decreasing the size of the inner region decreased the deformation of the inner part, meaning that the maximum absolute values of the mean and Gaussian curvatures increased with the size of the outer disk (Figure 8.3a–right). This can be explained by the presence of the additional voids distributed at the boundaries of the specimens as they were printed using the highest speed. The additional voids are created because the deposited filaments have less time to coalesce as the printing speed increases. The deformation is, therefore, more localized due to the existence of a higher density of initial voids in such structures.

We also inverted the printing speeds of the inner and outer disks (*i.e.*, the inner disk was printed at 80 mm s^{-1} and the outer at 20 mm s^{-1}) (Figure 8.3b). We observed that the final shape of the disk was highly dependent on the size of the inner and outer disks (Figure 8.3b–left). For example, when 90% of the inner disk was printed with the highest speed, more defects were present in the inner part of the disk. Given that the outer disk was printed with the lowest speed and was, thus, defect-free, the structure was over-constrained and ended up developing a negative Gaussian curvature (*i.e.*, $K < 0$ otherwise known as hyperbolic or saddle-like curvature) (Figure 8.3b–right). In addition, we performed an experiment in which the size of the outer layer was kept constant while varying the printing speed. Such adjustments modified the overall shape of the disk (Supplementary Figure S8.4).

In conclusion, combining a rational distribution of defects with a proper spatial distribution of the printing speed enables us to endow the 4D printed specimens with a non-Euclidean metric, which, upon activation, causes the sheet to adopt a non-Euclidean shape (*i.e.*, a sphere-like or a saddle-like shape) [46].

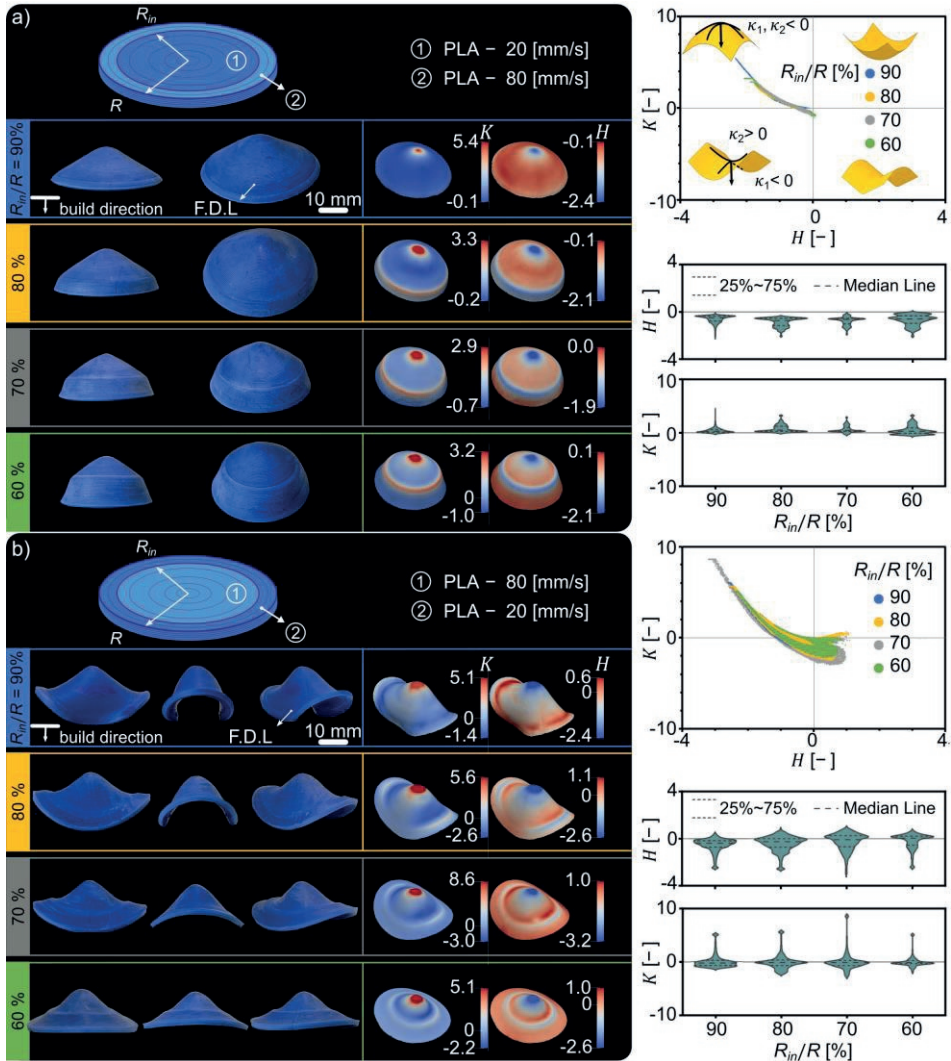


Figure 8.3. The effects of distribution of residual stresses on the out-of-plane deformation of 4D printed disks— The PLA disks were divided into two regions of which the inner part was printed at the minimum printing speed (*i.e.*, 20 mm s⁻¹) while the outer was printed with the maximum speed (*i.e.*, 80 mm s⁻¹). Four different ratios were used (*i.e.*, $R_{in}/R = 60\%$, 70%, 80%, and 90%). Such a segmentation of the disks resulted in a discontinuous out-of-plane deformation of the specimens (a–left) and the development of a positive Gaussian curvature (*i.e.*, $K > 0$) and a negative mean curvature (*i.e.*, $H < 0$) (a–right). We then switched the printing speed of the inner (80 mm s⁻¹) and outer (20 mm s⁻¹) parts of the disk. This change resulted in a completely different shape transformations (b–left) and local curvatures (b–right). The first deposited layers (F.D.L.) are illustrated in (a) and (b).

The role of bi-material positioning— To further study the effects of the boundary conditions on the overall shape-shifting behavior of the specimens, we used multi-material 4D printing with a soft polymer (*i.e.*, thermoplastic polyurethane or TPU) as the second material. The elastic modulus of TPU is an order of magnitude lower than that of PLA. It also does not exhibit the capability of storing residual stresses and relaxing them in the temperature range used in this study (*i.e.*, $40\text{ }^{\circ}\text{C} < T < 100\text{ }^{\circ}\text{C}$) (Figure 8.2c). We segmented the disk into two regions (*i.e.*, inner and outer). The inner region was printed with the highest speed (*i.e.*, 80 mm s^{-1}) while the outer region was made of TPU (printing speed = 25 mm s^{-1}). TPU does not show any shape transformation when the specimens are heated. The shape transformation of the PLA part can, therefore, be tuned by the amount of the soft material printed around it (Figure 8.4a–left). These boundary effects also contributed to the formation of local curvatures in the 4D printed multi-material disks. When 40% of the disk was printed from TPU, the local curvatures were close to zero within the TPU part (*i.e.*, no deformation) while a positive curvature (*i.e.*, dome-like or spherical) appeared at the disk center (Figure 8.4a–right). Decreasing the size of the TPU to 10% extended the range of achievable Gaussian and mean curvatures towards more negative and positive values (Figure 8.4a–right). A comparable behavior was observed across various printing and TPU deposition patterns (Supplementary Figures S8.1 and S8.5). We further demonstrated that the specific positioning of TPU did not affect the overall curvature profile (Supplementary Figure S8.5c). For example, when the TPU ring was placed internally (*i.e.*, in the inner ring), the global saddle-like curvature was achieved (Supplementary Figure S8.5c-left). Placing PLA atop the TPU in the middle ring (Supplementary Figure S8.5c-middle) affected the bending stiffness of the disk, resulting in diminished overall curvature. Hence, the synergy between multi-material printing and the strategic placement of imperfections effectively allows for the modulation of residual stresses and bending stiffnesses, thereby facilitating a wide range of curvature types (Supplementary Figure S8.5c).”

We also further delved into the effects of printing patterns (Supplementary Figure S8.1) and initial shape of the 2D plates (Supplementary Figures S8.5a and S8.5b) on the overall shape of the 4D printed structures. Toward that end, we printed plates, as concentrically printed filaments, at a speed of 80 mm s^{-1} . When exposed to high temperatures, independent from the printing patterns and the initial shape of the plates, they showed a dome-like out-of-plane deformation (Supplementary Figures S8.1b, S8.5a, and S8.5b).

When the multi-material approach was used (*i.e.*, printing TPU at the boundaries of the plate regardless of the printing direction), the parts printed from TPU remained unaffected and created discontinuity at the boundaries of the plate. This led to similar negative Gaussian curvatures as observed in disks (Supplementary Figures S8.1a-bottom and S8.1b-bottom).

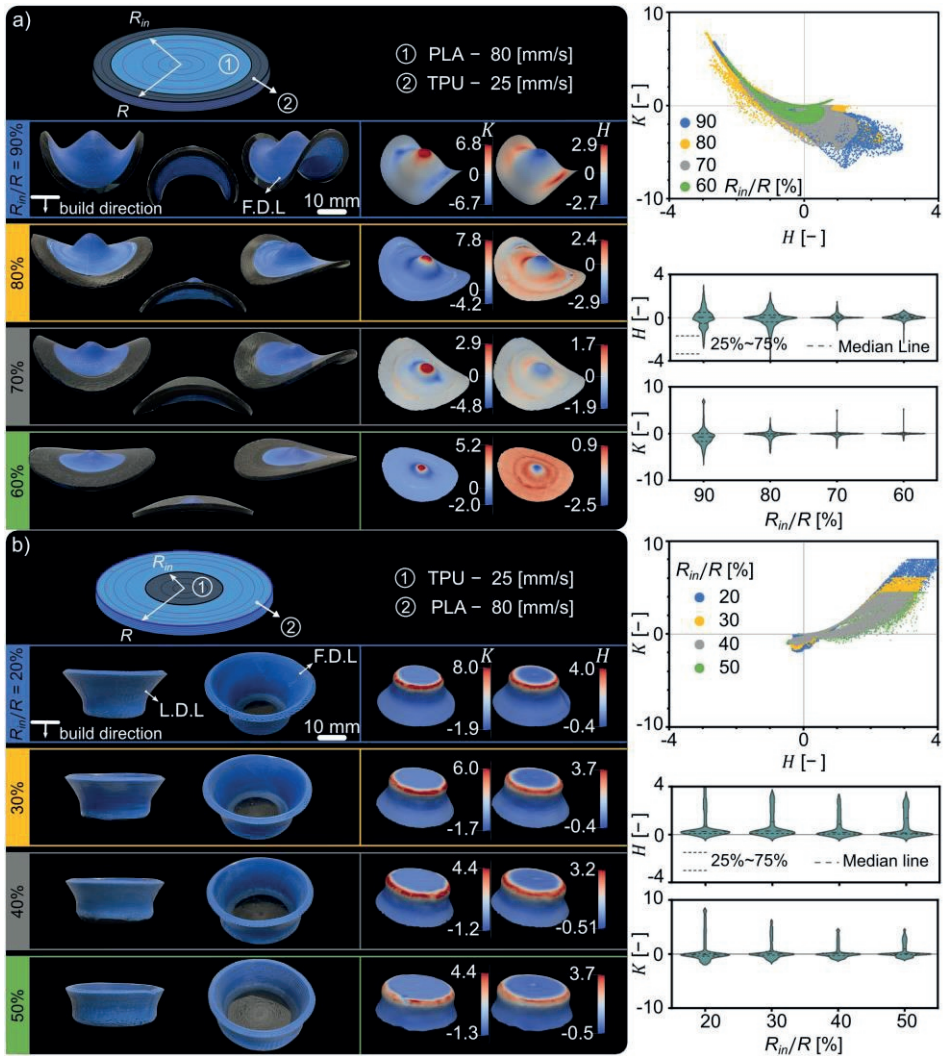


Figure 8.4. The effects of distribution of bi-material on the out-of-plane deformation of 4D printed disks— The peripheral edge of the PLA disks was printed from a softer material (*i.e.*, TPU) and its size was varied. Such designs resulted in diverse types of shape transformations depending on the size of the region printed from the soft phase (a-left). This multi-material design approach also altered the local mean and Gaussian curvatures of the shape-transformed specimens (a-right). Swapping the printing order of the soft and hard polymers such that the soft TPU was printed at the center of the disk completely changed the overall shape transformation of the disks (b-left) as well as the local curvature values (b-right) as compared to the case where the core of the disk was printed from the hard material. The first and last deposited layers are denoted as F.D.L and L.D.L, respectively.

We also switched the order of the hard and soft polymers, printing the inner part of the specimens from TPU while their outer ring was made of PLA. Since the TPU part of the disks could not spontaneously deform, a completely new type of shape transformation was observed (Figure 8.4b–left). Changing the material order resulted in more positive values of κ_1 and κ_2 leading to more positive mean and Gaussian curvatures (Figure 8.4b–right). In the other words, the magnitudes and signs of the mean and Gaussian curvatures were entirely shifted ($K > 0$, $H > 0$) and the outer section of the disk deformed opposite to the build direction (Figure 8.4b). These results clearly show the importance of rationally positioning the hard and soft polymers to tailor the local mean and Gaussian curvatures developed in the 4D printed objects.

We have so far shown that, in addition to programming the distribution of residual stress and imperfections density in-plane, these properties can also be adjusted across the section by changing the printing speed along the thickness of the disk. In Figure 8.5a, position 1, the bottom layers of the disk were printed at a low speed (*i.e.*, 20 mm s^{-1}) while the upper layers were printed with a higher speed (*i.e.*, 80 mm s^{-1}). As the contraction is stronger in the upper layer, the concavity of the resulting cone is on the opposite side of the printing build-plate. Inverting the printing recipe results into a symmetric shape (the thickness of the specimens is large enough to hinder significant curling effect). In this case, the initial printing layers closer to the printing build-plate were made with the maximum printing speed (*i.e.*, 80 mm s^{-1}) while the top layers of the disk were printed with the lowest printing speed (*i.e.*, 20 mm s^{-1}) (Figure 8.5a, position 2). In this way, we could also change the gradient of the expansion coefficients across the thickness. Transferring the imperfections to the top part of the specimens, adjusted the flexural rigidity of the disks and led to positive mean and Gaussian curvatures in the deformed state (*i.e.*, inverse bending) (Figure 8.5a–right).

More complex shape transformations can be realized by combining both proposed approaches. For example, we attached two disks with different expansion factors and different imperfection distributions at their center point (Figure 8.5b). The imperfections of the bottom disk were at the bottom, while those of the top disk were at the top, changing the gradient of the expansion factors across the thickness (Figure 8.5b–left). The interaction between these two disks resulted in the bending of both disks in the opposite directions (Figure 8.5b–left, Supplementary Movie 8.2).

We also combined this design with multi-material printing to realize a 3D structure that formed a combination of a dome-like (*i.e.*, spherical) and saddle-like (*i.e.*, hyperbolic) geometries (Figure 8.5b–right). Such complex types of shape transformations from a flat state are impossible to achieve with single material 4D printing.

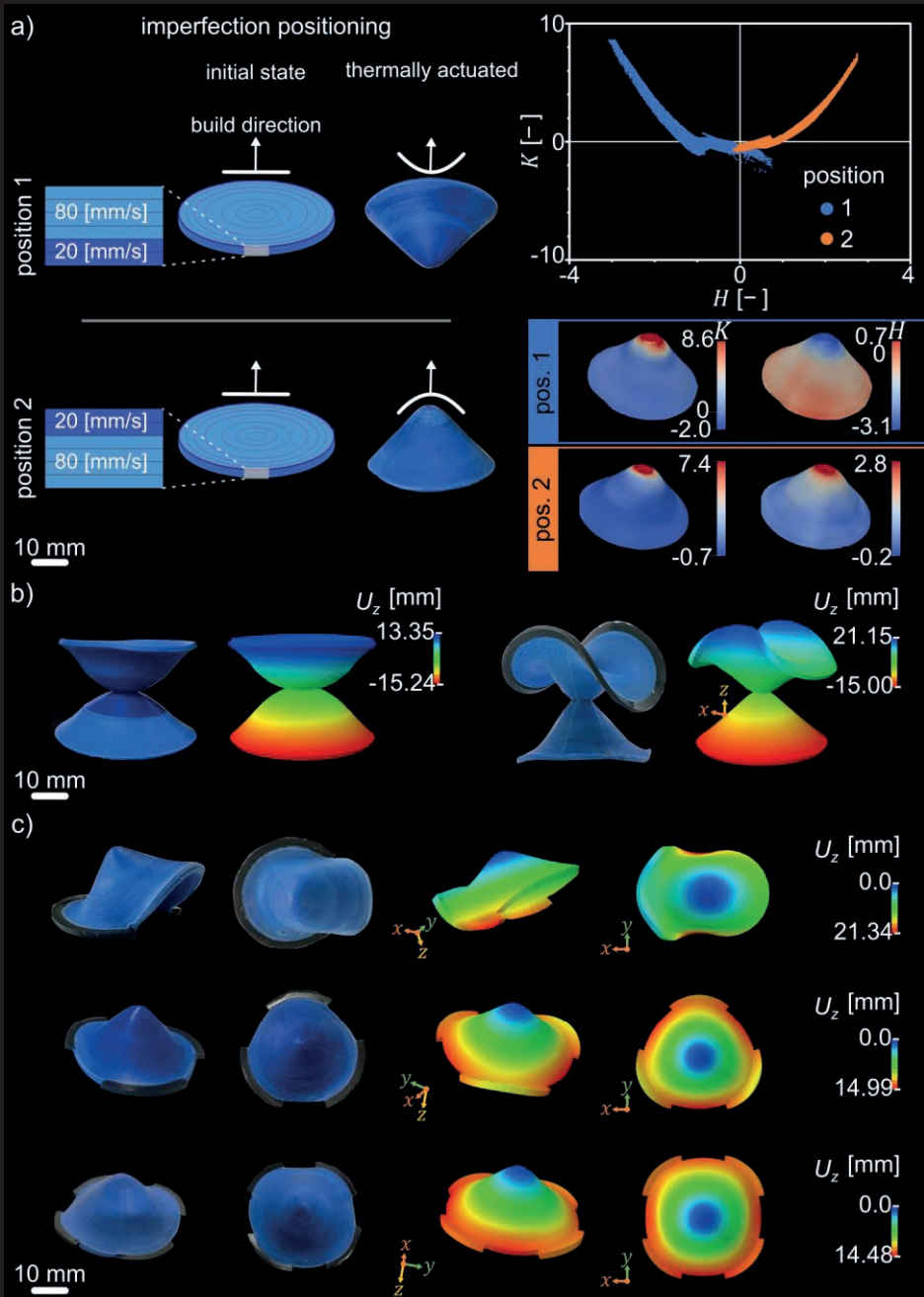


Figure 8.5. The combinatorial effects of distribution of residual stresses and bi-material on the out-of-plane deformation of 4D printed disks— The distribution of residual stresses across the thickness determines the bending orientation of the PLA disks. We introduced higher residual stress at the bottom layer of the PLA-disk (*i.e.*, the surface which is in contact with the printing build-plate) by using a faster printing strategy for the initial layers. Such manipulation of the imperfection resulted in an inverse bending of the PLA disks (a–left, position 2) with an opposite localized curvature as compared to the case where the higher gradient was located at the top layer of the PLA disks (a–left, position 1). By precisely positioning the imperfections in the PLA disks and integrating the concept of inverse bending with that of out-of-plane deformation, one can achieve more complex shape transformations (b–left) (see Supplementary Movie 2 for the dynamic visualization of the shape-shifting process). Even more complex shapes can be achieved by including the soft polymeric phase in the design of the 4D printed disks with alternating the position of the residual stress (b–right). The distribution of the soft phase around the periphery of the PLA disks can also contribute to its overall shape-shifting behavior (c).

We demonstrated that by introducing a second softer material into the design of 4D printed disks, one can change the local distribution of deformation within 4D printed objects. This can be done by constraining the deformation of the peripheral edges of the disk. The way in which the soft phase is distributed around the periphery of the disk could also influence its shape-shifting behavior (Figure 8.5c). To demonstrate those effects, we segmented the disk into two, three, or four sections to which the soft polymeric material was assigned (Figure 8.5c). The significant shape differences resulting from these designs confirm the utility of this strategy as an additional route for the adjustment of the shape transformation behavior of 4D printed disks.

8.3 Conclusion

We presented an approach in which we can control the differential deformation mechanisms in 4D printed structures. We were also able to control the spatial distributions of the printing imperfections and a second softer phase to achieve 4D printed structures with complex shape transformations and predictable final shapes. Our study also reveals the important underlying mechanisms responsible for the shape-shifting behavior of objects printed from SMPs using FDM-based 4D printing processes. One of these mechanisms is the formation of defects (voids) and residual strains during such printing processes. While such artifacts are often considered undesirable and their distributions are somewhat random at the level of individual filaments, their overall distributions at large enough length scales follow predictable patterns and are correlated with the parameters of the 4D printing process. We could, therefore, utilize the distribution of printing artifacts as one of the pillars of our proposed design strategy. This change in perspective in terms of how printing imperfections are seen can open up new opportunities for the design of defect-based metamaterials. The proposed designs have numerous potential applications of which one regarding the engineering of complex drug delivery systems or filters is highlighted here (Supplementary Movie 2). Our focus on the generation of complex curvature fields is partially motivated by the prominent role of curvature in biology [47] and, thus, regenerative medicine as well as the importance of

complex curvature in many technological areas, such as (soft) robotics [48-50], medical instruments [51, 52], and structural engineering [39, 53, 54].

8.4 Materials and methods

8.4.1 4D printing

We additively manufactured the disks (diameter = 55 mm) using PLA filaments (Ultimaker PLA-blue, 750 gr Natural with a filament diameter of 2.85 mm) for the hard and TPU for the soft phase using a fused deposition modeling (FDM) 3D printer (Ultimaker 3, Ultimaker B.V., The Netherlands). We customized the G-code for the 3D printing of the structures to adjust the printing parameters (*i.e.*, printing speed, printing temperature, multi-material printing, *etc.*). We used nozzles with a diameter of 0.4 mm, a fixed bed printing temperature of 60 °C, a constant layer thickness of 0.15 mm, and a steady extrusion temperature of 200 °C for PLA and 225 °C for TPU. As the default option, we used 100% of the cooling capacity of the printer to maximize the amount of residual stress and the number of the introduced defects. In specific areas, such as the initial layers and at the PLA/TPU interface, we reduced the cooling rate and print speed to build a good foundation, smoothly connecting individual layers and creating proper attachment between the disk and the build-plate. The first four layers of the specimens (~25% of their thickness) were printed at a printing speed equal to 50% of their overall printing speed and were cooled using 50% of the cooling capacity of the printer (specimens in Figures 8.1e–h, 8.3, 8.4, and 8.5c). For example, for the disks printed at the highest printing speed (*i.e.*, 80 mm s⁻¹), the first four layers were printed at 40 mm s⁻¹ and a cooling capacity of 50% was used. At the interface of TPU and PLA (*i.e.*, specimens in Figures 8.4 and Figures 8.5b–c), no cooling was used to improve the bonding of both materials and to achieve a higher printing quality.

For the specimens shown in Figure 8.5a, we applied different configurations of printing speeds and cooling rates along their thicknesses to alternate the gradient of residual stress and program the side of concavity. Towards this aim, 25% of the specimens were printed with the lowest printing speed (*i.e.*, 20 mm s⁻¹) while the rest were printed with the highest (*i.e.*, 80 mm s⁻¹) (position 1 in Figure 8.5a). To reverse the concavity, the bottom parts (75% of the overall thickness) of the specimens were printed with the highest printing speed (*i.e.*, 80 mm s⁻¹) while the top part was printed with the lowest (*i.e.*, 20 mm s⁻¹) (position 2 in Figure 8.5a). In position 2, the initial layer was also printed at a speed of 40 mm s⁻¹ with no print cooling.

In the specimens shown in Figures 8.5b, we employed the printing strategy described in sub-Figure 8.5a to print specimens 1 and 2 on top of each other. To print the specimens in one step, we placed an adhesive sheet (Tesa 4438 Blue Tape) between both disks in the middle of the printing process. Only a small section of the center ($R_{in}/R \sim$

5%) was not covered by the adhesive sheet to connect the specimens. For the multi-material printed specimens, a composition ratio of $V_{PLA}/V_{total} = 90\%$ was used. This ratio was maintained constant unless otherwise stated.

8.4.2 Activation

We used a temperature-controlled bath with a heating immersion circulator (CORIO CD, Julabo, Germany) to activate the shape transformation process of the 4D printed specimens. The specimens were submerged in boiling water for a minimum of 60 s to ensure the shape-shifting process was fully completed. They were then cooled down to their initial room temperature.

8.4.3 Micro-computed tomography (μ CT)

We used Phoenix X-ray Nanotom[®] (GE Sensing and Inspection Technologies GmbH, Wunstorf, Germany) for μ CT imaging of the PLA specimens printed at two printing speeds (*i.e.*, 20 and 80 mm s⁻¹) and the TPU disks. The specimens were scanned over 360° using a voxel size of 25 μ m and an angular rotation step of 1°. The images were acquired at 110 kV and 160 μ A for a total scan time of 24 min. We used Fiji (v 1.53) to analyze the acquired images and to calculate the porosity along the radius and depth of the specimens

8.4.4 3D optical scanning

The outer contour of the deformed structures was captured by a 3D scanner (Scan-In-A-Box, FX, DELL mini beamer, resolution of both cameras (IDS UI-3250LE-M-G-L): 1600 × 1200 pixels). The specimens were photographed from at least eight different angles. The images were then rigidly registered using the software accompanying the 3D scanner (IDEA). After noise removal, the point clouds were imported into CloudCompare software (V.2.9.1) for further analysis.

8.4.5 Dynamic mechanical analysis (DMA)

A dynamic mechanical thermal analyzer (TA Instruments, Q800 DMA) was used to measure the time-, temperature-, and frequency-dependent mechanical properties of the 3D printed cuboid bar-like structures made from PLA (at two printing speeds, 20 and 80 mm s⁻¹) and TPU. We designed and 3D printed bars (30 × 10 × 1.5 mm³) for force-controlled tensile DMA testing with a temperature ramp of 5 °C and at a constant frequency of force oscillation (1 Hz). From the $\tan(\delta)$ and the storage modulus measured by the DMA, we derived the glass transition temperature and the temperature-dependent elastic moduli of the PLA and TPU. Under dynamic mechanical loading, the complex elastic modulus in terms of the storage, E' , and loss modulus, E'' , is formulated as $E^* = E' + iE''$, where $E'' = E'\tan(\delta)$. Given the magnitude of the vector E^* , the magnitude

of the temperature-dependent elastic modulus is calculated as $E(T) = E' \sqrt{1 + \tan(\delta)^2}$ [55]. We also measured the glass transition temperature of the specimens, which was defined as the temperature corresponding to the peak value of $\tan(\delta)$.

8.4.6 Measurement of expansion factors

We measured the expansion factors along the printing direction (β_1 = longitudinal expansion factor) and perpendicular to the printing direction (β_2 = transverse expansion factor) using Equation (8.2) (Figure 8.1b) for PLA specimens printed at different printing speeds (Figure 8.1c) and thicknesses (Figure 8.2b). Although the actual shape transformation is not, from a physics viewpoint, a thermal expansion effect, it is numerically expedient to model it through a standard heat expansion routine with orthotropic expansion coefficients. We extracted the α_1 and α_2 values from the longitudinal and transverse expansion coefficients (β_1 and β_2):

$$\alpha_i = \frac{\beta_i - 1}{\Delta T}, \quad i = 1, 2 \quad \Delta T = 80 \text{ }^\circ\text{C} \quad (8.3)$$

The parameter α_3 was measured by comparing the thickness of the samples before and after thermal actuation. We also assumed that TPU is an incompressible material and employed orthotropic thermal expansion coefficients to ensure that its volume did not change after being exposed to high temperatures (see Supplementary Table S8.1).

8.4.7 Computational modeling

Finite element modeling was conducted using the commercial software suite Abaqus (Dassault Simulia, V6.14, USA). We used linear thermally-coupled brick elements with full integration points in three directions (C3D8T, Abaqus). We uniformly applied the temperature with a magnitude of 100 °C ($= T_{ambient} + \Delta T$) to perform a coupled temperature–displacement steady-state analysis. In order to mimic the anisotropic relaxation we observed above the glass transition temperature, we considered temperature-dependent elastic moduli ($E(T)$) and orthotropic thermal expansion coefficients as the material model in our computational models. These values were obtained from experimental data and are presented in Supplementary Tables S8.1 and S8.2.

We applied a symmetric boundary condition which enabled us to model half of the disk. The center of the disk was fixed. The model was discretized using five elements in thickness and radial elements with a size of 700 μm . The imperfections were introduced into the computational models by assigning extremely low mechanical properties (*i.e.*, $E = 1 \text{ Pa}$) to certain elements of the disk to trigger the instabilities in the system after applying the load [56-58]. The imperfections were distributed systematically to imitate the same distribution patterns as seen in the μCT images. The porosity of the PLA specimens printed at 80 mm s^{-1} was increased in both radial and build directions (Figure

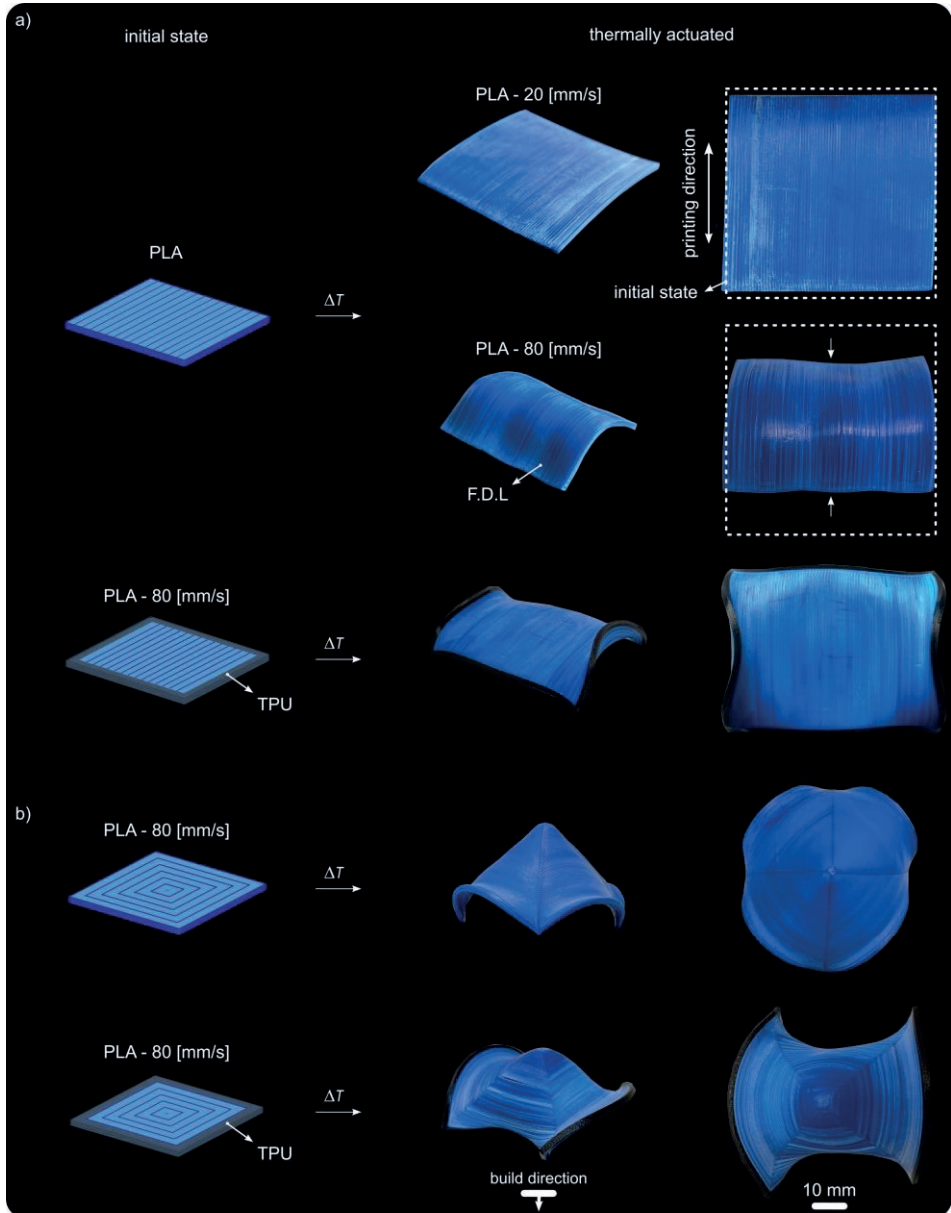
8.2e–f), assuming that the initial layer (20% of thickness) was effectively defect-free. The imperfections were, therefore, implemented every ~ 2.1 mm between $R_{in}/R \sim 30\%$ (this number can be $\sim 15\%$ for the top layers) and $R_{in}/R \sim 100\%$ (*i.e.*, the peripheral edge of the specimens) (Supplementary Figure S8.3a).

The sensitivity of the FE models to the distribution of the imperfections was analyzed computationally. We observed that the defects were not distributed uniformly at each layer (Figure 8.2d). We, therefore, implemented a non-symmetric distribution of the imperfections in the angular direction and examined the effects of varying the angle of the imperfection distribution (γ) (*i.e.*, from 30° to 150°) on the shape-shifting behavior of the constructs. Our results showed that the imperfection distribution in the angular direction (γ) does not significantly affect the cone angle (θ) (Supplementary Figure S8.3b). We considered the distribution of imperfections with $\gamma = 120^\circ$ in our model. A good agreement was achieved between the proposed computational model and our experimental observations (Supplementary Figure S8.3c).

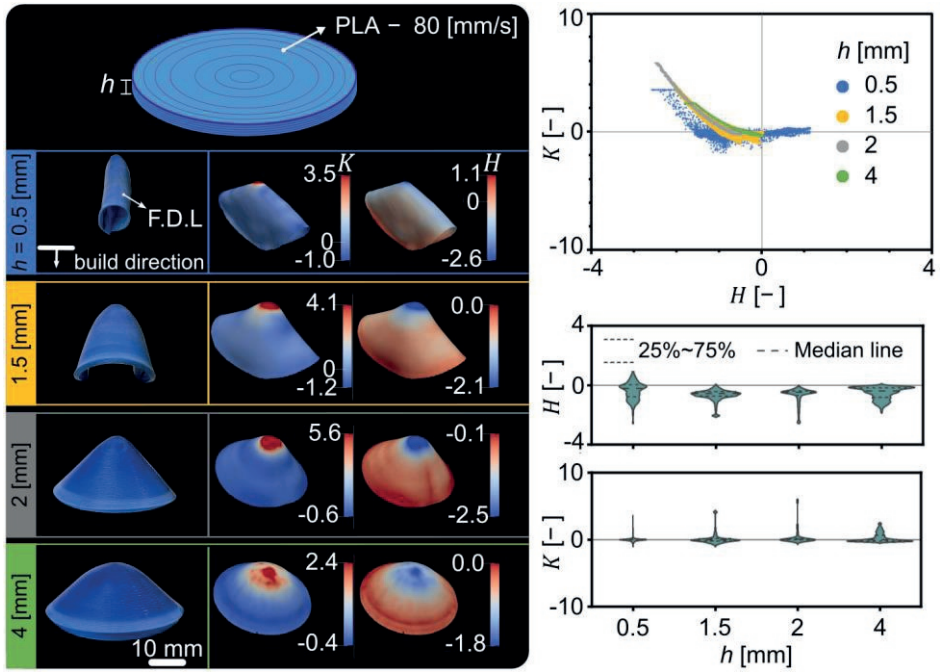
8.4.8 Curvature measurements

The principal surface curvatures were estimated from the triangulated meshes obtained through 3D scanning, using a surface fitting-based algorithm that was implemented in a recent mesh processing workflow [59]. Briefly, the robust curvature estimation algorithm in the Python-based libigl toolbox was used, which estimates the curvature at every vertex by fitting a second-order polynomial to a local neighborhood and quantifying the curvature using the fitted surface patch [60, 61]. The local neighborhood is defined as a spherical region with the radius r . We initially screened a range of values for r and found that $r = 15\langle e \rangle$, where $\langle e \rangle$ is the average edge length in the mesh, results in an appropriate balance between detecting the curvature of very small mesh features and only capturing the macroscale curvature of the structure. The principal curvatures κ_1 and κ_2 were then used to compute the mean ($H = \frac{1}{2}(\kappa_1 + \kappa_2)$) and Gaussian ($K = \kappa_1\kappa_2$) curvatures that are reported in the main text. To obtain non-dimensional curvature quantities, the curvature values were normalized using a characteristic length $S_v = \frac{V}{S}$, where V is the volume of the smallest rectangular box containing the specimen and S is the mesh surface area [59]. The 3D mesh reconstructions, color-coded by curvature, were visualized using Paraview.

8.5 Supplementary material

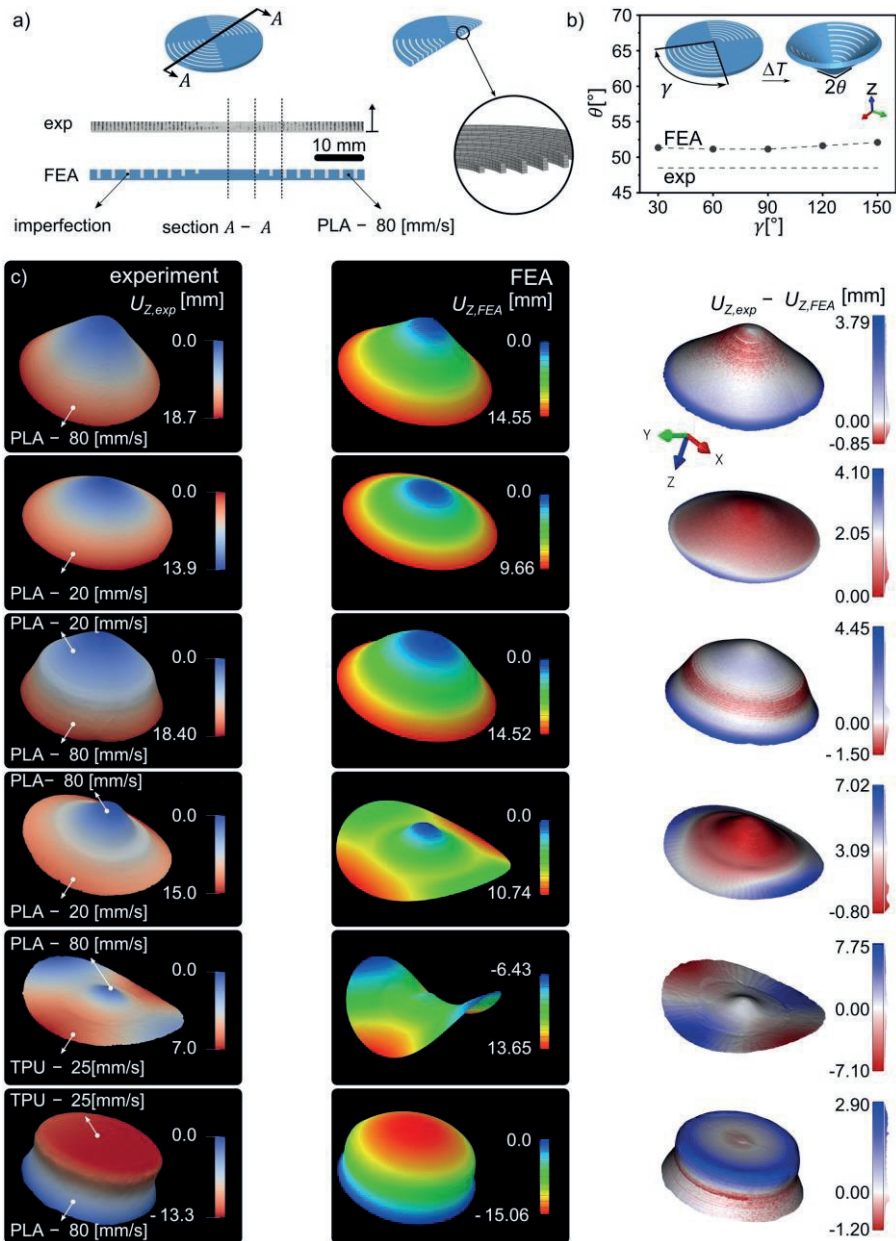


Supplementary Figure S8.1. The effects of distribution of residual stresses on the shape-shifting behavior of initially 4D printed square-shaped structures— PLA square plates were 3D printed at speeds of 20 and 80 mm s⁻¹, using linear patterns, and incorporating TPU (a), as well as using concentric patterns with and without TPU (b). All the specimens were printed with a uniform thickness of 2 mm. When a multi-material printing approach was used, $V_{\text{PLA}}/V_{\text{total}} = 90\%$ was maintained. The first deposited layers (F.D.L) are illustrated in (a) and (b).

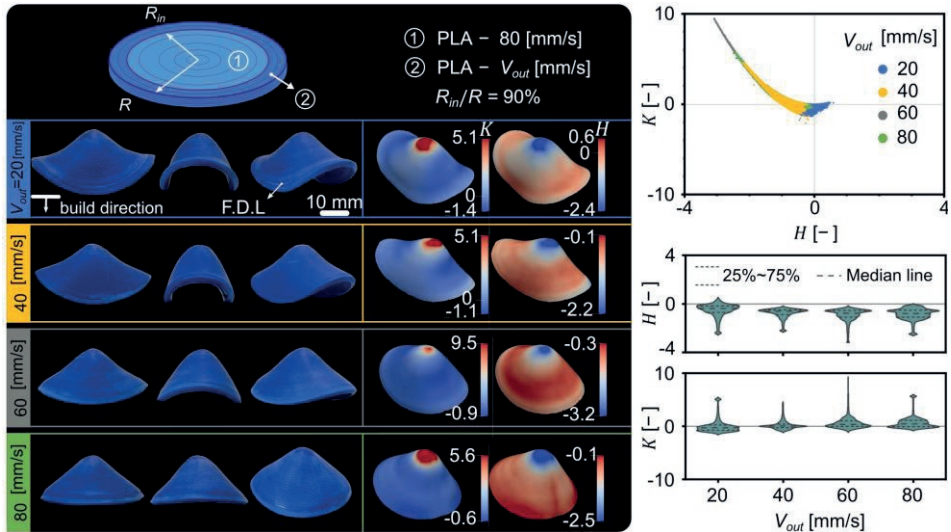


Supplementary Figure S8.2. The effects of the disk thickness (h) on the formation of the local curvature fields— PLA disks were printed at a speed of 80 mm s^{-1} with $h = 0.5, 1.5, 2,$ or 4 mm . Throughout this study, the thickness of the disk was kept constant at $h = 2 \text{ mm}$. The first deposited layers (F.D.L) are illustrated here.

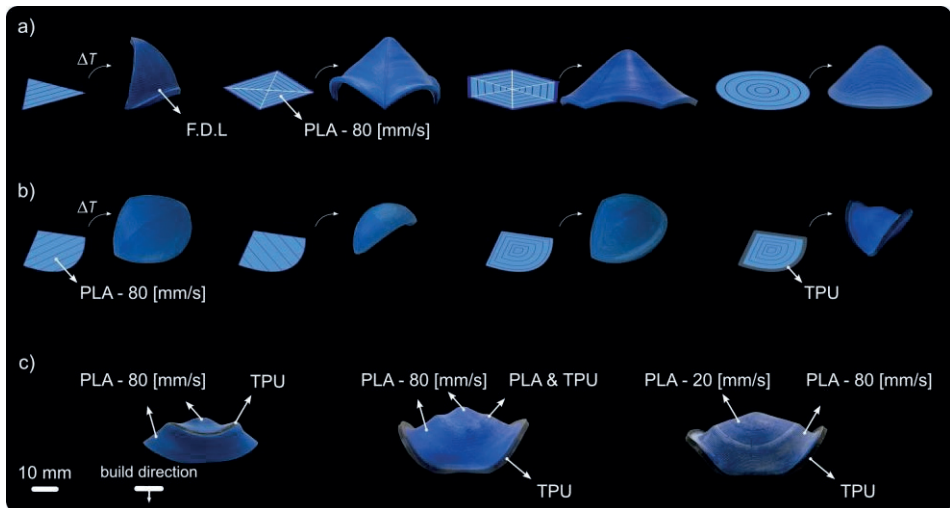
Design for adaption



Supplementary Figure S8.3. The finite element analysis of imperfection-induced deformations in thermally actuated disks— The finite element analysis was used to predict the final shape of thermally actuated disks. The imperfections were introduced into the model by assigning extremely low material properties to the elements distributed in the radial, angular, and printing directions. The distribution of the voids was similar to what was observed in the μ CT scans (a). The angular distribution of the imperfections (γ) does not have a marked effect on the out-of-plane deformations predicted by the model (b). The deformation obtained from our computational models agreed well with our experimental results (c).



Supplementary Figure S8.4. The effects of printing speed in local curvature formations— The difference in the printing speed in the radial direction affects the formation of local curvatures. For the PLA disks with $R_{in}/R = 90\%$, we decreased the printing speed of the outer layer (V_{out}) from 80 mm s^{-1} to 20 mm s^{-1} , which resulted in a higher level of local curvatures with a negative Gaussian curvature and a positive mean curvature ($V_{out} = 20 \text{ mm s}^{-1}$). The first deposited layers (F.D.L) are illustrated here.



Supplementary Figure S8.5. The effects of initial shapes, printing patterns, and material depositions on the out-of-plane deformation of 4D printed structures— The out-of-plane deformation in 2D structures made from different initial shapes (*i.e.*, triangle with horizontal filament patterns, as well as square, hexagon, and circle with concentric filament deposition) showed similar dome-shape result after triggered by temperature (a). In these specimens, we used a printing speed of 80 mm s^{-1} . We further combined these shapes (*i.e.*, triangle and semi-circle) and 3D printed 2D planes with four different printing patterns including linear-horizontal, linear-vertical, concentric and the combination of concentric and multi-material (b). The printing pattern can significantly affect the out-of-plane results. We also showed how deposition of TPU can change the curvature

Design for adaption

that can be achieved during 4D printing (c). All specimens were 3D printed with an out-of-plane thickness of 2 mm. $V_{\text{PLA}}/V_{\text{total}} = 90\%$ was considered in multi-material specimens. The first deposited layers (F.D.L) are illustrated in (a–c).

Supplementary Table S8.1. The thermal expansion coefficients for PLA and TPU materials which were used in the computational models.

Material	Thickness [mm]	Print speed [mm s ⁻¹]	α_1 [°C ⁻¹]	α_2 [°C ⁻¹]	α_3 [°C ⁻¹]
PLA	0.5	80	-0.00367	0.00023	0.00375
	1.5	80	-0.00367	0.00045	0.00233
	2	20	-0.00172	-0.00045	0.002
	2	80	-0.00346	-0.00068	0.002
	4	80	-0.00288	-0.00091	0.00162
TPU	2	25	-0.0002	-0.00002	0.0002

Supplementary Table S8.2. The temperature-dependent elastic moduli ($E(T)$) of PLA printed at 20 and 80 mm s⁻¹ and TPU printed at 25 mm s⁻¹, which were used in our computational models.

Temperature [°C]	E [MPa]		
	PLA – 20 [mm s ⁻¹]	PLA – 80 [mm s ⁻¹]	TPU – 25 [mm s ⁻¹]
40	2397.9	2334.67	58.234
43	2392.85	2325.14	56.820
46	2373.15	2304.41	55.383
49	2350.03	2284.69	53.866
52	2328.79	2258.1	52.411
55	2297.51	2220.38	50.917
58	2240.5	2151.83	49.457
61	2051.49	1986.19	47.970
64	1592.97	1619.69	46.463
67	928.349	1008.79	44.952
70	366.282	411.054	43.453
73	131.292	116.668	41.968
76	39.688	36.235	40.497
79	9.918	14.123	39.062
82	5.792	7.947	37.656
85	4.396	5.838	36.245
88	3.795	4.970	34.860
91	3.501	4.563	33.529
94	3.428	4.409	32.207
97	3.754	4.512	30.923
100	4.976	5.028	29.683

Supplementary movies

Supplementary Video 8.1. Distribution of imperfections in the 4D-printed structures (see <https://doi.org/10.1038/s43246-024-00448-w>)

Supplementary Video 8.2. Systematic distribution of imperfections in 4D-printed structures and the potential application in a drug delivery system (see <https://doi.org/10.1038/s43246-024-00448-w>)

Bibliography

1. c.l.f.u. Iierre/universcience/amàco, Drying a thin slice of wood, 2015. <https://vimeo.com/175694172>. (Accessed June 2022).
2. P. Oudet, Art in wood, 2022. <http://www.lavieenbois.com>. (Accessed June 2022)
3. W.M.v. Rees, E. Vouga, L. Mahadevan, Growth patterns for shape-shifting elastic bilayers, *Proceedings of the National Academy of Sciences* 114(44) (2017) 11597-11602.
4. J.W. Boley, W.M.v. Rees, C. Lissandrello, M.N. Horenstein, R.L. Truby, A. Kotikian, J.A. Lewis, L. Mahadevan, Shape-shifting structured lattices via multimaterial 4D printing, *Proceedings of the National Academy of Sciences* 116(42) (2019) 20856-20862.
5. P.T. Gonzalez-Bellido, A.T. Scaros, R.T. Hanlon, T.J. Wardill, Neural Control of Dynamic 3-Dimensional Skin Papillae for Cuttlefish Camouflage, *iScience* 1 (2018) 24-34.
6. J.M. Gosline, M.E. DeMont, Jet-propelled swimming in squids, *Scientific American* 252(1) (1985) 96-103.
7. S. Armon, E. Efrati, R. Kupferman, E. Sharon, Geometry and Mechanics in the Opening of Chiral Seed Pods, *Science* 333(6050) (2011) 1726-1730.
8. Y. Yang, X. Song, X. Li, Z. Chen, C. Zhou, Q. Zhou, Y. Chen, Recent Progress in Biomimetic Additive Manufacturing Technology: From Materials to Functional Structures, *Advanced Materials* 30(36) (2018) 1706539.
9. H. Kim, S.-k. Ahn, D.M. Mackie, J. Kwon, S.H. Kim, C. Choi, Y.H. Moon, H.B. Lee, S.H. Ko, Shape morphing smart 3D actuator materials for micro soft robot, *Materials Today* 41 (2020) 243-269.
10. Y. Sun, J. Guo, T.M. Miller-Jackson, X. Liang, M.H. Ang, R.C.H. Yeow, Design and fabrication of a shape-morphing soft pneumatic actuator: Soft robotic pad, 2017 IEEE/RSJ International Conference on Intelligent Robots and Systems (IROS), 2017, pp. 6214-6220.
11. K. Bertoldi, V. Vitelli, J. Christensen, M. van Hecke, Flexible mechanical metamaterials, *Nature Reviews Materials* 2(11) (2017) 1-11.
12. F. Wenz, I. Schmidt, A. Lechner, T. Lichti, S. Baumann, H. Andrae, C. Eberl, Designing Shape Morphing Behavior through Local Programming of Mechanical Metamaterials, *Advanced Materials* 33(37) (2021) 2008617.
13. C. Coulais, E. Teomy, K. de Reus, Y. Shokef, M. van Hecke, Combinatorial design of textured mechanical metamaterials, *Nature* 535(7613) (2016) 529-532.
14. C. Jiang, F. Rist, H. Wang, J. Wallner, H. Pottmann, Shape-morphing mechanical metamaterials, *Computer-Aided Design* 143 (2022) 103146.
15. L. Jin, R. Khajetourian, J. Mueller, A. Rafsanjani, V. Tournat, K. Bertoldi, D.M. Kochmann, Guided transition waves in multistable mechanical metamaterials, *Proceedings of the National Academy of Sciences* 117(5) (2020) 2319-2325.
16. M. Mirzaali, S. Janbaz, M. Strano, L. Vergani, A.A. Zadpoor, Shape-matching soft mechanical metamaterials, *Scientific reports* 8(1) (2018) 1-7.
17. E. Hajiesmaili, D.R. Clarke, Reconfigurable shape-morphing dielectric elastomers using spatially varying electric fields, *Nature Communications* 10(1) (2019) 183.
18. J. Zhang, Y. Guo, W. Hu, R.H. Soon, Z.S. Davidson, M. Sitti, Liquid Crystal Elastomer-Based Magnetic Composite Films for Reconfigurable Shape-Morphing Soft Miniature Machines, *Advanced Materials* 33(8) (2021) 2006191.
19. W. Xu, K.S. Kwok, D.H. Gracias, Ultrathin Shape Change Smart Materials, *Accounts of Chemical Research* 51(2) (2018) 436-444.
20. W. Hilber, Stimulus-active polymer actuators for next-generation microfluidic devices, *Applied Physics A* 122(8) (2016) 751.
21. J. Gu, D.E. Breen, J. Hu, L. Zhu, Y. Tao, T.V.d. Zande, G. Wang, Y.J. Zhang, L. Yao, Geodesy: Self-rising 2.5D Tiles by Printing along 2D Geodesic Closed Path, *Proceedings of the 2019 CHI Conference on Human Factors in Computing Systems*, Association for Computing Machinery, Glasgow, Scotland Uk, 2019, p. Paper 37.
22. Y. Xia, Y. He, F. Zhang, Y. Liu, J. Leng, A Review of Shape Memory Polymers and Composites:

Design for adaption

- Mechanisms, Materials, and Applications, *Advanced Materials* 33(6) (2021) 2000713.
23. A.K. Bastola, M. Paudel, L. Li, Dot-patterned hybrid magnetorheological elastomer developed by 3D printing, *Journal of Magnetism and Magnetic Materials* 494 (2020) 165825.
 24. E. Yarali, M. Baniasadi, A. Zolfagharian, M. Chavoshi, F. Arefi, M. Hossain, A. Bastola, M. Ansari, A. Foyouzat, A. Dabbagh, M. Ebrahimi, M.J. Mirzaali, M. Bodaghi, Magneto-/ electro-responsive polymers toward manufacturing, characterization, and biomedical/ soft robotic applications, *Applied Materials Today* 26 (2022) 101306.
 25. H. Aharoni, Y. Xia, X. Zhang, R.D. Kamien, S. Yang, Universal inverse design of surfaces with thin nematic elastomer sheets, *Proceedings of the National Academy of Sciences* 115(28) (2018) 7206-7211.
 26. M. Champeau, D.A. Heinze, T.N. Viana, E.R. de Souza, A.C. Chinellato, S. Titotto, 4D Printing of Hydrogels: A Review, *Advanced Functional Materials* 30(31) (2020) 1910606.
 27. Y. Dong, S. Wang, Y. Ke, L. Ding, X. Zeng, S. Magdassi, Y. Long, 4D Printed Hydrogels: Fabrication, Materials, and Applications, *Advanced Materials Technologies* 5(6) (2020) 2000034.
 28. T. Gao, E. Siéfert, A. DeSimone, B. Roman, Shape Programming by Modulating Actuation over Hierarchical Length Scales, *Advanced Materials* 32(47) (2020) 2004515.
 29. R.W. Mailen, C.H. Wagner, R.S. Bang, M. Zikry, M.D. Dickey, J. Genzer, Thermo-mechanical transformation of shape memory polymers from initially flat discs to bowls and saddles, *Smart Materials and Structures* 28(4) (2019) 045011.
 30. J. Cui, F.R. Poblete, Y. Zhu, Origami/Kirigami-Guided Morphing of Composite Sheets, *Advanced Functional Materials* 28(44) (2018) 1802768.
 31. C.M. Andres, J. Zhu, T. Shyu, C. Flynn, N.A. Kotov, Shape-Morphing Nanocomposite Origami, *Langmuir* 30(19) (2014) 5378-5385.
 32. L. Jin, A.E. Forte, B. Deng, A. Rafsanjani, K. Bertoldi, Kirigami-Inspired Inflatables with Programmable Shapes, *Advanced Materials* 32(33) (2020) 2001863.
 33. G.P.T. Choi, L.H. Dudte, L. Mahadevan, Programming shape using kirigami tessellations, *Nature Materials* 18(9) (2019) 999-1004.
 34. R.M. Neville, F. Scarpa, A. Pirrera, Shape morphing Kirigami mechanical metamaterials, *Scientific Reports* 6(1) (2016) 31067.
 35. H. Aharoni, E. Sharon, R. Kupferman, Geometry of Thin Nematic Elastomer Sheets, *Physical Review Letters* 113(25) (2014) 257801.
 36. Z. Li, Q. Wang, P. Du, C. Kadapa, M. Hossain, J. Wang, Analytical study on growth-induced axisymmetric deformations and shape-control of circular hyperelastic plates, *International Journal of Engineering Science* 170 (2022) 103594.
 37. M. Barletta, A. Gisario, M. Mehrpouya, 4D printing of shape memory polylactic acid (PLA) components: Investigating the role of the operational parameters in fused deposition modelling (FDM), *Journal of Manufacturing Processes* 61 (2021) 473-480.
 38. T. van Manen, S. Janbaz, A.A. Zadpoor, Programming the shape-shifting of flat soft matter, *Materials Today* 21(2) (2018) 144-163.
 39. A.S. Gladman, E.A. Matsumoto, R.G. Nuzzo, L. Mahadevan, J.A. Lewis, Biomimetic 4D printing, *Nature Materials* 15(4) (2016) 413-418.
 40. Q. Zhang, K. Zhang, G. Hu, Smart three-dimensional lightweight structure triggered from a thin composite sheet via 3D printing technique, *Scientific Reports* 6(1) (2016) 22431.
 41. S. Timoshenko, Analysis of bi-metal thermostats, *Josa* 11(3) (1925) 233-255.
 42. T. van Manen, S. Janbaz, A.A. Zadpoor, Programming 2D/3D shape-shifting with hobbyist 3D printers, *Materials Horizons* 4(6) (2017) 1064-1069.
 43. S. Janbaz, R. Hedayati, A.A. Zadpoor, Programming the shape-shifting of flat soft matter: from self-rolling/self-twisting materials to self-folding origami, *Materials Horizons* 3(6) (2016) 536-547.
 44. Z. Ding, O. Weeger, H.J. Qi, M.L. Dunn, 4D rods: 3D structures via programmable 1D composite rods, *Materials & Design* 137 (2018) 256-265.
 45. X. Wan, Y. He, Y. Liu, J. Leng, 4D printing of multiple shape memory polymer and nanocomposites with biocompatible, programmable and selectively actuated properties, *Additive Manufacturing* 53

- (2022) 102689.
46. Y. Klein, E. Efrati, E. Sharon, Shaping of Elastic Sheets by Prescription of Non-Euclidean Metrics, *Science* 315(5815) (2007) 1116-1120.
 47. S.J. Callens, R.J. Uyttendaele, L.E. Fratila-Apachitei, A.A. Zadpoor, Substrate curvature as a cue to guide spatiotemporal cell and tissue organization, *Biomaterials* 232 (2020) 119739.
 48. C.D. Santina, D. Rus, Control Oriented Modeling of Soft Robots: The Polynomial Curvature Case, *IEEE Robotics and Automation Letters* 5(2) (2020) 290-298.
 49. D. Rus, M.T. Tolley, Design, fabrication and control of soft robots, *Nature* 521(7553) (2015) 467-475.
 50. H. Wang, M. Totaro, L. Beccai, Toward Perceptive Soft Robots: Progress and Challenges, *Advanced Science* 5(9) (2018) 1800541.
 51. F. Khan, A. Donder, S. Galvan, F.R.y. Baena, S. Misra, Pose Measurement of Flexible Medical Instruments Using Fiber Bragg Gratings in Multi-Core Fiber, *IEEE Sensors Journal* 20(18) (2020) 10955-10962.
 52. A. De Greef, P. Lambert, A. Delchambre, Towards flexible medical instruments: Review of flexible fluidic actuators, *Precision Engineering* 33(4) (2009) 311-321.
 53. M.J. Mirzaali, A. Ghorbani, K. Nakatani, M. Nouri-Goushki, N. Tümer, S.J.P. Callens, S. Janbaz, A. Accardo, J. Bico, M. Habibi, A.A. Zadpoor, Curvature Induced by Deflection in Thick Meta-Plates, *Advanced Materials* 33(30) (2021) 2008082.
 54. C. Yuan, F. Wang, Q. Ge, Multimaterial direct 4D printing of high stiffness structures with large bending curvature, *Extreme Mechanics Letters* 42 (2021) 101122.
 55. M. Bodaghi, A.R. Damanpack, W.H. Liao, Adaptive metamaterials by functionally graded 4D printing, *Materials & Design* 135 (2017) 26-36.
 56. S. Nikravesi, D. Ryu, Y.-L. Shen, Direct numerical simulation of buckling instability of thin films on a compliant substrate, *Advances in Mechanical Engineering* 11(4) (2019) 1687814019840470.
 57. S. Nikravesi, D. Ryu, Y.-L. Shen, instabilities of thin films on a compliant Substrate: Direct numerical Simulations from Surface Wrinkling to Global Buckling, *Scientific reports* 10(1) (2020) 1-19.
 58. T. van Manen, V.M. Dehabadi, M.C. Saldívar, M.J. Mirzaali, A.A. Zadpoor, Theoretical stiffness limits of 4D printed self-folding metamaterials, *Communications Materials* 3(1) (2022).
 59. S.J.P. Callens, D.C. Tourolle Ne Betts, R. Muller, A.A. Zadpoor, The local and global geometry of trabecular bone, *Acta Biomater* 130 (2021) 343-361.
 60. D. Panozzo, E. Puppo, L. Rocca, Efficient multi-scale curvature and crease estimation, 2nd International Workshop on Computer Graphics, Computer Vision and Mathematics, GraVisMa 2010 - Workshop Proceedings, 2010, pp. 9-16.
 61. A. Jacobson, et al., libigl: A simple C++ geometry processing library, (2016).
 62. T. Adibaskoro, M. Makowska, A. Rinta-Paavola, S. Fortino, S. Hostikka, Elastic Modulus, Thermal Expansion, and Pyrolysis Shrinkage of Norway Spruce Under High Temperature, *Fire Technology* 57(5) (2021) 2451-2490.

9

Concluding remarks

*“To improve is to change;
to be perfect is to change often.”*

– Winston Churchill

9.1 Main findings

This thesis has contributed to advancing the design of patient-specific medical devices. Integrating digital manufacturing technologies, such as 3D printing, computational models, and advanced materials, has enhanced the customization and functionality of implants tailored to individual anatomical features.

9.2 General discussion

Shape personalization— This research's central theme was achieving a precise fit for patient-specific implants [1-3]. **Chapters 4 and 5** demonstrated how a design approach based on patient anatomy, using 3D reconstruction from patient data and 3D printing technology, could produce highly personalized implants that closely match the unique anatomical features of each patient. This approach ensured that the implants were not only anatomically accurate but also biomechanically compatible with the physiological demands of each individual. In **Chapter 7**, flexible design frameworks were introduced, allowing for the rapid customization of implants to match patient-specific requirements. These frameworks ensured anatomical fit while maintaining production efficiency, allowing for fast customization without compromising the biomechanical performance of the implant. The ability to modify and optimize designs without relying on patient data contributed significantly to improved time and cost efficiency without sacrificing the fit or strength of the implants. **Chapter 8** introduced 4D printing as an innovative concept to further enhance patient fit. This chapter explored the potential of shape-morphing implants that can adapt to patient anatomy over time in response to external stimuli. By examining different curvatures, this research highlighted the possibility of developing dynamic implants that can change shape, offering a more personalized and adaptive fit. This approach allows future implants to evolve continuously and improve patient care.

Time efficiency— One of this work's most impactful contributions is improving the time efficiency of the design and production of custom implants. The development of a streamlined workflow, as presented in **Chapter 4**, significantly reduces the time required to move from initial design concept to completed product. Traditional methods of producing custom implants often involve labor-intensive and time-consuming processes, leading to delays in patient care and increased costs. However, this thesis demonstrates a significant advancement in reducing these production bottlenecks by integrating advanced computational models and semi-automated workflows.

In **Chapter 4**, a semi-automated design process was developed, leveraging computational models and optimization techniques to create highly personalized implants more efficiently. This approach significantly reduced the manual labor and time required to design custom medical devices. The research showcased how the transition from

concept to a final implant can be expedited without sacrificing accuracy or performance by utilizing algorithms that automate critical stages of the design and manufacturing processes.

Topology optimization algorithms, discussed in **Chapters 4 and 5**, further contributed to time efficiency by allowing for the rapid generation of designs tailored to patient anatomy and biomechanical requirements. These computational tools enabled real-time adjustments to implant geometries, reducing design time. Additionally, the mechanical testing setups, which simulated physiological loading conditions, ensured that despite the accelerated design process, the implants met the necessary performance standards for durability and functionality.

Additionally, **Chapter 7** introduced a flexible design framework that allows for the rapid adaptation of generic implants to fit individual patients. This framework enables customization without requiring completely new designs for each patient, significantly reducing production time and associated costs. This development ensures that patient-specific solutions can be delivered promptly without compromising fit or functionality.

Enhancing Functionality— This thesis investigated several strategies to optimize implant design, enhancing customization and functionality for patient-specific applications. **Chapters 4 and 5** explored the application of topology optimization algorithms, which refine the initial design domain extracted from the patient's anatomical data by balancing stress distribution and material usage. These algorithms enabled the creation of designs that not only conformed precisely to each patient's unique anatomical features but also improved biomechanical performance by optimizing load transfer and structural integrity.

In **Chapter 4**, integrating lattice structures into the optimized designs further improved implant functionality. These structures are intended to provide a scaffold that promotes tissue integration and osseointegration while maintaining the mechanical strength required for long-term success. This approach enhances the potential for better tissue integration and overall implant performance, contributing to more reliable implants, less invasive surgical procedures, and faster healing times.

Chapter 6 advanced implant design by incorporating functionally graded materials (FGMs), which enable a gradual variation in material properties across the implant. This approach improves biomechanical integration by closely replicating the natural gradients in biological tissues, allowing for more effective load transfer and enhanced kinematics. As a result, the implant can better adapt to the physiological demands of the body, improving both biomechanical performance and the overall movement of the reconstructed tissue.

Biomechanical evaluation— The biomechanical evaluation in this thesis aimed to ensure that the implants could withstand critical physiological loading conditions.

Chapters 4, 5, 6, and 7 presented detailed discussions on the mechanical testing of the implants under both quasi-static and cyclic loading conditions. While the mechanical testing setup did not replicate all the forces and stresses experienced by implants *in vivo*, it addressed several critical loading conditions essential for assessing durability and performance. These tests validated the computational models and confirmed the reliability of the designs under critical loading conditions. Building on the validations, the research developed more complex models that better simulated physiological conditions. This approach ensured that the implants, optimized through computational methods and workflows, could meet the demanding requirements for long-term success in clinical applications.

9.3 General discussion

This thesis has explored multiple design methodologies to optimize patient-specific medical devices, focusing on improving the customization and functionality of implants. By integrating the digital manufacturing technologies, computational modeling, and advanced materials, new approaches have been developed to overcome the limitations of conventional implant design. This discussion will analyze the methodologies used in this research in the context of their practical applications and the broader landscape of existing literature, followed by acknowledging the remaining challenges and unresolved questions.

Design Methodologies

Topology optimization algorithms, discussed in **Chapters 4 and 5**, have been a critical contributor to improving implant design. By refining the design domain based on anatomical data, these algorithms provided a means to balance stress distribution and material usage, resulting in implants that conform more closely to patient-specific anatomies. This approach aligns with trends in the current literature, where optimization algorithms are increasingly recognized for improving biomechanical performance while reducing the implant weight [4-9]. The application of lattice structures, intended to enhance tissue integration and osseointegration, also reflects ongoing research efforts to improve medical implants' biological and mechanical performance [10-14].

Another significant advancement is using functionally graded materials (FGMs), as shown in **Chapter 6**. FGMs enable a gradual transition in material properties across the implant, closely mimicking natural tissue gradients and optimizing load transfer. The concept of FGMs has been increasingly explored in the literature for its ability to bridge the gap between artificial materials and biological tissues [15-21]. This method offers a promising solution to ensuring biomechanical compatibility between the implant and adjacent tissues, making it a noteworthy contribution to implant design.

The development of flexible design frameworks, as introduced in **Chapter 7**, also holds practical significance. The ability to rapidly customize implants without relying on individual patient data addresses the pressing need for time-efficient and cost-effective solutions in clinical settings. These frameworks allow for real-time design adaptation and directly impact the practicality of producing personalized implants on a larger scale without compromising performance. This flexibility positions the framework as a potential game-changer in the industry, providing a pathway for the mass customization of medical devices.

Miscommunication in the design process

Miscommunication between designers, surgeons, and patients is a significant challenge in patient-specific medical device design, leading to implants that may not fully meet clinical or patient needs [22, 23]. To address this, **Chapter 4** introduced a semi-automated platform developed from the input of both surgeons and designers. The platform guides the design process by embedding key objectives and requirements from each discipline at every stage. Considering surgical constraints, patient anatomy, and biomechanical performance helps prevent misaligned designs and ensures that all critical factors are addressed before finalizing the implant. This approach reduces the risk of miscommunication, streamlining the design process and improving implant outcomes.

The concept of one-design-fits-all: Good or Bad?

A critical reflection on the concept of one-design-fits-all raises questions about its suitability in medical device design. Traditionally, one-design-fits-all approaches have been used in mass production to meet the needs of a broad range of patients with standardized solutions. While this method offers clear benefits in cost-effectiveness and production efficiency, it inherently lacks the adaptability required to address the anatomical and biomechanical diversity found in individual patients. This limitation can result in poor fit, reduced functionality, and increased rates of complications or revision surgeries.

From the findings of this thesis, the customization of implants based on patient-specific data has proven to improve both the fit and biomechanical performance of implants significantly. This suggests that more than a one-size-fits-all approach is needed when meeting individual patients' diverse and complex needs. However, introducing flexible design frameworks in **Chapter 7** presents a middle ground, where a generic design can be quickly adapted to individual patients without requiring a completely new design each time. This approach offers a more efficient alternative to fully customized designs while maintaining an acceptable level of personalization.

Concluding remarks

Is one-design-fits-all needed?

Despite its limitations, there are situations where a one-design-fits-all approach may still be necessary. In emergencies, where rapid response is critical, having standardized designs that can be deployed immediately may outweigh the need for a perfect fit. Moreover, the cost and time required for fully customized implants may not be feasible in healthcare systems with limited resources. In such cases, standardized designs offer a practical solution, ensuring that more patients receive care within a reasonable timeframe.

That said, one-design-fits-all should not be seen as the ultimate solution but rather as a complement to more personalized approaches. Advances in digital manufacturing technologies, such as 3D and 4D printing, are gradually bridging the gap between standardization and personalization, making it possible to deliver solutions that can be rapidly adapted to individual patients while maintaining production efficiency.

The future of one-design-fits-all

The question of whether the concept of one-design-fits-all can evolve to adapt to every individual is intriguing. While achieving true one-design-fits-all in its traditional sense may not be possible, the future likely holds a hybrid approach. With the continued development of flexible design frameworks, real-time design adaptation, and advanced manufacturing techniques, creating "semi-custom" designs that combine standardization efficiency with personalization's adaptability may be possible.

For instance, implants could be designed with modular or adjustable components that can be fine-tuned to fit individual patients during surgery. Similarly, incorporating intelligent materials, such as those used in 4D printing, could allow for implants that dynamically adjust to patient anatomy changes over time. These advances suggest that the future of medical device design may lie in a more adaptable, scalable form of customization, where designs can be rapidly adjusted to meet individual needs without the resource-intensive process of creating fully customized implants from scratch.

How AI can help

Artificial intelligence (AI) can potentially transform the one-design-fits-all concept into a more adaptable and personalized approach [24, 25]. By leveraging predictive modeling, AI can analyze large anatomical and biomechanical data datasets to create designs that fit a wide range of patients [26-29]. This allows for semi-customized implants that maintain the efficiency of standardized production while offering a better fit for individual patients.

AI can also automate customization by rapidly adjusting base designs to match a patient's unique anatomy in real time. This reduces manual labor and time, enabling clinics to offer personalized solutions more efficiently. In manufacturing, AI-driven systems can monitor and adjust production in real time, ensuring that personalized

implants are produced accurately and quickly, further enhancing the scalability of these designs [30, 31].

Moreover, AI enables predictive maintenance through embedded sensors, which monitor performance and predict adjustments [31-34]. Combined with 4D printing, implants could adapt dynamically over time, reducing the need for revisions and improving long-term outcomes.

Finally, AI can optimize scalability by creating adaptable design algorithms that balance customization with production speed [35, 36]. This ensures personalized implants can be delivered quickly and efficiently, making them accessible in a broader range of healthcare settings. AI offers a promising future for one-design-fits-all, where implants can be rapidly customized and manufactured to meet individual needs without sacrificing efficiency.

Practical Applications

The methodologies presented in this thesis have clear applications in clinical settings, particularly in orthopedics and reconstructive surgery. The ability to create implants precisely tailored to individual anatomical features is expected to reduce the risk of implant failure, revision surgeries, and postoperative complications. Moreover, using advanced computational models and workflows to streamline the design process ensures that these solutions can be delivered promptly, directly addressing one of the most significant bottlenecks in patient-specific care.

Incorporating technologies like 3D printing and 4D printing into the design process also opens new avenues for practical applications in patient care. The capacity for dynamic, shape-morphing implants (discussed in **Chapter 8**) to adapt to patient anatomy offers an exciting prospect for long-term medical treatments, where implants can evolve in response to physiological changes. However, this area is still emerging, and further clinical validation is necessary before these implants can be widely adopted.

9.4 Challenges and unresolved questions

While this thesis made significant advancements, several challenges and unresolved questions remain. One major challenge is bridging the gap between computational models and outcomes observed in clinical practice. While mechanical testing validated the computational models, further *in-vivo* studies are necessary to fully understand how these implants behave under actual physiological conditions over time.

Future research should also focus on incorporating musculoskeletal modeling into computational workflows. This would allow for more comprehensive simulations of interactions between implants and surrounding muscles, tendons, and bones, improving the accuracy of force representations and predictions for implant performance.

Concluding remarks

In **Chapter 4**, one type of lattice structures was explored, and a topology-optimized structure capable of incorporating different lattice types was generated. Future research could explore how other lattice structures might be integrated to enhance mechanical performance, tissue integration, and overall implant stability.

In **Chapter 6**, the focus was on mandibular kinematics, specifically clenching and biting. Although increased movement during these actions could more closely mimic natural chewing, it is not the primary issue patients face. The real challenge is the need for mouth opening due to the absence of mandible translation from the neo fossa. Future research could explore how to mimic natural mouth-opening movements to address this issue better.

Another area for improvement is the scalability of some of the methods discussed. While the flexible design framework, discussed in **Chapter 7**, enables rapid customization, questions remain about efficiently scaling these technologies for widespread use in healthcare systems, particularly in low-resource settings where access to advanced technologies may be limited. Moreover, while functionally graded materials and lattice structures show promise, challenges remain in ensuring consistent and reliable production of these complex designs, especially as the complexity of implants continues to increase.

Finally, incorporating 4D printing and shape-morphing implants raises ethical and regulatory questions that have yet to be fully addressed. How will the regulatory framework evolve to accommodate dynamic, adaptive medical devices? And how do we ensure that these technologies are safe, reliable, and equitable?

Bibliography

1. A.A. Zadpoor, Design for Additive Bio-Manufacturing: From Patient-Specific Medical Devices to Rationally Designed Meta-Biomaterials, *International Journal of Molecular Sciences*, 2017.
2. A.A. Zadpoor, H. Weinans, Patient-specific bone modeling and analysis: The role of integration and automation in clinical adoption, *Journal of Biomechanics* 48(5) (2015) 750-760.
3. J.-A. Lee, Y.-G. Koh, K.-T. Kang, Biomechanical and Clinical Effect of Patient-Specific or Customized Knee Implants: A Review, *Journal of Clinical Medicine*, 2020.
4. J.J. Lang, M. Bastian, P. Foehr, M. Seebach, J. Weitz, C. von Deimling, B.J. Schwaiger, C.M. Micheler, N.J. Wilhelm, C.U. Grosse, M. Kesting, R. Burgkart, Improving mandibular reconstruction by using topology optimization, patient specific design and additive manufacturing?—A biomechanical comparison against miniplates on human specimen, *PLOS ONE* 16(6) (2021) e0253002.
5. L. Shi, H. Li, A.S. Fok, C. Ucer, H. Devlin, K. Homer, Shape optimization of dental implants, *International Journal of Oral & Maxillofacial Implants* 22(6) (2007).
6. H. Kang, J.P. Long, G.D.U. Goldner, S.A. Goldstein, S.J. Hollister, A paradigm for the development and evaluation of novel implant topologies for bone fixation: implant design and fabrication, *Journal of biomechanics* 45(13) (2012) 2241-2247.
7. N. Dai, J.-F. Zhu, M. Zhang, L.-Y. Meng, X.-L. Yu, Y.-H. Zhang, B.-Y. Liu, S.-L. Zhang, Design of a maxillofacial prosthesis based on topology optimization, *Journal of mechanics in medicine and biology* 18(03) (2018) 1850024.
8. T. Iqbal, L. Wang, D. Li, E. Dong, H. Fan, J. Fu, C. Hu, A general multi-objective topology optimization methodology developed for customized design of pelvic prostheses, *Med Eng Phys* 69 (2019) 8-16.
9. M. Peto, J. García-Ávila, C.A. Rodriguez, H.R. Siller, J.V.L. da Silva, E. Ramírez-Cedillo, Review on structural optimization techniques for additively manufactured implantable medical devices, *Frontiers in Mechanical Engineering* 10 (2024).
10. T.-M. De Witte, L.E. Fratila-Apachitei, A.A. Zadpoor, N.A. Peppas, Bone tissue engineering via growth factor delivery: from scaffolds to complex matrices, *Regenerative Biomaterials* 5(4) (2018) 197-211.
11. P. Kilina, A.G. Kuchumov, L. Sirotenko, V. Vassilouk, S. Golovin, A. Drozdov, E.V. Sadyrin, Influence of porous titanium-based jaw implant structure on osseointegration mechanisms, *Journal of the Mechanical Behavior of Biomedical Materials* 160 (2024) 106724.
12. F.A. Shah, P. Thomsen, A. Palmquist, Osseointegration and current interpretations of the bone-implant interface, *Acta Biomaterialia* 84 (2019) 1-15.
13. D. Martinez-Marquez, Y. Delmar, S. Sun, R.A. Stewart, Exploring Macroporosity of Additively Manufactured Titanium Metamaterials for Bone Regeneration with Quality by Design: A Systematic Literature Review, *Materials*, 2020.
14. Y.-T. Wang, C.-K. Hsu, Novel parameter optimization lattice design for improving osseointegration in hypo-loading regions – A case study of maxillary tumor reconstruction implant, *Materials & Design* 233 (2023) 112274.
15. W. Guo, Z. Jiang, H. Zhong, G. Chen, X. li, H. Yan, C. Zhang, L. Zhao, 3D printing of multifunctional gradient bone scaffolds with programmable component distribution and hierarchical pore structure, *Composites Part A: Applied Science and Manufacturing* 166 (2023) 107361.
16. C. Pitta Kruize, S. Panahkhahi, N.E. Putra, P. Diaz-Payno, G. van Osch, A.A. Zadpoor, M.J. Mirzaali, Biomimetic Approaches for the Design and Fabrication of Bone-to-Soft Tissue Interfaces, *ACS Biomaterials Science & Engineering* 9(7) (2023) 3810-3831.
17. H. Shi, P. Zhou, J. Li, C. Liu, L. Wang, Functional Gradient Metallic Biomaterials: Techniques, Current Scenery, and Future Prospects in the Biomedical Field, *Frontiers in Bioengineering and Biotechnology* 8 (2021).
18. M.J. Mirzaali, A. Herranz de la Nava, D. Gunashekar, M. Nouri-Goushki, E.L. Doubrovski, A.A. Zadpoor, Fracture Behavior of Bio-Inspired Functionally Graded Soft–Hard Composites Made by Multi-Material 3D Printing: The Case of Colinear Cracks, *Materials*, 2019.

Concluding remarks

19. M.J. Mirzaali, A. Herranz de la Nava, D. Gunashekar, M. Nouri-Goushki, R.P.E. Veeger, Q. Grossman, L. Angeloni, M.K. Ghatkesar, L.E. Fratila-Apachitei, D. Ruffoni, E.L. Doubrovski, A.A. Zadpoor, Mechanics of bioinspired functionally graded soft-hard composites made by multi-material 3D printing, *Composite Structures* 237 (2020) 111867.
20. M.J. Mirzaali, M. Cruz Saldívar, A. Herranz de la Nava, D. Gunashekar, M. Nouri-Goushki, E.L. Doubrovski, A.A. Zadpoor, Multi-Material 3D Printing of Functionally Graded Hierarchical Soft-Hard Composites, *Advanced Engineering Materials* 22(7) (2020) 1901142.
21. M.C. Saldívar, S. Salehi, R.P. Elias Veeger, E. Tay, M. Fenu, A. Cantamessa, M. Klimopoulou, G. Talò, M. Moretti, S. Lopa, D. Ruffoni, G.J.V.M. van Osch, L.E. Fratila-Apachitei, Z. Doubrovski, M.J. Mirzaali, A.A. Zadpoor, Rational positioning of 3D-printed voxels to realize high-fidelity multifunctional soft-hard interfaces, *Cell Reports Physical Science* 4(9) (2023).
22. S. Peel, D. Eggbeer, P. Dorrington, Standardizing the patient-specific medical device design process via a paper-based pro-forma, *Journal of Design, Business & Society* 6(Design for Medicine and Healthcare) (2020) 233-258.
23. C. Le, M. Okereke, V.H. Nguyen, V.D. Dao, S. Soe, N. Zlatov, T.H. Le, Personalised medical product development: Methods, challenges and opportunities, *Romanian Review Precision Mechanics, Optics and Mechatronics* 40 (2011) 11-20.
24. N.J. Schork, Artificial intelligence and personalized medicine, *Precision medicine in Cancer therapy* (2019) 265-283.
25. N. Noorbakhsh-Sabet, R. Zand, Y. Zhang, V. Abedi, Artificial Intelligence Transforms the Future of Health Care, *The American Journal of Medicine* 132(7) (2019) 795-801.
26. G.M. Mallow, Z.K. Siyaji, F. Galbusera, A.A. Espinoza-Orias, M. Giers, H. Lundberg, C. Ames, J. Karppinen, P.K. Louie, F.M. Phillips, R. Pourzal, J. Schwab, D.M. Sciubba, J.C. Wang, H.-J. Wilke, F.M.K. Williams, S.A. Mohiuddin, M.C. Makhni, N.A. Shepard, H.S. An, D. Samartzis, Intelligence-Based Spine Care Model: A New Era of Research and Clinical Decision-Making, *Global Spine Journal* 11(2) (2020) 135-145.
27. F. Galbusera, G. Casaroli, T. Bassani, Artificial intelligence and machine learning in spine research, *JOR SPINE* 2(1) (2019) e1044.
28. S. Mouloudi, H. Rahmanpanah, S. Gohari, C. Burvill, K.M. Tse, H.M.S. Davies, What can artificial intelligence and machine learning tell us? A review of applications to equine biomechanical research, *Journal of the Mechanical Behavior of Biomedical Materials* 123 (2021) 104728.
29. D.J. Saxby, B.A. Killen, C. Pizzolato, C.P. Carty, L.E. Diamond, L. Modenese, J. Fernandez, G. Davico, M. Barzan, G. Lenton, S.B. da Luz, E. Suwarganda, D. Devaprakash, R.K. Korhonen, J.A. Alderson, T.F. Besier, R.S. Barrett, D.G. Lloyd, Machine learning methods to support personalized neuromusculoskeletal modelling, *Biomechanics and Modeling in Mechanobiology* 19(4) (2020) 1169-1185.
30. C. Liu, W. Tian, C. Kan, When AI meets additive manufacturing: Challenges and emerging opportunities for human-centered products development, *Journal of Manufacturing Systems* 64 (2022) 648-656.
31. A. Boretti, A narrative review of AI-driven predictive maintenance in medical 3D printing, *The International Journal of Advanced Manufacturing Technology* 134(5) (2024) 3013-3024.
32. Z. Zhu, D.W.H. Ng, H.S. Park, M.C. McAlpine, 3D-printed multifunctional materials enabled by artificial-intelligence-assisted fabrication technologies, *Nature Reviews Materials* 6(1) (2021) 27-47.
33. M. Pech, J. Vrchota, J. Bednář, Predictive Maintenance and Intelligent Sensors in Smart Factory: Review, *Sensors*, 2021.
34. N.V. Kumar, D. Chakradhar, P. Abhilash, Advancing bioimplant manufacturing through artificial intelligence, *Bioimplants Manufacturing*, CRC Press 2024, pp. 284-312.
35. D. Mourtzis, N. Panopoulos, P. Stavropoulos, N. Papakostas, Artificial Intelligence for Production Management and Control Towards Mass Personalization of Global Networks, in: T. Tolio (Ed.), *CIRP Novel Topics in Production Engineering: Volume 1*, Springer Nature Switzerland, Cham, 2024, pp. 267-312.
36. J. Wan, X. Li, H.N. Dai, A. Kusiak, M. Martínez-García, D. Li, Artificial-Intelligence-Driven Customized Manufacturing Factory: Key Technologies, Applications, and Challenges, *Proceedings of the IEEE* 109(4) (2021) 377-398.

Acknowledgements



J.S. Bach | Chaconne from the Partita No. 2 in D minor for Solo Violin, BWV 1004

The sun is shining with its full power, and it is time to sit, reflect, and remember every moment of the academic life I have lived. Writing these words feels like closing a chapter, one that began long before I even realized it.

My journey into this academic life began with my mother, who first brought me into this world. She cared for my first steps and spent countless nights awake beside me, nurturing my growth with patience. **Maman**, my time has come. Thank you for everything.

This has been an incredible journey, and I am grateful for every twist and turn. What began as a pursuit of knowledge became a tapestry woven with the threads of collaboration, failure, and unexpected joy. Along the way, I met brilliant minds who shaped not only how I think but also what I think, making this experience unforgettable. To all of you who walked beside me, thank you.

I owe my deepest gratitude to my promoters and supervisors, **Amir**, **Mohammad**, and **Jie**, whose guidance was both compass and catalyst.

Amir, I must confess, I learned far more from you than just biomechanics. You taught me how to evolve, how to balance equations and fatherhood, how to measure forces and kindness with equal precision. Your critical thinking and generosity in teaching have left a lasting mark on me. Thank you for welcoming me into the world of biomechanics and for showing me how ideas can transcend the boundaries of the lab.

Mohammad, I still remember our first meeting in the additive manufacturing lab, where you introduced me to a world of endless possibilities. Thank you for giving me the freedom to explore, for always being open to wild ideas, and for standing by me during tough times. You never dismissed a "what if", even when the "how" seemed impossible.

Jie, your discipline, empathy, and structured thinking smoothed every rough edge of my PhD path. You showed me that rigor and laughter are not opposites but partners, like stress and strain, each revealing the other's purpose.

This thesis was built in labs and through experiments, and I could not have done it without **Sander** and **Arjan**. **Sander** Jan, thank you for always being there, for your discipline, your expertise, explaining every fact with graphs and sketches, and even your koobideh secrets. May the world one day grasp the value of "*No laugh in the lab*". **Arjan**, next to the samples, you CT-scanned our discussions, revealing hidden connections between academia and life. Thank you for the batch scans and the wisdom you shared.

To **Arthur, Ava, Leander, Naomi, Lorenzo, Simon, Afaq, Cindy**, and **Santiago**—this thesis stands on the foundation you helped build. Working alongside such dedicated researchers was one of the greatest privileges of this journey.

Collaborating with researchers across institutions and industries taught me that science is a constellation, not a solo star. **José Bico** and **Mehdi Habibi**, your critical feedback was the friction that polished my ideas. To **Rob Nelissen, Jasper Gerbers, Damien Broekhuis**, and **Bart Kaptein** (Leiden University Medical Center), **Brend Jonker** and **Eppo Wolvius** (Erasmus MC), **Vera Lagerburg** and **Melinda Witbreuk** (OLVG Hospital), and **Gerald Kraan** (Reinier de Graaf and Reinier Haga Orthopedisch Centrum)—thank you for bridging research and clinical practice. **Jasper**, those late nights wrapping up surgeries are etched in my mind; your dedication is inspiring. **Eric Garling** (Stryker), **Sepideh Ghodrati**, **Wolf Song**, **Zjenja Doubrovski** (Faculty of Industrial Design), **Wim van Paepegem** (Ghent University), and all the people I've met during the 3DMed project—your expertise elevated this work.

To my office mates, **Abdulrahman, Edwin, Ebrahim, Helda, Jason, Jelle, Jiahui, Jinlai, Keyu, Morteza, Niko**, and **Mohammad** (Mahmoodi), thank you for the jokes, cultural exchanges, and shared frustrations. **Edwin**, thank you for keeping the plants alive in our office. Keep up the good job.

The Biomaterials and Tissue Biomechanics (BTB) section became a second home. To **Lidy** and **Julian, Aikaterini, Ayman, Dirk, Giacomo, Giuly, Indra, Kai, Kardelen, Khashayar, Lenart, Lorenzo, Mahdiyeh, Mahya, Marco, Marina, Maarten, Mauricio, Michele, Monika, Nasim, Nazli, Pedro, Roderick, Saeed, Sahar, Sara, Sean, Sebastien, Shahram, Shima, Silvia, Tahir, Teunis, Zahra, and Zia**, thank you for the camaraderie and support.

Maneer Eka, you were always a surprise and a complete package of a good friend. If academia had a "Most Unexpected Hypothesis" award, you'd win it yearly. **Pier Hendrik de Jong**, our color debates may remain unresolved, but our collaboration was spectrophotometrically perfect. That framed "*Wanderer Above the Sea of Fog*" on the 3rd floor? It's you, always searching beyond the mist. **Ebi**, we started this PhD together on the same project but diverged like parallel lines, yet somehow, we still intersect where it matters. **Helda, Jinlai, Katerina, Lorenzo, Mahya, Mahmoodi, Morteza, Sahar**, and **Sara**, thank you for the coffee chats and much-needed breaks. **Katerina** and **Mahya**, your kindness during the final stretch reminded me what friendship means.

To my BMEchE colleagues, **Ajay, Ali, Alfred, Amanda, Angelique, Anneke, Behrooz, Camila, Corrina, Esther, Gabriele, Gerwin, Imas, Ioannis, Judith, Jette, Koen, Kirsten, Maria, Marjolijn, Matthew, Merle, Mostafa, Paul, Ragnhild, Sabrina, Tamas, Vera, and Vikash**, your kindness kept me going.

Moving to the Netherlands during a pandemic felt like debugging code without documentation, but **Sattar, Elham, and Rayeen**, you were my human API. **Sattar and Elham**, your kindness during the lockdown period was huge. **Rayeen**, you're a phenomenal footballer, never doubt it.

Amir and Helda, thank you for your companionship, for sharing experiences, laughter, and ice cream that melted my stress these past four years. Those simple moments of sweetness always arrived exactly when needed most. Saeede and I will always treasure the memories we've built with you, from life's breakthroughs to its simple joys.

To the hearts that made this journey beautiful—**Jiahui and Hensheng (and Bagel), Soroush and Shima, Ramin and Azadeh, Afshin and Reyhane, Niko and Ruud, Mc Ninja and Gangster, Anneke and Eric, Kath and Miguel (and Clay), Elise and Wout (and Lucas), Sander and Viviam (and Leache and Kippi), Saba and Nasibeh (and Aryana), Hossein and Elahe (and Aria), Sadegh and Meiling, Majid and Hengameh (and Shervin), Sahar and Abbas, Sara and Faraz (and Delara), Khashayar and Sara (and Dariush), Shokoufeh and Milad (and Niki and Nikan), Maedeh and Javad, Sobhan and Haniyeh (and Atrin), Hamed and Helia, Maryam and Ali (and Hana), Zahra and Hamed (and Sooma), Amir (Heidary), and Mahya and Hossein**—thank you for turning expat life into a potluck of joy. And to our neighbors, **Piet and Corry**, and the **Heilbijl community**, you made the Netherlands feel like home.

The path behind me glows with the light of those who walked alongside me. Whenever I look back, I see you all, not as footnotes, but as co-authors of this journey.

To my **Baba**, my first and finest hypothesis, no matter which chapter I revisit, your presence graces every page. You taught me that some truths defy peer review; they are felt in the quiet of a shared silence. You never demanded anything, only believed in me. That faith carried me further than you know.

To **Farideh**, my little sister, and **Salah**, my little brother, you were my control conditions, the constants that grounded me. Thank you for all your support. **Sina and Odin**, our family's newest lights, thank you for the joy you bring to our lives. **Baba Akbar and Maman Sima**, your stories and Gilaki lessons rooted me in culture. **Sara, Zizi, Zari, Mohammad, and Coco**, your love spans continents.

To my lifelong friends, **Hamed, Amin and Hakimeh (and Nila), Amir and Mojdeh (and Gandom), Amoo Ali, Ata, Mansour and Farnaz (and Arina), Mehran, Milad, Mohammad, Reza and Nasrin, and Siavash and Farzaneh, & Rahyab family**, distance never dimmed your support and distance was just another variable you controlled for.

Rose, *Rose-e-baba*, my little sunburst, you rewrote my definition of love. You taught me that love is not just something you feel, it's something you become. You taught me that the greatest discoveries aren't made in labs, but in the quiet moments, when your arms reach out, searching for mine. May your life be as boundless as your curiosity, and your path be as luminous as your laughter.

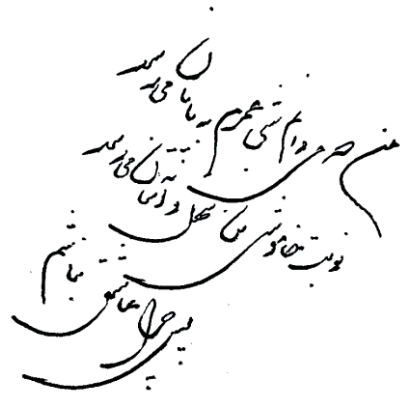
And finally, to my beautiful **Saeede**—my love, my rock, my *Jaan-o-Jahan*. You have been the steady solution to my chaos, the boundary condition that held me together. When the stress of looming deadlines felt overwhelming, you showed me the beauty of pausing to savor life's simplicity, wandering among the plants in the botanical garden with you. *Mooriook*, this thesis reflects our co-authored academic life—drafted in round-the-clock sessions, revised in patience, and published in shared dreams. Thank you for being my sanctuary in the storm, for every sacrificed weekend, every encouraging word, and for loving me not despite the PhD's chaos, but through it all. Your love has been the constant in the chaotic equation of my life.

As the clock's small hand nears midnight, this chapter ends, not with a full stop, but with an ellipsis. Tomorrow's sparrow will sing again; somewhere, a new equation will whisper its first variable. For now, I let go, trusting that every end is a seed carried by the wind of what's next—guided by Rose's laughter and Saeede's love.

Vahid Moosabeiki

April 2025

Oosterhout

A handwritten signature in Persian script, written in black ink. The signature is stylized and appears to be 'Vahid Moosabeiki'. It is written diagonally across the page.

List of publications

A. Publications

- **Moosabeiki, V.**, Leeﬂang, M.A., Gerbers, J.G., Broekhuis, D., Kaptein, B.L., Nelissen, R.G.H.H., Mirzaali, M.J., and Zadpoor, A.A., Additively manufactured shape-morphing implants for the treatment of acetabular defects, *Acta Biomaterialia*, Revised.
- de Jong, P.H., **Moosabeiki, V.**, Leeﬂang, M.A., Mirzaali, M.J., and Zadpoor, A.A., Lattice tracing of curved surfaces with metallic kinematic structures, *Applied Materials Today*, Under review.
- Putra, N.E., Raphaëlle, Y., **Moosabeiki, V.**, Leeﬂang, M.A., Klimopoulou, M., Mirzaali, M.j., Mol, J.M.C., Riool, M., Fratila-Apachitei, L.E., Zhou, J., Apachitei, I., and Zadpoor, A.A., Direct ink writing of sustainable multi-functional biodegradable porous Fe-eggshell scaffolds, *Acta Biomaterialia*, Under review.
- Isaakidou, A., Ganjian, M., **Moosabeiki, V.**, Goushki, M.N., Boukany, P., Wątroba, M., Groetsch, A., Schwiedrzik J., Mirzaali, M.J., Apachitei, I., Fratila-Apachitei, L.E., and Zadpoor, A.A., Microscale 3D printed pillars and porous structures: manufacturability and micromechanics, *Advanced Materials Technology*, Under review.
- Yarali, E., Mubeen, A.A., Cussen, K., van Zanten, L., **Moosabeiki, V.**, Zadpoor, A.A., Accardo, A., and Mirzaali, M.J., 4D printing of poly(N-isopropylacrylamide)-based hydrogel microarchitectures: two-photon polymerization for reversible shape morphing, *Scientific Reports*, Revised.
- **Moosabeiki, V.**, Khan, A., Cruz Saldivar, M., Van Paepegem, W., Jonker, B.P., Wolvius, E.B., Zhou, J., Tumer, N., Mirzaali, M.J. and Zadpoor, A.A., Multi-material 3D printing of functionally graded soft-hard interfaces for enhancing mandibular kinematics of temporomandibular joint replacement prostheses, *Communications Materials*, 5, 226, 2024.
- Putra, N.E., **Moosabeiki, V.**, Leeﬂang, M.A., Zhou, J. and Zadpoor, A.A., Biodegradation-affected fatigue behavior of extrusion-based additively manufactured porous iron-manganese scaffolds, *Acta Biomaterialia*, 178, p. 340-351, 2024.

- **Moosabeiki, V.**, Yarali, E., Ghalayaniesfahani, A., Callens, S.J., van Manen, T., Accardo, A., Ghodrat, S., Bico, J., Habibi, M., Mirzaali, M.J. and Zadpoor, A.A., Curvature tuning through defect-based 4D printing, *Communications Materials*, 5(1), p.10, 2024.
- Saldívar, M.C., Tay, E.T.W.S., Isaakidou, A., **Moosabeiki, V.**, Fratila-Apachitei, L.E., Doubrovski, E.L., Mirzaali, M.J. and Zadpoor, A.A., Bioinspired rational design of bi-material 3D printed soft-hard interfaces, *Nature Communications*, 14(1), p.7919, 2023.
- **Moosabeiki, V.**, de Winter, N., Saldivar, M.C., Leeflang, M.A., Witbreuk, M.M.E.H., Lagerburg, V., Mirzaali, M.J. and Zadpoor, A.A., 3D printed patient-specific fixation plates for the treatment of slipped capital femoral epiphysis: Topology optimization vs. conventional design, *Journal of the Mechanical Behavior of Biomedical Materials*, 148, p.106173, 2023.
- Brouwer de Koning, S.G., de Winter, N., **Moosabeiki, V.**, Mirzaali, M.J., Berenschot, A., Witbreuk, M.M.E.H. and Lagerburg, V., Design considerations for patient-specific bone fixation plates: a literature review, *Medical & Biological Engineering & Computing*, 61(12), pp.3233-3252, 2023.
- Mirzaali, M.J., **Moosabeiki, V.**, Rajaai, S.M., Zhou, J. and Zadpoor, A.A., Additive manufacturing of biomaterials—Design principles and their implementation, *Materials*, 15(15), p.5457, 2022.
- Van Kootwijk, A., **Moosabeiki, V.**, Saldivar, M.C., Pahlavani, H., Leeflang, M.A., Niar, S.K., Pellikaan, P., Jonker, B.P., Ahmadi, S.M., Wolvius, E.B., Tümer, N., Mirzaali, M.J., Zhou, J., and Zadpoor, A.A., Semi-automated digital workflow to design and evaluate patient-specific mandibular reconstruction implants, *Journal of the Mechanical Behavior of Biomedical Materials*, 132, p.105291, 2022.
- van Manen, T., **Moosabeiki, V.**, Saldívar, M.C., Mirzaali, M.J. and Zadpoor, A.A., Theoretical stiffness limits of 4D printed self-folding metamaterials. *Communications Materials*, 3(1), p.43, 2022.
- **Moosabeiki, V.**, Ghorbanpour, S., and Azimi, G., Application of artificial neural network to predict Vickers microhardness of AA6061 friction stir welded sheets, *Journal of Central South University*, 2016.
- **Moosabeiki, V.**, Zamani, J., Study of various clamped isotropic square plates simulating methods and compare with experimental results under high strain loads, *Modares Mechanical Engineering*, 14(13), 2015.

- Zamani, J., **Moosabeiki, V.**, and Alisalehi, O., The effect of various additives on the mechanical, thermal, and abrasive characteristics of ablative composites, *Sharif Journal of Mechanical Engineering*, 30(1), pp.137-141, 2014.
- Zamani, J., and **Moosabeiki, V.**, Manufacturing method of carbon/phenolic composites and its implication on ablative characteristics, *Journal of Polymer Science and Technology*, 26, pp.243-256, 2013.
- **Moosabeiki, V.**, Azimi, G., and Ghayoor, M., Influences of tool pin profile and tool shoulder curvature on the formation of friction stir welding zone in AA6061 aluminium alloy, *Advanced Materials Research*, 445, 789-794, 2012.
- Mehranfar, Y., **Moosabeiki, V.**, Zarshenas, M., Vakili, F., and Kadkhodaei, M., A modified Voith Schneider Propeller VSP—Manufacturing and test of a new mechanism of a cycloidal propeller, Iranian Patent No. 51433, 2009.
- Mehranfar, Y., **Moosabeiki, V.**, Babaie, H., Sedaghat, A., and Shirani, E., Free flow turbine with a specific circulation direction, Iranian Patent No. 42446, 2008.

B. Conference presentations

- **Moosabeiki, V.**, van Kootwijk, A., Saldivar, M.C., Pahlavani, H., Leeflang, M.L., Niar, S., Jonker, B.P., Ahmadi, S.M., Wolvius, E.B., Zhou, J., Tumer, N., Mirzaali, M.J., Zadpoor, A.A., Patient-specific mandibular reconstruction implant: design workflow and biomechanical performance, European Society of Biomechanics, Edinburgh, Scotland (2024, oral presentation)
- **Moosabeiki, V.**, Mirzaali, M.J., Zadpoor A.A., Efficient design process for patient-specific medical devices, BMEchE, Hoofddorp, The Netherlands (2024, poster presentations)
- **Moosabeiki, V.**, de Winter, N., Saldivar, M.C., Leeflang, M.L., Witbreuk, M.M.E.H, Lagerburg, V., Mirzaali, M.J., Zadpoor, A.A., Patient-specific bone plates: design strategies and biomechanical performance, European Society of Biomechanics, Maastricht, The Netherlands (2023, oral presentation)

